Compact antennas with radiation constraints manufactured using additive technologies for UAV and nanosatellite applications

Carlos David Morales Pena

Université Fédérale

Toulouse Midi-Pyrénées

THÈSE

En vue de l'obtention du

DOCTORAT DE L'UNIVERSITÉ DE TOULOUSE

Délivré par :

Institut Supérieur de l'Aéronautique et de l'Espace

Présentée et soutenue par :
Carlos David MORALES PEÑA
le mardi 7 décembre 2021

Titre :

Antennes compactes à base de technologie additive répondant à des contraintes en rayonnement pour drones et nanosatellites

Compact antennas with radiation constraints manufactured using additive technologies for UAV and nanosatellite applications

---

École doctorale et discipline ou spécialité :

ED GEET : Électromagnétisme et systèmes de haute fréquence

Unité de recherche :

ENAC-LAB - Laboratoire de Recherche ENAC

Directeur(s) de Thèse :

M. Alexandre CHABORY (directeur de thèse)
M. Romain PASCAUD (co-directeur de thèse)

Jury :

M. Xavier BEGAUD Professeur Télécom ParisTech - Président
M. Alexandre CHABORY Professeur ENAC - Directeur de thèse
Mme Marjorie GRZESKOWIAK Maître de Conférences INSA Toulouse - Examinatrice
M. Renaud LOISON Professeur INSA Rennes - Rapporteur
M. Cyrille MENUDIER Maître de Conférences Université de Limoges XLIM - Examinateur
M. Christophe MORLAAS Enseignant-chercheur ENAC - Examinateur
M. Romain PASCAUD Enseignant-chercheur ISAE-SUPAERO - Co-directeur de thèse
Mme Eva RAJO IGLESIAS Professeure Université Carlos III Madrid Espagne - Rapporteure

Acknowledgment

En primer lugar, quiero agradecer a mi familia, en especial a mis padres, abuela y hermano, por la motivación, la confianza y el apoyo brindado de forma permanente en este largo camino de tres años, el cual ha sido de gran aprendizaje, esfuerzo, dedicación, y también de momentos enriquecedores a nivel personal y profesional. ¡Este triunfo es también de Ustedes familia!

Asimismo, quisiera expresar mi especial gratitud hacia mis orientadores de tesis, Christophe, Romain, Alexandre, y Marjorie. Ha sido muy gratificante trabajar mancomunadamente en este proyecto de investigación, y además recibir su confianza, apoyo, enseñanzas, y todo el conocimiento adquirido, lo cual ha sido de vital importancia para cumplir con cada uno de los objetivos trazados desde el inicio de este inolvidable recorrido.

Mi especial gratitud a todos los miembros del jurado, Eva Rajo Iglesias, Renaud Loison, Xavier Begaud, y Cyrille Menudier, quienes han aceptado la invitación para valorar mi trabajo de tesis a través de sus valiosos comentarios y observaciones.

También agradezco profundamente a l'Ecole Nationale de l'Aviation Civile y a la Région Occitanie, por el financiamiento de mi tesis doctoral; así como a l'ISAE-SUPAERO y la Université de Toulouse por brindarme la magnífica oportunidad de desarrollar y culminar satisfactoriamente mi proyecto de investigación. Una especial muestra de afecto a todos los integrantes del laboratorio TELECOM (ENAC), especialmente al grupo EMA, así como también al grupo de investigación DEOS (ISAE-SUPAERO). Gracias por permitirme ser parte de su gran equipo de profesionales y seres humanos, de los cuales he aprendido continuamente, y quienes han sido claramente partícipes de este proceso. Además quisiera agradecer a Anywaves, y en especial a Gautier Mazingue, por la gestión realizada en la fabricación de los prototipos usando la impresión 3D. Gracias también a Cyrile Caihol, por su gran colaboración y trabajo en el desarrollo de las mediciones de las antenas y las muestras dieléctricas realizadas en ISAE-SUPAERO.

Quisiera expresar mi total agradecimiento a cada una de las personas que me han acompañado en el transcurso de mi tesis doctoral, entre ellos amigos y compañeros, franceses y extranjeros, quienes me han enseñado parte de su cultura, costumbres, gastronomía e idioma, lo cual ha tenido un significado muy especial e importante a nivel personal. No sin antes, quisiera dar gracias a todos mis amigos colombianos y españoles por acompañarme continuamente en este largo viaje. Especial gratitud a Lau, Tati, Alejo, Juli, Adri, Ori, Sarah, Jose, Kike, y a todos mis amigos en Colombia que fueron de gran apoyo en la preparación de mi sustentación de tesis. Finalmente, gracias a todos aquellos que han sido cómplices de largas conversaciones y de innumerables viajes llenos de experiencias y aventuras inolvidables!!.

Contents

List of Figures

List of Tables

List of abbreviations and symbols

UAV	*Unmanned aerial vehicles*
AM	*Additive manufacturing*
SLA	*Stereolithography apparatus*
FDM	*Fused Deposition Modeling*
SLM	*Selective lase melting*
RLC	*Equivalent electrical circuit made up of a resistor, an inductor, and a capacitor, connected in series or in parallel*
DR	*Dielectric resonator*
DRA	*Dielectric resonator antenna*
DWM	*Dielectric waveguide model*
TE	*Transverse electric mode*
TM	*Transverse magnetic mode*
PMC	*Perfect magnetic conductor*
PEC	*Perfect electric conductor*
PML	*Perfectly matched layer*
UHF	*Ultra high frequency band*
ISM	*Frequency band reserved internationally for industrial, scientific and medical purposes*
LHCP	*Left-hand circular polarization*
AR	*Axial ratio*
SME	*Spherical mode expansion*
MM	*Method of moments*
F/B **ratio**	*Front-to-back ratio*
f_0	*Resonance frequency*
Q	*Quality factor*
ω_0	Angular resonant frequency

w_{uc}, a_{uc}, l_{uc}, ,e_{uc}	*Dimensions of the unit cell*
a,b,d	*Dimensions of a rectangular dielectric resonator*
l_p	*Probe length*
d_p	*Probe diameter*
l_m	*length of the small metallic plate*
ε_{r}	Relative permittivity
μ_{r}	Relative permeability
c_0	*Speed of light in vacuum*
k_0	*Free-space wavenumber*
$\mathbf{S}$	Poynting vector
$\mathbf{A}$	Magnetic vector potential
$\mathbf{J_p}$	Volume polarization current density
$\mathbf{E}$	Electric field
$\mathbf{M}$	Magnetic field
$\mathbf{r}$	Vector from origin
W_e	*Stored electric energy*
p_m	*Magnetic dipole moment*
p_e	*Electric dipole moment*
P_{rad}	*Power radiated by an elementary dipole*
V	*Volume of a dielectric resonator*
z	*Impedance of the unit cell element*
$\mathbf{a}_\theta$, $\mathbf{a}_\phi$	Unit vectors
$\mathbf{a_{nm}}$, $\mathbf{b_{nm}}$	Coefficient vectors
$\mathbf{d_{mn}^{TE}}$, $\mathbf{d_{mn}^{TM}}$	TE and TM modal coefficients
m	*Azimuth index*
m	*Multipolar index*
$\mathbf{M_{mn}}(\mathbf{r})$, $\mathbf{N_{mn}}(\mathbf{r})$	Normalized vector spherical harmonics in far-field
$\mathrm{Y}^{\mathrm{e}}_{\mathrm{nm}}(\theta,\phi)$, $\mathrm{Y}^{\mathrm{e}}_{\mathrm{nm}}(\theta,\phi)$	Even and odd orthogonal spherical harmonics

ϵ_m	Neumann's number
$P_n^{\lvert m\rvert}$	Associated Legendre function
$h_n^{(2)}$	Spherical Hankel function of second kind
$j_n(kr')$	Spherical Bessel function of first kind

General introduction

Context

Nanosatellites and Unmanned Aerial Vehicles (UAVs) are emerging areas of research in aerospace and aeronautical engineering for the last two decades. For instance, more and more communication networks involving navigation and observation systems, integrate UAVs and nanosatellites to ensure a reliable connectivity in terms of coverage and efficiency for both rural and urban areas [1].

Over the past couple of years, the deployment of such solutions has been investigated in order to provide an efficient and secure on-demand network coverage. However, the deployment of this wireless network has several mechanical and electromagnetic constraints. The small volume of the platforms onboard represents an important challenge when designing antennas for UAV and nanosatellite applications [2, 3], as shown in Fig. 1. Small satellites are often classified based on their weights. For instance, femto (less than 0.1 kg), pico ($0.1 - 1$ kg), nano ($1 - 10$ kg), micro ($10 - 100$ kg), and mini ($100 - 1000$ kg). Among these, nano- and pico-satellites can be called CubeSats, and they are particularly interesting for the aforementioned applications. Regarding the volume of these platforms, the basic unit for a CubeSat has dimensions of 10 cm $\times$ 10 cm $\times$ 10 cm [4].

(a) Nanosatellite.

(b) UAV.

Figure 1: Small platforms onboard.

One of the key elements to ensure the wireless communication onboard for small satellites and UAVs is indeed the antenna. Antennas are important components that allow small satellites and UAVs to receive and transmit electromagnetic signals from/to ground and space. Considering the limited surface onboard, an antenna with low mass and small volume without the use of any ground plane or metallic reflectors is mainly required. Regarding their communication capabilities, compact-size antennas are generally demanded with broadside properties. For instance, reflector antennas, metasurface antennas, and reflect arrays have

been used at higher frequency bands such as the X- and Ka-band [5]. On the contrary, compact and low profile antennas, microstrip patches, monopoles, loops, and helical antennas have been mainly used for low-gain communication, for instance, in the ultra high frequency (UHF) and ISM band [6–8].

Due to the small size of the platforms onboard, small and compact antennas with cardioid radiation patterns are also particularly interesting to investigate. They are often referred to as Huygens sources. As shown in Fig. 2, such a cardioid pattern has improved radiation properties in the forward direction, namely $+z$-direction in Fig. 2, and low backward radiation. In the literature, it is also very common to call these type of antennas as magnetoelectric or complementary sources. Their operating principle rely on the combination of elementary electric and magnetic dipoles with equal radiation patterns in the E- and H-planes [9–13]. In addition to that, magnetoelectric sources generally provide a wide impedance bandwidth and a stable radiation pattern with low cross-polarization and back radiation levels [14]. However, in order to achieve either cardioid or end-fire radiation, both magnetoelectric and complementary antennas usually incorporate metallic structures, large ground planes and/or metallic reflectors, which make them unsuitable to be mounted on small platforms as UAVs and nanosatellites.

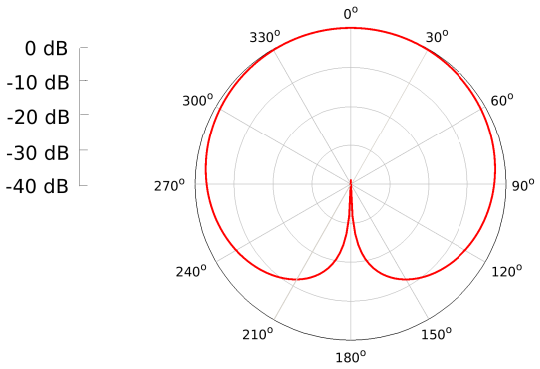

Figure 2: Radiation pattern of a Huygens source with improved radiation properties along the $+z$-direction and low backward radiation.

An original technique to achieve a Huygens source pattern relies on the combination of pairs of orthogonal elementary electric and magnetic dipoles. In addition to that, both collocated dipoles must satisfy certain conditions in amplitude and phase to achieve cardioid radiation patterns with equal properties in the E- and H- planes without the use of reflectors or large ground planes.

In this Ph.D. thesis, several Huygens sources made up of dielectric resonators are studied. Such dielectric resonator antennas (DRAs) rely on high permittivity ceramics, which are of particular interest to overcome space constraints.

Objectives and originality

The main objective of this Ph.D. thesis is to design compact antennas to be integrated on small-size platforms, *i.e.*, UAVs and nanosatellites, with strong constraints both in terms of size and radiation properties.

The design of dielectric resonator antennas exhibiting Huygens source properties, and more specifically, using additive manufacturing, represents the main goal of this work to overcome the aforementioned constraints.

Objectives

In this thesis, three main research axes are investigated:

I) Theoretical analysis of resonant modes in a 3-D dielectric resonator.

- Analyze the properties of TE and quasi-TM modes, *i.e.*, resonance frequency and quality factor, in a rectangular dielectric resonator with isotropic and anisotropic permittivities.

II) Design and manufacture a Huygens source antenna using dielectric resonators.

- Propose solutions to satisfy the mechanical and radiation constraints in antenna design for UAV and nanosatellite applications.

III) Design and manufacture a Huygens source antenna using engineered dielectric anisotropy within additive technologies.

Originality

The originality of this work resides in two distinct levels:

I. Few DRAs exploiting anisotropy have been studied in the literature [15–19]. Most of them exhibit anisotropic dielectric properties using multilayer structures. These properties have been mainly used to modify the electrical properties of resonant modes in a dielectric resonator for gain enhancement applications. However, none of them have taken advantage of additive technologies to achieve circular polarization in a square-based DRA fed by a single probe. As a contribution of this work, an original single-fed circularly polarized DRA has first been designed, manufactured and measured to demonstrate the possibilities offered by 3-D-printing of anisotropic ceramics.

II. The use of additive technologies have also been exploited to modify the shape and dielectric properties in DRAs to control, for instance, the impedance bandwidth and radiation

properties. Even if few DRAs have been studied to control the radiation pattern, none have taken advantage of additive technologies to design anisotropic DRAs with Huygens source properties. In this work, a compact Huygens source antenna made up of a uniaxial anisotropic dielectric resonator has thus been designed in the 2.45 GHz ISM band. The anisotropy has here been used to generate a pair of orthogonal electric and magnetic dipoles, with certain conditions in amplitude and phase, to realize a cardioid radiation pattern.

Outline

This dissertation is structured as follows:

Chapter 1 presents the necessary background information about Huygens source antennas. This chapter first covers the operating principle of Huygens sources in linear and circular polarizations. Furthermore, the state-of-the-art of Huygens source antennas based on complementary and magnetoelectric sources is presented. Afterwards, an overview of dielectric resonator antennas is presented for broadband, circular polarized, dual-band, and dual-polarized applications. This background is significantly important to identify what has been proposed in the literature, and propose new challenges for DRA design exploiting their numerous degrees of freedom in shape and material properties. For this, the properties of resonant modes in a rectangular dielectric resonator with isotropic permittivity are then studied based on the dielectric waveguide model. Finally, this chapter presents the state-of-the-art of DRAs with Huygens source properties.

Chapter 2 presents the design of two Huygens source antennas in linear and circular polarizations. First, a single-fed Huygens source antenna made up of two stacked dielectric resonators with isotropic dielectric permittivities is presented. Moreover, the analysis of the spherical mode expansion is here performed in order to identify the resonant modes which contribute to the half-space radiation. Finally, a Huygens source antenna formed by two stacked cross-shaped dielectric resonators is proposed in circular polarization. The antenna is fed by two feeding probes with certain conditions in amplitude and phase to generate two pairs of equivalent electric and magnetic dipoles, required to achieve a cardioid radiation pattern.

Chapter 3 presents the state-of-the-art of additive manufacturing technologies used to fabricate devices with complex shapes and/or homogeneous/heterogeneous materials. Afterwards, the state-of-the-art of additive manufacturing for microwave materials, circuits, and antenna applications is presented. It is shown that several 3-D-printed circuits, waveguides, filters, and indeed antennas, have been proposed in the literature in order to enhance their performances, reduce their volume, and reduce their prototyping time and costs with respect to conventional manufacturing techniques. It is also demonstrated that 3-D printing also

offers the possibility to create heterogeneous/anisotropic dielectric materials, which are particularly interesting for DRA applications since a new degree of freedom can be used to control polarization and radiation pattern. Finally, a methodology to design a uniaxial anisotropic dielectric material using additive manufacturing of ceramics is presented by designing a periodic structure of several unit cells at sub-wavelength scale.

Chapter 4 presents the design of a single-fed dielectric resonator antenna in circular polarization using a uniaxial anisotropic material. The first part of this chapter covers the operating principle of circularly polarized antennas. Afterwards, a theoretical model is presented in order to compute the DRA dimensions and its permittivity tensor to achieve circular polarization. This model relies on the adjustment in amplitude and phase of two fundamental TE modes resonating in a rectangular dielectric resonator with uniaxial anisotropic properties. The theoretical model is then validated to design and manufacture a single-fed circularly polarized DRA. Finally, measurements are performed in anechoic chamber and then compared with those obtained in simulations, in order to validate the possibilities offered by 3-D printing technologies to create anisotropic dielectric materials, which are particularly interesting in this Ph.D. thesis to control the radiation properties of DRAs.

Chapter 5 presents the design of a single-fed Huygens source antenna using engineered dielectric anisotropy. This chapter covers the antenna principle to design a compact Huygens source using an anisotropic dielectric resonator. This antenna is from a single resonator so that a reduced volume is obtained when comparing with the previous Huygens source design formed by stacked resonators. In addition to that, a uniaxial dielectric material is also engineered based on a periodized structure of unit cells at sub-wavelength scale. Finally, a 3-D-printed Huygens source antenna using a single anisotropic dielectric resonator is designed to demonstrate the possibilities offered by 3-D-printing of anisotropic ceramics to achieve a cardioid radiation pattern.

Conclusions are presented from the results obtained in this Ph.D. thesis. This includes new perspectives for research work topics that can be addressed in the future.

Chapter 1

Overview of Huygens Source Antennas using Dielectric Resonators

Sommaire

The interest in small-size autonomous platforms is growing rapidly. UAVs have been, for instance, widely used in the past 20 years in the fields of media, agriculture, and industry. Another example concerns the space industry where nanosatellites could yield a significant reduction in the launching and operation costs. These two applications share the common constraint of embedding complex systems on small platforms onboard. This constraint represents an important challenge for antenna design in terms of size and radiation properties since small antennas with cardioid radiation patterns are highly demanded.

In order to achieve cardioid radiation with equal E- and H- planes, two orthogonal elementary electric and magnetic dipoles must be combined with certain conditions in amplitude and phase. Such antennas are known as Huygens sources, but it is very common to find different terminology to define these antennas *e.g.*, magnetoelectric sources or complementary antennas, as will be detailed in the state-of-the-art.

An original technique to satisfy the aforementioned mechanical and radiation constraints relies on the design of compact Huygens sources using dielectric resonators. This chapter is organized as follows. The operating principle and the state-of-the-art of Huygens sources are first presented. Afterwards, dielectric resonator antennas (DRAs) are studied. More specifically, their ability to generate both equivalent electric and magnetic dipoles required to

achieve Huygens source performances is discussed. For this purpose, the properties of resonant modes in a rectangular dielectric resonator are analyzed. The analysis of the resonant modes provides an important background in order to understand how the various degrees of freedom in the DRA design can be exploited to control, for instance, its bandwidth and radiation properties. Finally, the state-of-the-art of DRAs with Huygens source properties is presented in order to identify and define new challenges when designing DRAs for UAV and nanosatellite applications.

1.1 Huygens source antennas

This chapter involves the operating principle of Huygens source antennas in linear and circular polarizations with improved radiation properties along the $+z$-direction and low backward radiation by combining pairs of elementary electric and magnetic dipoles.

1.1.1 Operating principle

1.1.1.1 Linearly polarized Huygens source

The concept of Huygens source was first proposed by Chlavin in 1954 [9]. The design of a linearly polarized Huygens source antenna with low backward radiation along the -z axis relies on the combination of two collocated and orthogonal infinitesimal y-directed electric and x-directed magnetic dipoles, as shown in Fig. 1.1.

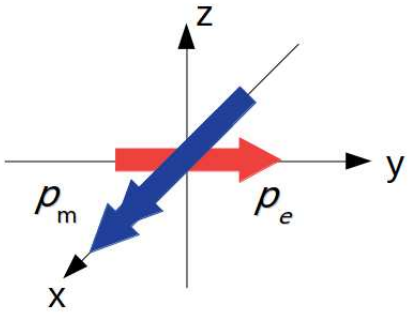

Figure 1.1: Configuration of the orthogonal magnetic and electric dipoles.

The far fields of the complementary dipoles can be obtained by superimposing their individual contributions. Note that there are two ways of characterizing elementary dipoles, using either the product of the current and dipole length $\mathbf{I}\ell$, or dipoles moments $\mathbf{p}$. The link between the current source and dipole moment is given by $\mathbf{p} = \frac{\mathbf{I}\ell}{j\omega}\hat{\boldsymbol{p}}$ [20].

Analyzing the E-fields of a infinitesimal y-directed electric dipole $\mathbf{E_e}$ of moment $\mathbf{p_e}$, and x-directed magnetic dipole $\mathbf{E_m}$ of moment $\mathbf{p_m} = \zeta_0 \mathbf{p_e} e^{j\delta}$, the following expressions can be found in the harmonic domain [21, 22]

$$\begin{aligned} E_{m\theta} &= -\frac{k_0^2 c_0}{4\pi r} p_m \sin(\phi) e^{-jkr} \\ E_{m\phi} &= -\frac{k_0^2 c_0}{4\pi r} p_m \cos(\theta)\cos(\phi) e^{-jkr} \\ E_{e\theta} &= \frac{k_0^2 c_0}{4\pi r} \zeta_0 p_e \cos(\theta)\sin(\phi) e^{-jkr} \\ E_{e\phi} &= \frac{k_0^2 c_0}{4\pi r} \zeta_0 p_e \cos(\phi) e^{-jkr} \end{aligned} \tag{1.1}$$

where $\zeta_0 = \sqrt{\mu_0/\epsilon_0}$ is the free-space wave impedance, δ is the phase difference between both dipoles, $k_0 = \omega\sqrt{\mu_0\epsilon_0}$ the free-space wavenumber, c_0 the speed of light in vacuum, and μ_0 and ε_0 the free-space permeability and permittivity, respectively. Then, the total electric field magnitude E can be expressed as

$$E = \sqrt{|E_\theta|^2 + |E_\phi|^2} \tag{1.2}$$

with

$$E_\theta = E_{e\theta} + E_{m\theta} \tag{1.3}$$

$$E_\phi = E_{e\phi} + E_{m\phi}. \tag{1.4}$$

Defining $A = \frac{k_0^2 c_0}{4\pi r}$, and assuming an amplitude balance between both electric and magnetic sources, namely $|p_m| = \zeta_0 |p_e|$, the following expression can be obtained

$$E = A\ |p_m| \sqrt{1 + \cos^2\theta - 2\cos\theta\cos\delta}. \tag{1.5}$$

Fig. 1.2 illustrates the elevation field pattern of the resulting antenna when varying the phase difference between both electric and magnetic dipoles. Note from (1.5) that the electric field is independent of the ϕ-variation. As observed in Fig. 1.2, a quasi-isotropic radiation pattern can be achieved by imposing $\delta = 90°$. On the other hand, an antenna with a cardioid radiation pattern with improved properties along the $+z$-direction can be obtained by choosing $\delta = 180°$. The direction of the backward radiation can also be switched by modifying the phase difference to $\delta = 0°$.

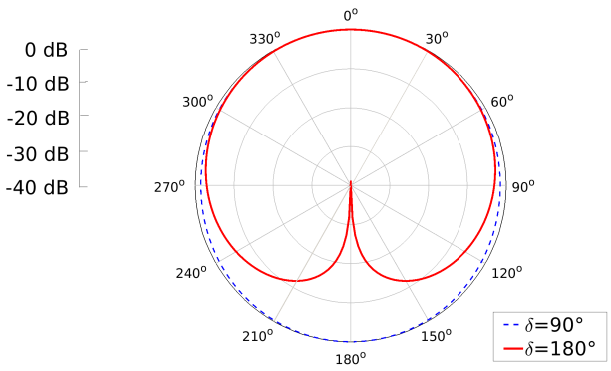

Figure 1.2: Radiation patterns due to the combination of two collocated and orthogonal electric and magnetic dipoles assuming $|p_m| = \zeta_0 |p_e|$, and for various phase differences δ between them.

The superimposition of a x-directed magnetic and a y-directed electric dipoles for $\delta = 180°$ can be summarized in Fig. 1.3. It is possible to note that the radiation pattern of both electric and magnetic dipoles have complementary characteristics. The resulting radiation pattern then corresponds to that of a linearly polarized Huygens source with maximum radiation properties along the $+z$ axis and low backward radiation.

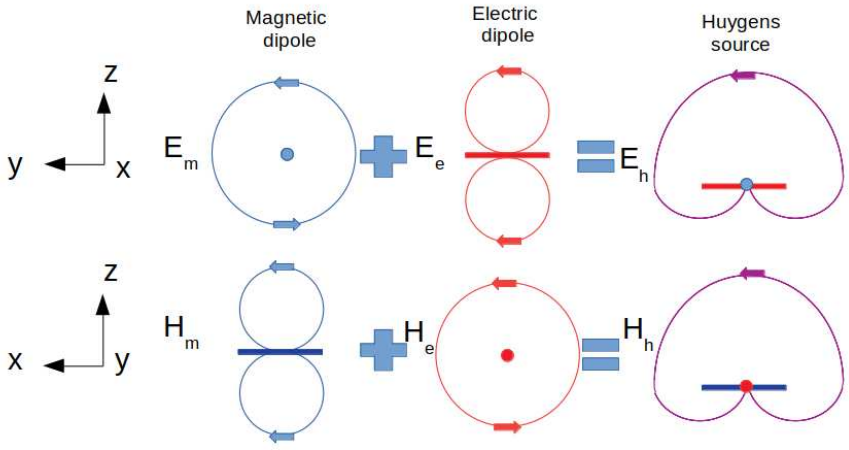

Figure 1.3: Orthogonal design concept of a linearly polarized Huygens source antenna radiating with cardioid direction.

It is important to note that an amplitude unbalance between both electric and magnetic sources can produce a distortion of the radiation patterns in the E- and H-planes, *i.e.*, for $\phi = 0°$ and $90°$. Fig. 1.4 shows for instance, that a lack of symmetry can be imposed for both planes when $\frac{p_m}{p_e} \neq \zeta_0$.

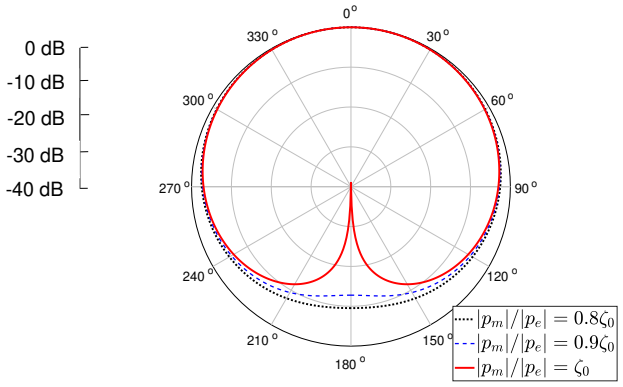

(a) $\phi = 0°$.

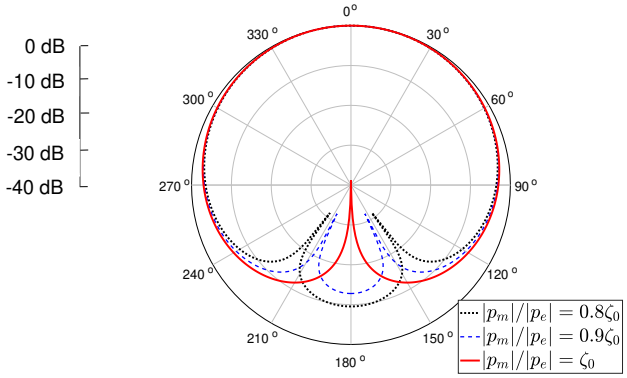

(b) $\phi = 90°$.

Figure 1.4: Radiation patterns due to the combination of two collocated and orthogonal infinitesimal electric and magnetic dipoles, assuming a phase shift $\delta = 180°$ and varying the amplitude of their dipole moments.

1.1.1.2 Circularly polarized Huygens source

It has been demonstrated by Wheeler [23] and Kraus [24], that a method to design a Huygens source antenna in circular polarization consists in combining pairs of collocated and aligned infinitesimal dipoles. The complementary antennas are then formed by two x-directed magnetic and electric dipoles and two y-directed magnetic and electric dipoles. Regarding the phase conditions to achieve a Huygens source pattern in circular polarization, two sources in phase quadrature must be considered to satisfy the required phase difference between the two pairs of dipoles [25, 26].

1.1.2 State-of-the-art of Huygens source antennas

In this section, practical implementations of antennas with such cardioid radiation properties are discussed. Few antennas with cardioid radiation properties have been proposed in the literature based on complementary antennas and magnetoelectric sources. For instance, Chlavin in 1954 [9] demonstrated that two complementary sources made up of an electric dipole and the open-ended coaxial line carrying the TE_{11} mode can be used to generate a cardioid radiation pattern with equal E- and H-planes.

Afterwards, the interest of Huygens source antennas has been particularly investigated by Luk *et al.* in 2006 [10]. The authors have shown that a complementary antenna formed by a planar dipole and a vertically-oriented quarter-wavelength patch antenna can generate two elementary electric and magnetic dipoles, respectively. Note that the proposed antenna has a metallic ground plane which reduce the backward radiation. In addition to that, it is fed by a Γ-shaped probe, as illustrated in Fig. 1.5a. As a result, the antenna achieves wide bandwidth of 43.8%, low cross polarization, and symmetrical cardioid radiation patterns in the E- and H- planes. The same authors have also designed a 45° dual-polarized dipole antenna formed by four square metallic plates, a ground plane, a box-shaped reflector, and two orthogonal Γ-shaped probes, as depicted in Fig. 1.5b [11]. It exhibits high input port isolation, wide bandwidth, low cross-polarization level, and cardioid radiation due to the effect of the box-shaped reflector. Moreover, the antenna can operate in circular polarization using a broadband 90° phase shifter and a power divider.

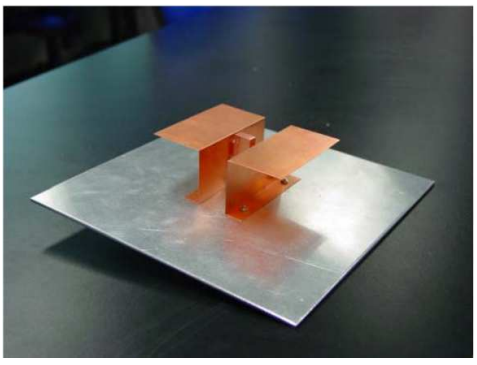

(a) Wideband complementary antenna with ground plane [10].

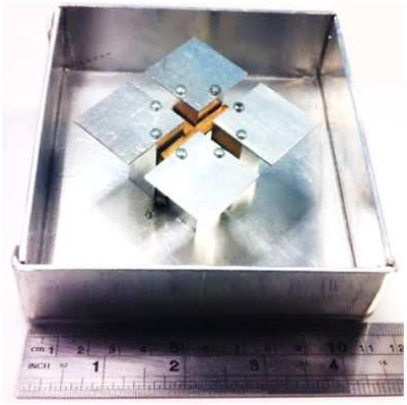

(b) Magnetoelectric dipole in dual or circular polarization [11].

Figure 1.5: Huygens sources based on complementary and magnetoelectric antennas.

It has been shown in the previous antennas, that magnetoelectric and complementary antennas usually have large volumes and involve metallic structures in order to achieve half-space radiation properties [10, 11]. These properties indeed do not satisfy the mechanical constraints demanded for the requested applications. In 2010 and 2011, Alitalo *et al.* [12, 27]

have proposed some Huygens source antennas made up of two chiral particles, as depicted in Fig. 1.6a. Each chiral particle generates a pair of electric and magnetic dipoles with equal magnitudes. Both particles are excited using two coaxial probes with 90° phase shift to achieve circular polarization. The radiation pattern of the proposed antenna presents directive properties, with a significant reduction of the backward radiation. However, due to the lack of symmetry of the prototype, the equivalent dipoles are not well collocated and the polarization and radiation pattern of the antenna are affected. Similarly, in 2012, the same authors have presented a dual omega-particle antenna in linear polarization [13]. The antenna is made up of a feed structure and a pair of radiating elements. The radiating elements consist of two omega particles (see Fig. 1.6b) that are able to generate two electric and two magnetic dipoles with equal amplitudes. Besides, the antenna has been numerically optimized to achieve a good matching and good isolation between both radiating elements.

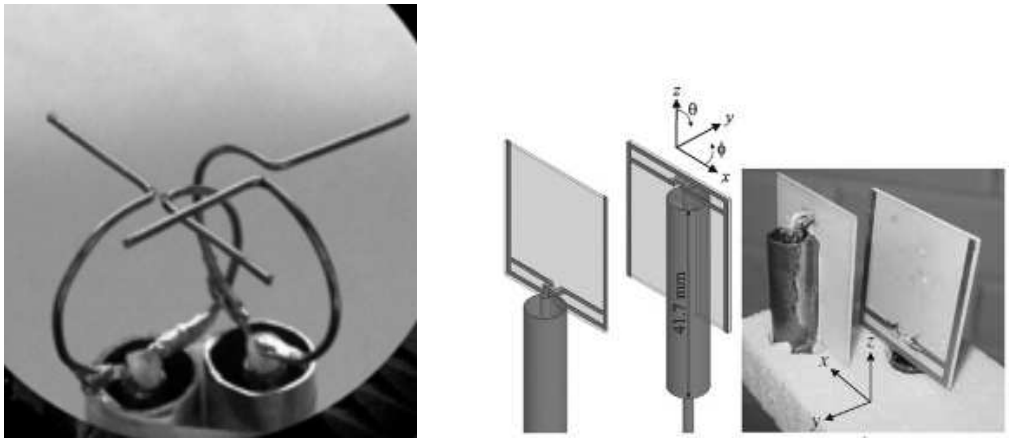

(a) Two chiral particles in circular polarization [12].

(b) Dual omega-particle antenna [13].

Figure 1.6: Huygens sources based on complementary antennas.

The complementary antennas presented in [12, 13] do not achieve good symmetrical radiation properties since they generate non-collocated elementary dipoles. In order to overcome these constraints, Huygens sources have also been proposed in 2010 and 2015 using helical-ring antennas [25, 26]. The authors have presented a compact helical-ring antenna with a cardioid radiation pattern in circular polarization. The helix configuration is composed of a ring of short turns and a metallic plate, as illustrated in Fig. 1.7. The length of each turn is small compared to the wavelength to ensure a uniform current. In addition to that, the helical ring is excited by means of in-quadrature capacitive probes. As a result, two sets of collocated electric and magnetic short dipoles are obtained. The proposed antenna has also been miniaturized by increasing the number of turns of the helical-ring structure.

Figure 1.7: Circularly polarized Huygens source based on a helical-ring antenna [25].

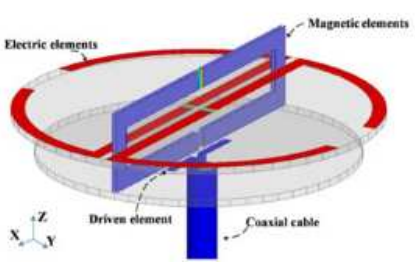

(a) Huygens source for wideband applications [28].

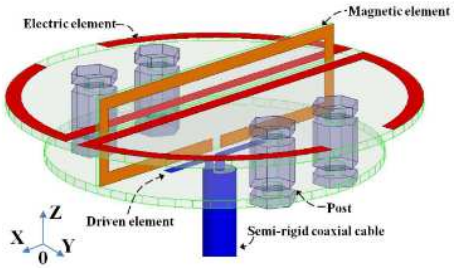

(b) Low-Profile Huygens Source [29].

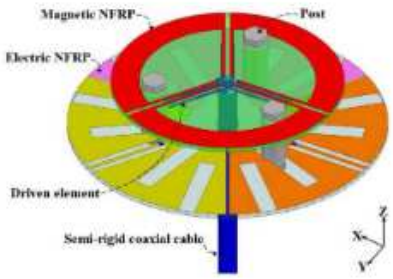

(c) Huygens source with pattern-reconfigurability [30].

Figure 1.8: Low profile, electrically small, Huygens source antenna using near-field resonant parasitic elements.

Recently, Huygens sources have also been proposed based on near-field resonant parasitic elements and metamaterial-inspired antennas, as shown in Fig. 1.8. In [31], the Huygens source relies on the combination of a driven dipole, an Egyptian axe dipole (EAD), and a capacitively loaded loop (CLL) near-field resonant parasitic (NFRP) elements to generate equivalent electric and magnetic dipoles. Due to this, the antenna achieves a high radiation

efficiency and cardioid radiation patterns. Similarly, a linearly polarized Huygens source antenna has been presented in [28]. The antenna relies on the combination of two pairs of NFRP electric and magnetic dipole elements, and non-Foster elements to achieve a stable cardioid radiation performances and wide impedance bandwidth. Other works have also been proposed in the literature [29, 30, 32–34] using NFRP elements electrically coupled to their driven electric dipole sources. However, these antennas are mainly composed of substrates with glass microfiber reinforced PTFE-based compositions, namely Teflon, which make them not suitable for nanosatellite applications.

Finally, it is interesting to notice that dielectric resonator antennas have also been investigated for Huygens source applications. In order to understand their implementation, a theoretical background on DRA is detailed in the next section.

1.2 Dielectric resonator antennas

DRAs are notably attractive due to the numerous degrees of freedom provided by their shape and material properties. These capabilities make DRA particularly interesting to control its radiation properties, and more specifically, achieve Huygens source properties. For this reason, in this chapter, a general state-of-the-art about DRAs is first presented. Afterwards, the electrical properties of the resonant modes in a dielectric resonator are studied in order to generate pairs of equivalent electric and magnetic dipoles. Finally, a state-of-the-art is then focused on DRAs with Huygens source properties.

1.2.1 Overview of dielectric resonator antennas

A dielectric resonator antenna is a resonant antenna made up of a dielectric material with low-loss, high relative permittivity, and thus high quality factor. DRA was first introduced by Long *et al.* in 1983 [35]. Since then, it has been extensively studied to take advantage of its reduced size, ease of excitation, high radiation efficiency, and wide bandwidth [36]. It has numerous degrees of freedom that depend on the antenna shape, *i.e.*, spherical [37–39], cylindrical [40–42], rectangular [43–46], or even more complex shapes [47–49].

DRA is an attractive alternative to traditional low-gain antennas, such as microstrip patches, monopoles, and dipoles. First of all, DRAs have a high radiation efficiency, above 90%, since dielectric materials, such as ceramics, present low dielectric losses. In addition to that, the antenna bandwidth can be controlled by using dielectric resonators with a wide range of permittivities. Several feeding mechanisms can also be adopted to excite numerous resonant TE, TM, quasi-TM and hybrid modes in dielectric resonators [50–53]. As shown in Fig. 1.9, the most common feeding mechanism are probes, slots, microstrip lines, dielectric image guides, and co-planar lines. This great variety makes DRA compatible with various fabrication technologies [54, 55].

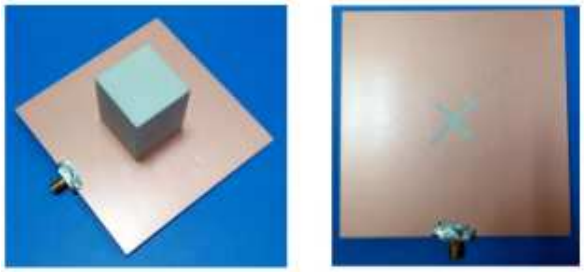

(a) Cross-slot-coupled dual-band circularly polarized DRA [50].

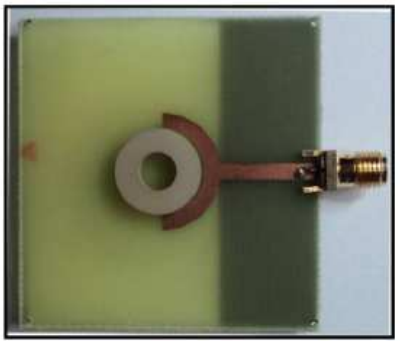

(b) Ring DRA with annular-shaped microstrip feed [51].

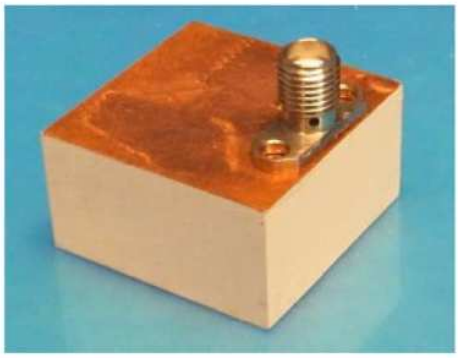

(c) DRA with feeding probe [21].

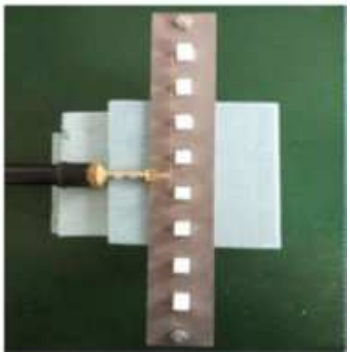

(d) Wideband series-Fed linear DRA array [53].

Figure 1.9: Dielectric resonator antennas with different feed mechanisms.

Several authors have taken advantage of the numerous degrees of freedom in the DRA design to achieve broadband properties. For instance, in [56], the authors present a broadband microstrip-fed DRA at the X-band. The hybrid DRA is composed of a square-based dielectric resonator with electrical dimensions of $0.35\lambda_0 \times 0.35\lambda_0 \times 0.08\lambda_0$, an intermediate substrate, and a feeding circuit. The feeding circuit is made up of a microstrip line connected to a stepped patch, as depicted in Fig. 1.10a. It has been shown that the effective dielectric constant of the DRA decreases while adding an intermediate substrate. This leads to reduce the quality factor of the dielectric resonator. Consequently, the proposed DRA offers a wide impedance bandwidth of 50%. Similarly, a broadband DRA composed of a cylindrical bowtie structure with notches (see Fig. 1.10b) has been proposed in [47]. The cylindrical dielectric resonator has radius of $0.18\lambda_0$ and height of $0.23\lambda_0$. It is fed by coaxial probe and placed on a metallic ground plane. The variation of the probe position and the notch shape are sensitive parameters which allow the antenna to achieve an impedance bandwidth of about 49% and broadside radiation patterns. Furthermore, the authors in [48] present a super-shaped DRA formed by a prism-shaped plastic dielectric resonator with height slightly exceeding λ_0, a circular metallic ground plane, and a coaxial probe, as shown in Fig. 1.10c. The antenna

offers a great flexibility in design due to the multiple degrees of freedom, which make it notably interesting to enhance the antenna bandwidth and achieve circular polarization by combining the proper modes in the dielectric resonator. As a result, the proposed antenna operates with a wide bandwidth of 70%.

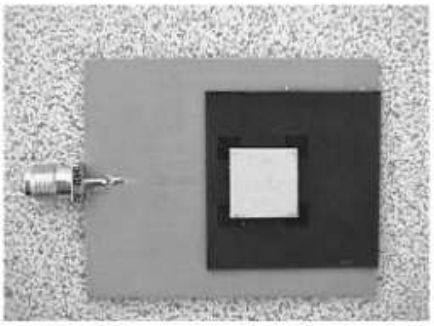

(a) Microstrip-fed DRA [56].

(b) Cylindrical bowtie DRA [47].

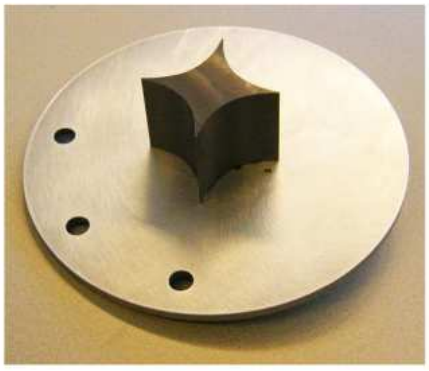

(c) Plastic-based super-shaped DRA [48].

Figure 1.10: DRAs for broadband applications.

Circularly polarized DRAs have also been designed using cross-shaped and stacked structures. These shapes particularly offer a new degree of freedom for DRA design so that several TE modes can be excited in a dielectric resonator. In [57], a cross-shaped DRA has been proposed to operate in circular and vertical polarizations, as illustrated in Fig. 1.11a. The DRA is composed of two notched rectangular slices with lengths of $0.31\lambda_0$. The antenna principle relies on the combination of several TE and quasi-TM modes in a dielectric resonator, with certain conditions in phase and amplitude to achieve circular polarization with a measured 3-dB axial ratio bandwidth of 6%. In [58], the authors have presented a stacked DRA in circular polarization. The antenna is formed by four dielectric layers with an overall height of $1.96\lambda_0$, and it is fed by a microstrip line (see Fig. 1.11b). Each layer is here rotated 30° in order to obtain the required phase shift between the two TE modes, which leads to achieve

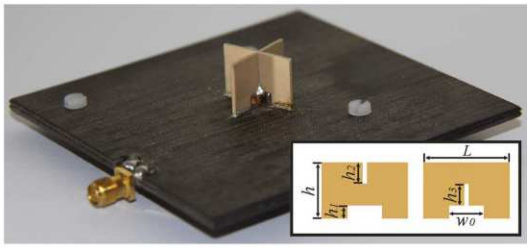

(a) Cross-shaped DRA [57].

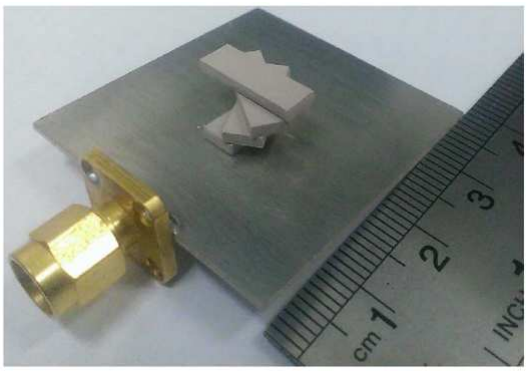

(b) stacked DRA [58].

Figure 1.11: Circularly polarized DRAs using cross-shaped and stacked configurations.

circular polarization with a measured axial ratio bandwidth of 5%. Hence, the layer rotation angle offers a new degree of freedom in design for polarization.

Recently, DRAs with multiband or pattern diversity properties have also been studied. In the literature, these properties have been achieved by exciting fundamental and higher-order modes using cross-shaped DRAs and complex hybrid-feeding structures. For instance, in [59], the authors present a dual-band and dual-polarization DRA. The cross-shaped dielectric resonator has electrical dimensions of $a = 0.21\lambda_0$ and $b = 0.16\lambda_0$. A pair of fundamental and higher-order TE modes are excited to achieve a dual-band response. In addition to that, each pair of orthogonal modes are used to achieve dual-polarized properties. These modes are excited using a feeding mechanism formed by two symmetric probes (see Fig. 1.12a), offering good performances for the two orthogonal polarization over both frequency bands since other higher-order modes can be suppressed. DRAs with cylindrical shapes have also been proposed in the literature. For instance, a cylindrical dual-band DRA has been proposed in [40]. The DRA is made up of a cylindrical dielectric resonator with radius $0.12\lambda_0$ and height of $0.15\lambda_0$, a coaxial probe to excite a TM mode, and two orthogonal microstrip lines in quadrature phase used to excite hybrid modes, as depicted in Fig. 1.12b. As a contribution, the antenna operates with a vertically polarized monopole-like omnidirectional pattern and a broadside circularly polarized radiation pattern at separate frequencies. In [60], a cylindrical DRA centrally loaded by a dielectric layer has been proposed to realize a multiband diversity at 2.4 GHz, as observed in Fig. 1.12c. The proposed dielectric resonator has radius $0.29\lambda_0$ and height of $0.12\lambda_0$. The feeding mechanism is composed of a coaxial probe and a rectangular cross slot, used to excite a unidirectional hybrid mode and an omnidirectional TM mode. Both modes can operate at the same operating frequency by modifying the electrical properties of the loading dielectric layer, allowing to use a new degree of freedom for antenna design.

Regarding the impact of the DRA geometry on the properties of its resonant modes, literature survey shows that cylindrical and spherical shapes usually radiate both degenerate and hybrid modes, which enhance the cross-polarized radiation of DRAs, limiting its perfor-

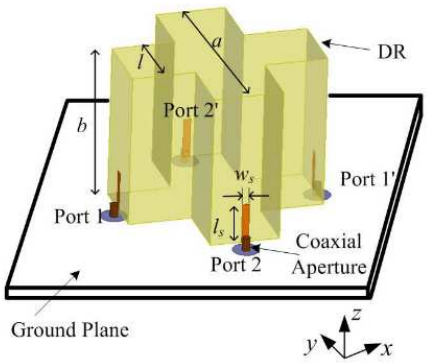

(a) Cross-shaped DRA [59].

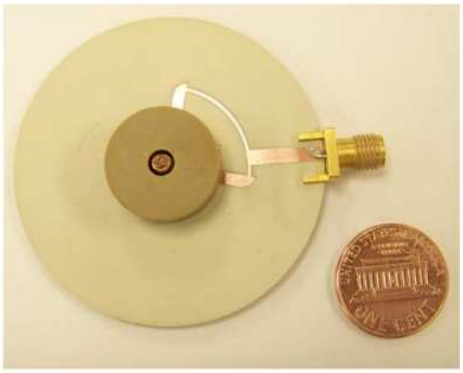

(b) Compact DRA with vertically polarized omnidirectional and broadside circularly polarized radiation [40].

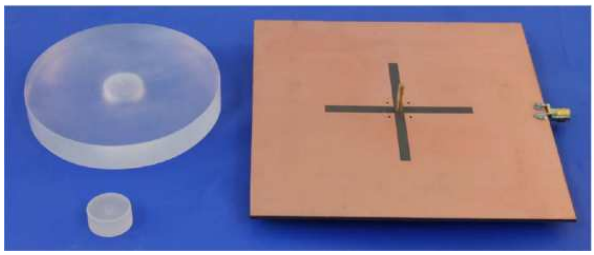

(c) Pattern-diversity cylindrical DRA [60].

Figure 1.12: DRAs for multiband and pattern diversity applications.

mances in far-field zone. On the other hand, it has been shown that rectangular shapes offer particular advantages when designing DRAs since TE modes can radiate by properly selecting the three dimensions of the dielectric resonator. In addition to that, rectangular-shaped DRAs provide more flexibility in antenna design by selecting independently the aspect ratios (height/length and width/length) to control the electrical properties of resonant modes in the dielectric resonator [43].

In the next section, the resonant modes in a rectangular dielectric resonator are investigated. The analysis of the resonant modes provides an important background in order to understand how they are affected by the numerous degrees of freedom in DRA.

1.2.2 Focus on the rectangular dielectric resonator antenna

As illustrated in Fig. 1.13, a rectangular dielectric resonator is here considered with dimensions a, b, and d along x-, y-, and z-directions, respectively. The rectangular configuration offers great flexibility since it is possible to take advantage of its two aspect ratios, namely height/length and width/length, in order to control the electrical properties of resonant modes in the dielectric resonator.

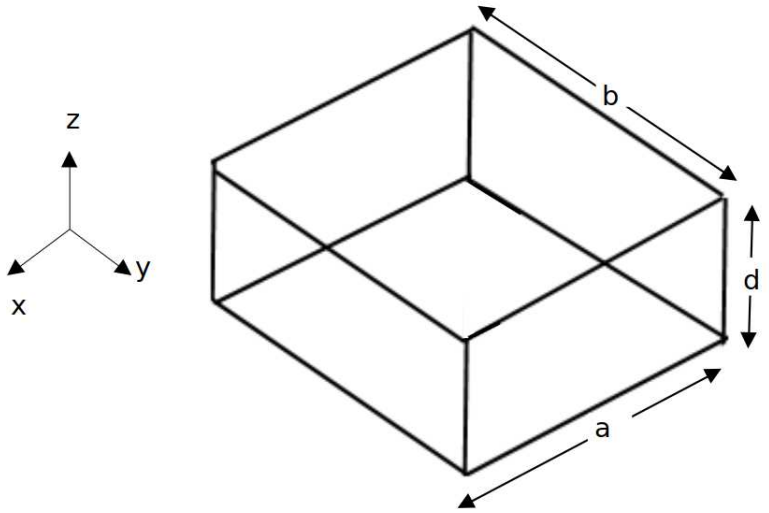

Figure 1.13: Rectangular dielectric resonator.

According to Van Bladel, several modes resonate in a dielectric resonator. These modes can be classified as confined or nonconfined modes [61]. The confined modes can be supported by spherical and cylindrical resonators. On the other hand, a rectangular resonator can only support nonconfined modes [43, 62].

These modes in a rectangular dielectric cavity can be divided into transverse electric TE and transverse magnetic TM modes. It has been demonstrated in [43], that only TE modes can resonate in a rectangular dielectric resonator. This resonator can support TE^x, TE^y, and TE^z modes, respectively [55]. Moreover, the electrical properties of these modes are a function of the dielectric resonator (DR) dimensions. Generally, these modes are noted as TE_{mnp}, where m, n, and p can take values different that zero. These indices represent the number of half period made by the field in the dielectric resonator in a given direction.

1.2.2.1 Fundamental TE modes in a rectangular dielectric resonator

In order to calculate the properties of TE modes, dielectric boundary conditions must be imposed on the walls of the dielectric resonator. An approximation method thus consists in imposing perfect magnetic conductor (PMC) boundary conditions on all the walls of the rectangular dielectric cavity, so that the normal component ($\hat{\boldsymbol{n}}$) of the electric field must be zero on each wall [43]

$$\mathbf{E} \cdot \hat{\boldsymbol{n}} = 0 \tag{1.6}$$

and the tangential component of the magnetic field as well [43]

$$\hat{\boldsymbol{n}} \times \mathbf{H} = 0. \tag{1.7}$$

However, this method provides low accuracy while compared with experimental results. For this, the dielectric waveguide model (DWM) has been widely used in the literature with reliable results to calculate the resonance frequencies of TE modes [43, 55]. Here, boundary conditions are defined so that two walls with air-dielectric interfaces are fixed along the direction of exponential decay of electric field, and four PMC walls along the other directions. For instance, analyzing the fundamental TE^z_{111} mode, four PMC walls are fixed along x- and y-directions, and two walls with air-dielectric interfaces are located along the z-direction. For the latter, the fields decay exponentially along the z-direction, outside the resonator, as detailed in [43].

As first step, separation of variables must be applied, so that k_z can be computed from the following expression for the TE^z_{111} mode

$$k_x^2 + k_y^2 + k_z^2 = \varepsilon_r k_0^2 \tag{1.8}$$

where $k_x = \frac{\pi}{a}$, $k_y = \frac{\pi}{b}$, $k_0 = (2\pi f_0)/c_0$ the free-space wavenumber related to the corresponding resonance frequency, and ε_r is the relative permittivity of the dielectric resonator. Afterwards, the transcendental equation can thus be found applying the DWM [43]

$$k_z \tan\left(k_z \frac{d}{2}\right) = \sqrt{k_0^2(\varepsilon_r - 1) - k_z^2}. \tag{1.9}$$

The resonance frequency of the TE^z_{111} mode can thus be numerically calculated from (1.8) and (1.9). The same procedure can be applied to calculate the transcendental equation for the TE^x_{111} and TE^y_{111} modes. As an example, assuming that $a = 50$ mm, $b = a/2$, $d = a/3$, and $\varepsilon_r = 20$, the DWM gives 2.48 GHz, 2.33 GHz, and 1.89 GHz for the resonance frequencies of the fundamental TE^x_{111}, TE^y_{111}, and TE^z_{111} modes, respectively.

Regarding the field components for the TE^z_{111} mode in a rectangular dielectric resonator, they can be written as

$$
\begin{aligned}
E_x &= \frac{A}{\varepsilon} k_y \cos(k_x x) \sin(k_y y) \cos(k_z z) \\
E_y &= -\frac{A}{\varepsilon} k_x \sin(k_x x) \cos(k_y y) \cos(k_z z) \\
E_z &= 0 \\
H_x &= -j \frac{A}{\omega \mu \varepsilon} k_x k_z \sin(k_x x) \cos(k_y y) \sin(k_z z) \\
H_y &= -j \frac{A}{\omega \mu \varepsilon} k_y k_z \cos(k_x x) \sin(k_y y) \sin(k_z z) \\
H_z &= -j \frac{A}{\omega \mu \varepsilon} (k_x^2 + k_y^2) \cos(k_x x) \cos(k_y y) \cos(k_z z)
\end{aligned}
\tag{1.10}
$$

where A is an arbitrary constant and μ the permeability of the dielectric material.

Fig. 1.14 illustrates the theoretical electric and magnetic fields in a rectangular dielectric resonator for the TE^z_{111} mode. As observed, the E- and H-fields of the TE^z_{111} mode are equivalent to those radiated by an elementary magnetic dipole along the z-direction.

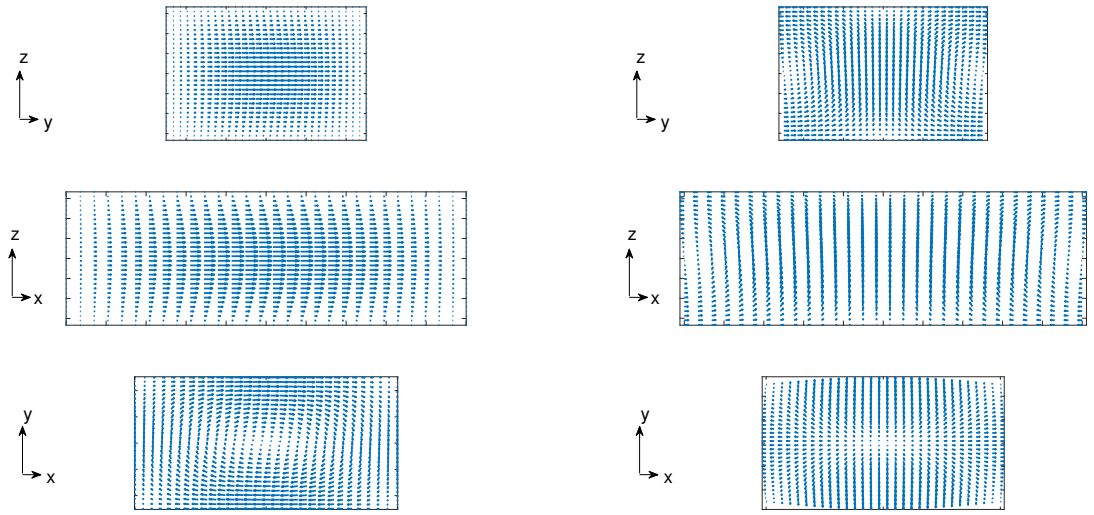

(a) E-field. (b) H-field.

Figure 1.14: E- and H-fields in a rectangular dielectric resonator with dimensions a, b, and d along x-, y-, and z-directions, respectively, and with dimension ratios of $b = a/2$ and $d = a/3$ for the TE^z_{111} mode.

Therefore, the TE^z_{111} mode radiates as an elementary magnetic dipole of moment $\mathbf{p_m}$. This can also be explained based on the magnetic dipole moment equation detailed in [43].

Note that $\mathbf{p_m}$ can be written as a function of the volume polarization current density $\mathbf{J_p}$, which depends on the electric field $\mathbf{E}$ inside the resonator, as follows

$$\mathbf{p_m} = \frac{1}{2}\int_V \mathbf{r} \times \mathbf{J_p} dV \tag{1.11}$$

where V denotes the volume of the DRA, and

$$\mathbf{J_p} = j\omega\varepsilon_0(\varepsilon_r - 1)\mathbf{E} \tag{1.12}$$

$$\mathbf{r} = x\hat{\boldsymbol{x}} + y\hat{\boldsymbol{y}} + z\hat{\boldsymbol{z}}. \tag{1.13}$$

Similarly, the TE^x_{111} and TE^y_{111} modes are equivalent to the magnetic dipole moment of an infinitesimal magnetic dipole along the x- and y-directions, respectively.

1.2.2.2 Quasi-TM modes

The existence of TM modes in a rectangular resonator has been doubted by Mongia in [43] and [62], since these modes have not been confirmed by experiments. However, in [63–65], the authors have proved that the superposition of a pair second-order TE modes, *i.e.*, m, n or p equal to 2, can generate a quasi-TM mode in a rectangular dielectric resonator. For instance, the quasi-TM^y_{111} mode is denoted here in reference to the corresponding cylindrical resonator mode, namely TM_{011} mode. Hence, the quasi-TM^y_{111} mode is the degenerated result of the combination of the TE^x_{112} and TE^z_{211} modes in a rectangular dielectric resonator by imposing a square cross section along the x- and z-directions. This quasi-TM^y_{111} mode presents similar E- and H-fields when compared with those generated by an y-directed electric dipole.

The E- and H-fields of the TE^z_{211} mode and TE^x_{112} mode are depicted in Fig. 1.15 and 1.16. The TE^z_{211} mode exhibits two loop patterns in the electric field along the x-direction. On the contrary, two loop shapes along the z-direction are observed for the TE^x_{112} mode. Finally, the superimposed field distribution of the quasi-TM^y_{111} mode is illustrated in Fig. 1.17. A loop pattern can be observed in the magnetic field distribution along y axis, which is equivalent to the radiated by a y-directed electric dipole.

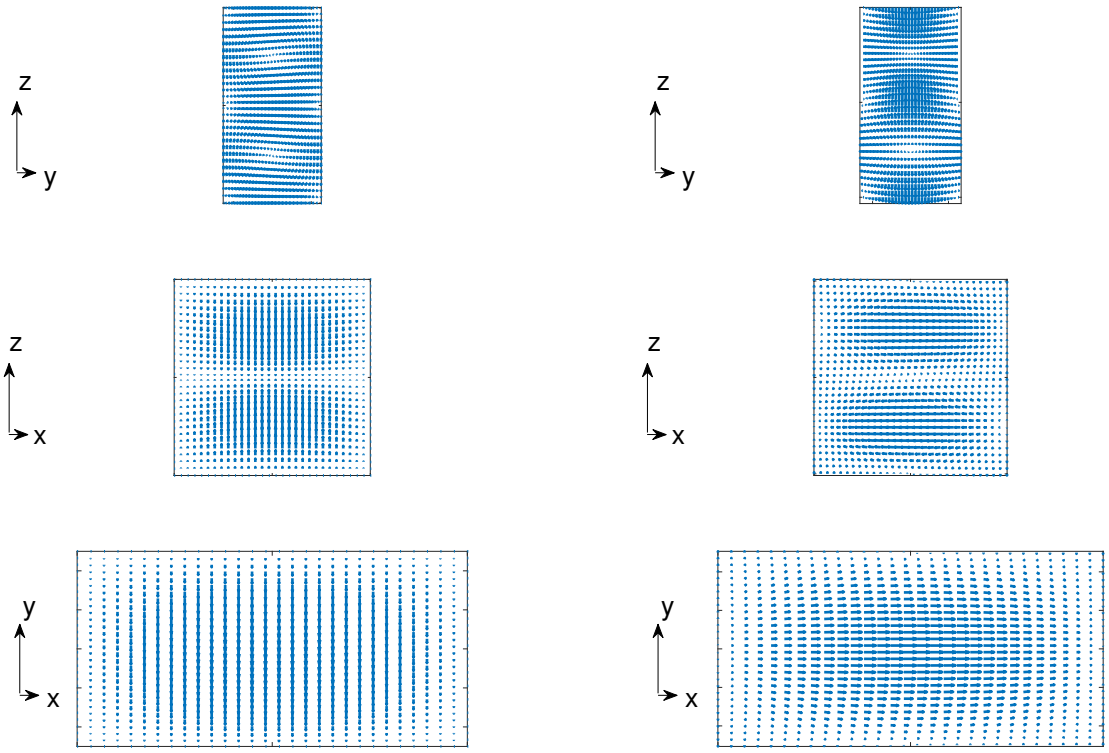

(a) E-field

(b) H-field.

Figure 1.15: E- and H-fields in a rectangular dielectric resonator with dimensions a, b, and d along x-, y-, and z-directions, respectively, and with dimension ratios of $b = a/2 = d/2$ for the TE^{x}_{112} mode.

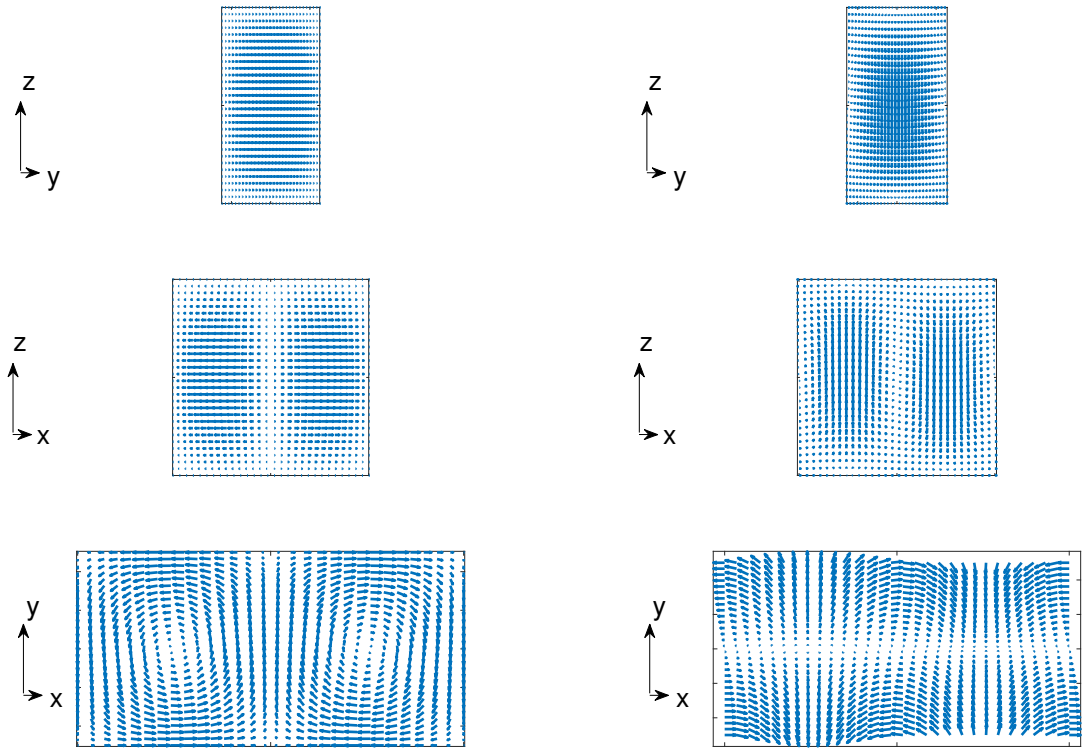

(a) E-field. (b) H-field.

Figure 1.16: E- and H-fields in a rectangular dielectric resonator with dimensions a, b, and d along x-, y-, and z-directions, respectively, and with dimension ratios of $b = a/2 = d/2$ for the TE^{z}_{211} mode.

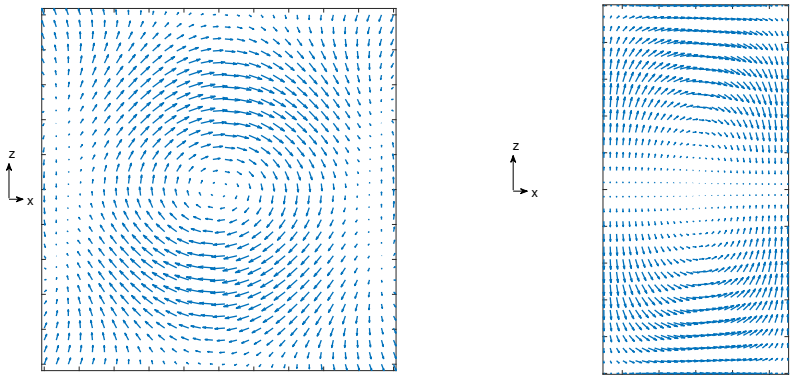

(a) E-field. (b) H-field.

Figure 1.17: E- and H-fields in a rectangular dielectric resonator with dimensions a, b, and d along x-, y-, and z-directions, respectively, and with dimension ratios of $b = a/2 = d/2$ for the quasi-TM^{y}_{111} mode.

1.2.2.3 Quality factor

In addition to its resonance frequency, each mode can also be described by its quality factor Q. For instance, a decrease of Q produces an increase of the antenna bandwidth [43]. The quality factor can be calculated by determining the total stored energy W_e and power radiated P_{rad} by the DRA, as detailed in [43]. In addition to that, it is assumed that the DRA has a purely real input impedance [66]. Therefore, the quality factor can be written as

$$Q_{rad} = \frac{2\omega_0 W_e}{P_{rad}} \tag{1.14}$$

where ω_0 denotes the angular resonant frequency. Moreover, the time average stored electric energy in a volume for a lossless isotropic, homogeneous, and linear media is given by [67]

$$W_e = \frac{\varepsilon}{4}\int_{-\frac{a}{2}}^{\frac{a}{2}}\int_{-\frac{b}{2}}^{\frac{b}{2}}\int_{-\frac{d}{2}}^{\frac{d}{2}}\left(\|\mathbf{E^2}\|\right)dxdydz. \tag{1.15}$$

Analyzing TE^{z}_{111} mode ($E_z = 0$), (1.15) becomes

$$W_e = \frac{\varepsilon}{4}\int_{-\frac{a}{2}}^{\frac{a}{2}}\int_{-\frac{b}{2}}^{\frac{b}{2}}\int_{-\frac{d}{2}}^{\frac{d}{2}}\left(|E_x|^2 + |E_y|^2\right)dxdydz. \tag{1.16}$$

that is to say

$$W_e = \frac{\varepsilon_r \varepsilon_o abdA^2}{32}\left(1+\frac{\sin(k_z d)}{k_z d}\right)\left(k_x^2+k_y^2\right). \tag{1.17}$$

On the other hand, P_{rad} can be calculated by integrating the real part of the Poynting vector over a spherical surface

$$P_{rad} = \oiint_S \mathbf{S}\cdot\mathbf{ds} = \frac{1}{2}\oiint_S Re(\mathbf{E}\times\mathbf{H}^*)\cdot\mathbf{ds}. \tag{1.18}$$

It has been demonstrated in [43] that the power radiated by an elementary magnetic dipole can be written as a function of the dipole moment, as follows

$$P_{rad} = 10k_0^4|\mathbf{p_m}|^{\mathbf{2}} \tag{1.19}$$

where $\mathbf{p_m}$ is the magnetic dipole moment of the DRA. Solving (1.11), $\mathbf{p_m}$ can be written as

$$\mathbf{p_m} = \frac{-j8\varepsilon_o(\varepsilon_r-1)A}{k_x k_y k_z}\sin(k_z d/2)\hat{\boldsymbol{z}}. \tag{1.20}$$

The final expression of the quality factor for the TE^z_{111} mode is expressed as

$$Q = \frac{\omega_0\mu_0\pi^6}{2560k_0^6 abd}\frac{[1+\mathrm{sinc}(k_z d)]}{\mathrm{sinc}^2(k_z d/2)}\frac{\varepsilon_r(k_x^2+k_y^2)}{(\varepsilon_r-1)^2}. \tag{1.21}$$

The previous theoretical analysis can also be applied for rectangular DRAs mounted on ground planes. In fact, the TE modes in a rectangular DRA of height d (see Fig. 1.13) have identical electrical properties to those obtained using a rectangular DRA of height $d/2$ placed on a metallic ground plane [43].

1.2.3 State-of-the-art of DRA with Huygens source properties

An original solution to generate the required pair of equivalent dipoles to achieve a Huygens source in a compact structure without the use of reflectors or large ground planes relies on the excitation of several TE and TM modes in dielectric resonator antennas [68–71].

In the literature, few DRAs exhibiting Huygens source properties have been proposed using rectangular shapes. These shapes have been employed in order to excite some TE, TM and/or hybrid HEM modes, which leads to generate a pair of orthogonal elementary electric and magnetic dipoles. For instance, in [22], a probe-fed rectangular dielectric resonator antenna (DRA) with a small ground plane has been proposed, as depicted in Fig. 1.18a. The antenna principle relies on the combination of a pair of equivalent y-directed magnetic and

z-directed electric dipoles generated by a dielectric resonator carrying the TE^{y}_{111} mode and a probe placed along the z axis, respectively. As a result, the antenna achieves similar E- and H-planes patterns with cardioid-shaped unilateral radiation pattern along the x-direction. As shown in Fig. 1.18b, this pattern is oriented transversely with respect to the feed position.

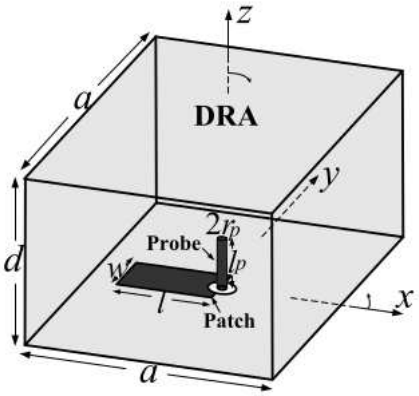

(a) DRA configuration.

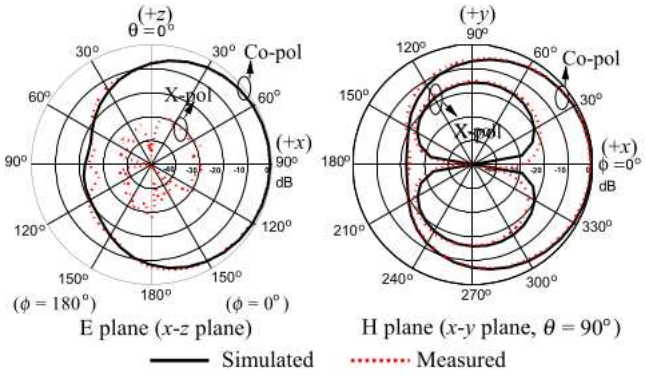

(b) Cardioid-shaped unilateral radiation pattern.

Figure 1.18: Laterally radiating rectangular DRA with small ground plane [22].

A unilateral rectangular DRA has also been proposed in [72] with wide beamwidth properties. The principle relies on the combination of the fundamental TE^{x}_{111} and a higher-order mode, namely TE^{y}_{211} mode, which provide cardioid and quasi-omnidirectional radiation properties, respectively. These modes have been excited using a single feeding probe, as shown in Fig. 1.19a. As a result, a measured impedance bandwidth of 13.2% has been accomplished. Moreover, the proposed antenna achieves cardioid-shaped unilateral radiation properties along the y-direction, with a maximum front-to-back ratio of 36.6 dB at 2.4 GHz and a front-to-back (F/B) ratio bandwidth of 4.1%, considering F/B ratio $>$ 15 dB. Similarly, a notched rectangular DRA with a small ground plane (see Fig. 1.19b) has been presented in [71] to realize a unilateral radiation pattern along the x-direction. The dielectric resonator has electrical dimensions of $0.23\lambda_0 \times 0.17\lambda_0 \times 0.29\lambda_0$. In order to achieve Huygens source ra-

diation properties, the equivalent magnetic dipole has been generated by exciting the TE^{y}_{111} mode in the DR, whereas the electric dipole is obtained by breaking the symmetry of the rectangular resonator. This can be done by introducing an arbitrary notch and/or metallic strips. Furthermore, the notch shape provides a new degree of freedom in design so that it can be used to tune the amplitude and phase difference between both electric and magnetic sources, which leads to achieve a half-space radiation pattern. The proposed antenna achieves a front-to-back ratio above 24 dB at 2.45 GHz.

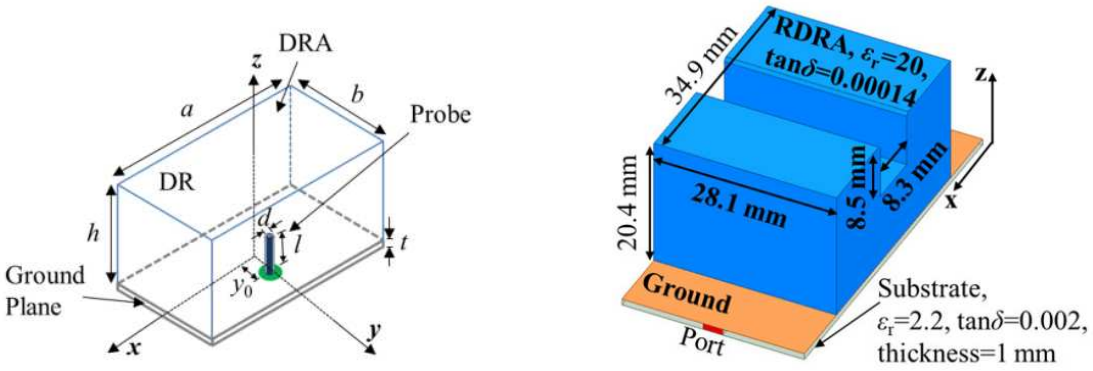

(a) Rectangular DRA [72]. (b) Notched rectangular DRA [71].

Figure 1.19: Rectangular DRAs with cardioid-shaped unilateral radiation pattern.

DRAs with cylindrical shapes have also been proposed in the literature in order to obtain Huygens source properties. In [69], the authors have proposed a cylindrical DRA with radius of $0.19\lambda_0$ and height of $0.17\lambda_0$, as illustrated in Fig. 1.20a. It is also made up of a modified Alford loop, comprising a circular patch and four stubs printed on the ground plane, and a probe at the DR centre in order to excite a pair of fundamental TE and TM modes, respectively, which produce the first circularly polarized field. The second circularly polarized field has been obtained using a cross-slot fed printed in the ground plane of the DRA. As a result, cardioid-shaped unilateral radiation properties in circular polarization along the y-direction has been accomplished, with a measured F/B ratio of 15.5 dB at 2.44 GHz, and a F/B ratio bandwidth above 4%, considering F/B ratio $>$ 15 dB. In addition to that, an impedance bandwidth and a 3-dB axial ratio bandwidth of 9.4% and 4.9% has been accomplished, respectively. On the other hand, in [68], the authors have presented a compact ring DRA with unilateral radiation patterns along the y-direction. The antenna is made up of a dielectric resonator with height of $0.31\lambda_0$, and a ground plane of size $0.38\lambda_0 \times 0.31\lambda_0$, as shown in Fig. 1.20b. The unidirectional patterns have been achieved by combining a horizontal magnetic dipole and a vertical electric dipole. These dipoles have been generated by exciting hybrid modes and using a monopole placed at the DR centre, respectively. Therefore, the proposed DRA achieves a front-to-back ratio of 15 dB at 2.4 GHz, and a measured impedance bandwidth of 12.1%.

It has been shown that few DRAs have been studied to achieve a Huygens source pattern.

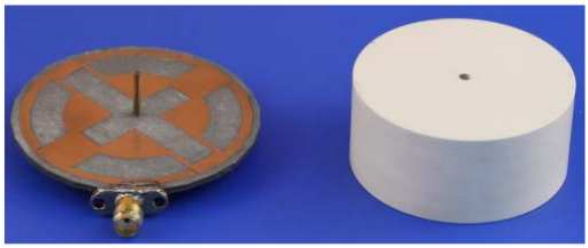

(a) Cylindrical DRA with lateral radiation [69].

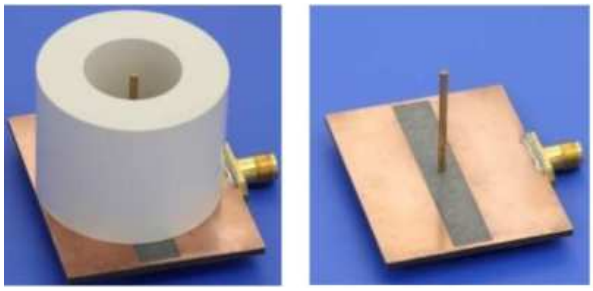

(b) Ring DRA with unidirectional radiation pattern [68].

Figure 1.20: Cylindrical DRAs with cardioid-shaped unilateral radiation pattern.

However, none have achieved a cardioid radiation pattern with improved radiation properties along the $+z$-direction using rectangular dielectric resonators. It is important to note that it is very challenging to achieve this kind of radiation pattern due to the position of feeding probe located along the -z axis (see Fig. 1.19a), which may have an impact on the low backward radiation of the antenna.

1.3 Conclusion

Antennas with half-space radiation patterns, as for instance, magnetoelectric or complementary source usually share the common constraint of using metallic structures, namely reflectors and/or ground planes. However, the use of such metallic ground planes or the volume of these antennas make them unsuitable for UAV and nanosatellite applications due to the small size of platforms onboard. Huygens source antennas represent original solutions to satisfy the aforementioned mechanical and radiation constraints. Huygens source combines pairs of collocated and orthogonal electric and magnetic dipoles without the use of ground planes.

For this purpose, the design of a dielectric resonator antenna with capabilities to generate a pair of equivalent x-directed magnetic and y-directed electric dipoles with certain conditions in amplitude and phase, represents the main objective of this Ph.D. thesis in order to achieve Huygens source patterns with a low backward radiation along the -z-direction.

DRAs are particularly interesting to investigate since numerous degrees of freedom can be exploited in design to control, for instance, their radiation properties. Furthermore, the use of ceramic materials for DRA design provides high dielectric permittivities, low dielectric loss, robustness, and high temperature stability, which are mainly required for the requested applications in order to survive space environment [3, 6].

It has been demonstrated that several TE and quasi-TM modes can be excited in a rectangular dielectric resonator antenna in order to generate two orthogonal electric and magnetic dipoles, required to achieve a Huygens source pattern. The fundamental TE modes are here interesting since they radiate like magnetic dipoles. Moreover, the combination of second-order TE modes can generate a quasi-TM_{111} mode, which presents similar E- and H-fields as those radiated by an electric dipole.

In the next chapter, two Huygens source antennas in linear and circular polarizations are presented using stacked dielectric resonators. The stacked configuration is formed by two resonators with different physical and electrical properties in order to generate a pair of orthogonal electric and magnetic dipoles, required to achieve cardioid radiation patterns.

Chapter 2

Quasi-Huygens Sources using Stacked Dielectric Resonators

Sommaire

As detailed in Chapter 1, an antenna with a cardioid radiation pattern is often required for nanosatellite and UAV applications. These applications also demand for antennas without the use of reflectors or large ground planes which can satisfy their mechanical requirements due to the small volume of the platforms onboard. An original solution to achieve a cardioid radiation pattern without a ground plane consists in designing a Huygens source antenna.

It has been shown that a Huygens source antenna is equivalent to two orthogonal electric and magnetic dipoles radiating the same field in the E- and H-planes. For this purpose, both equivalent electric and magnetic sources can be generated by exciting TE and quasi-TM modes in a rectangular dielectric resonator, taking advantage of its numerous degrees of freedom for the shape and material properties.

However, it has been shown in the literature, that the proposed Huygens source DRAs [22, 68, 69, 71, 72] radiate perpendicular to the feeding probe due to the difficulty to generate a

horizontal equivalent electric dipole, *i.e.*, a y-directed electric dipole, in a rectangular dielectric resonator using a coaxial probe located along the -z axis.

In order to demonstrate the possibilities offered by DRAs in order to achieve a half-space radiation pattern, a single-fed linearly polarized Huygens source antenna using rectangular resonators is first presented. The dielectric resonators are here arranged in a stacked configuration with different isotropic permittivities to generate a pair of orthogonal electric and magnetic dipoles. As a result, the antenna achieves a cardioid radiation pattern without the use of a large ground plane. However, the radiation patterns still present slight asymmetric characteristics in the E- and H-planes. In order to demonstrate which modes are the main contributors, the spherical mode expansion is then performed. It is shown that several higher-order TE modes have an impact on the symmetry of the radiation patterns. Finally, this chapter presents a circularly polarized Huygens source antenna made up of two stacked dielectric resonators arranged in a cross-shaped configuration, and two coaxial probes. By exciting two pairs of electric and magnetic dipoles, a cardioid radiation pattern in circular polarization is achieved.

2.1 Linearly polarized Huygens source antenna using stacked dielectric resonators

This section is intended to demonstrate how a Huygens source antenna in linear polarization can be designed by combining pairs of orthogonal and collocated dipoles in stacked dielectric resonators in order to achieve improved radiation properties along +z-direction and low backward radiation.

2.1.1 Operating principle

In order to achieve a Huygens source pattern in linear polarization with improved radiation properties in the +z-direction and low backward radiation in the -z-direction, the TE^{x}_{111} and quasi-TM^{y}_{111} modes must be excited in a rectangular dielectric resonator. The electric and magnetic fields of these modes are equivalent to those radiated by a pair of x-directed magnetic and y-directed electric dipoles, respectively.

Figure 2.1 depicts the E- and H- field distributions of the TE^{x}_{111} mode in a rectangular dielectric resonator. As observed, the TE^{x}_{111} mode have similar fields to those radiated by a magnetic dipole along x axis since the E-field is circular around the x axis, and the H-field is vertical and strong along the x axis.

On the contrary, the TE^{x}_{121} and TE^{z}_{211} modes can be excited with equal amplitude and phase using a dielectric resonator with square cross section along the x- and z-directions in order to generate an equivalent quasi-TM^{y}_{111} mode. Figure 2.2 illustrates the E- and H- field distributions of the quasi-TM^{y}_{111} mode in a rectangular dielectric resonator. As observed, this

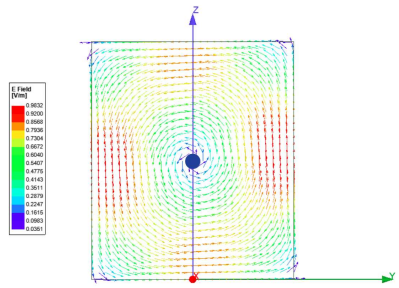

(a) E-field.

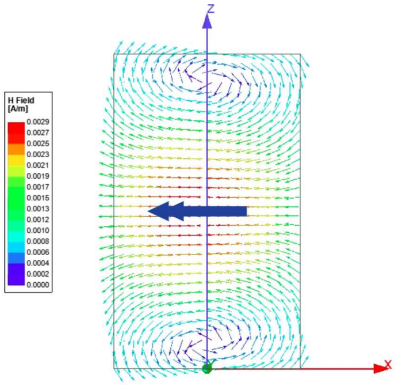

(b) H-field.

Figure 2.1: Field distributions of the TE^x_{111} mode in a dielectric resonator with dimensions a, b, and d along x-, y-, and z-directions, respectively, and with dimension ratios of $a = b/2 = d/2$.

mode radiates like an equivalent electric dipole along y-direction.

Regarding the design of a Huygens source antenna using rectangular dielectric resonators, it can be shown that a single resonator with a square cross section is insufficient to realize a pair of orthogonal electric and magnetic dipoles at close enough frequencies to achieve a cardioid radiation pattern.

Thus, the frequencies of resonant modes in a square-based DR are analyzed using eigen modes in Ansys HFSS. The analysis consists in performing a parametric analysis of the DRA dimensions and its relative permittivity. As an example, the properties of the TE^x_{111}, TE^x_{112} and TE^z_{211} modes in a dielectric resonator with square section $a = d = 39.4$ mm, $b = 19.6$ mm, and $\varepsilon_r = 13$ are analyzed, as depicted in Fig. 2.3. Table 2.1 shows the resonant modes in the dielectric resonator. It possible to note that the TE^x_{112} and TE^z_{211} modes resonate at the same frequency so that their combination generates the quasi-TM^y mode. However, a frequency difference of $\Delta_f = 450$ MHz between the TE^x_{111} and quasi-TM^y_{111} modes is obtained. This can also be explained considering that it is not possible to excite a fundamental and a higher-order mode along the same axis, namely TE^x_{111} and TE^x_{112} modes, at the same frequency in a single dielectric resonator, as observed in Fig. 2.4.

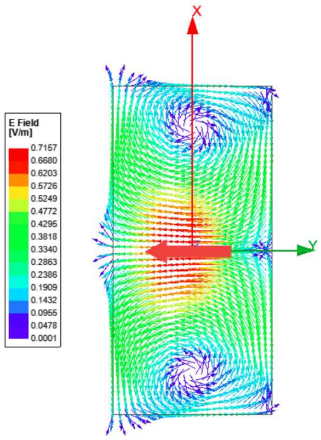

(a) E-field.

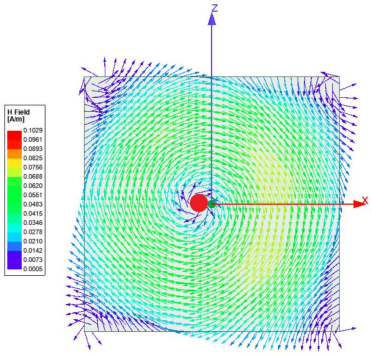

(b) H-field.

Figure 2.2: Field distributions of a quasi-TM^{y}_{111} mode in a dielectric resonator with dimensions a, b, and d along x-, y-, and z-directions, respectively, and with dimension ratios of $b = a/2 = d/2$.

	TE^{y}_{111}	TE^{x}_{111} TE^{z}_{111}	TE^{y}_{112} TE^{y}_{211}	TE^{z}_{211} TE^{x}_{112}
Resonance frequency (GHz)	1.95	2.46	-	2.91

Table 2.1: Resonant modes in an isotropic dielectric resonator using eigen mode analysis, when $a = d = 39.4$ mm, $b = 19.6$ mm, and $\varepsilon_r = 13$.

It is also possible to observe in Fig. 2.4a that the frequency difference between both TE^{x}_{111} and quasi-TM^{y}_{111} modes cannot be reduced by varying the relative permittivity of the isotropic dielectric resonator. The same behaviour is found by varying the square DRA dimensions (see Fig. 2.4b). Even if the DR is fed using a coaxial probe and its physical and electrical properties are optimized in order to generate a pair of elementary electric and magnetic dipoles at nearby frequencies, a Huygens source pattern cannot be achieved due to the large frequency difference which does not allow the fulfillment of the phase condition. Therefore, a single isotropic dielectric resonator is insufficient to fulfill the required properties

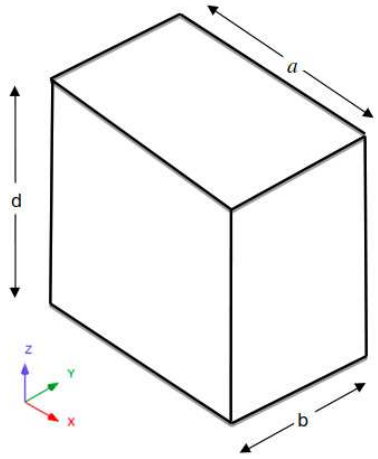

Figure 2.3: Exploded view of the square-based DRA.

to obtain a Huygens source pattern.

An original solution to reduce the frequency difference between the two TE^{x}_{111} and quasi-TM^{y}_{111} modes consists in using two stacked dielectric resonators with different dielectric permittivities or a single dielectric resonator with anisotropic properties, as will be discussed in Chapter 5.

This Chapter will focus on the design of a Huygens source antenna using two stacked dielectric resonators, as depicted in Fig. 2.5. Here, each resonator is supposed to generate either an electric or magnetic dipole, with the required conditions in amplitude and phase to achieve a cardioid radiation pattern. However, it is expected that both equivalent dipoles are not collocated using this stacked configuration, making difficult the achievement of a perfect Huygens source pattern.

Although both electric and magnetic dipoles are not collocated, a phase shift can be adjusted to partially compensate the asymmetry of the cardioid radiation patterns. This antenna is here called 'Quasi-Huygens source'. Regarding its principle of operation, it relies on tuning the resonant TE^{x}_{111} mode in the lower DR, and both TE^{x}_{121} and TE^{z}_{211} modes in nearby frequencies in the upper DR, so that the required phase difference between the equivalent magnetic and electric dipoles can be satisfied to accomplish a cardioid radiation pattern.

2.1.2 Antenna Design

A Huygens source antenna is here designed in the $2.4 - 2.5$ GHz ISM band. It is made up of two stacked dielectric resonators with different dimensions and dielectric permittivities, and it is fed by a single feeding probe, as illustrated in Fig. 2.5.

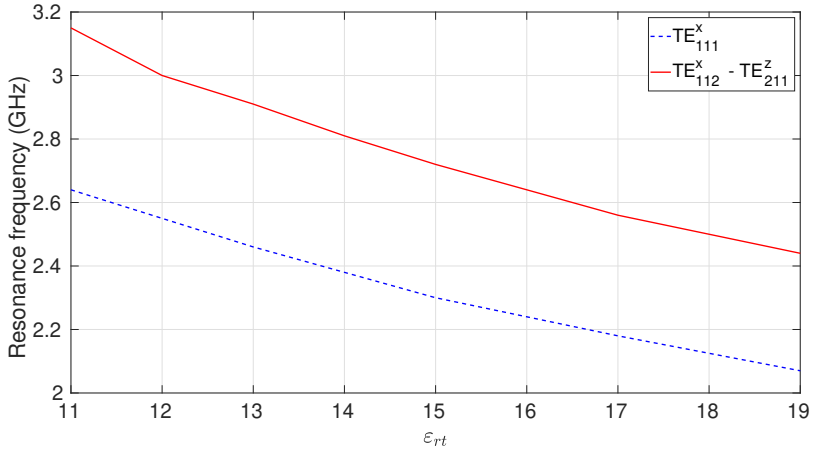

(a) Resonance frequency vs. relative frequency ε_t, when $a = d = 39.4$ mm .

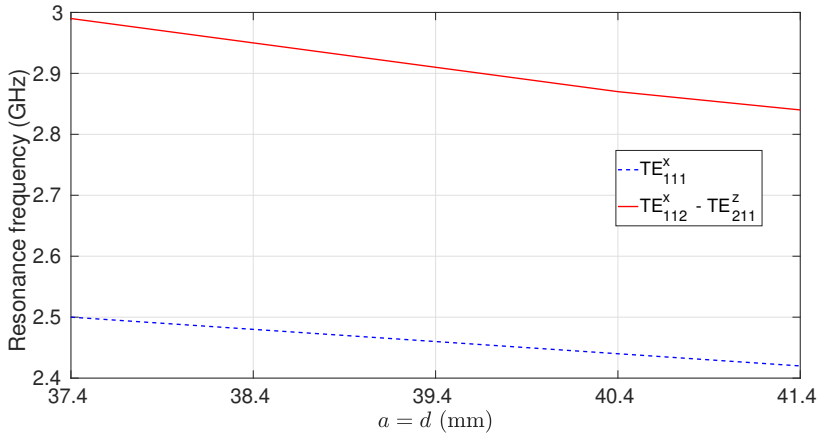

(b) Resonance frequency vs. square dimensions $a = d$, when $\varepsilon_r = 13$.

Figure 2.4: Variation of the resonance frequency in a single DR as a function of ε_t and $a = d$, when $b = 19.6$ mm.

Two stacked dielectric resonators with different dielectric constants are used to produce both TE^x_{111} and quasi-TM^y_{111} modes. The dimensions of the dielectric resonator located at the bottom of the structure, namely DR_1, are computed theoretically based on the dielectric waveguide model, as detailed in section 1.2.2. As first step, $\varepsilon_{r1} = 18$ related to DR_1 is fixed. This value is here chosen since it can be easily obtained using ceramic dielectric materials. Using the DMW, $a = 16$ mm, $b = 23$ mm, and $d = 27$ mm are found. Regarding the resonant modes in DR_1, it was observed that the required TE^x_{111} mode resonates at $f_0 = 2.43$ GHz.

Afterwards, the dielectric waveguide model is also used for DR_2 by fixing $\varepsilon_{r2} = 25$, in order to tune the quasi-TM mode at f_0. Consequently, $e = h = 33$ mm, and $g = 20.8$ mm are obtained. Table 2.2 shows the resonant modes of DR_2. The TE^x_{112} and TE^z_{211} modes resonate at the same frequency.

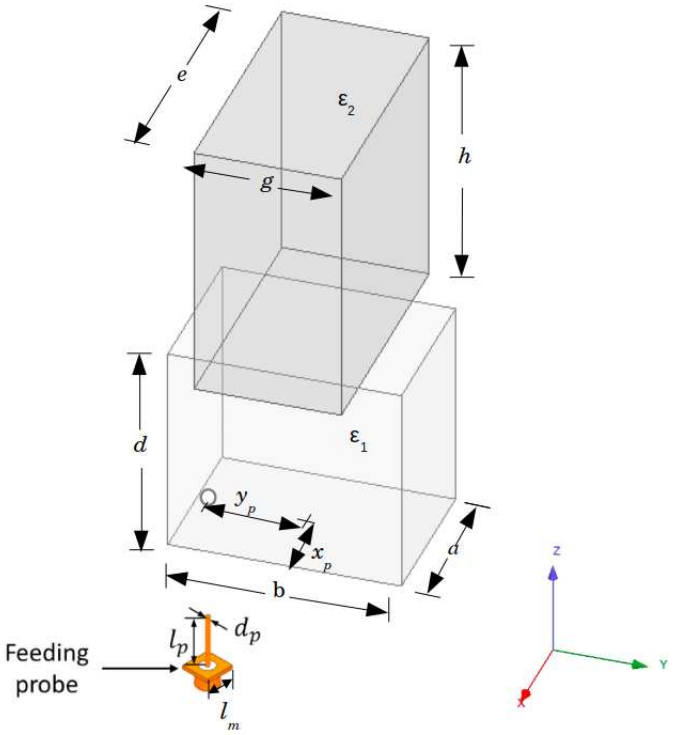

Figure 2.5: Exploded view of the stacked Huygens source DRA ($a = 16$ mm, $b = 23$ mm, $d = 21$ mm, $e = h = 26$ mm, $g = 14.5$ mm, $\varepsilon_{r1} = 18$, $\varepsilon_{r2} = 25$, $d_p = 1.23$ mm, $l_p = 12.8$ mm, $l_m = 7$ mm, $x_p = 0$ mm, and $y_p = 10.89$ mm)

.

Modes	TE^{y}_{111}	TE^{x}_{111} TE^{z}_{111}	TE^{y}_{112} TE^{y}_{211}	TE^{z}_{211} TE^{x}_{112}
Resonance frequency (GHz)	1.56	1.84	2.27	2.43

Table 2.2: Resonant modes in DR_2 using the DWM.

In order to excite the TE^{x}_{111} mode, DR_1 can be fed using a coaxial probe. The probe has a diameter of $d_p = 1.23$ mm and height of $l_p = 12.8$ mm. The probe is here supported by a small patch with square dimensions of $l_m = 0.06\ \lambda_0$, allowing to achieve the impedance matching. Afterwards, DR_2 is fed using the electric field distribution of the x-directed magnetic dipole. The goal is to excite the quasi-TM^{y}_{111} mode by electromagnetic coupling to generate an equivalent electric dipole along the y-direction with the required phase difference. The phase difference can be controlled by optimizing the dimensions d related to DR_1 and $e = h$ of DR_2, taking into account that both equivalent dipoles are not collocated due to the relative position of each resonator. In addition to that, the coupling between both dielectric resonators, using the stacked configuration, generates a frequency shift that can be corrected by optimizing the antenna dimensions.

A parametric analysis is then performed on the antenna dimensions in order to compensate the frequency shift due to the coupling between both dielectric resonators. For this, a and b

are first fixed. Afterwards, the dimensions d, $e = h$, and g are selected so that they allow the antenna to maximize the F/B ratio in the ISM band. The F/B ratio, in dB, is here defined as the mathematical substraction between the total antenna gain found at $\theta = 0°$ and its maximum value within $160° \leq \theta \leq 200°$ (based on Fig. 2.10), namely backward radiation, as expressed in the following equation

$$F/B\ ratio = G(\theta = 0°) - max[G(160° \leq \theta \leq 200°)]. \tag{2.1}$$

As a result of the optimization process, $d = 21$ mm and $g = 14.5$ mm are found. Furthermore, it is possible to observe in Fig. 2.6, that an adjustment of the square dimensions $e = h$ can improve the F/B ratio. A maximum F/B ratio considering $\phi = 0°$ at $f_0 = 2.43$ GHz can be achieved for $e = h = 26$ mm. Finally, the electrical antenna dimensions are $a = 0.13\ \lambda_0$, $b = 0.19\ \lambda_0$, $d = 0.17\ \lambda_0$, $e = h = 0.21\ \lambda_0$, and $g = 0.12\ \lambda_0$.

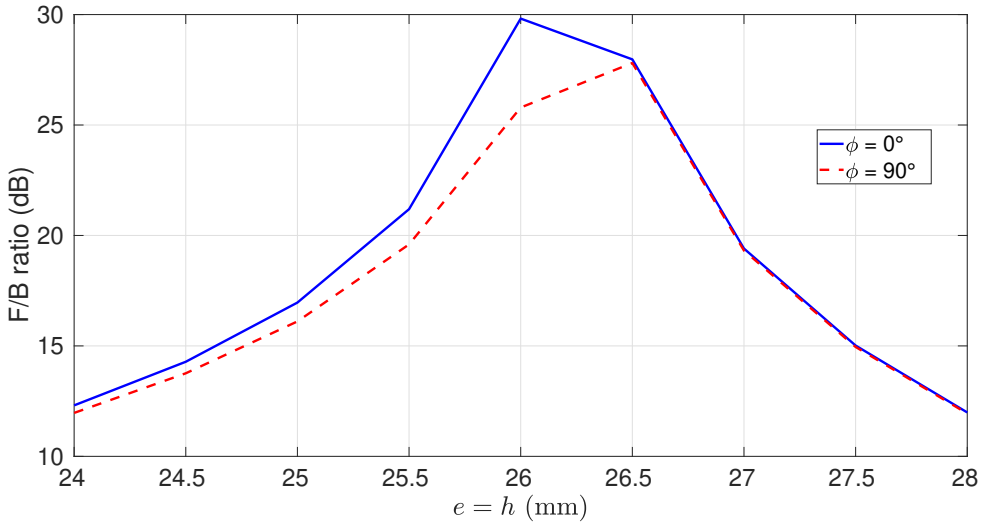

Figure 2.6: Variation of the dimensions $e = h$ vs. F/B ratio considering $\phi = 0°$ and 90° at 2.43 GHz, when $a = 16$ mm, $b = 23$ mm, $d = 21$ mm, $g = 14.5$ mm, $\varepsilon_{r1} = 18$, and $\varepsilon_{r2} = 25$.

2.1.3 Simulated results

Table 2.3 shows the resonant modes in the optimized stacked dielectric resonator using eigen mode analysis in Ansys HFSS. This simulation is performed using perfectly matched layers (PML) in order to obtain accurate results. Observe that both TE^x_{111} and quasi-TM^y_{111} modes resonate at 2.38 GHz and 2.56 GHz, respectively. The required TE and TM modes are thus tuned at nearby frequencies so that a proper phase difference between both equivalent electric and magnetic sources can be achieved at f_0.

Figure 2.7 depicts the electric field distribution of the stacked dielectric resonator using modal simulation in Ansys HFSS at 2.43 GHz. As observed, loops shapes are observed in

Modes	TE^{x}_{111}	TE^{z}_{111}	TE^{y}_{112}	TE^{z}_{211} TE^{x}_{112}
Resonance frequency (GHz)	2.38	2.47	2.52	2.56

Table 2.3: Resonant modes in the optimized stacked dielectric resonator using eigen mode analysis, when $a = 16$ mm, $b = 23$ mm, $d = 21$ mm, $e = h = 26$ mm, $g = 14.5$ mm, $\varepsilon_{r1} = 18$, and $\varepsilon_{r2} = 25$.

the E- and H-fields so that the confined fields in the stacked DRs are equivalent to those radiated by two x-directed magnetic and y-directed electric dipoles. Furthermore, it is shown that both equivalent dipoles are not collocated and not found at the interface between the two dielectric resonators. This result is indeed expected since each resonator produces a single equivalent dipole.

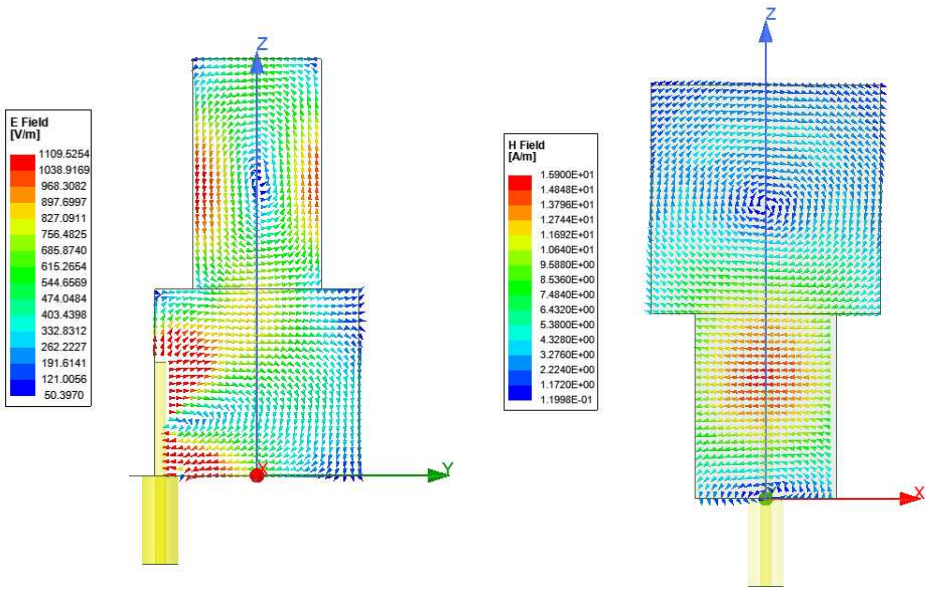

(a) Electric field. (b) Magnetic field.

Figure 2.7: Field distributions of the equivalent dipoles in the optimized dielectric resonator found at 2.43 GHz.

Fig. 2.8 and 2.9 show the simulated reflection coefficient and the F/B ratio of the proposed antenna. The antenna has an impedance bandwidth of 9.5% from 2.27 to 2.5 GHz, for a reflection coefficient of $|S_{11}| \leq -10$ dB. Furthermore, the proposed Huygens source DRA has a maximum F/B ratio of 31.8 dB at 2.43 GHz, considering $\phi = 0°$ and 90°, that is to say xz- and yz-planes on Fig. 2.5, respectively. The F/B ratio bandwidth (F/B ratio ≥ 15 dB) is 3.3%, from 2.39 GHz to 2.47 GHz.

Fig. 2.10 and 2.11 show the simulated results for the total antenna gain, as well as the co-polarization (Co-pol.) and cross-polarization (X-pol.) gain of the proposed Huygens source DRA at 2.43 GHz, considering $\phi = 0°$ and 90°. Observe that the backward radiation is

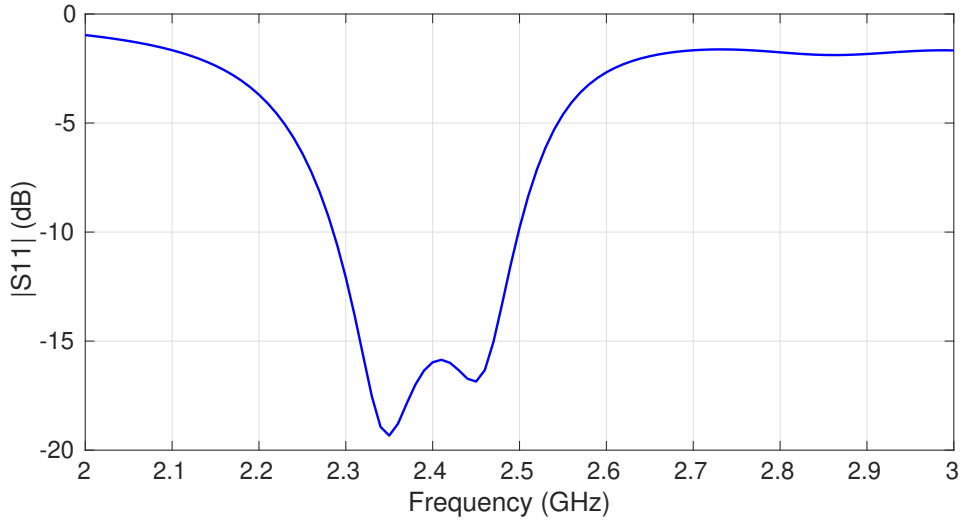

Figure 2.8: Simulated reflection coefficient of the isotropic stacked Huygens source DRA.

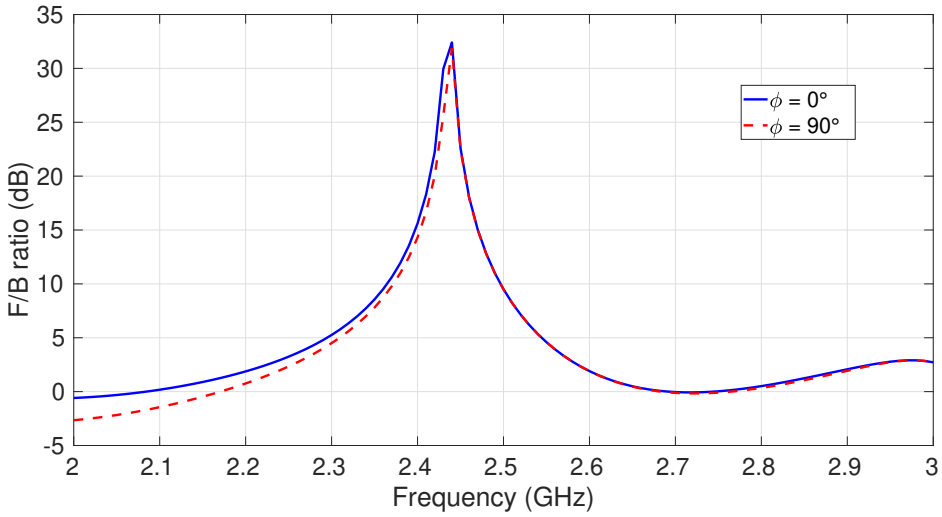

Figure 2.9: Simulated front-to-back ratio the isotropic stacked Huygens source DRA, considering $\phi = 0°$ and $90°$.

significantly reduced. Furthermore, the antenna has a maximum gain ($\theta = 0°$) of 5.86 dBi at 2.43 GHz. However, both E- and H-planes of the radiation pattern are not perfectly symmetric. It may be to the fact that both equivalent dipoles are not collocated and they may have unbalanced amplitudes and phases, as it will be discussed in the next section. The X-pol. gain at $\phi = 90°$ is lower than -40 dB. Besides, the X-pol. gain at $\phi = 0°$ is mainly due to the lack of symmetry of the stacked dielectric resonators and the use of a single feeding probe. This latter will be discussed later in Chapter 5.

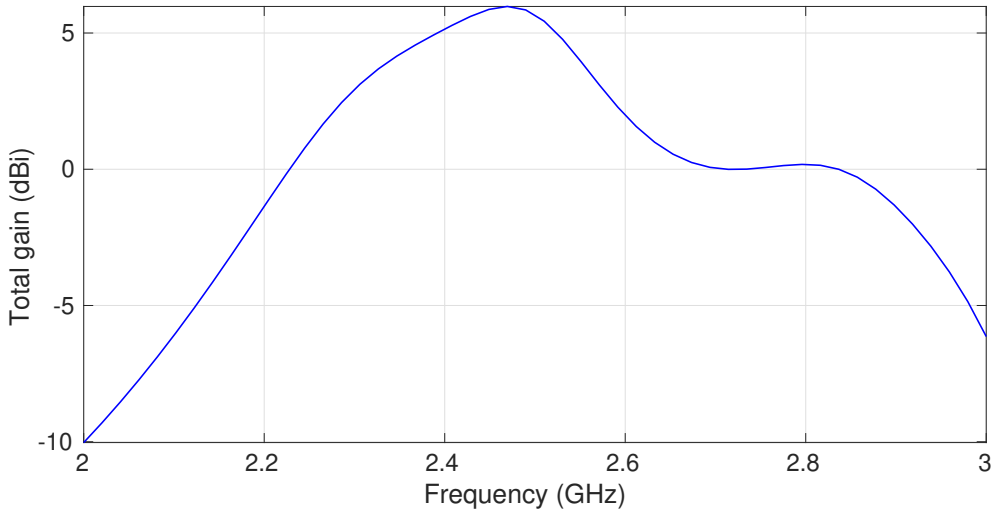

Figure 2.10: Simulated gain of the isotropic stacked Huygens source DRA at 2.43 GHz for $\theta = 0°$.

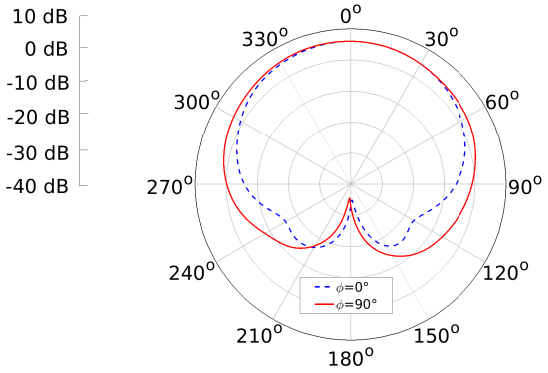

(a) Total gain considering $\phi = 0°$ and 90°.

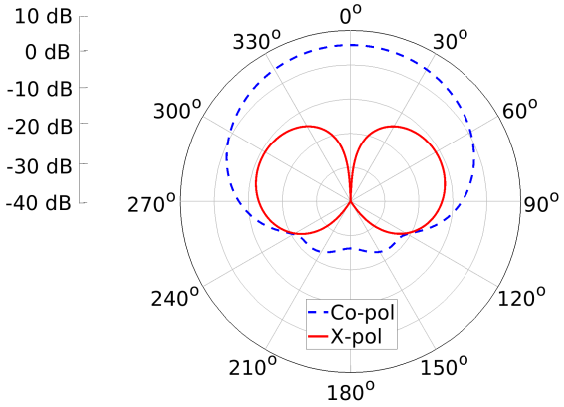

(b) Co-pol. and X-pol. gain considering $\phi = 0°$.

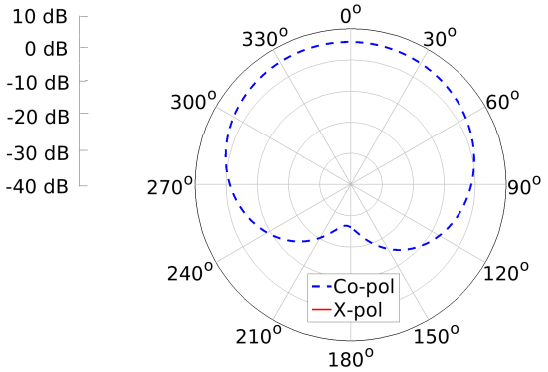

(c) Co-pol. and X-pol. gain considering $\phi = 90°$.

Figure 2.11: Simulated gain of the stacked Huygens source DRA at 2.43 GHz.

2.2 Spherical mode analysis of the proposed DRA

A spherical mode analysis is here performed in order to determine the contribution of the fundamental TE modes that generate a pair of non-collocated electric and magnetic dipoles in the proposed stacked DRA. Furthermore, the impact of higher-order modes on the lack of symmetry of its radiation pattern in the E- and H-planes are analyzed in this section.

2.2.1 Theory of spherical mode expansion

The spherical mode expansion (SME) is an interesting tool to better understand the antenna behavior. For this, the radiated field by the antenna under test is expanded in electric and magnetic spherical modes, as detailed in Appendix A. Thus, the expanded electric field can be written as [73, 74]

$$\mathbf{E}(\mathbf{r}) = \sum_{n=1}^{\infty} \sum_{m=-n}^{n} \left[d_{mn}^{TE} \mathbf{M}_{mn}(\mathbf{r}) + d_{mn}^{TM} \mathbf{N}_{mn}(\mathbf{r}) \right] \tag{2.2}$$

where d_{mn}^{TE} and d_{mn}^{TM} are the complex spherical (sph) coefficients of the TE^{sph} and TM^{sph} components of the radiated field, $\boldsymbol{M}_{mn}(\boldsymbol{r})$ and $\boldsymbol{N}_{mn}(\boldsymbol{r})$ describes the normalized vector spherical harmonics in far-field, and m and n are the mode indices ($\mid m \mid \leq n$).

The index m defines the ϕ-variation of the spherical mode in the interval $0° \leq \phi \leq 360°$ *i.e.*, the number of oscillations along the azimuth. For instance, if $m = 1$, the variation of the field occurs from the x axis towards the y axis. Otherwise, the opposite rotation defines $m = -1$. On the contrary, n is the multipolar order so that θ-variation depends on the indices m and n.

In Fig. 2.12, the spherical harmonic modes are represented in a sphere by varying the indices m and n. For instance, it is shown that an increment of n gives an increase of the number of oscillations in the radiation pattern. In addition to that, it is possible to observe that an elementary dipole radiation pattern-like can be obtained for $n = 1$.

2.2.2 Spherical mode expansion for elementary dipoles

In order to better understand the output of the spherical mode expansion, simulations in FEKO are performed for elementary electric and magnetic dipoles. For instance, the spherical coefficients for an elementary electric source placed along y axis (see Fig. 2.13) are calculated in simulation using FEKO. As a result, note that the fundamental TM$_{-11}^{sph}$ and TM$_{11}^{sph}$ modes are the only modes that exist in the SME when the electric source along y axis is placed at the origin of the coordinate system, *i.e.* at $x = y = z = 0$, as shown in Table 2.4. Besides, the spherical coefficients associated to the TM$_{-11}^{sph}$ and TM$_{11}^{sph}$ have identical amplitudes and phases.

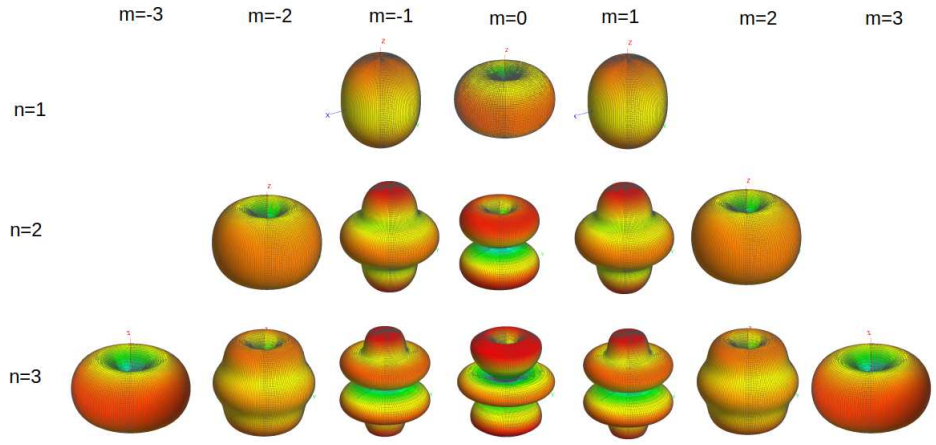

Figure 2.12: Vector pherical harmonics by varying the indices n and m.

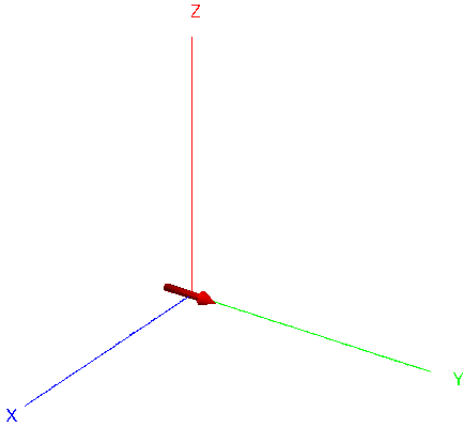

Figure 2.13: y-directed electric dipole.

Mode	m	n	Phase (degrees)	Rel. power (%)
TM^{sph}	-1	1	90	50
TM^{sph}	1	1	90	50

Table 2.4: Spherical coefficients of an electric source located along y axis and at the origin of the coordinate system.

On the contrary, if the y-directed electric dipole is located outside the origin (see Fig. 2.14), higher-modes exist in the SME. Table 2.5 shows the spherical coefficients for a y-directed elementary electric dipole located at $h = \lambda/4$. As observed, several TE and TM modes of first and second order now appear at the spherical mode expansion.

Regarding the far-field properties of a x-directed elementary magnetic dipole located at

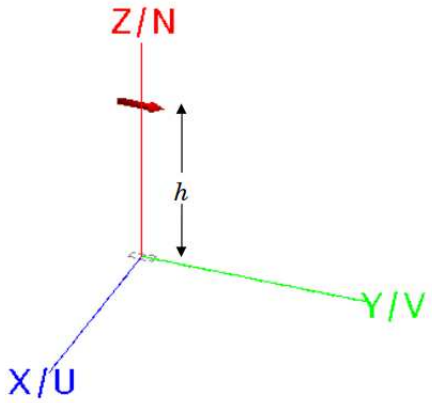

Figure 2.14: y-directed electric dipole with an offset of $\lambda/4$.

Mode	m	n	Phase (degrees)	Rel. power (%)
TE^{sph}	-1	1	180	18.5
TM^{sph}	-1	1	90	16.1
TE^{sph}	1	1	0	18.5
TM^{sph}	1	1	90	16.1
TE^{sph}	-1	2	-180	3.6
TM^{sph}	-1	2	90	9.9
TE^{sph}	1	2	0	3.6
TM^{sph}	1	2	90	9.9

Table 2.5: Spherical coefficients of a y-directed electric dipole with an offset of $\lambda/4$.

$x = y = z = 0$, it radiates a pair of fundamental TE_{-11}^{sph} and TE_{11}^{sph} modes with same amplitudes and 180° out of phase, as shown in Table 2.6.

Mode	m	n	Phase (degrees)	Rel. power (%)
TE^{sph}	-1	1	0	50
TE^{sph}	1	1	-180	50

Table 2.6: Spherical coefficients of a magnetic source located along x axis and at the origin of the coordinate system.

Finally, two orthogonal and collocated elementary y-directed electric and x-magnetic dipoles are analyzed using the SME. Both orthogonal dipoles are defined with equal amplitudes and excited in phase quadrature in order to obtain a perfect Huygens source pattern, as observed in Fig. 2.15. Table 2.7 shows the associated modes of the ideal Huygens source. As expected, the sum of the spherical TE_{-11}^{sph} and TE_{11}^{sph} modes radiate with a relative power of 50%. The remaining power is distributed over the TM_{-11}^{sph} and TM_{11}^{sph} modes, which also have same amplitudes. Regarding the phase difference between the TE_{11}^{sph} and TM_{11}^{sph} modes, they radiate 180° out of phase so that a Huygens source pattern with symmetric radiations patterns in the E- and H-planes can be achieved.

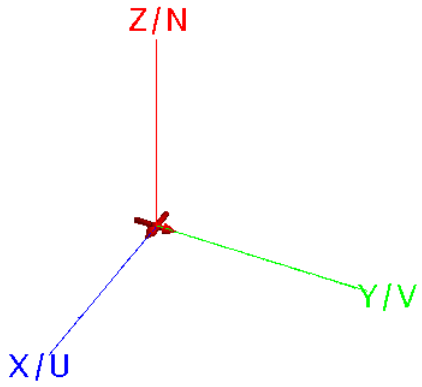

Figure 2.15: Combination of two orthogonal x-directed magnetic and y-directed electric dipoles.

Mode	m	n	Phase (degrees)	Rel. power (%)
TE^{sph}	-1	1	90	25
TM^{sph}	-1	1	90	25
TE^{sph}	1	1	-90	25
TM^{sph}	1	1	90	25

Table 2.7: Spherical coefficients of an ideal Huygens source.

2.2.3 Spherical mode expansion for the proposed DRA

Based on the previous SME analysis, it is shown that spatial location of the electric and magnetic sources plays an important role to correctly determine the spherical coefficients. For that reason, in order to perform the SME analysis for the proposed DRA, it is important to fix the origin of the coordinate system. Arbitrarily, the origin is here located at the interface between the two dielectric resonators. However, it is expected that higher-order spherical modes radiate in the proposed antenna.

Fig. 2.16 shows the relative power of spherical coefficients in the proposed DRA as a function of the frequency. As a matter of simplicity, the relative power of the spherical modes is calculated so that the $TE^{sph}_{|\pm1|1}$ mode corresponds to the sum of its fundamental TE^{sph}_{-11} and TE^{sph}_{11} modes, since their magnitudes are identical. The same procedure is applied to the $TM^{sph}_{-11}/TM^{sph}_{11}$, $TE^{sph}_{-12}/TE^{sph}_{12}$ and $TM^{sph}_{-12}/TM^{sph}_{12}$ modes.

The amplitude difference of the fundamental $TE^{sph}_{|\pm1|1}$ and $TM^{sph}_{|\pm1|1}$ modes at 2.43 GHz is 23.58%. Regarding the second-order modes, only the TE^{sph}_{12} mode contributes with a relative power higher than 4%. The other modes, such as the TE^{sph}_{22}, TM^{sph}_{12}, and TM^{sph}_{22}, have a negligible relative power. The TM^{sph}_{01} mode radiates due to the coaxial probe placed along z axis based on the SME.

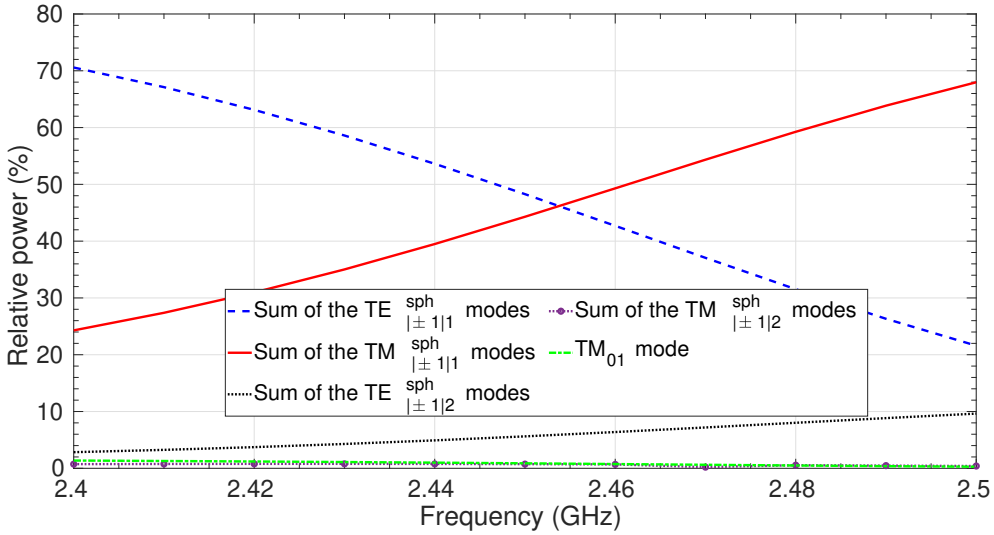

Figure 2.16: Relative power of the spherical modes in the stacked Huygens source DRA.

Fig 2.17 depicts the phase difference between the TE_{11}^{sph} and TM_{11}^{sph} coefficients. It is shown that these fundamental TE and TM modes are 168° out of phase at 2.43 GHz. This result can partially satisfy the requirements to achieve a quasi-Huygens source radiation pattern since the dipoles are not collocated so that higher-order modes also exist in the SME. Therefore, the compensation of the phase difference and radiation of higher-order modes leads to obtain asymmetric cardioid radiation patterns in the E- and H-planes.

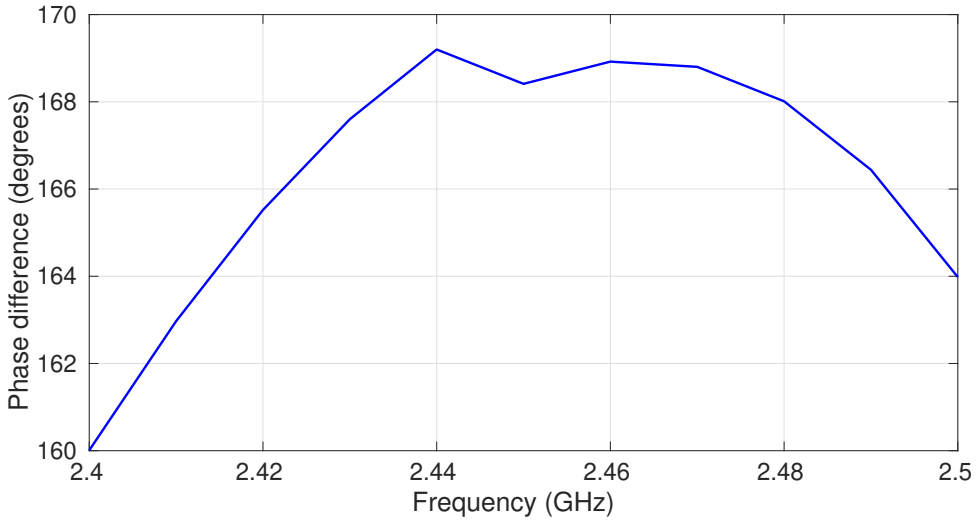

Figure 2.17: Phase difference between the fundamental TE_{11}^{sph} and TM_{11}^{sph} modes in the stacked Huygens source DRA.

Fig. 2.18a illustrates the normalized total gain patterns of the proposed DRA at 2.43 GHz. Moreover, due to the fact that equal amplitudes for the TE_{11}^{sph} and TM_{11}^{sph} modes are found at

2.45 GHz (see Fig. 2.16), the radiation pattern is also depicted at this frequency in Fig. 2.18b. A comparison between the radiation patterns obtained with the proposed DRA and an ideal Huygens source can be performed based on this figure. As observed, the radiation pattern at 2.43 GHz, considering $\phi = 90°$, behaves similar to that obtained using an ideal Huygens source (see Fig. 2.18a). The F/B ratio of the proposed DRA is large enough to satisfy the radiation constraints for UAV and nanosatellite applications. However, the radiation pattern at 2.43 GHz is not perfectly symmetric.

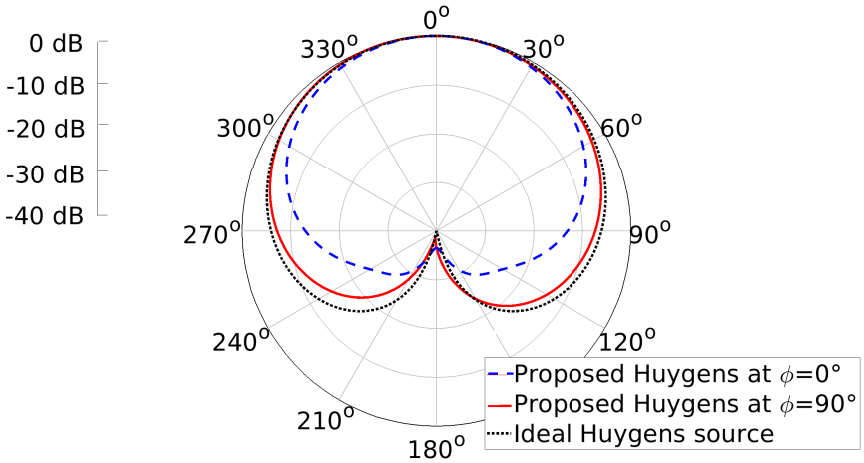

(a) $f = 2.43$ GHz.

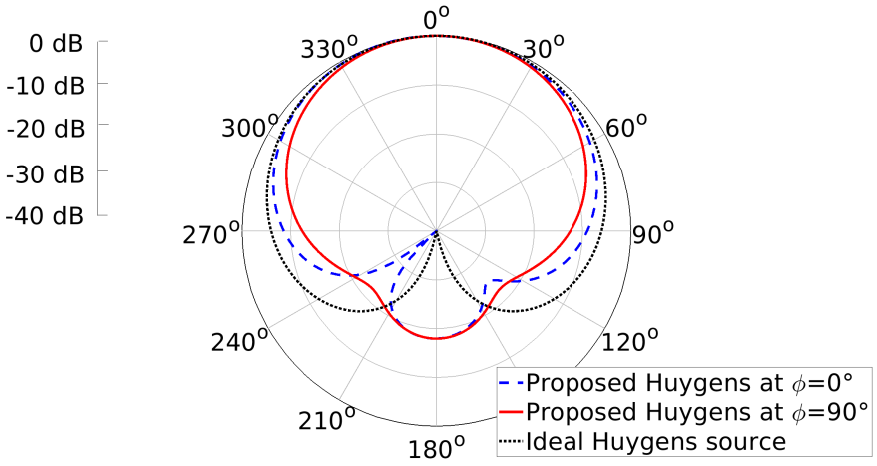

(b) $f = 2.45$ GHz.

Figure 2.18: Normalized simulated gain of the stacked Huygens source DRA.

On the other hand, the antenna performances in far-field at 2.45 GHz presents an opposite

behavior. The radiation pattern present better symmetry in the E- and H-planes. However, the F/B ratio is lower than the obtained at 2.43 GHz. As a conclusion, the unbalance amplitude of the fundamental modes is here compensated by the radiation of higher-order modes in order to achieve a quasi-Huygens source pattern with asymmetric properties in the E- and H-planes.

2.2.4 Impact of higher-order modes on the radiation pattern symmetry

The contribution of higher-order modes is here investigated in order to understand the lack of symmetry of the radiation patterns at $\phi = 0°$ and $90°$. For this, the spherical mode expansion is performed at two different frequencies, at 2.43 GHz and 2.45 GHz. The first frequency is here selected since the antenna radiates with a quasi-Huygens source radiation pattern. For the latter, a perfect amplitude balance between the $\mathrm{TE}^{sph}_{|\pm1|1}$ and $\mathrm{TM}^{sph}_{|\pm1|1}$ modes is found at 2.45 GHz. As an objective of the SME, the impact of higher-order modes on the radiation pattern is analyzed in this section by imposing certain properties in phase and amplitude on the fundamental spherical TE and TM modes.

2.2.4.1 Higher-order modes at 2.43 GHz

Fig. 2.19 shows the radiation patterns of the original antenna (as shown Fig. 2.18a) and antenna under test by keeping all the modes found in Fig. 2.16 and imposing artificially (a) just a phase difference of 180° between the fundamental TE^{sph}_{11} and TM^{sph}_{11} modes, and (b) ideal Huygens source properties, *i.e.*, phase difference of 180° and same amplitudes. As a result, almost symmetric patterns can be achieved for both cases. However, the F/B ratio decreases, as observed in Fig. 2.19.

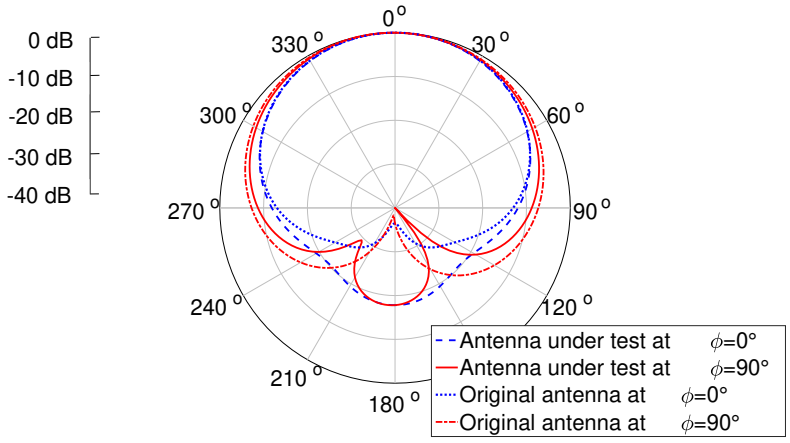

(a) 180° phase difference between the fundamental TE_{11}^{sph} and TM_{11}^{sph} modes.

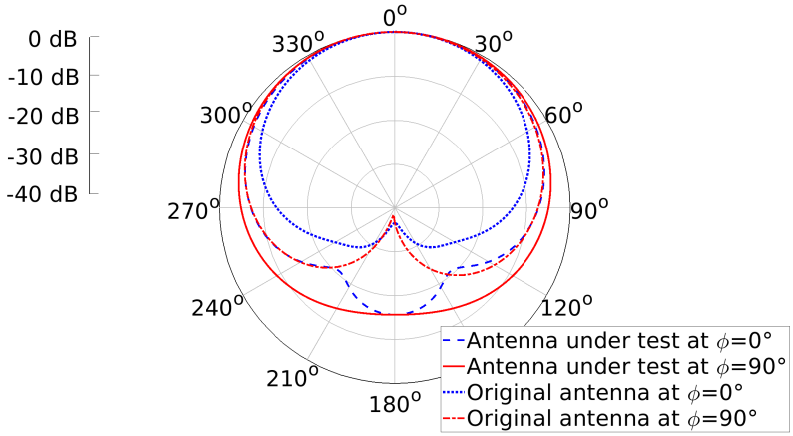

(b) Equal amplitudes and 180° phase difference between the fundamental TE_{11}^{sph} and TM_{11}^{sph} modes.

Figure 2.19: Normalized simulated gain of the stacked Huygens source DRA at 2.43 GHz with specific conditions on fundamental modes.

Then, considering far-field radiation of the proposed antenna by suppressing all the higher-order modes ($\mathrm{TE}_{|\pm1|2}^{sph}$, $\mathrm{TM}_{|\pm1|2}^{sph}$, and TM_{01}^{sph}), the radiation patterns are obtained as depicted in Fig. 2.20a. It is observed that both planes at $\phi = 0°$ and 90° now have symmetric shapes. However, the F/B ratio only achieves 15 dB, that is to say a lower value than that obtained with the proposed antenna. On the other hand, it is shown that the TE_{12}^{sph} mode has a significant impact on the F/B ratio and the symmetry of the radiation patterns at 2.43 GHz.

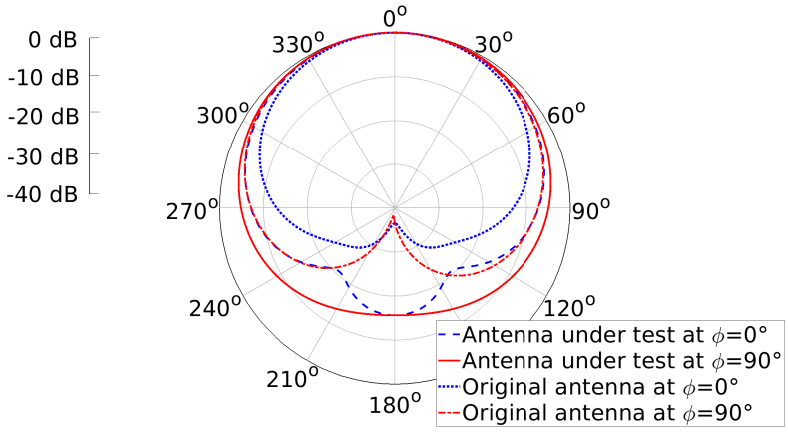

(a) Radiation pattern suppressing all the higher-order modes.

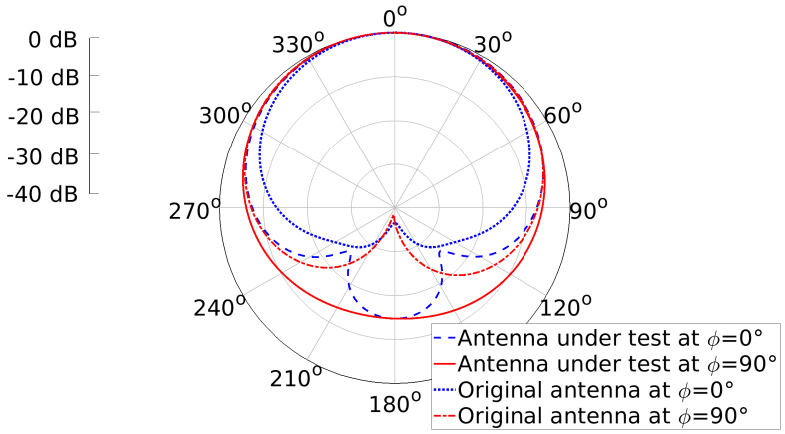

(b) Radiation pattern suppressing only the TE_{12}^{sph} mode.

Figure 2.20: Normalized simulated gain of the stacked Huygens source DRA suppressing higher-order modes at 2.43 GHz.

Fig. 2.21 illustrates the far-field radiation of the proposed antenna by suppressing the TM_{12}^{sph} and TM_{01}^{sph} modes. As observed, the TM_{12}^{sph} mode also has an impact on the far-field radiation properties of the DRA. In addition to that, the F/B ratio of the antenna decreases about 15 dB by suppressing the TM_{12}^{sph} mode with respect to that obtained in absence of higher-order modes. On the contrary, a negligible impact occurs when suppressing the TM_{01}^{sph} mode. Here, an identical behavior is obtained while comparing the original radiation pattern and that produced by the antenna under test.

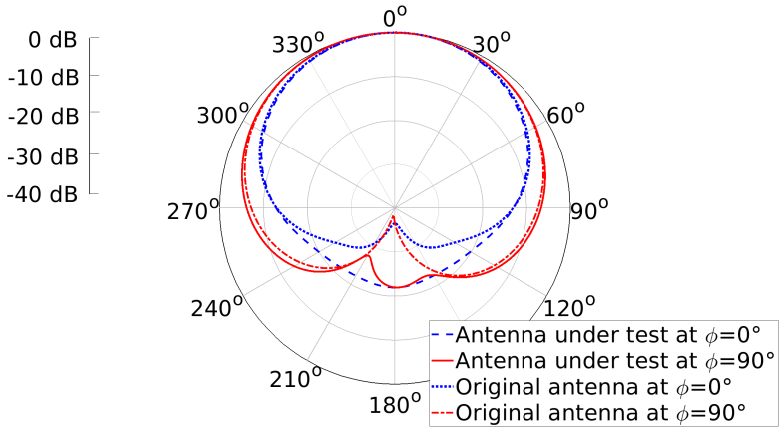

(a) Radiation pattern suppressing only the TM_{12}^{sph} mode.

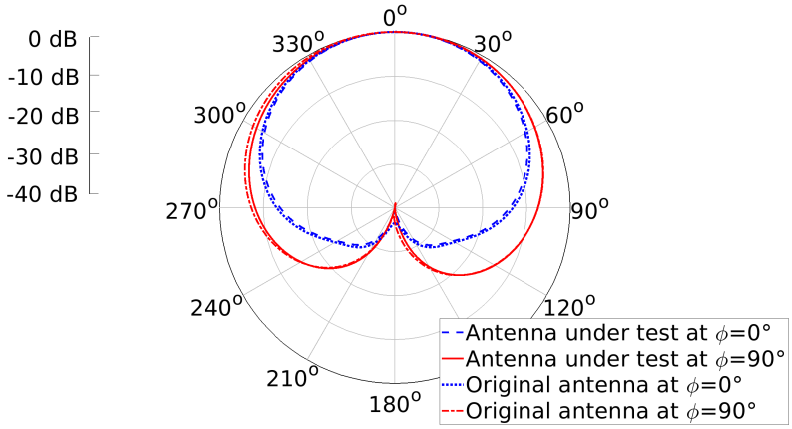

(b) Radiation pattern suppressing only the TM_{01}^{sph} mode.

Figure 2.21: Normalized simulated gain of the stacked Huygens source DRA suppressing the TM_{12}^{sph} and TM_{01}^{sph} modes at 2.43 GHz.

2.2.4.2 Higher-order modes at 2.45 GHz

The spherical mode expansion is also performed at 2.45 GHz since the fundamental $\mathrm{TE}_{|\pm1|1}^{sph}$ and $\mathrm{TM}_{|\pm1|1}^{sph}$ modes present a balanced amplitude, which is required to achieve a perfect Huygens source radiation pattern. However, the impact of higher-order modes is here analyzed since the equivalent electric and magnetic dipoles are not collocated.

Fig. 2.22 shows the radiation pattern of the proposed antenna by suppressing (a) all the higher-order modes, and (b) only the TE_{12}^{sph} mode. For case (a), a perfect symmetry of the radiation patterns at $\phi = 0°$ and 90° is achieved. Furthermore, the antenna achieves a

F/B ratio of 23 dB, which is a reasonable value when designing Huygens source antennas. Comparing these results with the radiation pattern of the original antenna, it is possible to conclude that the radiation of higher-order modes affects the symmetry of the radiation patterns at 2.45 GHz. For case (b), the suppression of the TE_{12}^{sph} mode has an important impact on the symmetry of the radiation patterns and the F/B ratio. In addition to that, similar F/B ratios and far-field radiation are achieved at $\phi = 90°$ when comparing Fig. 2.22a and Fig. 2.22b.

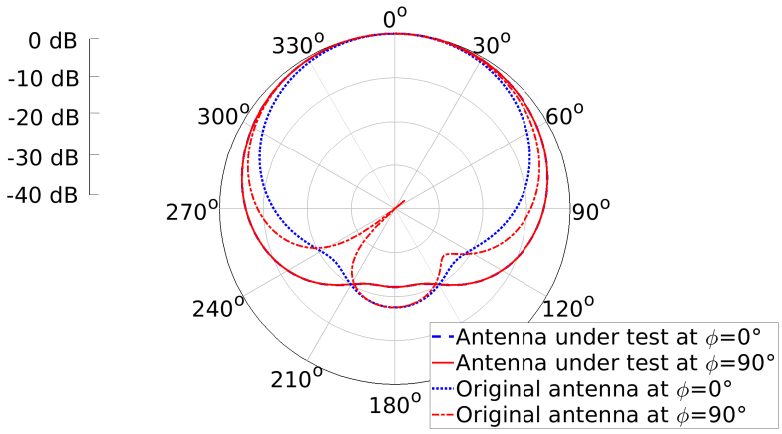

(a) Radiation pattern suppressing all the higher-order modes.

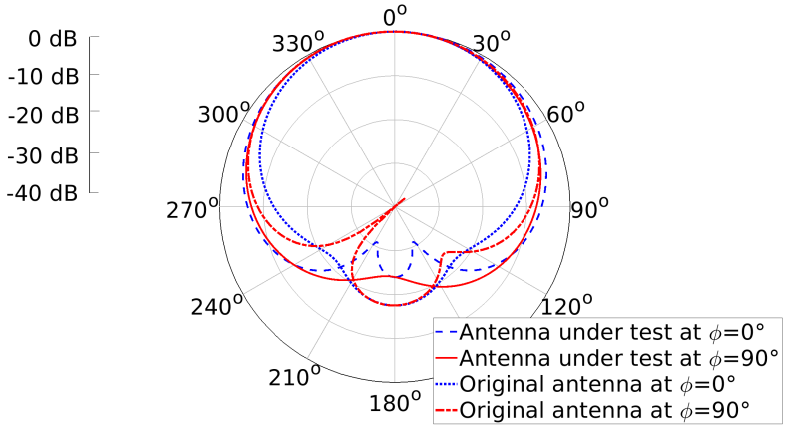

(b) Radiation pattern suppressing only the TE_{12}^{sph} mode.

Figure 2.22: Normalized simulated gain of the stacked Huygens source DRA suppressing higher-order modes at 2.45 GHz.

A new test is finally performed using the SME by suppressing only the (a) TM_{12}^{sph} or (b) TM_{01}^{sph} modes, as shown in Fig. 2.23. It is possible to observe that similar far-field radiation is found when comparing with the original antenna at 2.45 GHz.

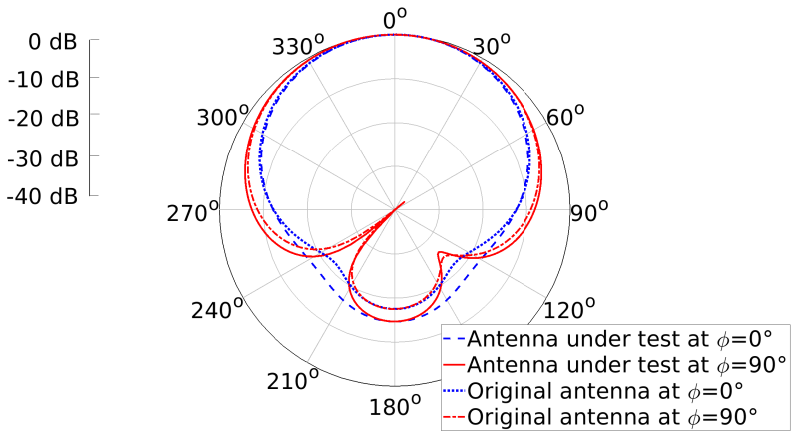

(a) Radiation pattern suppressing only the TM_{12}^{sph} mode.

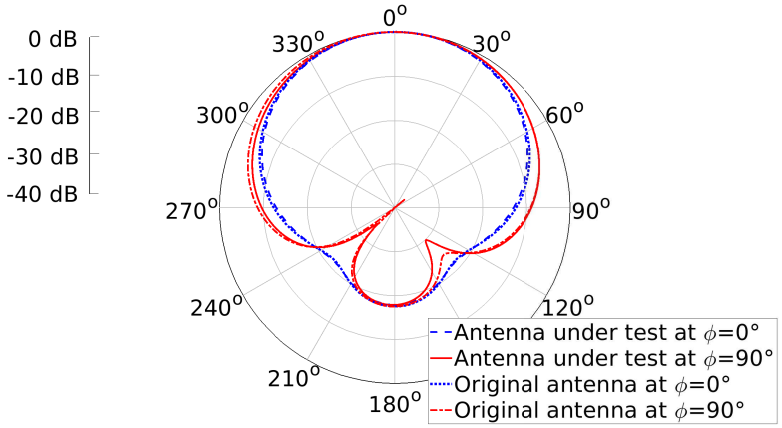

(b) Radiation pattern suppressing only the TM_{01}^{sph} mode.

Figure 2.23: Normalized simulated gain of the stacked Huygens source DRA suppressing only the TM_{12}^{sph} mode and TM_{01}^{sph} mode at 2.45 GHz.

It is shown that fact of not having collocated dipoles in the stacked DRA leads to the radiation of higher order modes. More specifically, the TE_{12}^{sph} and TM_{12}^{sph} modes have an important impact on the the asymmetry of the radiation patterns in the E- and H-planes, at 2.43 GHz. On the other hand, the unbalance amplitude between the fundamental modes is here compensated with the radiation of higher-order modes in order to achieve quasi-Huygens source properties.

2.3 Circularly polarized quasi-Huygens source antenna using stacked DRs

In the previous section, a single-fed linearly polarized quasi-Huygens source antenna was presented based on stacked dielectric resonators. In this section, its possible extension to circular polarization is presented. It consists of a cross-shaped antenna made of two stacked dielectric resonators.

2.3.1 Principle of operation

The Huygens source in circular polarization relies on the orthogonal combination of two linearly polarized Huygens sources. According to the coordinate system shown in Fig. 2.24, the first Huygens source which is linearly polarized in the xz-plane, is due to the TE^{x}_{111} and quasi-TM^{y}_{111} modes in the dielectric resonators. The second Huygens source which is linearly polarized in the yz-plane, is generated by the TE^{y}_{111} and quasi-TM^{x}_{111} modes. Finally, two ports with phase quadrature are used to achieve circular polarization.

2.3.2 Antenna design

The proposed antenna concept is designed to obtain a quasi-Huygens source in the 2.45 GHz ISM band. Given the previous linearly polarized quasi-Huygens source antenna detailed in section 2.1, a new structure is designed by duplicating the stacked dielectric resonator and rotating it 90° along the z axis to form a stacked cross-shaped resonator, as shown in Fig. 2.24. The proposed dielectric resonator is fed using two coaxial probes 90° out of phase to excite the TE^{x}_{111} and TE^{y}_{111} modes with the required phase difference to achieve circular polarization. In addition to that, the quasi-TM^{x}_{111} and quasi-TM^{y}_{111} modes are excited using the electric field distribution of the x-directed and y-directed magnetic dipoles, respectively. Here, a proper frequency shift between TE and quasi-TM modes allows to satisfy the requirements to obtain a cardioid-like radiation pattern. This frequency shift is accomplished by setting the electrical and physical properties of the stacked dielectric resonator.

Firstly, considering the same dimensions for the DRA as the one used for the linearly polarized Huygens source, the resonance frequencies of the eigen modes in the stacked cross-shaped dielectric resonator are found, as reported in table 2.8. The required TE and quasi-TM modes resonates at frequencies below $f_0 = 2.45$ GHz. This frequency shift downwards of the resonant modes may be due to the cross shape of the dielectric resonators. It can be corrected by optimizing the dimensions and electrical properties of the stacked cross-shaped dielectric resonator.

A parametric analysis is then performed on the antenna dimensions in order to adjust the frequency shift between TE and quasi-TM modes and tune the antenna at $f_0 = 2.45$ GHz. As a result, the electrical and physical properties of the dielectric resonators are $a = 13$ mm,

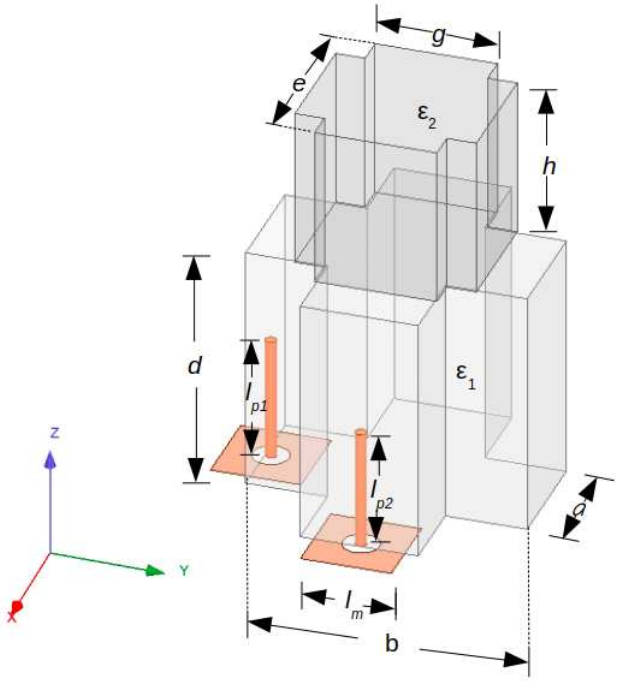

Figure 2.24: Exploded view of the stacked cross-shaped Huygens source DRA (a = 13 mm, $b = d$ = 31 mm, $e = h$ = 20 mm, g = 13.5 mm, ε_{r1} = 11.5, ε_{r2} = 18, l_{p1} = 15.5 mm, l_{p2} = 15 mm, and l_m = 10 mm).

Modes	TE^x_{111} TE^y_{111}	TE^z_{111}	quasi-TM^x_{111} quasi-TM^y_{111}
Resonance frequency (GHz)	1.85	2.02	2.20

Table 2.8: Resonance frequencies of the eigen modes in the stacked cross-shaped dielectric resonator with a = 16 mm, b = 23 mm, d = 21 mm, $e = h$ = 26 mm, g = 14.5 mm, ε_{r1} = 18, and ε_{r2} = 25.

$b = d$ = 31 mm, $e = h$ = 20 mm, g = 13.5 mm, ε_{r1} = 11.5, and ε_{r2} = 18. Similarly, the total electrical antenna dimensions are $d + h = 0.41\lambda_0$, and $b = 0.25\lambda_0$. The probes have a diameter of d_p = 1.23 mm, and heights of l_{p1} = 15.5 mm, and l_{p2} = 15 mm. They are supported by small metallic plates with square dimensions of $l_m = 0.08\ \lambda_0$ to ensure the impedance matching. Table 2.9 shows the computed resonance frequencies of the eigen modes for the stacked cross-shaped DRA.

2.3.3 Simulated results

Fig 2.25 shows the simulated reflection S_{11} and coupling S_{21} coefficients. The antenna has an impedance bandwidth of 21.2% from 2.26 to 2.78 GHz, for a reflection coefficient of $\mid S_{11} \mid \leq -10$ dB. Furthermore, a low coupling, lower than -15 dB, between the two coaxial probes

Modes	TE^{x}_{111} TE^{y}_{111}	TE^{z}_{111}	Quasi-TM^{x}_{111} Quasi-TM^{y}_{111}
Resonance frequency (GHz)	2.35	2.70	2.72

Table 2.9: Resonance frequencies of the eigen modes in the optimized stacked cross-shaped dielectric resonator with $a = 13$ mm, $b = d = 31$ mm, $e = h = 20$ mm, $g = 13.5$ mm, $\varepsilon_{r1} = 11.5$, and $\varepsilon_{r2} = 18$.

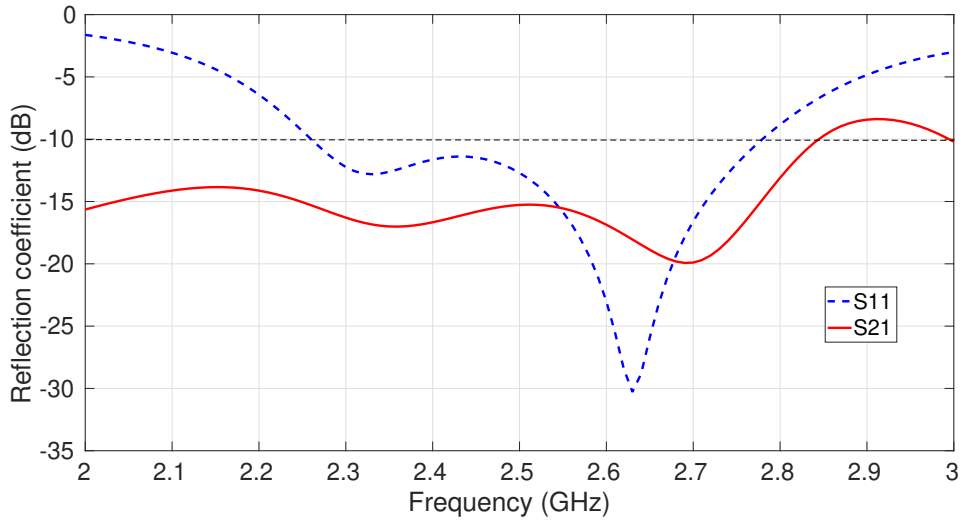

Figure 2.25: Simulated reflection S_{11} and coupling S_{21} coefficients of the stacked cross-shaped Huygens source DRA.

ensures a good orthogonality between the two combined quasi-Huygens sources.

The simulated front-to-back ratio and axial ratio (AR) of the antenna as a function of the frequency is shown in Fig. 2.26 and 2.27, respectively. The Huygens source antenna achieves a maximum F/B ratio of 26.3 dB at 2.45 GHz. The F/B ratio bandwidth (F/B ratio $\geq$ 15 dB) is 4.9%, from 2.39 GHz to 2.51 GHz. On the other hand, the axial ratio bandwidth ($AR \leq 3$ dB) is 22.9%, from 2.22 GHz to 2.78 GHz.

Fig. 2.28 depicts the simulated axial ratio as a function of θ at 2.45 GHz, considering $\phi = 0°$ and 90°. The simulated axial ratio of the Huygens source antenna is below 3 dB for $-15° \leq \theta \leq 49°$, considering $\phi = 0°$. In addition to that, the axial ratio covers $-62° \leq \theta \leq 11°$ and $51° \leq \theta \leq 80°$, considering $\phi = 90°$, respectively.

Fig. 2.29 illustrates the simulated radiation patterns of the proposed antenna. It corresponds to a Huygens source pattern. Furthermore, the DRA operates in left-hand circular polarization at 2.45 GHz, with a maximum simulated gain at boresight of 5.93 dBi. Right-hand circular polarization can be obtained by changing the sign of the phase shift between the two feeding probes.

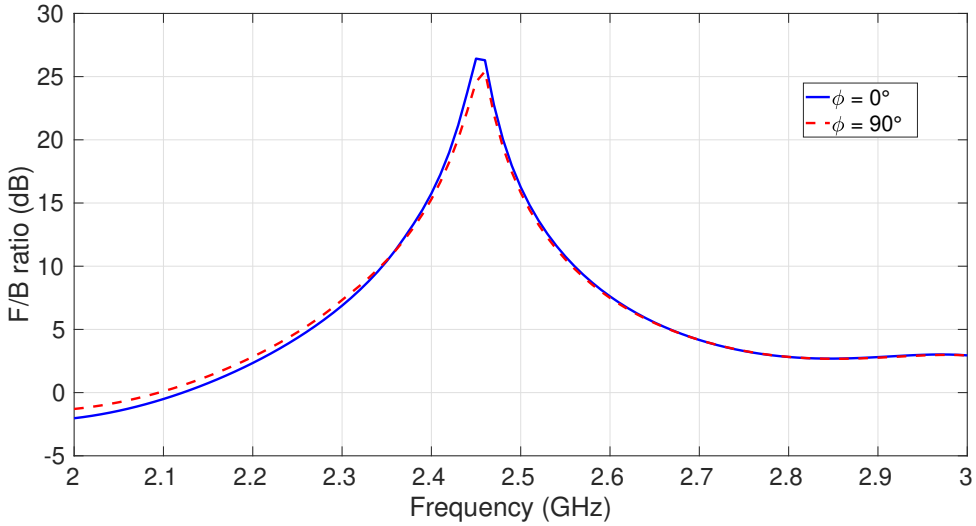

Figure 2.26: Simulated front-to-back ratio of the stacked cross-shaped Huygens source DRA.

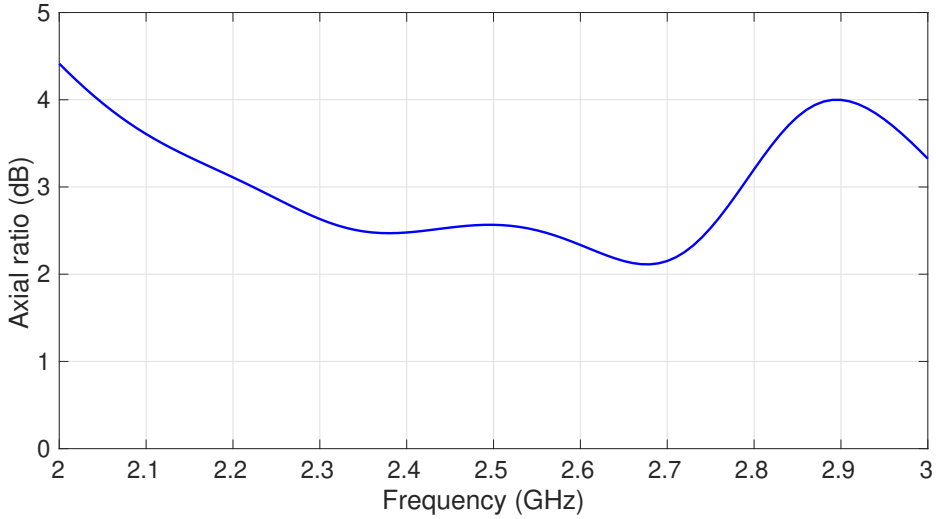

Figure 2.27: Simulated axial ratio vs. frequency of the stacked cross-shaped Huygens source DRA, considering $\theta = 0°$ and $\phi = 0°$.

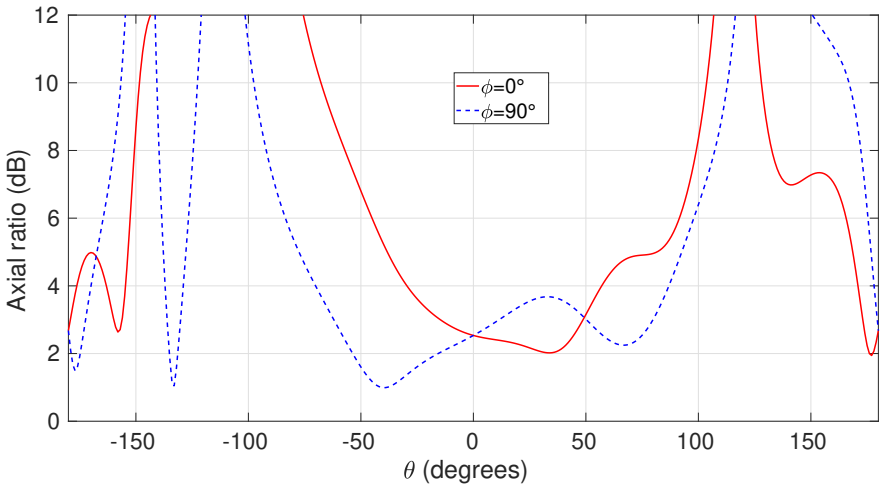

Figure 2.28: Simulated axial ratio vs. θ of the stacked cross-shaped Huygens source DRA, considering $f_0 = 2.45$ GHz.

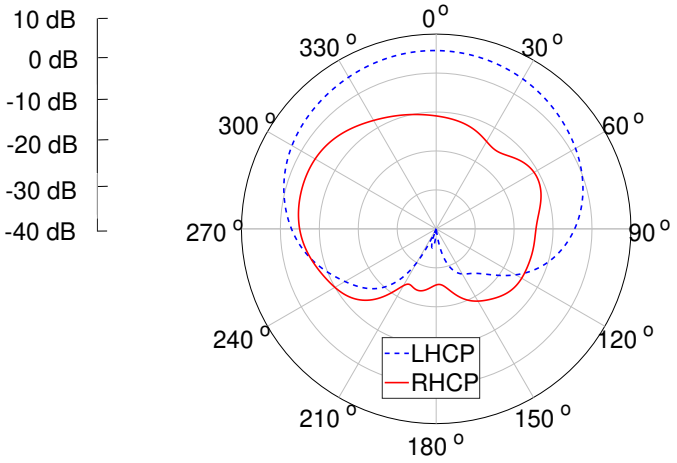

(a) RHCP and LHCP gain considering $\phi = 0°$.

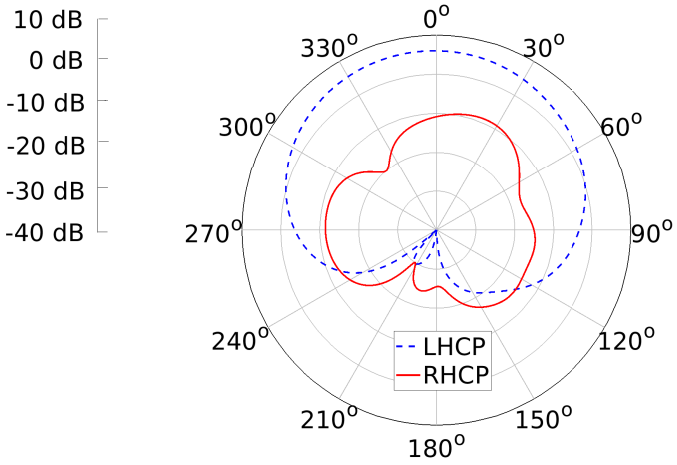

(b) RHCP and LHCP gain considering $\phi = 90°$.

Figure 2.29: Simulated gain of the stacked cross-shaped Huygens source DRA at 2.45 GHz.

2.4 Conclusion

A stacked DRA has been designed to achieve a cardioid radiation pattern with no backward radiation, *i.e.*, a quasi-Huygens source. The antenna principle of operation relies on the combination of two electric and magnetic dipoles generated by two stacked rectangular dielectric resonators with different physical and electric properties.

The combination of TE^{x}_{111} and quasi-TM^{y}_{111} modes contributes to achieve a cardioid radiation without ground plane. However, it has been shown in the spherical wave expansion analysis that the equivalent electric and magnetic dipoles are not perfectly collocated within the DRA, which leads to achieve a radiation pattern with asymmetric planes at $\phi = 0°$ and $90°$.

The proposed stacked Huygens source antenna has a F/B ratio of 31.8 dB and a maximum simulated gain of 5.86 dB at 2.43 GHZ. Furthermore, the impedance and F/B ratio bandwidth of the stacked DRA are 9.5% and 3.3%, respectively.

Besides, a stacked cross-shaped DRA fed by two coaxial probes has also been designed with a cardioid radiation pattern in circular polarization and an impedance bandwidth of 21.2%. It achieves a 3-dB axial and F/B ratio bandwidth of 22.9% and 4.9%, respectively. Its maximum simulated gain is 5.93 dBi at 2.45 GHz.

Finally, in this chapter, a stacked configuration made up of two dielectric resonators has been proposed to generate a quasi-Huygens source pattern. The lack of symmetry in the radiation pattern has represented the main difficulty since the equivalent electric and magnetic dipoles are not collocated in the stacked resonators. In order to overcome this problem, another degree of freedom can be needed to be able to use only one dielectric resonator in which both TE and quasi-TM modes can be tuned almost independently. It will be shown in Chapter 5 that it can be done using an anisotropic dielectric resonator. But prior to that, the next Chapter will discuss how to create such engineered anisotropic dielectric material exploiting the capabilities of additive manufacturing of ceramics.

Chapter 3

Engineering Anisotropy within Dielectric Materials using Additive Manufacturing

Sommaire

In the previous chapter, two Huygens sources made up of stacked dielectric resonators have been proposed in the ISM band. The electrical properties of the proposed dielectric resonators have been selected in order to achieve a half-space radiation pattern. However, the use of dielectric materials with isotropic dielectric constants does not allow for a more compact Huygens source antenna.

Recently, it has been shown that 3-D printing technologies are opening up new perspectives in antenna design [75–77]. Regarding DRA applications, in addition to allow for complex shapes, additive manufacturing provides also a new way to control the effective permittivity of the 3-D-printed materials such as its value, homogeneity, or isotropy.

This chapter covers the state-of-the-art of additive manufacturing techniques used to create complex materials with homogeneous/heterogeneous properties. Afterwards, it is shown

how 3-D printing can be exploited for microwave and antenna applications. Finally, an engineered anisotropic dielectric material made up of several sub-wavelength unit cells and suitable for DRA applications is proposed and studied.

3.1 Additive manufacturing technologies

Additive manufacturing (AM) has been defined by the American Society of Testing and Materials (ASTM) as a printing process for joining materials layer upon layer to make 3-D-printed objects [78]. Since the late 1980s, additive manufacturing has been investigated and used to create models and prototype parts. It provides a higher mechanical accuracy than conventional technologies and prevents excessive material wastage, which leads to enhance time/cost efficiency. These capabilities make it useful for designing structures with complex and/or heterogeneous properties [79].

Over the past 20 years, additive manufacturing has been applied to several applications. In the aerospace field, it has been used to create complex components for satellites, helicopters and engines [80]. In the medical sector, AM has been used to fabricate 3-D-printed medicine, tissues and organs, medical devices, and prosthetics [81]. And in the last decade, additive manufacturing has been particularly interesting for microwave and radio frequency (RF) applications to build filters [82, 83], lenses [84–86], or antennas [15–17, 87].

Different 3-D printing technologies have been developed in the past two decades. Stereolithography apparatus (SLA), fused deposition modeling (FDM), Polyjet, laminated object manufacturing (LOM), selective laser sintering (SLS), selective laser melting (SLM), laminated engineered net shaping (LENS), and electron beam melting (EBM) are the most common methods used in the industry. Each technology involves several distinct processes and materials for printing 3-D objects [78], [79]. Several materials such as polymers, thermoplastics, ceramics, metals, and composites can be used. Inspired by [88], Table 3.1 includes the most important categories and technologies currently used to manufacture 3-D-printed structures. These technologies are described in the following sections.

3.1.1 Stereolithography apparatus

The stereolithography apparatus (SLA) is a 3-D printing process used to fabricate complex pieces with high level of accuracy. SLA relies on the solidification of a liquid photosensitive resin by applying a laser beam [89]. Fig. 3.1 illustrates the photopolymerization process used to manufacture dielectric pieces using SLA [89]. The process begins when the building platform is lowered and an ultraviolet laser is applied to cure the resin in order to solidify the liquid polymer. Afterwards, a scan mirror is employed to focus the ultraviolet laser on the layer surface with a specific thickness [78, 88]. Finally, the solid dielectric sample must be cleaned using a chemical bath for removing wet resin, and it is exposed again to the ultraviolet light in order to polish the dielectric sample [89].

Categories	Technology	Materials
Vat Photopolymerization	Stereolithography, Digital Light Processing	Photopolymers, ceramic materials
Material extrusion	Fused Deposition Modeliong	Polymers
Binder Jetting	3-D printing, Ink-jetting S-print, M-print	Metals, polymers, ceramic materials
Direct Energy Deposition	Direct Metal Deposition, laser Deposition, Laser Consolidation, Electron Beam Direct Melting	Metals: Powder and wire
Material Jetting	Polyject, Ink-jetting, Thermojet	Photopolymer
Powder bed fusion	Selective Laser Sintering, Selective Laser Melting, Electron Beam Melting	Metals, polymers, ceramic materials

Table 3.1: Additive manufacturing technologies, inspired by [88].

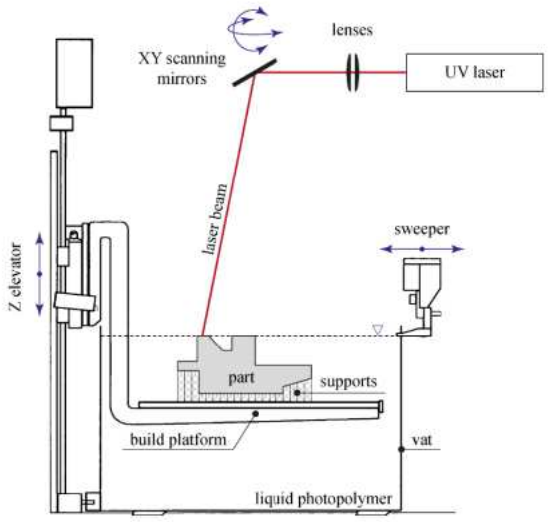

Figure 3.1: Stereolithography setup [88].

Stereolithography is currently the most used technique in 3-D printing. It usually employs photopolymers or ceramic materials to create 3-D-printed shapes. The main advantage of SLA is its capability to manufacture structures with smooth properties and high accuracy. Moreover, a good resolution of about 50 μm along x, y- and z axis, and low surface roughness below 10 μm can be achieved with this technology [90].

3.1.2 Fused deposition modeling

Fused deposition modeling (FDM) is a 3-D printing technology consisting in the extrusion and deposition of a polymeric material. Fig. 3.2 depicts the setup of the FDM process. Firstly, a thin filament of polymer is softened and melted at very high temperature by means of electrical resistances. After, the structure is pushed and forced using a nozzle in order to extrude the material and form the desired shape. The nozzle is used to press the extruded material on the building platform [88].

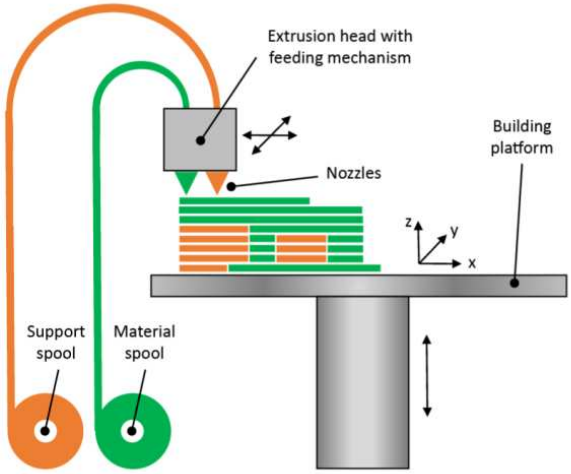

Figure 3.2: Fused deposition modeling setup [88].

The main advantage of this process is that no chemical process is needed. However, the resolution of the machine on the longitudinal axis *i.e.*, z axis in Fig. 3.2, is limited to 0.25 mm [89]. This is an important constraint while designing complex shapes since the manufacturing process can take long and its accuracy is compromised.

3.1.3 Selective laser melting

Fig. 3.3 shows the manufacturing setup of the selective laser melting (SLM) technique. The SLM consists in putting a dielectric or metallic powder into a substrate plate in a building chamber. Afterwards, a high power laser is employed to melt and fuse selected areas along the cross-section. During this process, the material is exposed under a controlled oxygen environment using an inert gas or nitrogen, due to the high temperatures to melt the dielectric or metallic powder [88]. SLM generally employs polymers, metallic, or ceramic materials to create 3-D-printed samples.

SLM technology provides a mechanical accuracy ranging from 0.03 mm to 0.1 mm [82]. It is useful to create complex 3-D-printed structures and it is mainly used in the aircraft and aerospace industry given the suitable mechanical properties provided by this technology.

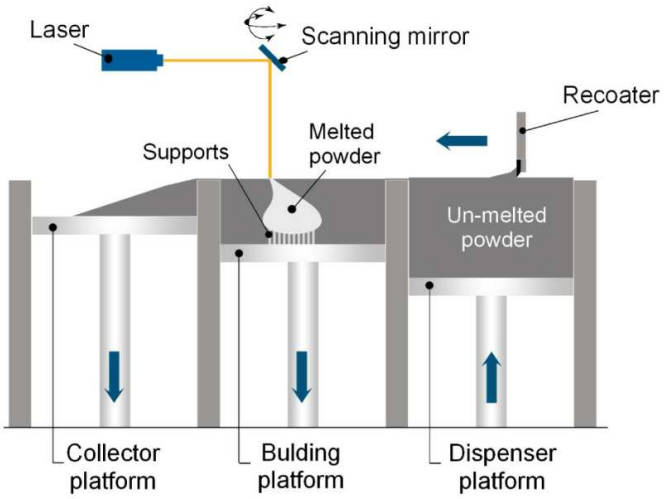

Figure 3.3: Selective laser melting setup [88].

3.1.4 Material Jetting

Material jetting uses a movable inkjet print head that ejects droplets selectively on the building area, as illustrated in Fig. 3.4. The process begins curing the selected material by applying an ultraviolet light to convert it into a layer of a solid material. The jetting printers has a resolution of about $10 - 30$ μm and it is usually employed to 3-D print materials with a viscosity that can form drops as photopolymers [88].

Material jetting is widely employed in aerospace applications to develop printed parts of aircraft due to the high accuracy of the process to manufacture 3-D-printed structures and the versatility to built parts of multiple colors. However, this technology fabricates weaker structures than SLA [89].

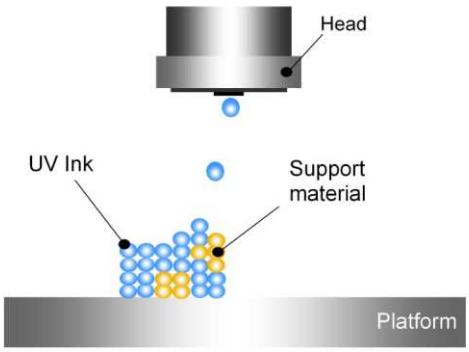

Figure 3.4: Material jetting setup [88].

3.2 Additive manufacturing for microwave applications

This section presents a state-of-the-art of additive manufacturing for microwave applications. It will be shown that 3-D printing allows great flexibility in the design of microwave materials, circuits, and antennas, by modifying their shapes or electromagnetic properties.

3.2.1 AM for microwave materials

Over the last two decades, additive manufacturing has been widely used to 3-D print microwave materials by controlling their electromagnetic properties, for instance, dispersion, anisotropy, or inhomogeneity.

3.2.1.1 General properties of 3-D-printed materials

One of the first applications of additive manufacturing for microwave applications has been dedicated to the control of the properties of artificial materials, namely their conductivity, permittivity, or permeability. For instance, AM has been used to control the effective permittivity of dielectric materials by incorporating nanoparticles and high-permittivity polymers. In [91], 3-D-printed materials using FDM and SLA technologies have been created by incorporating higher concentrations of different ceramic nanoparticles that have a high relative permittivity and low loss. These capabilities represents an alternative way for certain RF and microwave devices which generally use industry-standard FR-4.

3.2.1.2 Control of the permittivity

3-D printing can take advantage of their degrees of freedom to create multiple-material objects in order to affect the properties of a host material. Fig. 3.5 illustrates different air-filling percentages in a dielectric substrate [92]. It has also been shown in [92–94], that the effective permittivitty of a dielectric material can be controlled by modifying its air volume fraction.

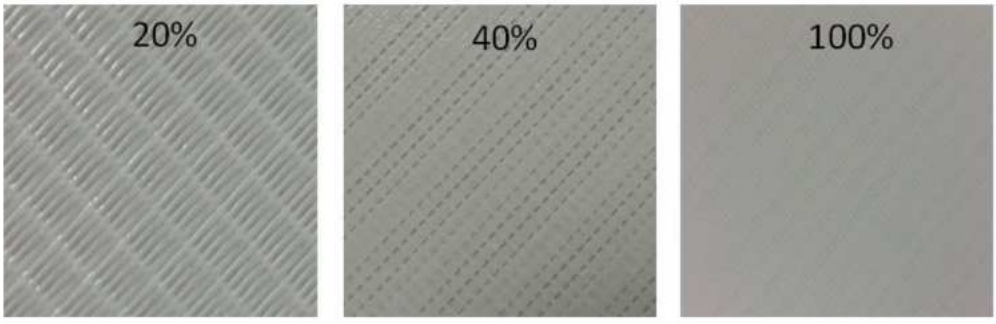

Figure 3.5: Examples of a dielectric material with different different infill percentages [92].

Similarly, 3-D printing has been exploited to create thermoplastic materials with high dielectric properties. More specifically, it has been shown in [95], that the adjustment of the infill factor of a composite material made up of polymers and nanoparticles can be used to control its effective dielectric constant of 3-D-printed structures, as shown in Fig. 3.6. It is shown that the reduction in the material infill (increase of the percentage of air gaps) leads to decrease the relative permittivity and modify the material losses.

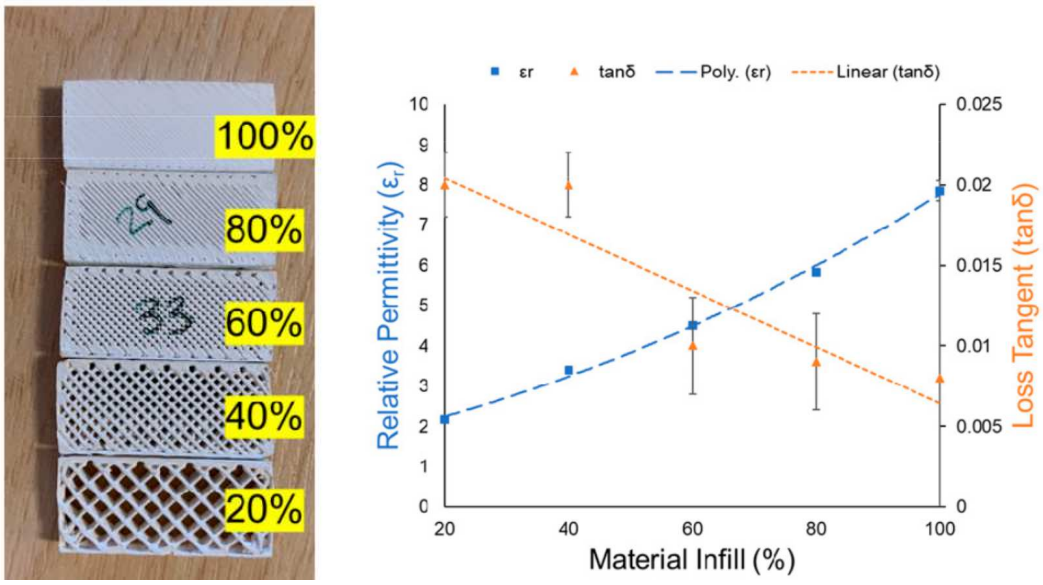

(a) Examples of test samples with variable infill.

(b) Material infill.

Figure 3.6: 3-D-printed materials with variable infill factor. [95].

3.2.1.3 Control of the dispersion

The capabilities of 3-D-printed has also been exploited to fabricate new artificial and low-loss composite and inhomogeneous structures for electromagnetic bandgap (EBG) applications. For instance, in [96], these artificial structures are formed by macroscopic inclusions in order to control the dispersion of a periodic lattice substrate. Furthermore, in [97], the authors have designed 3-D submillimeter-wave EBG crystals from an artificial periodic structure of unit cells, as depicted in Fig. 3.7. It has been demonstrated that the fact of increasing the amount of dielectric in the unit cell leads to reduce the bandgap edges and centre frequencies.

3.2.1.4 Control of the anisotropy

Over the last couple of years, the capabilities of additive manufacturing have been exploited to 3-D-print anisotropic materials using FDM Technology. In [94], it has been proposed to

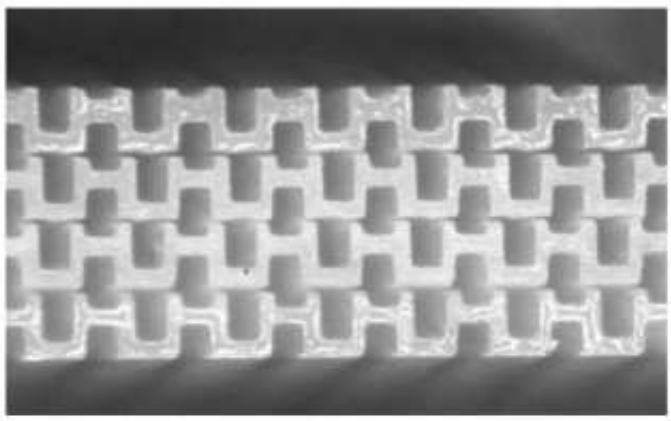

Figure 3.7: 3-D-printed periodic lattice for EGB applications. [97].

control the effective permittivity of dielectrics by structuring the 3-D-printed material, as depicted in Fig. 3.8a. In that case, sub-wavelength unit cells consisting of both air and dielectric metamaterial are periodically printed so as to obtain a material which effective dielectric permittivity is controlled by the volume fill rate of its unit cells. The proposed unit cells included arrays of holes, dielectric rods, and different shaped holes and rods. Furthermore, in order to ensure a homogeneous macroscopic behavior of the final material, the unit cell must remain small with respect to the wavelength.

In [98], the use of AM has also been exploited to produce an artificial anisotropic dielectric material. Several layers made up of a single polymer and a mix of polymer plus inorganic particles have been used in order to alternate low and high dielectric constant materials, respectively. As a result, the resonance frequency of the dielectric samples are controlled using the numerous degrees of design freedom offered by 3-D printing. Another example relies on the design of an artificial anisotropic material formed by dielectric layers and metallic inclusions (see Fig. 3.8b), also called meta-atoms [99]. The size of these metallic inclusions are smaller than the wavelength of operation. In addition to that, this structure is arranged in a cubic regular and irregular lattice so that the relative permeability and permittivity of the artificial dielectric can be controlled to achieve heterogeneous metamaterial properties.

3.2.1.5 Control of the inhomogeneity

Inhomogeneous or heterogeneous structures have been investigated in the literature by including several dielectric and metallic elements which are spatially distributed into a host material. For instance, [100] presents a heterogeneous substrate with local variations of the dielectric permittivity. The relative permittivity has been controlled by including cubes and spheres in the host material using additive manufacturing techniques, as shown in Fig. 3.9. SLA technology has been used to vary the air cavity size and spacing in order to adjust the local electric properties of the substrate. As observed, the size of the inclusions is not homogeneous. A range size from 100 μm to 200 μm, and 50 μm to 500 μm have been ap-

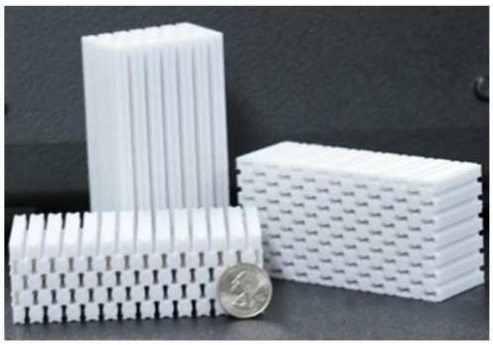

(a) Artificially anisotropic metamaterial [94].

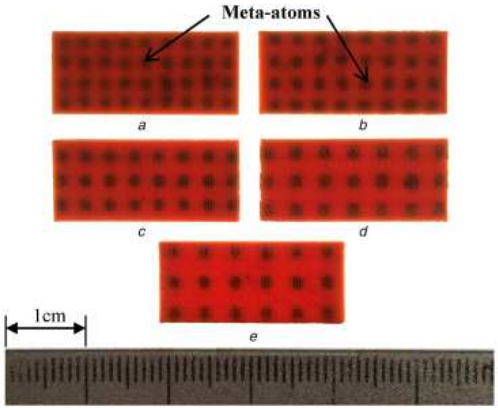

(b) Anisotropic dielectric with different periodicities of metallic inclusions [99].

Figure 3.8: 3-D printed artificial anisotropic dielectric materials.

plied to the cubes and spheres, respectively. Measurements have been performed using 23%, 30%, and 40% air volume fractions employing air cubes with length 2 mm, obtaining relative permittivity values of 2.65, 2.50 and 2.32, respectively.

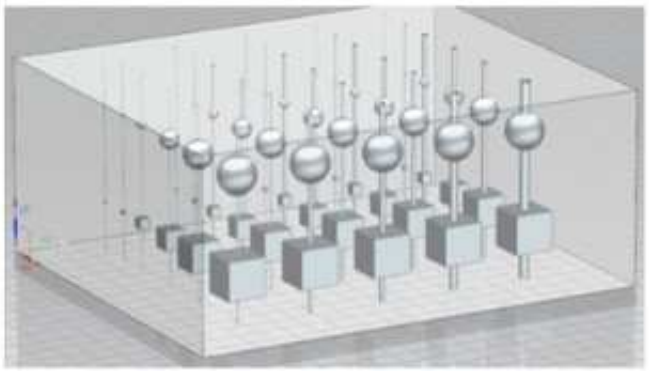

Figure 3.9: Heterogeneous substrate with spherical and cuboid inclusions [100].

Another practical implementation to create heterogeneous materials relies on spatially vary a lattice of several unit cells, without affecting the symmetry of unit cell [101]. The orientation of the unit cells, lattice spacing, air-filling ratio, symmetry of the inclusions and material properties are then studied using self-collimating photonic crystals, band gap materials, and anisotropic metamaterials.

3.2.2 AM for microwave circuits

One of the most attractive applications to demonstrate the capabilities of additive manufacturing relies on the design of microwave circuits. Waveguides, transmission lines, filters, and

RF passive and active devices are examples of microwave circuits that can take advantage of the possibilities of 3-D printing to improve their performances.

3.2.2.1 AM for waveguides and transmission lines

In microwave circuits, 3-D printing has been used to manufacture waveguides. For instance, in [90], the authors have proposed an air-filled metal-pipe rectangular waveguide (MPRWGs) using 3-D printing techniques, as illustrated in Figure 3.10. FDM and SLA technologies have been employed to 3-D print a waveguide at high frequencies. As a result, the 3-D-printed waveguide using FDM technology achieves better performances in terms of dissipative attenuation when compared with a commercial waveguide. Besides, it has been proved that FDM presents low-cost but a low-resolution for microwave applications, whereas SLM provides a high-cost and a high-resolution for millimeter-wave applications.

Figure 3.10: Metal-pipe rectangular waveguide [90].

In addition to that, additive manufacturing based on polymer jetting technology has been used to create microwave passive components such as waveguides, couplers, and filters in the Ka-band [102]. These microwave elements have been fabricated using complex geometries, as depicted in Fig. 3.11a, and applying a metallization technique based on the application of a low-cost silver paint on all inner faces of a waveguide in order to evaluate the robustness of the 3-D printing approach as a proof-of-concept. On the other hand, in [103], the authors have proposed complex millimeter-wave waveguides (see Fig. 3.11b) by combining a digital light processing and 3-D printing technologies. As a part of the manufacturing process, a metallized curved corner design has been proposed instead of a straight one in order to obtain low insertion losses in the W-band.

Other studies analyze the applicability of additive manufacturing for waveguide components using SLA and SLM technology. It has been shown in [104], that 3-D-printed elliptical and circular waveguide sections offer promising results to reduce losses with respect to conventional rectangular waveguides in the Ku-band. Similarly, a dual-polarization waveguide operating Ka-band has been design in [105] using metallic parts with a better surface roughness when compared with conventional machining process.

(a) Bended waveguide [102].

(b) Metallized millimeter-wave waveguide [103].

Figure 3.11: 3-D printed waveguides with metallized inner walls.

3.2.2.2 AM for filters

In the literature, AM has also been widely used to create 3-D filters using SLA and SLM technologies. For instance, in [106], SLA technology has been exploited to create narrow filtering devices with high unloaded quality factor. As a novelty, a periodic structure formed by high-permittivity ceramics has been used to create a high quality factor resonant structure needed for narrow filters with enhanced insertion and return losses. Moreover, high unloaded quality factors can be achieved by combining dielectric resonators and/or a ceramic metallized cavity [107]. In addition to that, the geometrical and manufacturing requirements to create multipole filter have been successfully satisfied using SLA technology. Lately, additive manufacturing has been envisaged in [108], as a solution to overcome mechanical and assembly problems in TM dielectric resonator filters such as poor contact between ceramic and metallic interfaces, and misalignment of dielectric parts. 3-D printing has thus been exploited to create a monoblock ceramic dielectric resonator and a metallic enclosure in order to reduce the overall volume of the filter [108].

It has also been demonstrated in [83], that an improvement of the surface roughness in complex-shaped filters can be overcome using SLM technology, as depicted in Fig. 3.12a. For this purpose, circular/elliptic cross-section irises has been used in order enhance the overall filter quality factor for a given far-out-of-band response and reduce the surface currents on the filter. As a result, the insertion losses in the Ku-band can be reduced. On the other hand, it has also been shown in [109], that additive manufacturing provides a new degree of freedom in the filter design using 3-D resonators made up of complex shapes (see 3.12b). More specifically, the increase of the height of the rings which form each resonator conducts to enhance the coupling for designing bandpass filters with a wider fractional bandwidth.

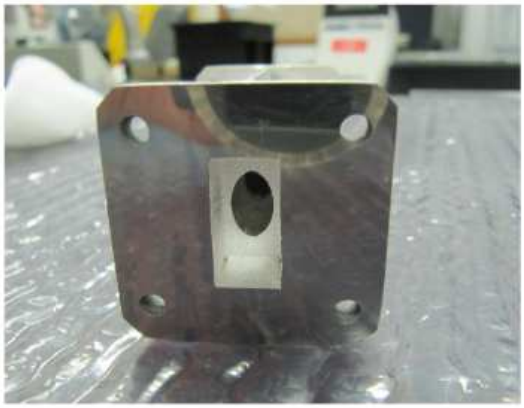

(a) Third-order filter [83].

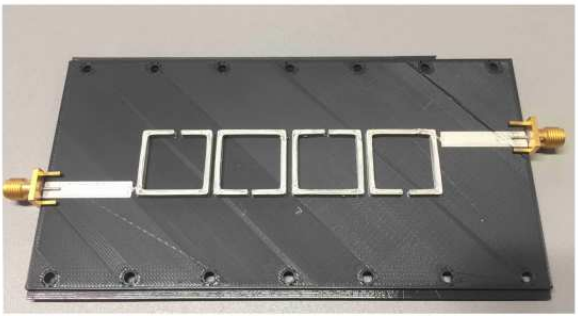

(b) Square split ring resonator bandpass filter [109].

Figure 3.12: 3-D printed filters.

3.2.2.3 AM for RF passive and active devices

RF circuits and systems at microwave and millimeter (mm)-wave frequencies has also been designed and manufactured using 3-D printing. For instance, in [110], AM has been exploited to fabricate RF passive elements, such as capacitors and inductors (see Fig. 3.13a), reducing cost and time in comparison with traditional technologies. As a novelty, the authors have used two technologies based on metal adhesive laminate and multilayer inkjet using a RF metal-insulator metal (MIM), and a flexible substrate made up of a cellulose-based paper in order to fabricate several passive elements for a variety of IoT applications. In [111], active and passive devices have been designed and fabricated using a multilayer 3-D printing process, as shown in Fig. 3.13b. The RF system is composed of a T-line resonator, a metamaterial phase shifter, and a patch antenna. The use of additive manufacturing has been very useful to simplify the difficult embedding process of the RF system by merging and encapsulating the electronic elements into a substrate, reducing the size of the circuit, prototyping time and cost.

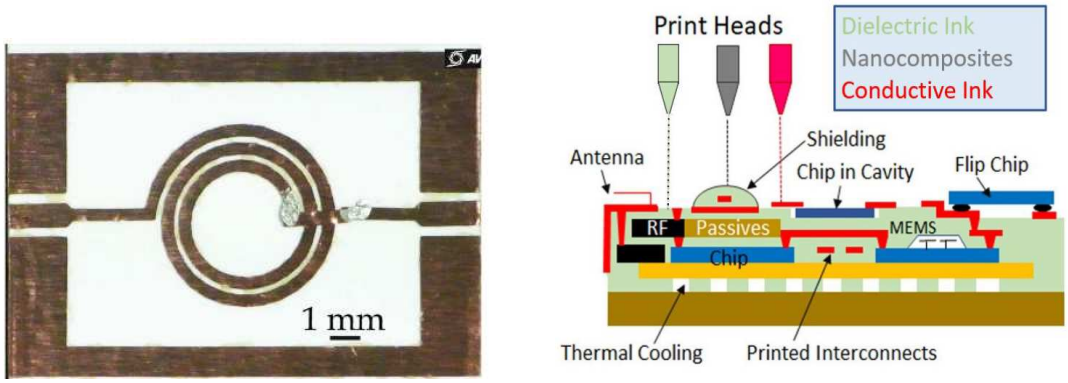

(a) 3-D-printed inductor made up of metal-insulator metal materials [110].

(b) 3-D-printed RF circuit made up of active and passive elements [111].

Figure 3.13: 3-D-printed RF circuits.

3.2.3 AM for antennas

Recent advances in Additive Manufacturing (AM) pave the way for new antennas. AM progress allows new capabilities in complex-shaped antennas and heterogeneous material manufacturing by controlling the effective permittivity of the dielectric medium. Such properties are particularly interesting for designing new wire, aperture, patch, lens, reflectarray, and dielectric resonator antennas.

3.2.3.1 Wire antennas

Over the last decade, 3-D printing has been widely studied to take advantage of its numerous degrees of freedom for the shape and material properties for wire antennas. For instance, in [112], a quarter-wavelegth monopole above a finite ground plane has been proposed. The antenna is placed surrounded by a 10×10 array of unit dielectric cells. The effective permittivity of the dielectric material is adjusted by combining a 3-D-printed polymer material and air gaps inside a unit cell. Besides, the authors have designed three different antennas with different patterns (see Fig. 3.14), using a genetic algorithm to obtain maximum radiation at $\theta = 60°$. Results have proved that there is an increment of the antenna gain with a continuous variation of the relative permittivity. Another interesting example has been proposed in [113]. A biconical antenna has been designed by introducing a complex-shaped inhomogeneous dielectric lens in the aperture (see Fig. 3.15) in order to reduce the level of lateral radiation and enhance the antenna gain and bandwidth.

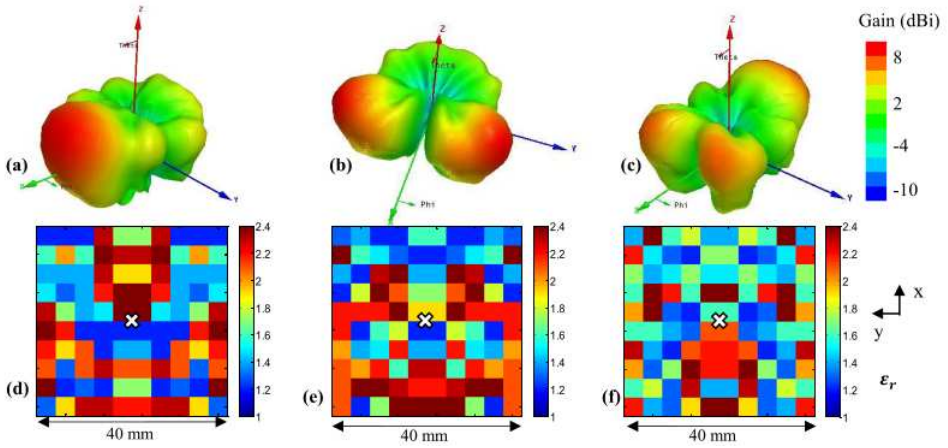

Figure 3.14: 3-D radiation patterns at 15 GHz of the (a) one-beam antenna, (b) two-beam antenna, and (c) three-beam antenna. The dielectric constant distributions around the monopole of the (d) one-beamantenna, (e) two-beam antenna, and (f) three-beam antenna [112].

Figure 3.15: Biconical antenna with dielectric lens.

3.2.3.2 Aperture antennas

Other examples evidence the great potential and versatility of additive manufacturing for building aperture antennas. In [114], a dual-polarized leaky-wave directive antenna formed by a dual-mode perforated waveguide and an orthomode transducer has been proposed for higher-gain array applications, as depicted in Fig. 3.16a. The use of SLA allows the integration of the transducer with the antenna structure. As a result, good performances in terms of antenna matching and high isolation between polarization and ports have been achieved. In addition to that, several waveguides and horn antennas have been designed in the Ku-band in order to improve the electromagnetic performances of the printed elements and achieve stabilised-pattern and dual-polarized properties, respectively [115, 116]. Similarly, a 3-D printed single-

fed circularly polarized horn antenna operating has been designed in [117]. The complex shape of this structure made up of a pair of twisted ridges (see Fig. 3.16b) has been selected in order to convert the linearly polarized fields intro circularly polarized fields, and achieve a wide impedance bandwidth.

(a) Dual-polarized leaky-wave antenna [114].

(b) Wideband twisted-ridge antenna [117].

Figure 3.16: 3-D-printed aperture antennas.

3.2.3.3 Patch antennas

Additive manufacturing has also been recently employed to build patch antennas. In [94], the authors have presented a bulk substrate formed by several metallic layers placed in a stacked configuration. Here, three top dielectric solid layers under the top metal foil (see Fig. 3.17) have been implemented with individual thickness of 100 μm and 2 bottom dielectric layers over the bottom metal foil with thickness of 200 μm and 100 μm. These layers have been used to reduce the porosity and roughness of the structure. Additionally, 6 inner layers made up

of a flexible NinjaFlex substrate of 100 μm have been implemented and its infill percentage has been adjusted to modify the effective dielectric constant of the host material.

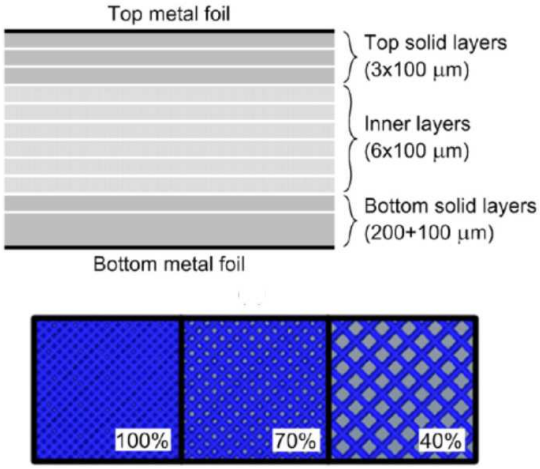

(a) Stacked dielectric material made up of several printed layers with different infill percentages.

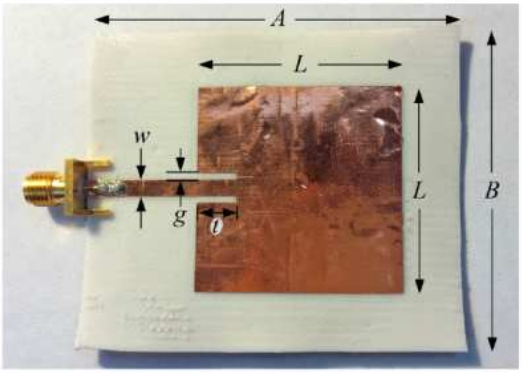

(b) Square patch antenna on NinjaFlex substrate with 100% infill.

Figure 3.17: 3-D-printed patch antenna made up of a NinjaFlex substrate [94].

Another example relies on the use of a inhomogeneous substrate and superstate to design a stacked patch antenna, as shown in Fig. 3.18. In [118], the new degree of freedom provided by AM in the patch design has been used to achieve dual-band and dual-circularly polarized properties. In addition to that, the impact of the inhomogeneous structure has been used to achieve a good isolation between the left-hand and right-hand circular polarization.

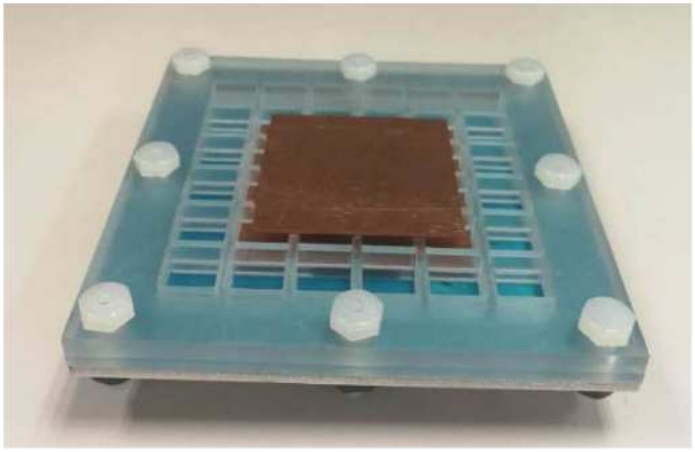

Figure 3.18: 3-D printed antenna made up of an inhomogeneous substrate and superstrate [118].

3.2.3.4 Lens antennas

Developments in lens antennas using additive technologies have been investigated in the last two decades. For instance, SLA technology has been exploited to 3-D print a monolithic sub-wavelength periodic lattice made up of a ceramic material [119], as shown in Fig. 3.19a. As a novelty, the integration of this structure with good isolation and proper field localization properties of the dielectric photonic crystals leads to a periodic lattice with low-loss characteristics. Afterwards, a 3-D-printed elliptical monolithic lens antenna has been designed using SLA [120], as depicted in Fig. 3.19b. Linear corrugations have been integrated on the lens surface in order to reduce the losses produced by the internal reflections at the dielectric/free space interface, and improve the antenna performances.

Other works based on 3-D printed lens antennas have been presented in the literature with circular polarized and gain enhanced properties. For instance, in [121], it has been demonstrated that the Fresnel lens can operate in circular polarization by integrating a dielectric anisotropic metamaterial and using a linearly polarized open-ended waveguide feeding. Moreover, a planar Fresnel lens made up of 16 annular rings has been designed and manufactured using FDM in [122], as depicted in Fig. 3.20. The capabilities of AM has been exploited to reduce the undesired cross-polarization and enhance the co-polarization gain by using an asymmetric design in the direction of the cross-polarization, and properly adjusting the orientation of the Fresnel lens to the receiving antenna. In addition to that, mechanical details in the manufacturing process such as step heights, surface roughness, and radii of each cylindrical ring have been analyzed, showing good improvements in the antenna performances in comparison with conventional designs using Fresnel lenses. Recently, Gradient index (GRIN) and hyperbolic flat lenses have also been studied in the literature to achieve wideband properties [123, 124].

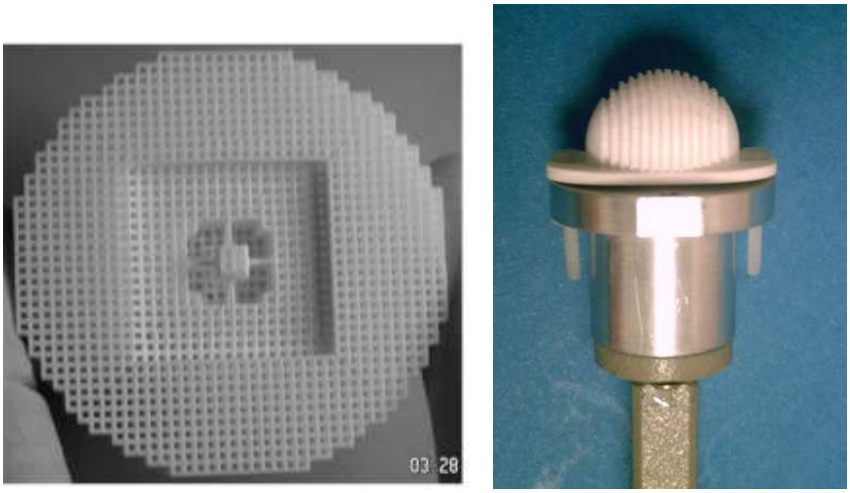

(a) Monolithic lens design [119]. (b) Synthesized elliptical integrated lens antenna [120].

Figure 3.19: 3-D-printed lens antennas.

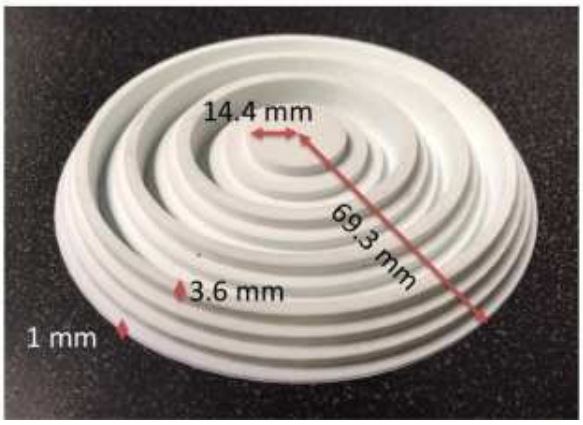

Figure 3.20: 3-D printed Fresnel lens [122].

3.2.3.5 Reflectarrays antennas

Numerous challenges have been addressed for the design of reflectarray antennas using 3-D printing. Polymer-jetting technology has been used, for instance in [125], to manufacture a dielectric reflectarray antenna formed by low dielectric-constant slabs. It has also been shown that AM represents an interesting solution to reduce conductor losses at THz frequencies, and achieve low-cost and high-gain properties. Reflectarray antennas manufactured using the FDM technology have also been proposed in the literature. For instance, a reflectarray composed of 625 3-D-printed dielectric resonator elements has been presented in [126], as shown in Fig. 3.21a. The reflectarray has been manufactured using FMD for millimetre wave (mm-wave) applications. A high-gain reflectarray of 28 dBi at 30 GHz with pencil beam

properties have been achieved. In addition to that, it has been demonstrated that the use of the 3-D printing approach can be deployed for high-gain mm-wave antenna fabrication with significantly reduced labour time and material costs. Similarly, a wideband circularly polarized dielectric reflectarray composed of a cross-shaped dielectric elements operating in the Ka-band has been proposed in [127], as depicted in Fig. 3.21b. The antenna has been fabricated using 3-D-printing technologies, achieving a maximum gain of 24.2 dBi.

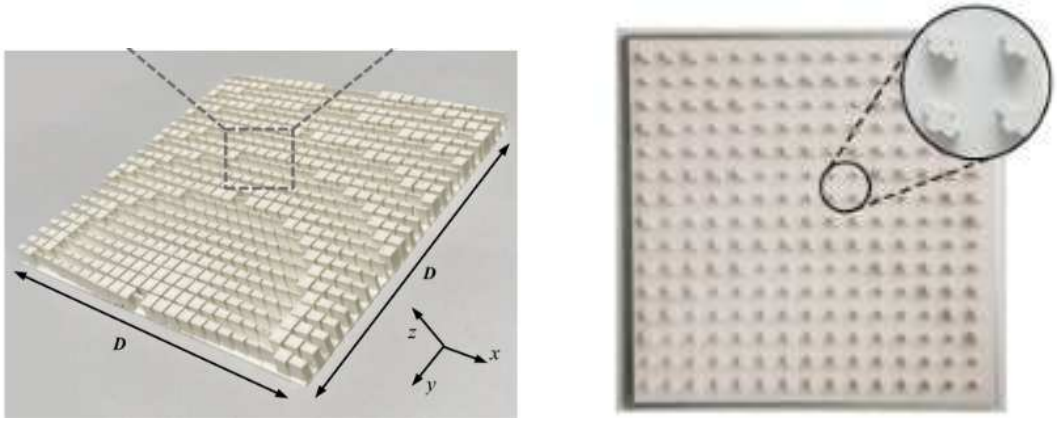

(a) Millimetre wave dielectric resonator reflectarray [126].

(b) Wideband circularly polarized dielectric reflectarray [127].

Figure 3.21: 3-D-printed dielectric reflectarrays.

3.2.3.6 Dielectric resonator antennas

As mentioned in section 3.2.1, 3-D printing has been investigated to control the effective permittivity of dielectric materials by structuring a dielectric host in several unit cells at sub-wavelegth scale. The engineered sub-wavelength unit cells are made up of both air and dielectric, these latter periodically printed, so as to obtain a material which effective relative permittivity is controlled by their volume fill rate. Such control is interesting in designing dielectric resonator antennas. For instance, a wideband DRA made up of four concentric dielectric rings (see Fig. 3.22) with decreasing effective dielectric constants in the radial direction has been studied and printed using the FDM technique [128]. It is fed by a coaxial probe to excite several fundamental and higher-order TE modes, which leads to achieve a wide impedance bandwidth with omnidirectional radiation patterns.

Recently, several 3-D-printed DRAs have been manufactured using SLA [76, 77]. The antennas are formed by a homogeneous ceramic material, which effective permittivity is controlled by the 3-D-printed lattice. For this purpose, the proposed DRAs have been designed and manufactured using a high performance zirconia dielectric material, as depicted in Fig. 3.23. The same technique has been successfully applied to design a circularly-polarized elliptical DRA using SLA of ceramics [77].

Figure 3.22: 3-D-printed wideband multi-ring DRA [128].

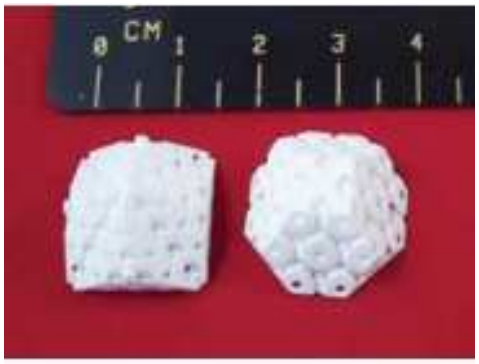

(a) DRA with permittivity controlled by a 3-D-printed lattice [76].

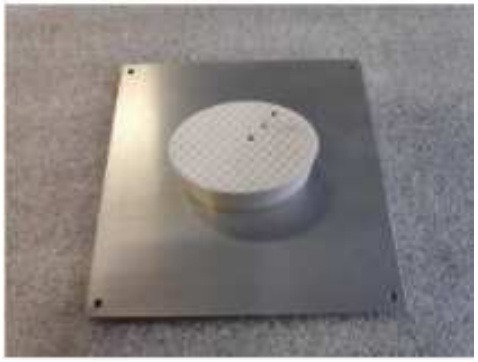

(b) Elliptical DRA in circular polarization [77].

Figure 3.23: 3-D-Printed DRAs using SLA technology.

Another examples relies on the design of DRAs based on complex shapes. For instance, in [129], antennas with complex shapes have been designed using super-shaped dielectric resonators and manufactured using photopolymer SLA, as depicted in Fig. 3.24. As a contribution, the potential of the SLA technique has been demonstrated to manufacture DRAs for 5G applications. The proposed antenna is based on a cross-star shape geometry with different twist angles that make the structure complex and difficult to fabricate using conventional manufacturing techniques. Hence, the proposed super-shaped DRAs achieves good performances in terms of bandwidth exploiting the capabilities of additive manufacturing, considering a volume reduction of the proposed antenna of about 85% compared to classic DRAs.

In [130], it has been demonstrated that 3-D-printed ceramics offers several degrees of freedom to design dielectric resonator antennas for space applications. More specifically, AM has been used to obtain circularly polarized and dual-band properties, required for CubeSat applications. Similarly, in [131], a 3-D-printed hemispherical DRA has been proposed using a metallic cap, as shown in Fig. 3.25. The use of a dielectric material with different infill

Figure 3.24: Super-shaped DRAs for 5G applications using Stereolithography [129].

percentages and the variation of the metallic structure leads to reduce the effective dielectric constant of the DRA, and therefore, its resonant frequencies.

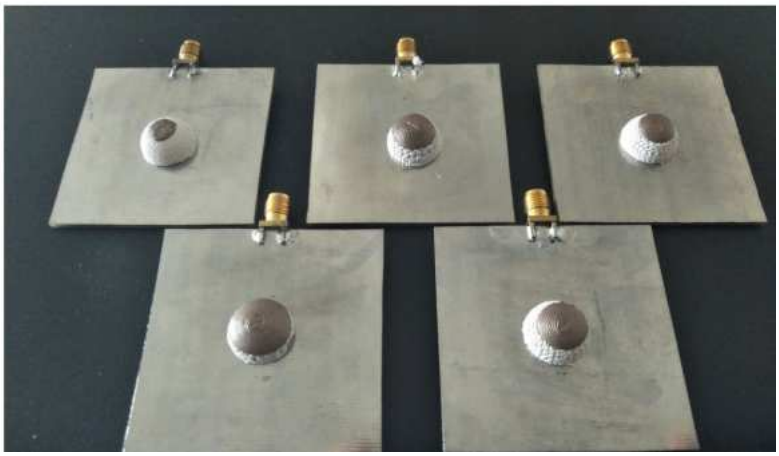

Figure 3.25: Hemispherical DRA with different metallic cap dimensions [131].

The capabilities offered by 3-D printing can also be exploited to design heterogeneous/anisotropic dielectric materials by structuring several sub-wavelength unit cells [75, 132]. Then, in the next section, the use of anisotropy in dielectric resonators is discussed, and a methodology to design a sub-wavelength unit cell for uniaxial anisotropy compatible with the process of additive manufacturing is presented.

3.3 Additive manufacturing of uniaxial anisotropic ceramics

3.3.1 Anisotropic materials

By definition, an anisotropic material has different relative permittivities depending on the direction of the polarization or magnetization, respectively [133]. Thus, the relative permittivity ε_r and/or permeability μ_r can be expressed as tensor quantities. For instance, for a dielectric anisotropic material, the relative permeability is expressed as a scalar and the relative permittivity as a tensor given by

$$\varepsilon_r = \begin{bmatrix} \varepsilon_{xx} & \varepsilon_{xy} & \varepsilon_{xz} \\ \varepsilon_{yx} & \varepsilon_{yy} & \varepsilon_{yz} \\ \varepsilon_{zx} & \varepsilon_{zy} & \varepsilon_{zz} \end{bmatrix}. \tag{3.1}$$

On the contrary, for a magnetic anisotropic material, the relative permittivity is an scalar and the relative permeability can be written as a tensor given by

$$\mu_r = \begin{bmatrix} \mu_{xx} & \mu_{xy} & \mu_{xz} \\ \mu_{yx} & \mu_{yy} & \mu_{yz} \\ \mu_{zx} & \mu_{zy} & \mu_{zz} \end{bmatrix}. \tag{3.2}$$

3.3.1.1 Symmetrical properties of anisotropic media

Anisotropic materials can be classified as reciprocal or nonreciprocal media. In order to obtain their permittivity and permeability tensors, the complex Poynting vector is then analyzed in a source-free and nonconducting medium [134]. The divergence of the average Poynting vector is expressed as

$$\bigtriangledown \cdot \mathbf{S} = \bigtriangledown \cdot \left[\frac{1}{2}\Re\left(\mathbf{E} \times \mathbf{H}^*\right)\right] = \frac{1}{2}\Re\left[j\omega\left(\mathbf{E} \cdot \mathbf{D}^* - \mathbf{B} \cdot \mathbf{H}^*\right)\right] \tag{3.3}$$

where $\mathbf{D} = \varepsilon \cdot \mathbf{E}$, $\mathbf{B} = \mu \cdot \mathbf{H}$, $\varepsilon = \varepsilon_0\varepsilon_r$, $\mu = \mu_0\mu_r$, and for an arbitrary complex quantity $\Re(z) = \frac{1}{2}(z + z^*)$. Then, (3.3) becomes

$$\bigtriangledown \cdot \mathbf{S} = \frac{j\omega}{4}\left[\mathbf{E} \cdot \varepsilon^* \cdot \mathbf{E}^* - \mu \cdot \mathbf{H} \cdot \mathbf{H}^* - \mathbf{E}^* \cdot \varepsilon \cdot \mathbf{E} + \mu^* \cdot \mathbf{H}^* \cdot \mathbf{H}\right]. \tag{3.4}$$

Applying the conjugate transposed tensor, (3.4) can be written as

$$\bigtriangledown \cdot \mathbf{S} = \frac{j\omega}{4}\left[\mathbf{E}^* \cdot (\varepsilon^\dagger - \varepsilon) \cdot \mathbf{E} + \mathbf{H}^* \cdot (\mu^\dagger - \mu) \cdot \mathbf{H}\right] \tag{3.5}$$

where ε^* and μ^* are the conjugate tensor of ε and μ, respectively, and the conjugate transposed tensor $\varepsilon^\dagger = \varepsilon^{*\mathbf{T}}$ and $\mu^\dagger = \mu^{*\mathbf{T}}$.

In a source-free and nonconducting media, $\bigtriangledown \cdot \mathbf{S} = 0$, so that $\varepsilon^\dagger = \varepsilon$, $\mu^\dagger = \mu$; or $\varepsilon^T = \varepsilon^*$, $\mu^T = \mu^*$.

If ε_{ij} and μ_{ij} values are real in (3.1) and (3.2), the tensors ε and μ are symmetrical tensors, namely $\varepsilon^{\mathbf{T}} = \varepsilon$ and $\mu^{\mathbf{T}} = \mu$, so that the anisotropic medium is known as a reciprocal one. It is therefore possible to write (3.1) and (3.2) as a diagonal tensor in terms of its principal x, y and z axes, as follows

$$\varepsilon_r = \begin{bmatrix} \varepsilon_{rx} & 0 & 0 \\ 0 & \varepsilon_{ry} & 0 \\ 0 & 0 & \varepsilon_{rz} \end{bmatrix} \tag{3.6}$$

$$\mu_r = \begin{bmatrix} \mu_{rx} & 0 & 0 \\ 0 & \mu_{ry} & 0 \\ 0 & 0 & \mu_{rz} \end{bmatrix} \tag{3.7}$$

where ε_{rx}, ε_{ry}, and ε_{rz} are the permittivity values at their principal x, y and z axes.

On the contrary, nonreciprocal media can be obtained when $\varepsilon_{ij} = -\varepsilon_{ji}$ and $\mu_{ij} = -\mu_{ji}$. The corresponding ε_r and μ_r can be represented as hermitian matrices, so that they can also be called gyrotropic media with tensor

$$\varepsilon_r = \begin{bmatrix} \varepsilon_{rx} & j\varepsilon_{ry} & 0 \\ -j\varepsilon_{ry} & \varepsilon_{rx} & 0 \\ 0 & 0 & \varepsilon_{rz} \end{bmatrix} \tag{3.8}$$

$$\mu_r = \begin{bmatrix} \mu_{rx} & j\mu_{ry} & 0 \\ -j\mu_{ry} & \mu_{rx} & 0 \\ 0 & 0 & \mu_{rz} \end{bmatrix} \tag{3.9}$$

where the z axis is known as gyrotropic axis.

3.3.1.2 Uniaxial and biaxial anisotropic tensors

Uniaxial and biaxial anisotropic tensors are special cases of reciprocal materials. In fact, when the diagonal elements have two or three identical values, the anisotropic tensor refers to a uniaxial or biaxial anisotropic material, respectively. For the uniaxial material, the two equal values are also called ordinary elements, and the different value refers to extraordinary element.

In order to obtain engineered or artificial uniaxial or biaxial anisotropic dielectrics at microwave frequencies, a periodic structure made up of unit cells that do not exhibit rotational symmetry can be used [135]. When the unit cell is kept sufficiently small compared to the wavelength, the resulting material can behave, for instance, as a uniaxial anisotropic dielectric which effective relative permittivity is given by

$$\varepsilon_r = \begin{bmatrix} \varepsilon_{rx} & 0 & 0 \\ 0 & \varepsilon_{rt} & 0 \\ 0 & 0 & \varepsilon_{rt} \end{bmatrix} \tag{3.10}$$

with the optical axis placed along the x-direction.

Nowadays, such periodic structures can easily be manufactured by 3-D-printing unit cells made up of a mix of air and dielectric using unit cells, as presented in Fig. 3.26. However, the strength of the anisotropy, or birefringence, defined as $\Delta\varepsilon = |\varepsilon_{rx} - \varepsilon_{rt}|$ remains limited when using low dielectric constant materials.

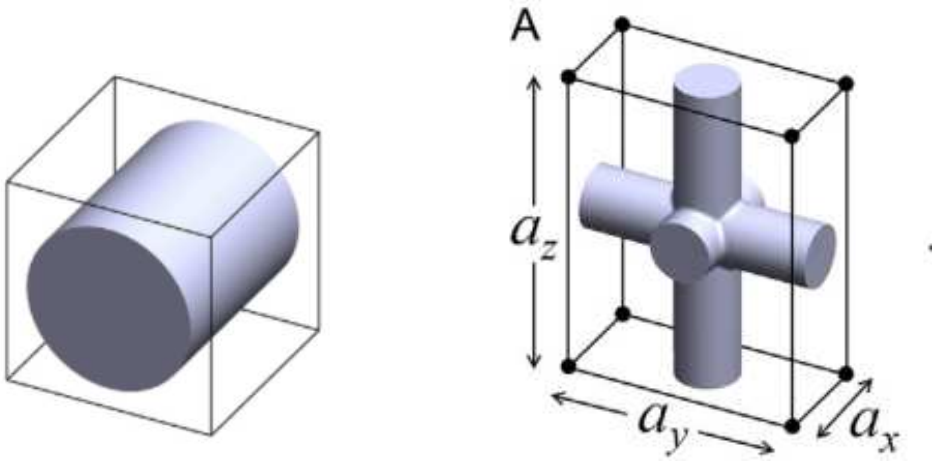

(a) Cylindrical unit cell. (b) Tetragonal unit cell.

Figure 3.26: 3-D-printed anisotropic unit cells [135].

In the next section, an anisotropic sub-wavelength unit cell is proposed and studied. This unit cell will then be used to manufacture anisotropic samples which performances will be measured.

3.3.2 Unit cell design

The 3-D-printer C900 FLEX from 3DCERAM has been used to 3-D print the proposed uniaxial anisotropic dielectric materials. It relies on SLA with a photosensitive paste compound

containing zirconia powder [136]. In addition to the interesting mechanical properties of ceramics, the high dielectric constant $\varepsilon_r = 32.5$ and low dielectric loss tangent $\tan\delta = 0.002$ of zirconia make it a good candidate for manufacturing 3-D-printed anisotropic dielectrics with large dielectric constants and birefringence for DRA applications [132].

The proposed sub-wavelength unit cell and its simulations setup are described in Fig. 3.27a. It is a cubic unit cell made up of zirconia and air holes. Its anisotropy is due to the air holes placed along the x-direction that break its rotational symmetry, namely a cross-shaped in its centre and cylindrical holes on its sides. This design leads to uniaxial anisotropy since the same effective dielectric constant ε_{rt} along the y- and z-directions is find as in (3.10). In addition to that, the cross-shaped hole in the unit cell leads to achieve a large birefringence in comparison with cubic and cylindrical holes located at its centre. Finally, both ε_{rx} and ε_{rt} can be controlled by changing the air-filling ratio of the unit cell through the parameters ℓ_{uc}, w_{uc}, and e_{uc}. Nevertheless, a minimum thickness of 0.5 mm for zirconia walls must be respected to satisfy the manufacturing constraints of the 3-D printer.

This unit cell is simulated and optimized using periodic boundary conditions on Ansys HFSS, and its effective permittivity tensor is retrieved through the simulated S-parameters, as detailed in [137] and in Appendix B. In order to find ε_{rx} and ε_{rt}, the incident electric field is successively polarized along the x- and y-directions. Respecting manufacturing constraints, and assuming $a_{uc} = 3.30$ mm, a birefringence $\Delta\varepsilon$ up to 8 can be obtained, for instance, at the 2.45 GHz ISM band as illustrated in Fig. 3.27b.

In order to validate the manufacturing process, a specific unit cell has been designed in simulation to obtain $\varepsilon_{rx} = 20$ and $\varepsilon_{rt} = 12$ at 2.45 GHz. Its optimized dimensions are $a_{uc} = 3.30$ mm, $l_{uc} = 2.80$ mm, $e_{uc} = 0.40$ mm, and $w_{uc} = 0.84$ mm. The unit cell size a_{uc} finally remains smaller than one eighth of the wavelength in the dielectric at 2.45 GHz for the largest value of the permittivity tensor.

Besides, a sensitivity analysis of this unit cell is performed at 2.45 GHz, as reported in Table 3.2 and Fig. 3.28, considering the manufacturing tolerances of the 3-D-printing technology, namely a maximum tolerance of ± 0.1 mm for linear dimensions and hole diameters [138].

	a_{uc}	ℓ_{uc}	w_{uc}	e_{uc}
Sensitivity ε_{rx}	3.5%	2.7%	5.2%	1.8%
Sensitivity ε_{rt}	8.3%	8.2%	7.0%	2.1%

Table 3.2: Parametric analysis of the unit cell dimensions for a variation of ± 0.1 mm.

As observed, an error of $\pm 3.5\%$ on ε_{rx} is obtained, namely for a relative permittivity range of $19.29 \leq \varepsilon_{rx} \leq 20.74$, and $\pm 8.3\%$ for ε_{rt}, that is to say a relative permittivity range of $10.97 \leq \varepsilon_{rt} \leq 13.0$ at 2.45 GHz by varying $a_{uc} \pm 0.1$ mm. It is reported in Table 3.2 that ε_{rx} is mainly sensitive to w_{uc} and a_{uc}, while ε_{rt} depends on w_{uc}, ℓ_{uc}, and a_{uc}. It is important to notice however, that it corresponds to worst case where all the unit cells that make up the material have the same large error on their dimensions. Practically, it is unlikely and

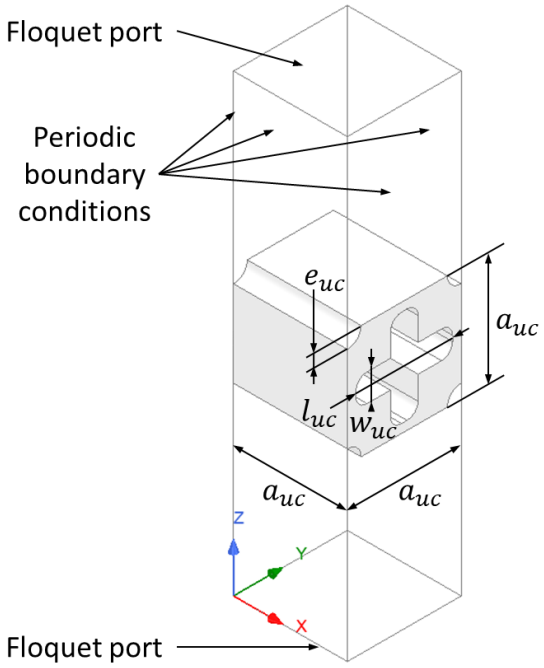

(a) 3-D-printed uniaxial anisotropic unit cell.

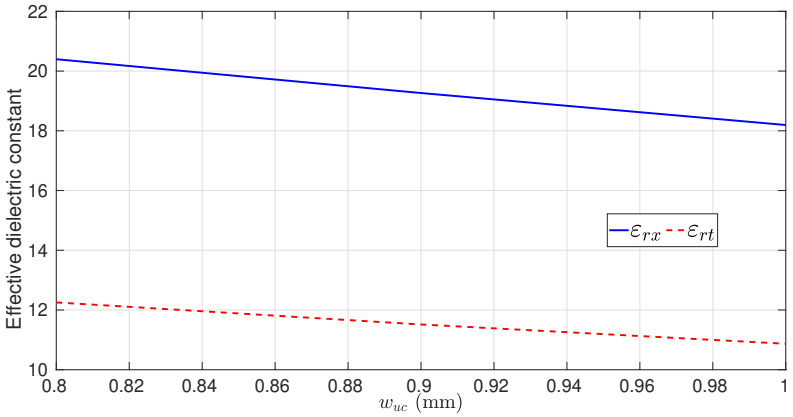

(b) Example of simulated effective permittivity tensor for this unit cell as a function of the dimension w_{uc} at 2.45 GHz ($a_{uc} = 3.30$ mm, $l_{uc} = 2.80$ mm, and $e_{uc} = 0.40$ mm).

Figure 3.27: Design of the proposed 3-D-printed uniaxial anisotropic unit cell with its simulated effective permittivity tensor as a function of w_{uc}.

an average response may be obtained when the material is looked at the macroscopic level through its permittivitty tensor.

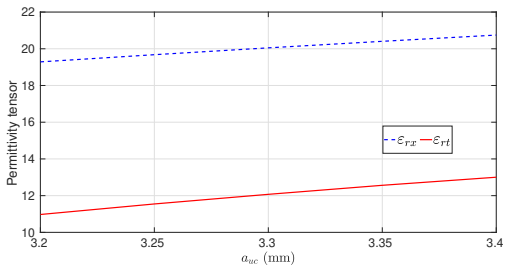

(a) Variation of a_{uc} vs permittivity.

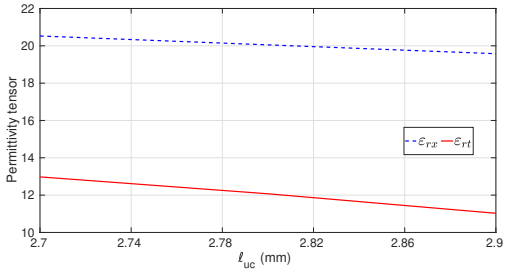

(b) Variation of ℓ_{uc} permittivity.

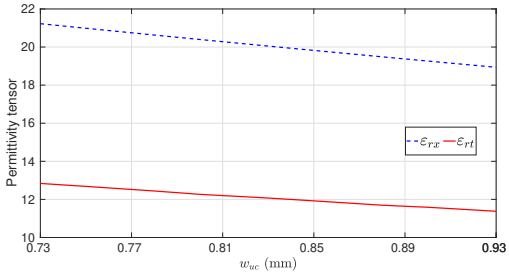

(c) Variation of w_{uc} permittivity.

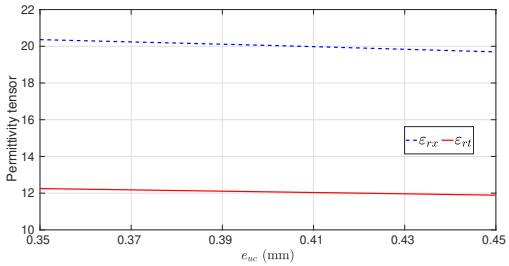

(d) Variation of e_{uc} permittivity.

Figure 3.28: Permittivity tensor by varying the unit cell dimensions for a variation of ±0.1 mm.

3.3.3 Measurements of the 3-D printed samples

Two samples have been 3-D-printed as shown in Fig. 3.29a and 3.29b to measure ε_{rx} and ε_{rt}, respectively. Their thickness is equal to 5 mm, while their lateral dimensions are equal to 86.3 mm and 43.1 mm to fit in a WR340 rectangular waveguide. The samples were inserted into a waveguide section, or sample holder, and measured separately. Afterwards, the S-parameters are obtained using the measured setup shown in Fig. 3.30 that has been developed specifically for this application. It is made up of waveguide sections, waveguide-to-coax transitions, coaxial cables, and a vector network analyser (VNA). A Thru-Reflect-Line (TRL) calibration procedure is done to measure the S-parameters directly on the input and output planes of the sample holder. Finally, the Nicolson-Ross-Wier (NRW) method has been applied for parameter retrieval from the measured S-parameters [139, 140]. In addition to that, a full wave simulation of this measurement configuration with the 3-D-printed samples has been performed using Ansys HFSS.

Fig. 3.31 illustrates the expected simulated and measured dielectric constants retrieved from the measured S-parameters of both dielectric samples. From the simulated results, $\varepsilon_{rx} = 19.1$ and $\varepsilon_{rt} = 12.0$ are found at 2.4 GHz. Note that some discontinuities are observed at 2.45 GHz. The hypothesis of this behaviour is that several higher-order modes resonate in the anisotropic dielectric samples at the ISM band. These resonances are produced by the sample made up of unit cells due to the large values of ε_{rx} and ε_{rt}, which produce a large

(a) Dielectric sample used to measure ε_{rx}.

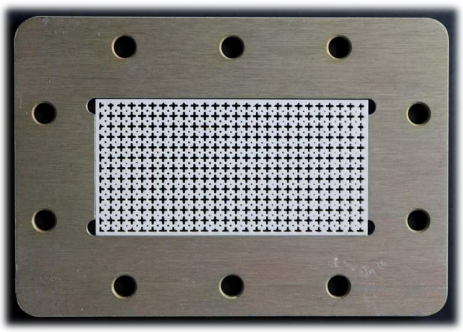

(b) Dielectric sample used to measure ε_{rt}.

Figure 3.29: Pictures of 3-D-printed samples ($a_{uc} = 3.30$ mm, $l_{uc} = 2.80$ mm, $e_{uc} = 0.40$ mm, and $w_{uc} = 0.84$ mm) within a WR340 sample holder to measure ε_{rx} and ε_{rt} at 2.45 GHz.

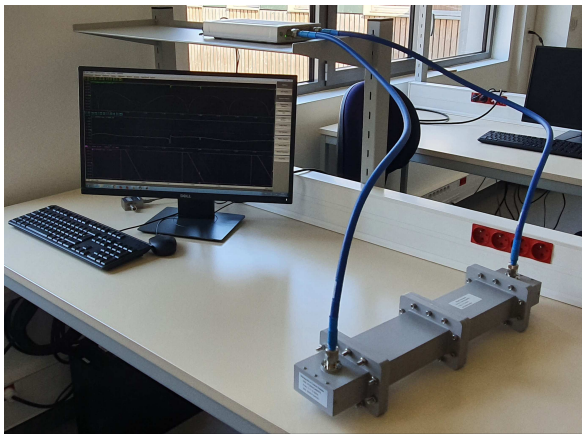

Figure 3.30: Measurement setup to retrieve the permittivity tensor of the anisotropic dielectric samples.

index of refraction so that part of net energy is transmitted and radiated by these higher-order modes that are not taken into account by the NRW method. In fact, this measurement technique has been rather designed for moderate permittivities and isotropic materials.

Applying the measurement procedure, $\varepsilon_{rx} = 18.9$ and $\varepsilon_{rt} = 11.5$ are found at 2.45 GHz (see Fig. 3.31), that is to say a maximum error of 5.5% and 4.1% for ε_{rx} and ε_{rt}, respectively. These uncertainties are due to manufacturing tolerances, namely the resolution of the 3-D-printer, as well as the accuracy of the measurement technique [141].

On the other hand, this measurement technique does not provide accurate results of the loss tangent, as shown in Fig. 3.32. A reason of the disagreement between the simulated and measured results relies on the fact that a thin material with very low dielectric loss is used to retrieve the S-parameters, that is used to calculate the complex effective permittivity. In addition to that, the tolerance of the measurement setup also has an impact on the accuracy

of the dielectric losses. It is also possible to note in Fig. 3.32 that a rapid fluctuation of the measured tangent loss is found. However, mixing zirconia and air in the unit cell may lead to a dielectric loss tangent lower than 0.002. The simulated tan δ_{rx} and tan δ_{rt} are 0.0018 and 0.0019, respectively, at 2.4 GHz.

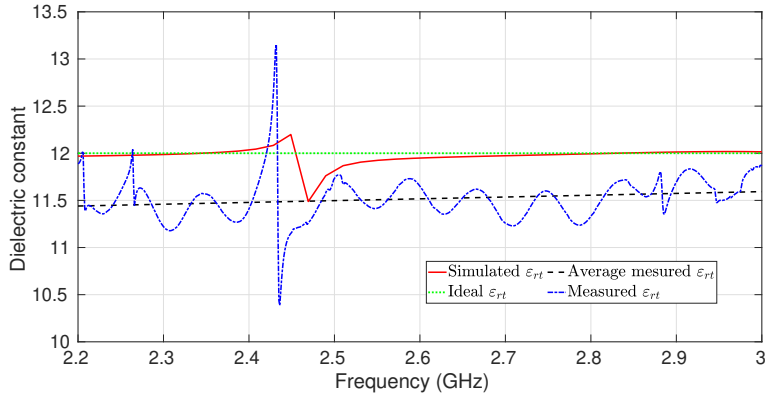

(a) ε_{rt}.

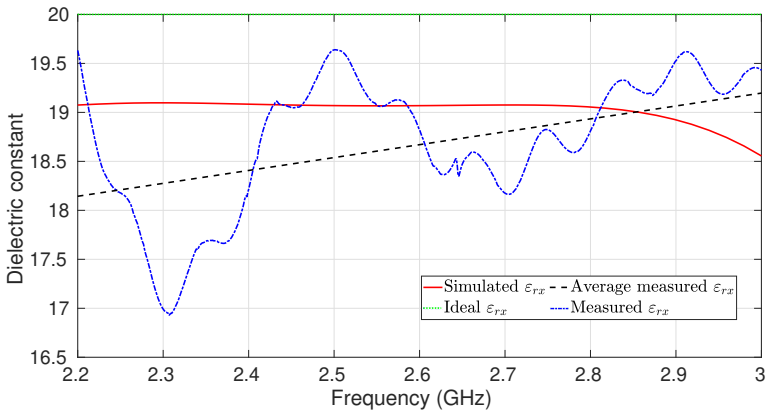

(b) ε_{rx}.

Figure 3.31: Simulated and measured permittivity tensor of the uniaxial anisotropic dielectric sample.

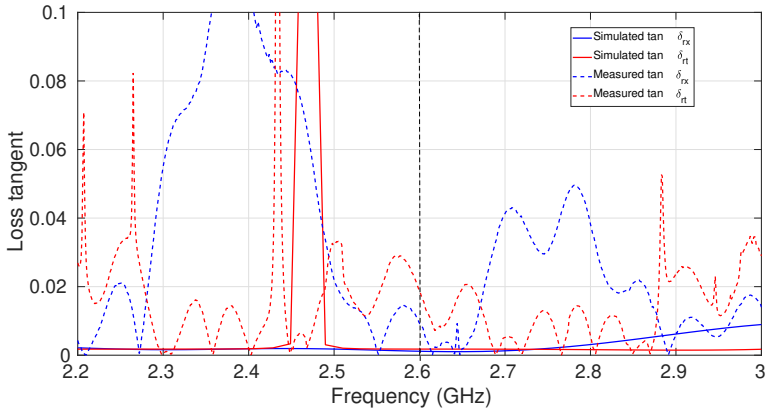

Figure 3.32: Simulated and measured loss tangent of the uniaxial anisotropic dielectric sample.

3.4 Conclusion

3-D printing has been widely investigated to design microwave materials, circuits, and antennas. It has been shown that the use of additive manufacturing of ceramics can also open up interesting perspectives in the design of new dielectric-based antennas due to the various degrees of freedom in shape and material properties.

3-D-printed ceramics with engineered dielectric anisotropy have thus been presented. More specifically, their permittivity tensor has been controlled by 3-D-printing a periodic structure of sub-wavelength cubic unit cells that do not exhibit rotational symmetry. A sample has been designed and 3-D-printed by controlling the filling ratio of zirconia and air in its unit cells. It finally exhibits uniaxial dielectric anisotropy with a large birefringence of 8.

A sensitivity analysis of the unit cell dimensions has been performed. It corresponds to the tolerance of the 3-D printer. It has been shown that an error of $\pm 3.5\%$ can be found for the minimum value of the permittivity tensor, namely ε_{rx}; and an error of $\pm 8.3\%$ for ε_{rt}, which represents the largest value of the tensor. However, such errors are representing the worst case since the tolerance will average when printing multiples unit cells for a full sample of material.

If the use of additive manufacturing of ceramics have already opened up interesting perspectives in design of new dielectric-based antennas due to the various degrees of freedom in their shape, few works have conducted controlling the anisotropy to obtain new degrees of freedom in DRA design. In the next chapter, the design of a uniaxial anisotropic square-based DRA to achieve a single-fed circularly polarized DRA in thus proposed.

Chapter 4

Single-Fed Circularly Polarized DRA using a 3-D-Printed Uniaxial Anisotropic Ceramic

Sommaire

In Chapter 2, two Huygens source antennas have been proposed using a stacked configuration formed by two isotropic dielectric resonators. However, it has been shown in Chapter 3 that 3-D printing of ceramics can provide a new degree of freedom in DRA design by controlling the effective permittivity of dielectric materials. More specifically, additive manufacturing of ceramics paves the way for new antennas using complex shapes and engineered electromagnetic properties to control, for instance, their polarization and radiation pattern.

The possibilities offered by additive manufacturing to create an anisotropic dielectric material to design a compact Huygens source antenna will be studied in the next Chapter. As a previous step, this chapter is intended to validate, as a proof-of-concept, the use of anisotropic materials for DRA applications. For this purpose, the single-fed circularly polarized DRA is proposed. In addition to that, an anisotropic dielectric material is engineered using Stereolithography apparatus. Anisotropy is obtained from periodized unit cells at sub-wavelength scale.

This chapter is organized as follows. The principle of operation and a theoretical model are first presented to design a square-based DRA in circular polarization using a uniaxial

anisotropic dielectric material. Afterwards, a single-fed circularly polarized antenna using a uniaxial anisotropic resonator is designed, 3-D-printed, and measured.

4.1 Principle of operation

Let's consider a rectangular dielectric resonator, as shown in Fig. 1.13, and with dimensions a, b, and d along x-, y-, and z-directions, respectively. A classical technique to obtain circular polarization with a single feed is to excite two orthogonal modes in phase quadrature inside this dielectric resonator, namely the TE^{x}_{111} and TE^{y}_{111} modes [142, 143].

It has been demonstrated in [144, 145], that the resonance frequencies of both modes must satisfy certain conditions in order to achieve circular polarization at the centre frequency f_0 as follows

$$f_1 \approx f_0 \left(1 - \frac{1}{2Q_1}\right) \tag{4.1}$$

$$f_2 \approx f_0 \left(1 + \frac{1}{2Q_2}\right) \tag{4.2}$$

where f_1 and Q_1 are the resonance frequency and quality factor of the TE^{y}_{111} mode, while $f_2 > f_1$ and Q_2 refer to the TE^{x}_{111} mode.

Practical implementations for having two modes respecting these criteria include, for example, rectangular shape DRA [146], or a square one with truncated corners [147], as shown in Fig. 4.1.

However, instead of modifying the DRA shape, a square-based antenna can also be considered by modifying the permittivity tensor of a uniaxial anisotropic ceramic material to tune correctly the two orthogonal modes. In order to design a single-fed antenna using anisotropic dielectric resonators, a theoretical analysis of the resonant modes is studied in the next section.

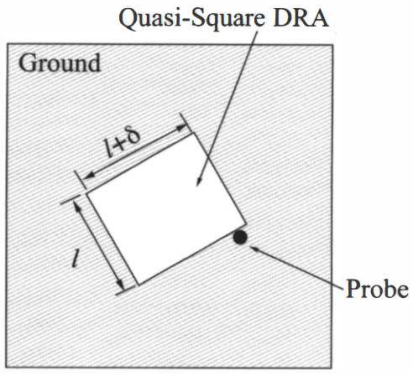

(a) Rectangular or quasi-square DRA.

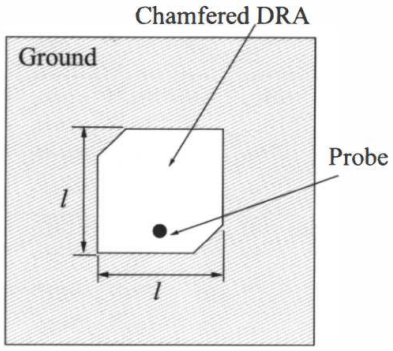

(b) Chamfered DRA.

Figure 4.1: Single-fed circularly polarized DRA [148].

4.2 Theoretical analysis of TE modes in an anisotropic DRA

Inspired by [149], a theoretical analysis is presented in this section in order to calculate the resonance frequencies and quality factors of the fundamental TE^x_{111} and TE^y_{111} modes in a rectangular dielectric resonator with anisotropic properties. The properties of the aforementioned resonant modes are necessary to calculate the DRA dimensions and permittivity tensor so that they satisfy the requirements in amplitude and phase to achieve circular polarization, as expressed in (4.1) and (4.2).

4.2.1 Resonance frequencies of fundamental TE modes

As discussed in 4.1, the resonance frequencies of two modes in a square-base dielectric resonator, namely TE^x_{111} and TE^y_{111} modes, must satisfy certain conditions to achieve circular polarization. The following theoretical analysis is thus performed in order to calculate the resonance frequencies of fundamental TE modes in an anisotropic dielectric resonator.

Based on the Maxwell equations, the field distribution inside the DRA can be expressed as

$$\bigtriangledown \times \mathbf{E} = -j\omega\mu_0\mu_r\mathbf{H} \tag{4.3}$$

$$\bigtriangledown \times \mathbf{H} = j\omega\varepsilon_0\varepsilon_r\mathbf{E}. \tag{4.4}$$

A dielectric resonator (*i.e.* $\mu_r = 1$) is considered with an anisotropic medium of permittivity tensor given by

$$\varepsilon_r = \begin{bmatrix} \varepsilon_{rx} & 0 & 0 \\ 0 & \varepsilon_{ry} & 0 \\ 0 & 0 & \varepsilon_{rz} \end{bmatrix}. \tag{4.5}$$

Analyzing the TE^y mode, namely $E_y = 0$, so that $\mathbf{E}(x, y, z) = \mathbf{E}(x, z)e^{-k_y y}$, the following expressions can be derived from (4.3) and (4.4)

$$\begin{aligned} -jk_yE_z &= -j\omega\mu_0H_x \\ \frac{\partial E_x}{\partial z} - \frac{\partial E_z}{\partial x} &= -j\omega\mu_0H_y \\ jk_yE_x &= -j\omega\mu_0H_z \\ -jk_yH_z - \frac{\partial H_y}{\partial z} &= j\omega\varepsilon_0\varepsilon_{rx}E_x \\ \frac{\partial H_x}{\partial z} - \frac{\partial H_z}{\partial x} &= 0 \\ \frac{\partial H_y}{\partial x} + jk_yH_x &= j\omega\varepsilon_0\varepsilon_{rz}E_z. \end{aligned} \tag{4.6}$$

The equations in (4.6) can also be expressed in terms of H_y

$$\begin{aligned} E_x &= \frac{j\omega\mu_0}{(k_0^2\varepsilon_{rx} - k_y^2)}\frac{\partial H_y}{\partial z} \\ E_z &= -\frac{j\omega\mu_0}{(k_0^2\varepsilon_{rz} - k_y^2)}\frac{\partial H_y}{\partial x} \\ H_x &= \frac{1}{(k_0^2\varepsilon_{rz} - k_y^2)}\frac{\partial^2 H_y}{\partial x\partial y} = -\frac{jk_y}{(k_0^2\varepsilon_{rz} - k_y^2)}\frac{\partial H_y}{\partial x} \\ H_z &= \frac{1}{(k_0^2\varepsilon_{rx} - k_y^2)}\frac{\partial^2 H_y}{\partial x\partial z} = -\frac{jk_y}{(k_0^2\varepsilon_{rx} - k_y^2)}\frac{\partial H_y}{\partial z} \end{aligned} \tag{4.7}$$

where $k_0 = (2\pi f_0)/c_0$ is the free-space wavenumber, f_0 the resonance frequency of the TE^y_{111} mode, and c_0 the speed of light in vacuum. From (4.3) and (4.4), the following equation is found

$$\bigtriangledown \times(\bigtriangledown \times \mathbf{H}) = j\omega\varepsilon_r \bigtriangledown \times(\varepsilon_r \mathbf{E}) \tag{4.8}$$

and considering that

$$\bigtriangledown \times(\bigtriangledown \times \mathbf{H}) = \bigtriangledown(\bigtriangledown \cdot \mathbf{H}) - \bigtriangledown^2 \mathbf{H} \tag{4.9}$$

then, (4.8) becomes

$$\bigtriangledown^2 \mathbf{H} + j\omega\varepsilon_0 \bigtriangledown \times(\varepsilon_r \mathbf{E}) = 0. \tag{4.10}$$

Solving (4.10) for H_y gives

$$\bigtriangledown^2 H_y + j\omega\varepsilon_0 \left(\varepsilon_{rx}\frac{\partial E_x}{\partial z} - \varepsilon_{rz}\frac{\partial E_z}{\partial x}\right) = 0. \tag{4.11}$$

By substituting (4.7) in (4.11), the following equation is found

$$\bigtriangledown^2 H_y + j\omega\varepsilon_0 \left(\varepsilon_{rx}\frac{j\omega\mu_0}{k_0^2\varepsilon_{rx} - k_y^2}\frac{\partial^2 H_y}{\partial^2 z} + \varepsilon_{rz}\frac{j\omega\mu_0}{k_0^2\varepsilon_{rz} - k_y^2}\frac{\partial^2 H_y}{\partial^2 x}\right) = 0 \tag{4.12}$$

namely,

$$\frac{\partial^2 H_y}{\partial^2 x}\left(1 - \frac{k_0^2\varepsilon_{rz}}{k_0^2\varepsilon_{rz} - k_y^2}\right) + \frac{\partial^2 H_y}{\partial^2 y} + \frac{\partial^2 H_y}{\partial^2 z}\left(1 - \frac{k_0^2\varepsilon_{rx}}{k_0^2\varepsilon_{rx} - k_y^2}\right) = 0. \tag{4.13}$$

Multiplying (4.13) by $\frac{-k_0^2}{k_y}$, it is found that

$$\frac{\partial^2 H_y}{\partial^2 x}\left(\frac{k_0^2}{k_0^2\varepsilon_{rz} - k_y^2}\right) + k_0^2 H_y + \frac{\partial^2 H_y}{\partial^2 z}\left(\frac{k_0^2}{k_0^2\varepsilon_{rx} - k_y^2}\right) = 0. \tag{4.14}$$

On the other hand, solving (4.3) and (4.4), using $k_0 = \omega\sqrt{\mu_0\varepsilon_0}$, the following expression can be found

$$\bigtriangledown \times\varepsilon_r^{-1}(\bigtriangledown \times \mathbf{H}) = k_0^2 \mathbf{H}. \tag{4.15}$$

4.2.1.1 Fields in an infinite dielectric waveguide with PMC walls

In order the calculate the E- and H-fields in a dielectric waveguide for the TE^{y}_{111} mode, PMC boundary conditions must be imposed along the x- and z-directions. It requires that the tangential components of magnetic field vanish on these walls so that that the following expression can be found

$$H_y = H_0 \sin(k_x x) \sin(k_z z)(A\ e^{-jk_{y0}y} + B\ e^{jk_{y0}y}) \tag{4.16}$$

with $k_x = \pi/a$ and $k_z = \pi/d$. The E- and H-fields components in the infinite dielectric waveguide can be expressed as

$$\begin{aligned}
E_x =& -\frac{j\omega\mu_0 H_0 k_z}{k_0^2\varepsilon_{rx} - k_y^2} \sin(k_x x) \cos(k_z z)(A\ e^{-jk_{y0}y} + B\ e^{jk_{y0}y}) \\
E_y =& 0 \\
E_z =& \frac{j\omega\mu_0 H_0 k_x}{k_0^2\varepsilon_{rz} - k_y^2} \cos(k_x x) \sin(k_z z)(A\ e^{-jk_{y0}y} + B\ e^{jk_{y0}y}) \\
H_x =& \frac{jH_0 k_x k_y}{k_0^2\varepsilon_{rz} - k_y^2} \cos(k_x x) \sin(k_z z)(A\ e^{-jk_{y0}y} + B\ e^{jk_{y0}y}) \\
H_z =& \frac{jH_0 k_y k_z}{k_0^2\varepsilon_{rx} - k_y^2} \sin(k_x x) \cos(k_z z)(A\ e^{-jk_{y0}y} + B\ e^{jk_{y0}y}).
\end{aligned} \tag{4.17}$$

Afterwards, the waveguide is truncated with dielectric walls at $y = \pm b/2$ to model the dielectric resonator antenna. The fields are then calculated within the DRA at $-b/2 \leq |y| \leq b/2$, as detailed in the following analysis.

4.2.1.2 Fields in a dielectric cavity

In order to find the fields confined in the dielectric cavity $-b/2 \leq |y| \leq b/2$, the waveguide is truncated at $y = \pm b/2$. Therefore, magnetic field component H_y found at $-b/2 \leq |y| \leq b/2$ can be written as

$$H_y = H_0 \sin(k_x x) \cos(k_y y) \sin(k_z z). \tag{4.18}$$

By substituting (4.18) in (4.14), the transcendental equation is obtained as follows

$$\frac{k_x^2}{k_0^2\varepsilon_{rz} - k_y^2} + \frac{k_z^2}{k_0^2\varepsilon_{rx} - k_y^2} = 1. \tag{4.19}$$

It is possible to note that k_y can be calculated from (4.19). In addition to that, this solution depends on the two permittivities of the anisotropic permittivity tensor along x- and z-directions, namely ε_{rx} and ε_{rz}. This is the main difference with respect to a dielectric resonator with isotropic permittivity, which only depends on a scalar value, as shown in (1.9).

On the other hand, the field distribution inside the dielectric cavity can be expressed as

$$\begin{aligned}
E_x =& -\frac{j\omega\mu_0 H_0 k_z}{k_0^2\varepsilon_{rx} - k_y^2}\cos(k_x x)\cos(k_y y)\sin(k_z z)\\
E_y =& 0\\
E_z =& \frac{j\omega\mu_0 H_0 k_x}{k_0^2\varepsilon_{rz} - k_y^2}\sin(k_x x)\cos(k_y y)\cos(k_z z)\\
H_x =& \frac{H_0 k_x k_y}{k_0^2\varepsilon_{rz} - k_y^2}\sin(k_x x)\sin(k_y y)\cos(k_z z)\\
H_z =& \frac{H_0 k_y k_z}{k_0^2\varepsilon_{rx} - k_y^2}\cos(k_x x)\sin(k_y y)\sin(k_z z).
\end{aligned} \tag{4.20}$$

Applying continuity of the tangential fields to $y = \pm\frac{b}{2}$, and assuming propagation in the $+y$ direction in the infinite dielectric waveguide with $e^{-jk_{y0}y}$, E_x can be then written as

$$\frac{\cos(k_y y)}{k_0^2\varepsilon_{rx} - k_y^2} = \frac{e^{-jk_{y0}y}}{k_0^2\varepsilon_{rx} - k_{y0}^2}. \tag{4.21}$$

The derivative of (4.21) according to y is

$$-\frac{k_y\sin(k_y y)}{k_1^2\varepsilon_{rx} - k_y^2} = -j\frac{k_{y0}e^{-jk_{y0}y}}{k_1^2\varepsilon_{rx} - k_{y0}^2}. \tag{4.22}$$

Solving (4.21) and (4.22) with $y = \frac{b}{2}$, the following expression can be found

$$k_y b = 2\tan^{-1}\left(\frac{k_{y0}}{k_y}\right). \tag{4.23}$$

Since there are two distinct regions with different wavenumbers, namely k_{y0} and k_y, the field in these regions and match tangential fields across the interface $y = \frac{b}{2}$ must be separately considered [67]. The cutoff wavenumbers for the two regions are thus defined as

$$k_y^2 = \varepsilon_r k_0^2 - \beta^2 \tag{4.24}$$

$$k_{y0}^2 = \beta^2 - k_0^2. \tag{4.25}$$

where β defines a common propagation constant in both regions to ensure phase matching of the fields along the interface $y = \frac{b}{2}$. Using separation of variables as in (1.8), the solution (4.23) can be written as

$$k_y \tan\left(\frac{k_y b}{2}\right) = \sqrt{k_x^2 + k_z^2 - k_0^2}. \tag{4.26}$$

In order to calculate the resonance frequency of the TE_{111}^y mode, namely k_0 value, in a rectangular anisotropic DRA, (4.19) and (4.26) must finally be numerically solved.

4.2.2 Quality factor

In order to calculate the quality factor of TE modes in a lossless dielectric resonator, the stored electric energy W_e and radiated power by a magnetic dipole of moment P_{rad} must be considered, as detailed in section 1.2.2.3. Applying the same analysis, the final expression of the quality factor for the TE_{111}^y mode in the proposed anisotropic dielectric resonator can thus be expressed as

$$Q = \frac{\omega_0 \mu_0 \pi^6}{640 k_0^6 abd} \frac{(1 + sinc(k_y b))}{\mathrm{sinc}(k_y b/2)^2} \cdot \frac{\left[\frac{\varepsilon_{rz} k_x^2}{(k_0^2 \varepsilon_{rz} - k_y^2)^2} + \frac{\varepsilon_{rx} k_z^2}{(k_0^2 \varepsilon_{rx} - k_y^2)^2}\right]}{\left[\frac{(\varepsilon_{rz}-1) k_x a}{k_0^2 \varepsilon_{rz} - k_y^2} + \frac{(\varepsilon_{rx}-1) k_z d}{k_0^2 \varepsilon_{rx} - k_y^2}\right]^2}. \tag{4.27}$$

Note that, since $\varepsilon_{rt} = \varepsilon_{ry} = \varepsilon_{rz}$ in the proposed uniaxial anisotropic material, the TE_{111}^x mode remains as with an isotropic dielectric due to the equality of the dielectric constants along the y- and z-directions. Applying the dielectric waveguide model, it is possible to determine the unknown k_x wavenumber along the x-direction, and thus the resonance frequency f_0 of the TE_{111}^x mode, using the transcendental equation as similarly obtained in (1.9) [43]

$$k_x \tan\left(k_x \frac{a}{2}\right) = \sqrt{k_0^2(\varepsilon_{rt} - 1) - k_x^2}. \tag{4.28}$$

with $k_0 = (2\pi f_0)/c_0$ the free-space wavenumber, as well as the separation equation

$$k_x^2 + k_y^2 + k_z^2 = \varepsilon_{rt} k_0^2 \tag{4.29}$$

where $k_y = \pi/b$ and $k_z = \pi/d$ are the wavenumbers along y- and z-directions, respectively. The final expression of the quality factor for the TE_{111}^x mode then simplifies to

$$Q = \frac{\omega_0 \mu_0 \pi^6}{2560 k_0^6 abd} \frac{[1 + \mathrm{sinc}(k_x a)]}{\mathrm{sinc}^2(k_x a/2)} \frac{\varepsilon_{rt}(k_y^2 + k_z^2)}{(\varepsilon_{rt} - 1)^2}. \tag{4.30}$$

The quality factors of the TE^y_{111} and TE^x_{111} modes can finally be determined by solving (4.27) and (4.30), respectively. On the other hand, the resonance frequency of the TE^x_{111} mode can be calculated by solving (4.28) and (4.29), considering that $\varepsilon_{rt} = \varepsilon_{ry} = \varepsilon_{rz}$.

4.3 Antenna design and fabrication

This section is intended to design a single-fed antenna in circular polarization using a uniaxial anisotropic dielectric resonator, following the theoretical model proposed in section 4.2.

4.3.1 Analytical design

Instead of modifying the DRA shape for having these two TE^x_{111} and TE^y_{111} modes respecting (4.1) and (4.2), a perfectly square DRA is here considered with $a = b$ for which resonance frequencies are tuned by modifying the permittivity tensor of a uniaxial anisotropic dielectric medium given by

$$\varepsilon_r = \begin{bmatrix} \varepsilon_{rx} & 0 & 0 \\ 0 & \varepsilon_{rt} & 0 \\ 0 & 0 & \varepsilon_{rt} \end{bmatrix}. \tag{4.31}$$

Based on the conditions to achieve circular polarization shown in (4.1) and (4.2), the index 1 here denotes the TE^y_{111} mode, and the index 2 is here considered when dealing with the TE^x_{111} mode. Given the permittivity tensor of (4.31), the resonance frequency f_2 remains as with an isotropic dielectric resonator since the x-component of the electric field vanishes ($E_x = 0$) and the dielectric constants along the y- and z-directions are both equal to ε_{rt}. On the contrary, the resonance frequency f_1 is altered by the anisotropic properties of the dielectric resonator.

In order to design a single-fed circularly polarized DRA at the centre frequency f_0 using a uniaxial anisotropic dielectric material, d and ε_{rt}, are first fixed. Furthermore, $a = b$ is imposed. The theoretical model of section 4.2 is then used to assess a and ε_{rx}, as follows.

For a, a list of discrete possible values is considered. For each of theses values, f_2 is found by solving (4.28) and (4.29). Then Q_2 is determined from (4.30). Finally, the value of a is chosen for which f_2 and Q_2 best satisfy (4.2).

Similarly, by means of (4.19), (4.26), and (4.27), from a list of discrete possible values, the value of ε_{rx} is selected for which f_1 and Q_1 best satisfy (4.1).

The proposed methodology is applied to design a single-fed circularly polarized DRA for the $f_0 = 2.45$ GHz ISM band, as presented in Table 4.1. First, $d = 25.20$ mm, $\varepsilon_{rt} = 12$, and $f_0 = 2.45$ GHz are fixed. In order to satisfy (4.2), the DRA size must be $a = b = 27.60$ mm. Finally, the dielectric constant ε_{rx} must be equal to 18 to satisfy (4.1). From the theoretical model, $f_1 = 2.34$ GHz, $Q_1 = 12.5$, $f_2 = 2.58$ GHz, and $Q_2 = 9.6$ are obtained. These results are verified using an eigenmode analysis with Ansys HFSS of the dielectric resonator with perfectly matched layers. A good agreement is achieved with $f_1 = 2.36$ GHz, $Q_1 = 12.7$, $f_2 = 2.59$ GHz, and $Q_2 = 10.1$. Note that these values respect (4.1) and (4.2), as expected.

	f_1 (GHz)	Q_1	f_2 (GHz)	Q_2
Theory	2.34	12.5	2.58	9.6
Eigen mode analysis	2.36	12.7	2.59	10.1

Table 4.1: Theoretical and simulated results of the properties of TE^x_{111} and TE^y_{111} modes.

4.3.2 Antenna configuration

A single-fed circularly polarized DRA in left-hand circular polarization is then designed for the 2.45 GHz ISM band. Fig. 4.2 presents the exploded view of the final antenna design. Note that the dielectric resonator has been modeled including both a solid isotropic dielectric material for the walls with $\varepsilon_r = 32.5$ (in grey in Fig. 4.2), and a solid anisotropic dielectric material for the core resonator (in white in Fig. 4.2) for mechanical reasons of the 3-D printer. It is referred as the solid model thereafter.

A numerical optimization is performed using Ansys HFSS to tune the DRA in order to take into account the feeding coaxial probe, finite size ground plane, and solid dielectric walls effect. The final DRA dimensions are $a = b = 25.80$ mm ($0.21\lambda_0$) and $d = 25.20$ mm ($0.21\lambda_0$), and its permittivity tensor in the anisotropic region is $\varepsilon_{rt} = 12$ and $\varepsilon_{rx} = 20$. When compared with the theoretical model, a slight adjustment of 6.9% on dimensions a and b, and 10% on ε_{rt} is needed to tune the modes.

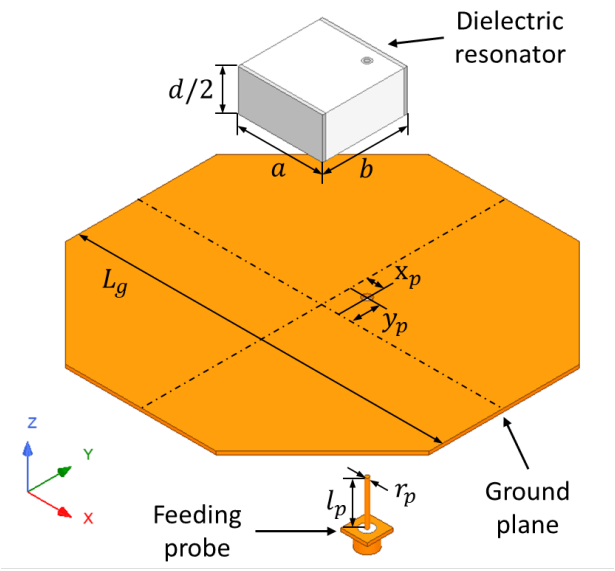

Figure 4.2: Exploded view of the solid uniaxial anisotropic DRA ($a = b = 25.80$ mm, $d = 25.20$ mm, $L_g = 110.87$ mm, $l_p = 12.60$ mm, $d_p = 1.23$ mm, $x_p = 5.29$ mm, and $y_p = 8.29$ mm). The grey parts of the dielectric resonator represent the isotropic zirconia walls.

4.3.3 Sensitivity analysis

A sensitivity analysis of the proposed DRA is performed on its physical and electrical properties in order to determine the impact of the manufacturing process on the antenna performances. To perform this analysis, the dielectric constants ε_{rx} and ε_{rt} are varied of $\pm 5\%$ from the original values and the antenna dimensions are also varied with steps of 1 mm. It is possible to observe that these variation are larger than the expected tolerances.

Fig. 4.3 shows the simulated reflection coefficients and axial ratios of the solid DRA by varying its square dimensions $a = b$. As expected, the increase of a produces a decrease of the resonance frequency. Regarding the axial ratios, the antenna operates properly with a frequency shift of 2.4% for a variation of a of 1 mm.

Fig. 4.4 illustrates the simulated reflection coefficients and axial ratios of the solid DRA by varying its height d. An increase of d generates a frequency shift downwards. Moreover, the antenna matching improves when increasing the antenna height. Regarding the antenna performances in circular polarization, the antenna operates properly with a frequency shift of 1.6% for a variation of d of ± 1 mm.

A variation of $\pm 5\%$ of the dielectric constant ε_{rx} is now conducted, as illustrated in Fig. 4.5. As expected, an increase of ε_{rx} implies a reduction of the resonance frequency of only the TE^{y}_{111} mode. In addition to that, the antenna operates properly in circular polarization with a frequency shift of about 0.4% for a variation of $\pm 5\%$ of the relative permittivity value of ε_{rx}.

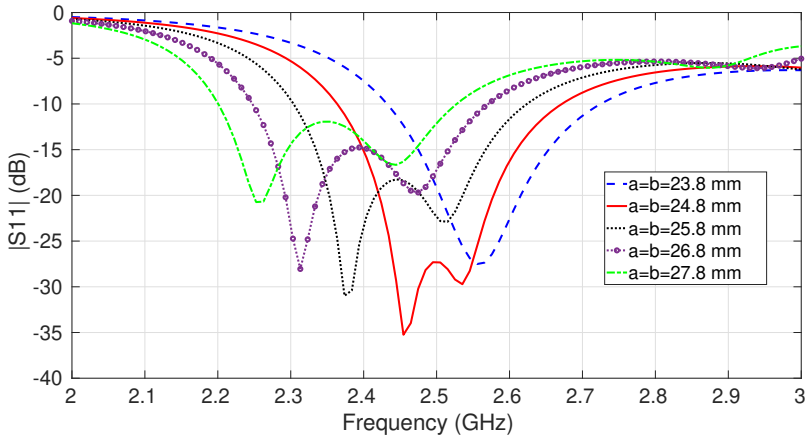

(a) Reflection coefficient.

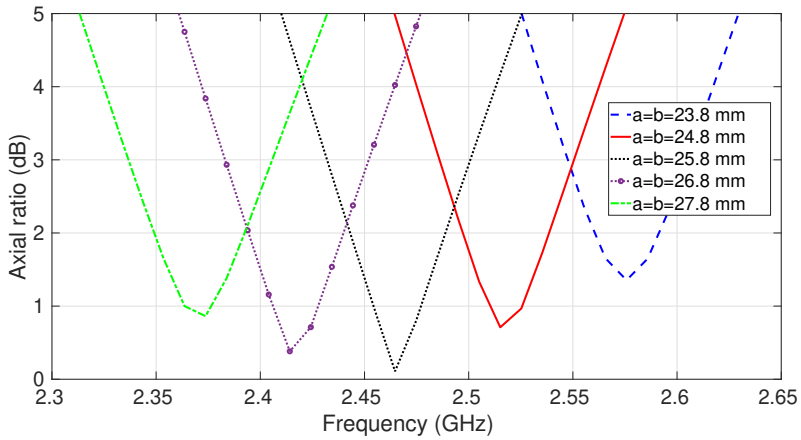

(b) Axial ratio.

Figure 4.3: Simulated reflection coefficients and axial ratios of the solid DRA by varying the dimensions $a = b$.

A sensitivity analysis is finally performed for a ±5% variation of the relative permittivity value of ε_{rt}, as shown in Fig. 4.6. An increase of ε_{rt} produces a frequency shift downwards, as expected. It is noticed that both modes are modified in that case, since their properties (*i.e.*, resonance frequencies and quality factors) depends on ε_{rt}, namely ε_{ry} or ε_{rz}. Regarding the antenna performances in circular polarization, the antenna operates properly with a frequency shift of about 1.6% for a variation of ±5% of the permittivity ε_{rt}.

Based on the sensitivity analysis, it is shown that properties of the resonant modes can be affected by a variation of the DRA dimensions and its permittivity tensor. The worst case occurs for a variation of the square dimensions $a = b$, that exhibit a frequency shift of 2.4% for a variation of ±1 mm of its value.

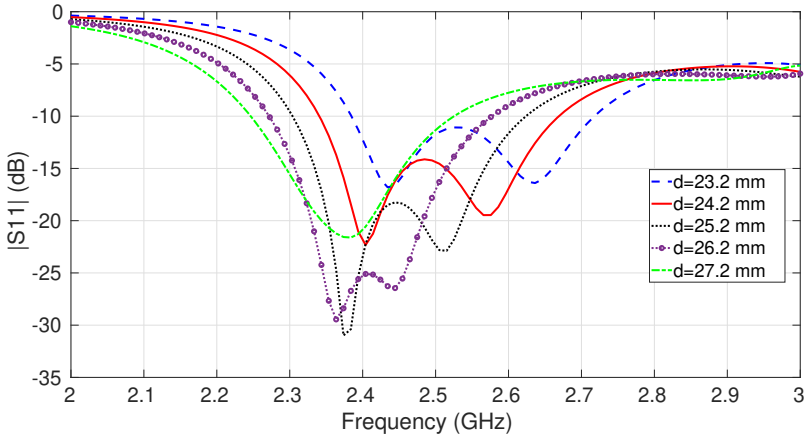

(a) Reflection coefficient.

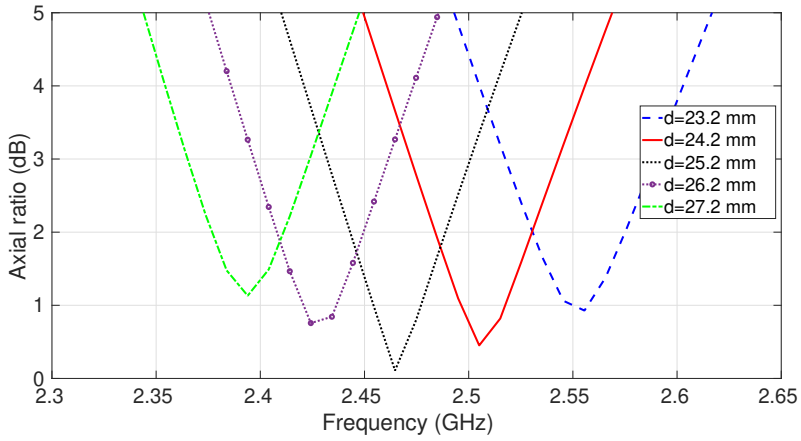

(b) Axial ratio.

Figure 4.4: Simulated reflection coefficients and axial ratios of the solid DRA by varying the dimension d.

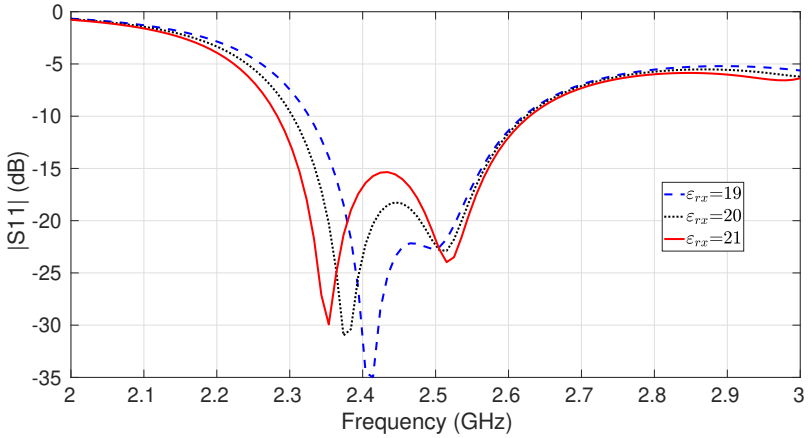

(a) Reflection coefficient.

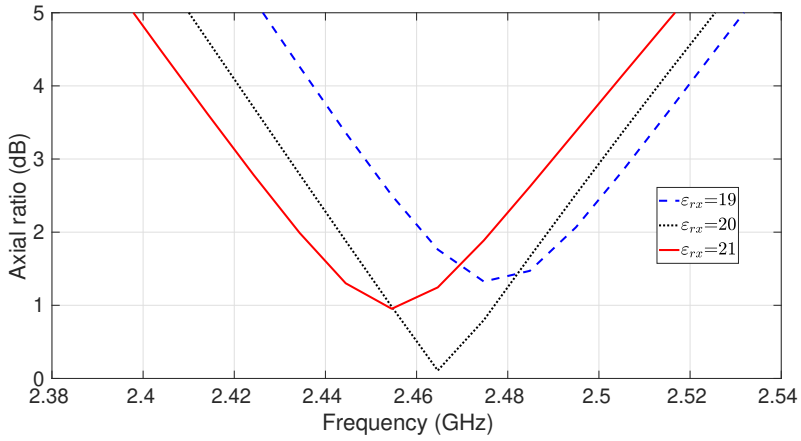

(b) Axial ratio.

Figure 4.5: Simulated reflection coefficients and axial ratios of the solid DRA by varying the relative permittivity ε_{rx}.

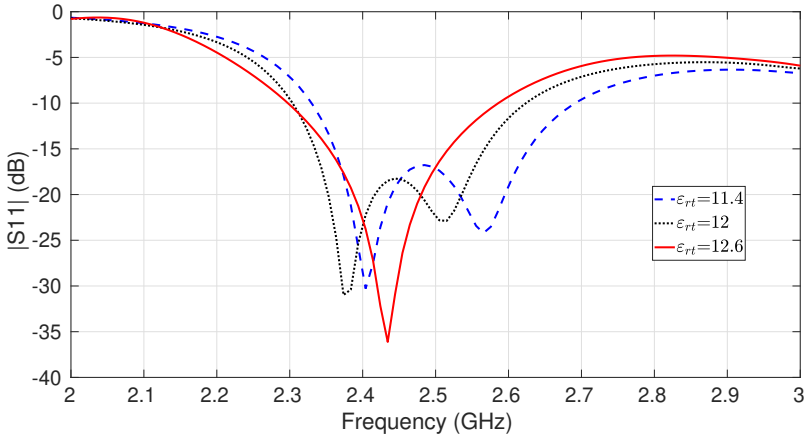

(a) Reflection coefficient.

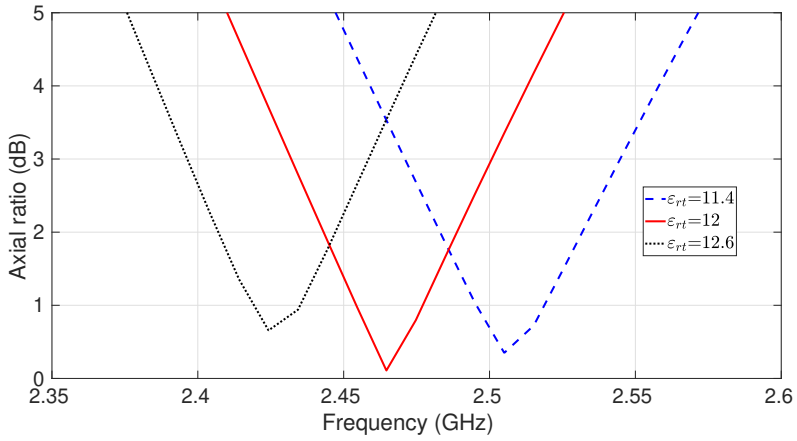

(b) Axial ratio.

Figure 4.6: Simulated reflection coefficients and axial ratios of the solid DRA by varying the relative permittivity ε_{rt}.

4.4 Simulated and measured results

Fig. 4.7 presents a picture of the manufactured DRA. The 3-D-printed sub-wavelength unit cell of Fig. 3.27a is here used to retrieve the permittivity tensor of the proposed uniaxial anisotropic dielectric resonator. The dimensions of the realized 3-D-printed dielectric resonator are $a = 26.0$ mm, $b = 26.1$ mm, and $d = 25.5$ mm, that is to say a maximum error of only 1.2% with respect to the original dimensions.

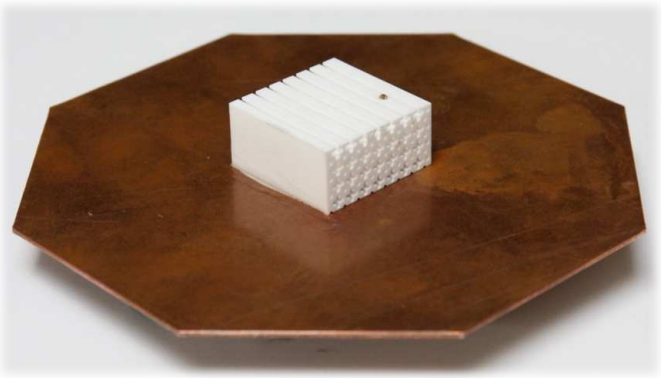

Figure 4.7: Picture of the 3-D-printed uniaxial anisotropic DRA.

The 3-D-printed uniaxial anisotropic DRA of Fig. 4.7 was measured with a Rohde & Schwarz ZVL-13 vector network analyzer in the indoor far-field test range of ISAE-SUPAERO. Fig. 4.8 shows the simulated and measured reflection coefficients as a function of the frequency. Two different models have been simulated using Ansys HFSS, namely the solid model shown in Fig. 4.2 for which the uniaxial anisotropic ceramic is represented with a bulk dielectric material, and the 3-D-printed model that considers the 3-D-printed antenna shown in Fig. 4.7 with all the details of its lattice. As observed, a good agreement between the numerical and experimental results is achieved. The measured 10 dB impedance bandwidth (*i.e.*, $|S_{11}| \leq -10$ dB) is equal to 16% from 2.3 to 2.7 GHz.

Fig. 4.9 shows the simulated and measured axial ratio as a function of the frequency at boresight ($\theta = 0°$). First, a difference in magnitude and a 1% frequency shift between the solid and 3-D-printed simulated models is observed. The hypothesis to justify this frequency shift relies on the longitudinal variation of the dielectric permittivity around the coaxial probe. In fact, the 3-D-printed simulated model is made up of a ceramic material with air holes. Thus, the variation of permittivity along the z-direction may have an impact on the coupling of the fundamental TE^{x}_{111} and TE^{y}_{111} modes, as will be discussed in the next Chapter.

A good agreement is also observed between simulated and measured results. The minimum value for the measured axial ratio is obtained at 2.47 GHz with a 3 dB axial ratio bandwidth of 2.4% from 2.44 to 2.5 GHz. It is also possible to note a slight difference in magnitude between the simulated and measured axial ratio that is due to manufacturing tolerances during the 3-D-printing process. As detailed in 4.3.3, the minimum value for the axial ratio can mainly be affected by varying ε_{rx}, that is to say due to the manufacturing tolerances.

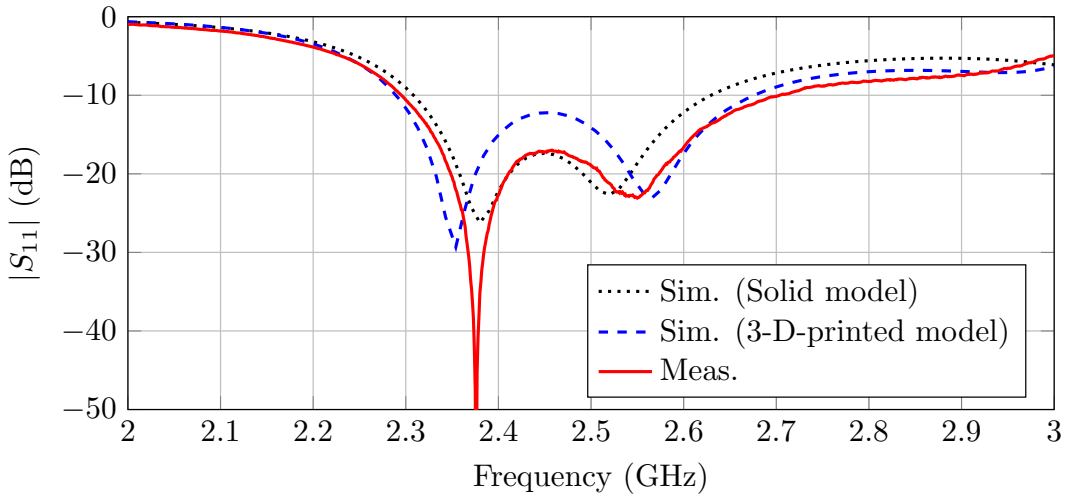

Figure 4.8: Simulated reflection coefficients of the solid and 3-D-printed DRAs, along with measured results.

Furthermore, the axial ratio bandwidth is much lower than the 10 dB impedance bandwidth. This behaviour has been previously studied by Oliver *et al.* in [146], and Haneishi *et al.* in [147]. Their work have proved that single-fed resonant antennas, such as DRA or microstrip antennas, that use two orthogonal modes identical in magnitude and in phase quadrature to obtain circular polarization are known to not provide a wide bandwidth for their axial ratio. In addition to that, W. L. Langston and D. R. Jackson have developed several equations to evaluate for instance the impedance and axial ratio bandwidths of single-fed circularly polarized microstrip antennas, as detailed in [144]. Inspired by their work, theoretical impedance and axial ratio bandwidths of $BW_{IMP} = 12.4\%$ and $BW_{AR} = 3\%$ are obtained, respectively. These theoretical results reasonably agree with those values obtained in measurements (*i.e.*, $BW_{IMP} = 16\%$ and $BW_{AR} = 2.8\%$). As a conclusion, this difference is not due to the anisotropy of the dielectric resonator, but rather to the use of a single-fed circularly polarized DRA relying on the excitation of two orthogonal modes in phase quadrature as observed in [144, 146].

Fig. 4.10 depicts the simulated axial ratio as a function of θ at 2.47 GHz, considering $\phi = 0°$ and $\phi = 90°$. The simulated axial ratio of the solid model is below 3 dB for $-62° \leq \theta \leq 34°$, whereas the measured axial ratio of the 3-D-printed model covers $-92° \leq \theta \leq -60°$ and $-14° \leq \theta \leq 46°$, considering $\phi = 0°$. On the other hand, the simulated axial ratio of the solid model is below 3 dB for $-34° \leq \theta \leq 37°$, whereas the measured axial ratio of the 3-D-printed model covers $-4° \leq \theta \leq 61°$, considering $\phi = 90°$.

Finally, Fig. 4.11 shows the simulated and measured realized gain patterns of the 3-D-printed DRA at 2.47 GHz. The antenna is operating in left-hand circular polarization (LHCP). Once again, a good agreement is obtained between measurement and simulations. The measured realized gain at boresight and simulated radiation efficiency are equal to 6.4 dBi and 97%, respectively, at 2.47 GHz.

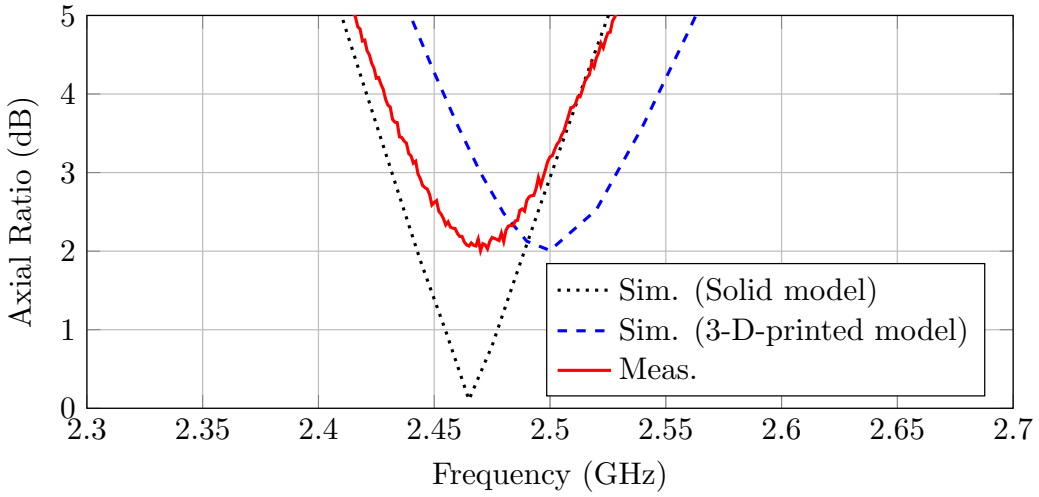

Figure 4.9: Simulated axial ratios of the solid and 3-D-printed DRAs, along with measured results at $\theta = 0°$ and $\phi = 0°$.

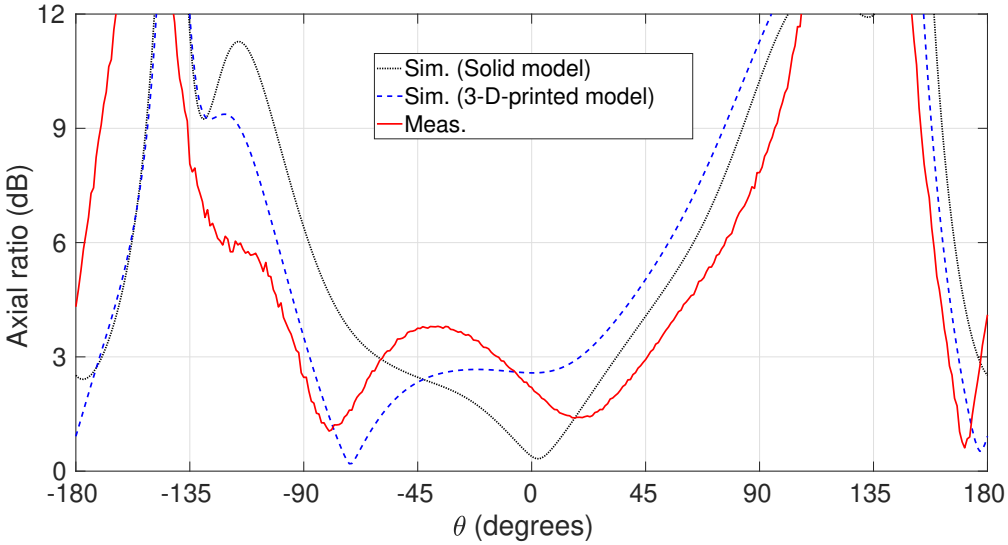

(a) AR vs. θ considering $\phi = 0°$.

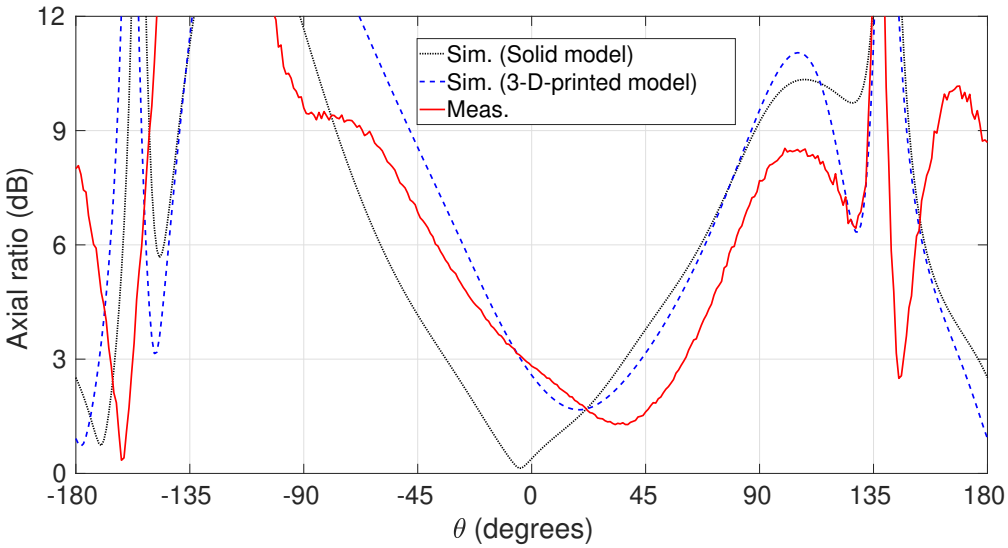

(b) AR vs. θ considering $\phi = 90°$.

Figure 4.10: Simulated axial ratios of the solid and 3-D-printed DRAs vs. θ, along with measured results at 2.47 GHz.

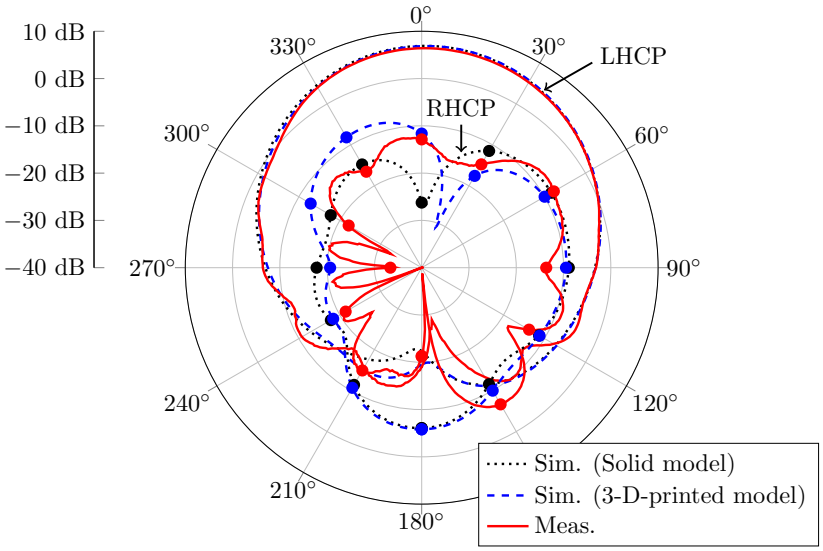

(a) Realized gain considering $\phi = 0°$.

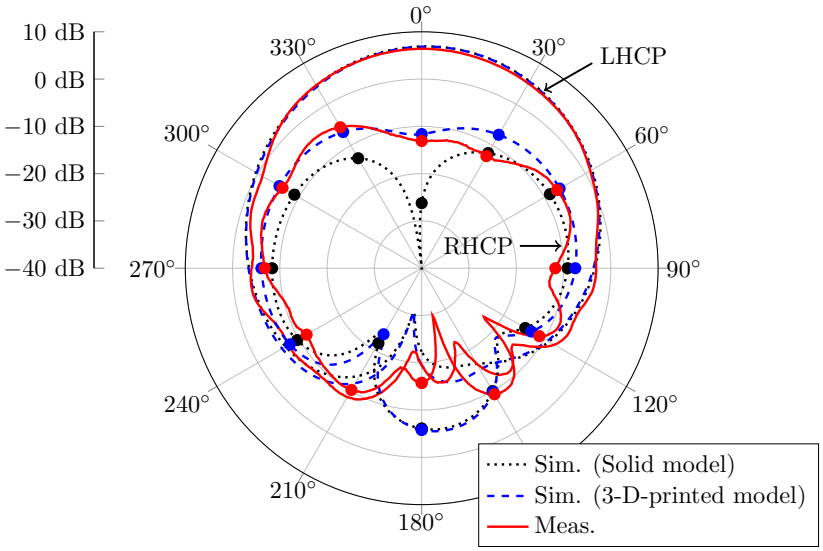

(b) Realized gain considering $\phi = 90°$.

Figure 4.11: Simulated realized gain of the solid and 3-D-printed DRAs, along with measured results at $f = 2.47$ GHz.

4.5 Conclusion

A single-fed DRA in circular polarization has been designed in the 2.45 GHz ISM band using a 3-D-printed uniaxial anisotropic dielectric ceramic material. Its principle of operation relies on the excitation of two orthogonal TE^{x}_{111} and TE^{y}_{111} modes which magnitudes and phase difference are tuned by modifying the anisotropy of the dielectric resonator instead of its shape.

A theoretical model to analyze the TE modes in an anisotropic dielectric resonator has also been presented, achieving good agreement with those obtained in simulations. It validates the use of the proposed theoretical model to calculate the dimensions and permittivity tensor of square-based DRAs in order to achieve circular polarization using a single feeding probe.

The anisotropic dielectric resonator has been manufactured by 3-D-printing of zirconia ceramic. More specifically, anisotropy is obtained by structuring the material during 3-D-printing. A good agreement is observed between simulated and measured results. It has been found that the 3-D-printed DRA prototype has a measured 10-dB impedance bandwidth of 16%, a 3-dB AR bandwidth of 2.4%, and a 6.4 dBi realized gain at 2.47 GHz.

It has been demonstrated that 3-D printed anisotropic dielectric resonators exhibit reliable and promising results to control the radiation characteristics, *i.e.*, polarization of DRAs, which open up interesting perspectives in the design of new dielectric-based antennas. This has been proved in this chapter by designing a single-fed uniaxial anisotropic DRA in circular polarization.

Finally, in the next chapter, the capabilities of additive manufacturing are exploited to design a compact anisotropic DRA with Huygens source properties. As novelty, this new Huygens source DRA takes advantage of the numerous degrees of freedom due to 3-D printing in order to reduce the size of the previous antennas presented in section 2.

Chapter 5

Novel Compact Huygens Source Antenna using an Anisotropic Dielectric Resonator

Sommaire

In Chapter 2, it has been shown that a single dielectric resonator with isotropic properties cannot satisfy the requirements in phase to achieve a Huygens source pattern with improved radiation properties along the $+z$-direction and low backward radiation. As an original solution, two Huygens source antennas made up of stacked dielectric resonators with isotropic permittivities have been designed in the $2.4 - 2.5$ GHz ISM band. The stacked configuration have been used to generate pairs of non-collocated electric and magnetic dipoles at nearby frequencies in each isotropic dielectric resonator in order to achieve a cardioid radiation pattern. However, the use of this configuration is limited due to its bulky size and the impossibility to obtain collocated dipoles. As a consequence, a lack of symmetry of their radiation patterns have been exhibited so that this type of antenna has been called 'Quasi Huygens source'.

It has also been demonstrated in Chapters 3 and 4 that the use of anisotropy is particularly interesting to study since a new degree of freedom for material properties can be used to control the radiation properties of dielectric resonator antennas. As an original solution, it

will be shown that a pair of collocated electric and magnetic dipoles can be generated in a single DRA with uniaxial anisotropic properties in order to achieve a Huygens source pattern.

In this chapter, the principle of operation of a linearly polarized Huygens source using an anisotropic dielectric resonator is presented. A compact Huygens source DRA is then designed in the 2.45 GHz ISM band using a uniaxial anisotropic dielectric material. In addition to that, the spherical mode analysis is performed in order to determine the modes which contribute to the radiation of the proposed antenna. Afterwards, the 3-D-printed Huygens source antenna is exhibited using engineered dielectric anisotropy within 3-D-printed ceramics. Finally, the simulated antenna performances are presented and discussed.

5.1 Principle of operation

As mentioned in Chapter 1 and 2, a Huygens source antenna relies on the combination of two elementary magnetic and electric dipoles radiating same field in their E- and H- planes [9] [22]. In order to obtain a cardioid radiation pattern in linear polarization, two orthogonal x-directed magnetic and y-directed electric dipoles must be combined with certain conditions of amplitude and phase between both sources. For this purpose, the fundamental TE^{x}_{111} and quasi-TM^{y}_{111} modes, this latter from both TE^{x}_{112} and TE^{z}_{211} modes, can be excited using a square-based dielectric resonator. However, these modes cannot resonate at frequencies close enough in a single rectangular dielectric resonator with isotropic properties, as demonstrated in Chapter 2.

As a solution, the use of 3-D printing is thus exploited in order to take advantage of a new degree of freedom for the dielectric properties, namely ε_{ry} in the permittivity tensor given in (5.1), using a uniaxial anisotropic dielectric resonator. In order to reduce the frequency difference between the two TE^{x}_{111} and quasi-TM^{y}_{111} modes, the following permittivity tensor is thus proposed

$$\varepsilon_r = \begin{bmatrix} \varepsilon_{rt} & 0 & 0 \\ 0 & \varepsilon_{ry} & 0 \\ 0 & 0 & \varepsilon_{rt} \end{bmatrix} \tag{5.1}$$

where the optical axis of the anisotropic medium is here placed along the y-direction. As expected, the TE^{y}_{111} mode remains as an isotropic dielectric since the y-component of the electric field vanishes ($E_y = 0$), and the dielectric constants along the x- and z-directions are both equal to ε_{rt}. On the contrary, the TE^{x}_{111}, TE^{x}_{112}, and TE^{z}_{211} modes are altered by the anisotropic properties of the dielectric resonator. This tensor is thus selected so that the resonance frequencies between these modes can be reduced, and therefore, the phase difference can be accomplished at 2.45 GHz to realize a Huygens source pattern.

5.2 Antenna design

In this section, a Huygens source antenna is designed in the $f_0 = 2.45$ GHz ISM band. It has been shown in Chapter 2 the impossibility to obtain a Huygens source pattern using a single dielectric resonator with isotropic properties. In fact, the frequency difference between both TE^x_{111} and quasi-TM^y_{111} modes cannot be reduced enough, as shown in Fig. 2.4, so that the required conditions in amplitude and phase may not be satisfied in order to achieve a cardioid radiation pattern.

An original solution to reduce the frequency difference between the two required TE^x_{111} and quasi-TM^y_{111} modes relies on the use of a uniaxial anisotropic dielectric resonator, considering the aforementioned DRA dimensions, namely $a = d = 39.4$ mm, $b = 19.6$ mm, and $\varepsilon_{rt} = 13$. It is shown in Fig. 5.1a, that the use of anisotropy, more specifically the increase of ε_{ry} reduces the frequency difference between both TE^x_{111} and quasi-TM^y_{111} modes. For instance, $\Delta_f = 270$ MHz is obtained for $\varepsilon_{ry} = 21$, as also reported in Table 5.1. This result represents a reduction of 180 MHz with respect to the single isotropic dielectric resonator with $\varepsilon_r = 13$, studied in Chapter 2. In addition to that, it is show in Fig 5.1b that the maximum F/B ratio can be achieved at 2.45 GHz using a uniaxial anisotropic dielectric with permittivity values of $\varepsilon_{ry} = 21$ and $\varepsilon_{rt} = 13$.

	TE^y_{111}	TE^x_{111} TE^z_{111}	TE^y_{112} TE^y_{211}	TE^z_{211} TE^x_{112}
Resonance frequency (GHz)	1.96	2.34	-	2.61

Table 5.1: Resonant modes in a uniaxial anisotropic DR using eigen mode analysis, when $a = d = 39.4$ mm, $b = 19.6$ mm, $\varepsilon_{ry} = 21$, and $\varepsilon_{rt} = 13$.

Fig. 5.2 shows the exploded view of the solid uniaxial anisotropic Huygens source DRA. It consists of a uniaxial anisotropic dielectric resonator, a thin dielectric layer, a quarter-wavelength sleeve, and a semi-rigid coax probe. The dielectric layer is Rogers RO3003 [150], with thickness of 0.75 mm, and electrical properties of $\varepsilon_r = 3.0$ and $\tan\delta = 0.001$. This dielectric layer is used to allow the antenna to have a mechanical support without affecting its far-field response.

In order to excite the required modes, the resonator is fed using a 50 Ω coaxial probe. The TE^x_{111}, TE^x_{112} and TE^z_{211} modes can be excited using a single coaxial probe located on the edge of the DR, more specifically on the y axis. The selected probe is a semi-rigid coaxial cable RG405 [151], which inner conductor is extended by a length of $l_p = 13.7$ mm. In addition to this, the probe is supported by a small square metallic surface with dimensions $l_m = 6$ mm printed at the bottom of the dielectric layer.

Finally, a quarter-wavelength sleeve is placed along the semi-rigid coaxial cable to obtain a balanced current and reduce the current flowing on the outer conductor of the probe. This structure is used to reduce the effect of the coaxial cable on the radiation of the antenna. The configuration of the selected quarter-wavelength sleeve is detailed in [152]. Note that a classical balun can also be used [21, 153].

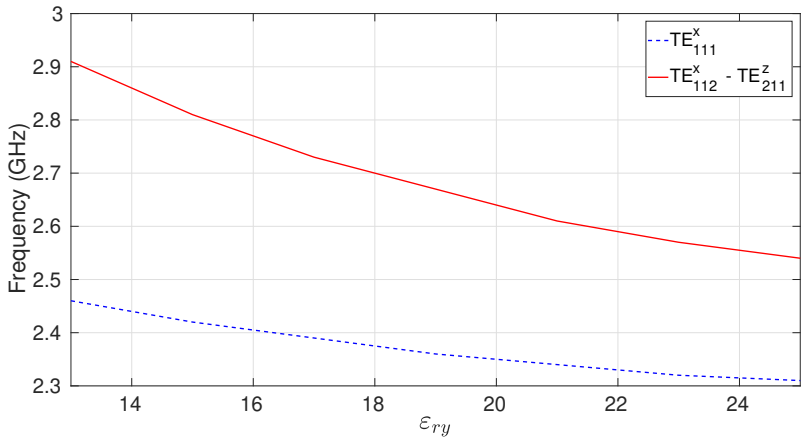

(a) Variation of the frequencies of resonant modes as a function of ε_{ry}, when $a = d = 39.4$ mm, $b = 19.6$ mm, and $\varepsilon_{rt} = 13$.

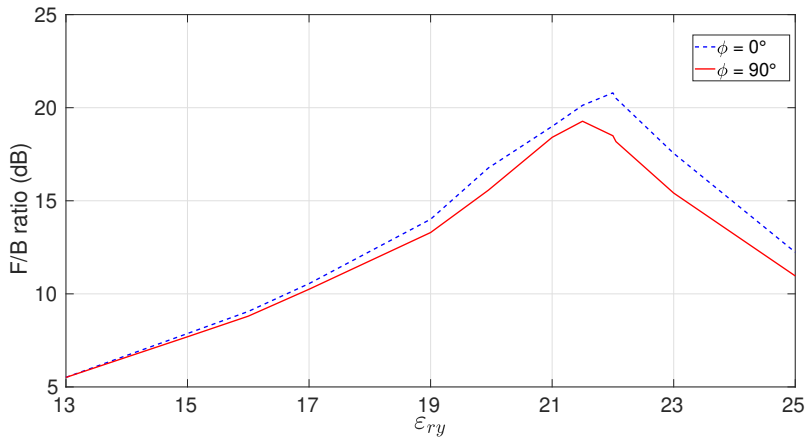

(b) Variation of the F/B ratio as a function of ε_{ry}, when $a = d = 39.4$ mm, $b = 19.6$ mm, and $\varepsilon_{rt} = 13$.

Figure 5.1: Impact of ε_{ry} on the frequencies of resonant modes and F/B ratio of the antenna at 2.45 GHz.

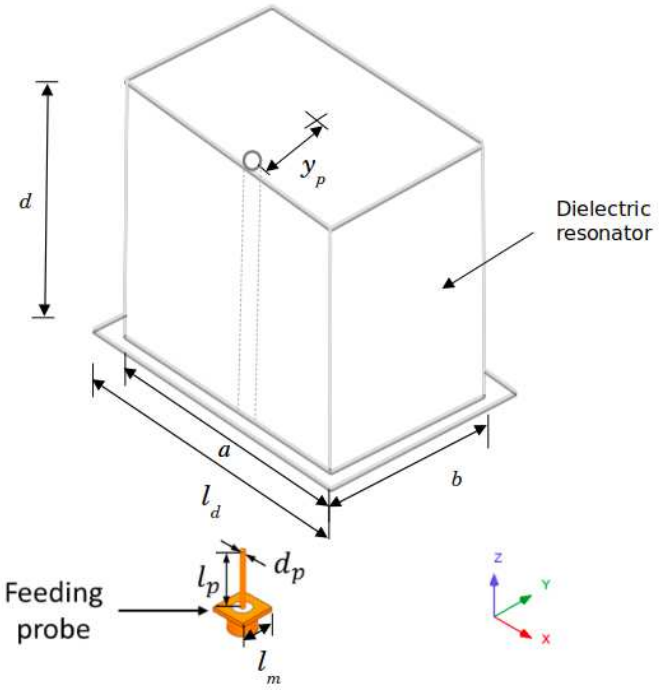

Figure 5.2: Exploded view of the solid uniaxial anisotropic Huygens source DRA ($a = d =$ 39.4 mm, $b = 19.6$ mm, $l_d = 23$ mm, $l_p = 13.7$ mm, $d_p = 0.51$ mm, $l_m = 6$ mm, and $y_p = 8.7$ mm).

5.3 Simulated results

Fig. 5.3 and 5.4 show the simulated reflection coefficient and the front-to-back ratio of the proposed Huygens source DRA, respectively. It has an impedance bandwidth of 10.6% from 2.28 GHz to 2.54 GHz, for a reflection coefficient of $|S_{11}| \leq -10$ dB. Moreover, the proposed DRA has a F/B ratio of 18.47 dB and 17.64 dB at 2.45 GHz, considering $\phi = 0°$ and 90°, respectively. The F/B ratio bandwidth (F/B ratio $\geq$ 15 dB) is 2.9%, from 2.42 GHz to 2.49 GHz.

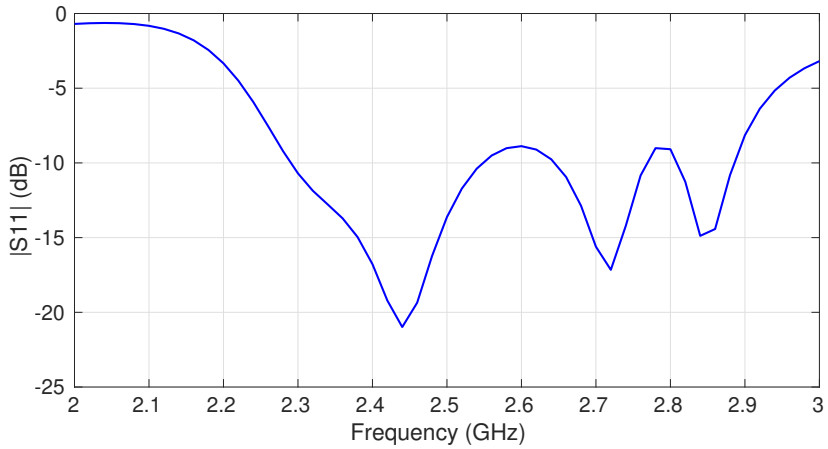

Figure 5.3: Simulated reflection coefficient of the compact Huygens source DRA.

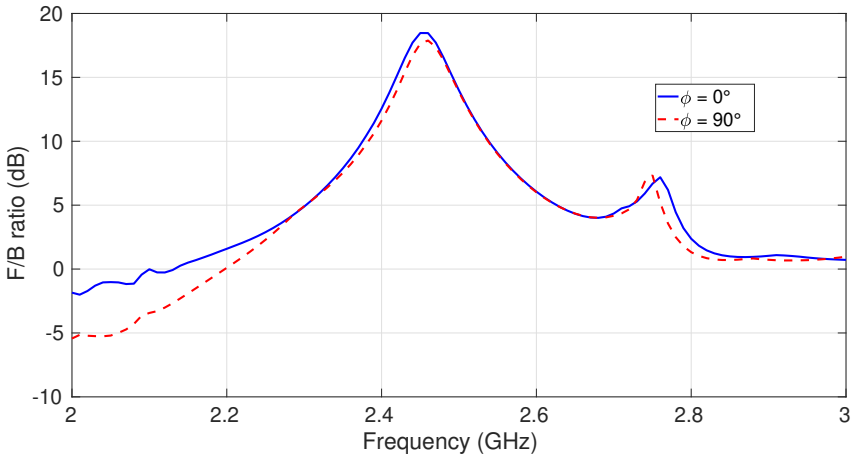

Figure 5.4: F/B ratio of the compact Huygens source DRA, considering $\phi = 0°$ and 90°.

Fig. 5.5 depicts the simulated total antenna gain, and the simulated Co-pol. and X-pol. realized gain patterns of the 3-D-printed Huygens source at 2.45 GHz, considering $\phi = 0°$ and 90°, respectively. Note that the proposed antenna radiates with symmetric cardioid radiation patterns in the E- and H-planes. Besides, the simulated realized gain at boresight is 5.75 dBi at 2.45 GHz.

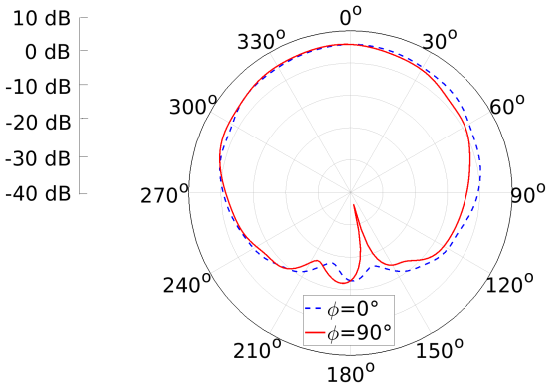

(a) Total gain considering $\phi = 0°$ and 90°.

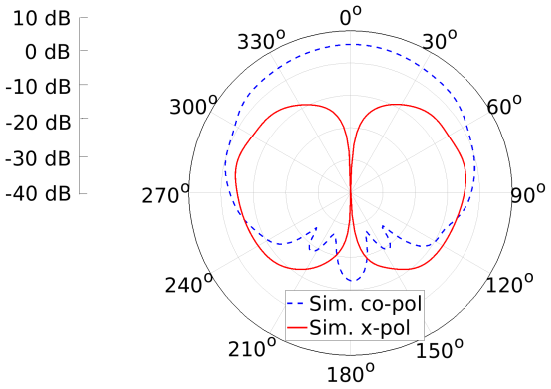

(b) Co-pol. and X-pol. gain considering $\phi = 0°$.

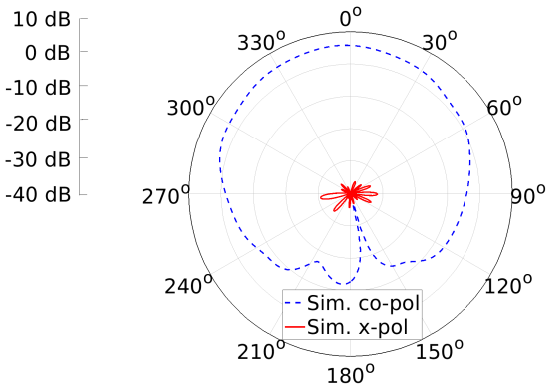

(c) Co-pol. and X-pol. gain considering $\phi = 90°$.

Figure 5.5: Simulated gain of the compact Huygens source DRA at 2.45 GHz.

In the next section, the spherical mode analysis is performed in order to determine the modes contributing to the radiation of the Huygens source antenna. For this purpose, the coefficients of the fundamental and higher-order modes modes are calculated using FEKO.

5.4 Spherical mode analysis of the proposed DRA

In order to analyze the spherical mode expansion of the proposed antenna, simulations in FEKO are performed placing the origin of the coordinate system at the centre of the DRA. Fig. 5.6 shows the relative power of spherical modes as a function of the frequency for the proposed DRA shown in Fig 5.2. Here, the relative power of $\mathrm{TE}^{sph}_{|\pm 1|1}$ corresponds to the sum of the TE^{sph}_{11} and TE^{sph}_{-11} modes because their values are symmetrical regardless the frequency. The same procedure is performed for the $\mathrm{TE}^{sph}_{|\pm 1|2}$, $\mathrm{TM}^{sph}_{|\pm 1|1}$, and $\mathrm{TM}^{sph}_{|\pm 2|1}$ modes. Note that the amplitude of the fundamental TE^{sph} and TM^{sph} modes matches at 2.45 GHz with a value of 36.2%. Fig. 5.7 shows the phase difference between the TE^{sph}_{11} and TM^{sph}_{11} modes. As observed, the fundamental TE and TM modes are of about 188° out of phase at 2.45 GHz, reasonable value to achieve a Huygens source pattern.

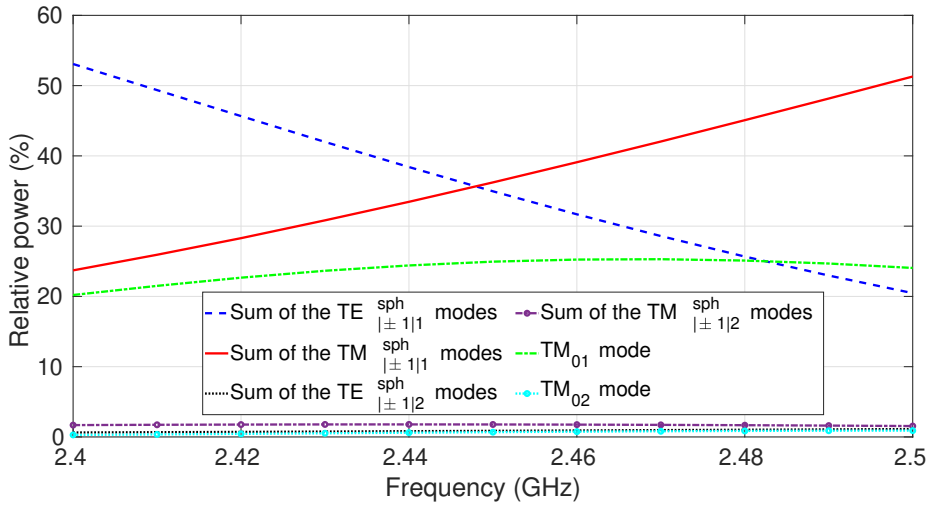

Figure 5.6: Relative power of the spherical mode expansion.

On the other hand, the TM^{sph}_{01} mode radiate with a relative power of about 24.4%. The radiation of this spherical mode is due to the coaxial probe located along the z-direction. In addition to that, this mode is the main responsible of the cross-polarization of the proposed Huygens source antenna, as shown in Fig. 5.5b. In order to understand the impact on the coaxial probe on the cross-polarization gain, the spherical mode expansion is now performed on the proposed Huygens source using two symmetrical probes 180° out of phase, placed on the y axis, as shown in Fig. 5.8.

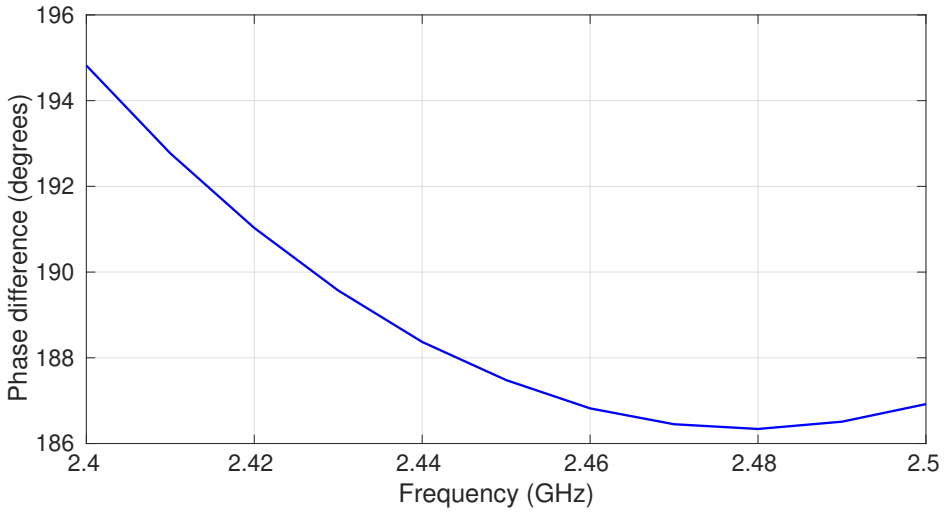

Figure 5.7: Phase difference between the fundamental TE_{11}^{sph} and TM_{11}^{sph} modes.

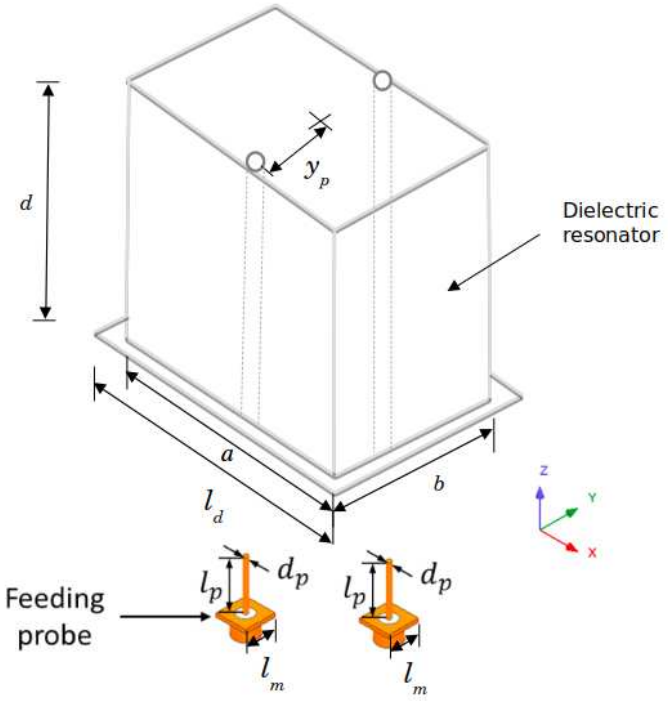

Figure 5.8: Exploded view of the solid uniaxial anisotropic Huygens source DRA with two symmetric coaxial probes ($a = d = 39.4$ mm, $b = 19.6$ mm, $l_d = 23$ mm, $l_p = 13.7$ mm, $d_p = 0.51$ mm, $l_m = 6$ mm, and $y_p = 8.7$ mm).

Fig. 5.9 shows the relative power of the spherical modes of the proposed antenna using the two symmetrical coaxial probes. As observed, the TM_{01}^{sph} mode does not radiate anymore. Furthermore, the $TE_{|\pm1|1}^{sph}$ and $TM_{|\pm1|1}^{sph}$ coefficients radiate with identical amplitudes at

2.45 GHz. The phase difference between both fundamental TE_{11}^{sph} and TM_{11}^{sph} modes is 180°, so that it satisfies the requirements to achieve a Huygens source pattern, as depicted in Fig. 5.10.

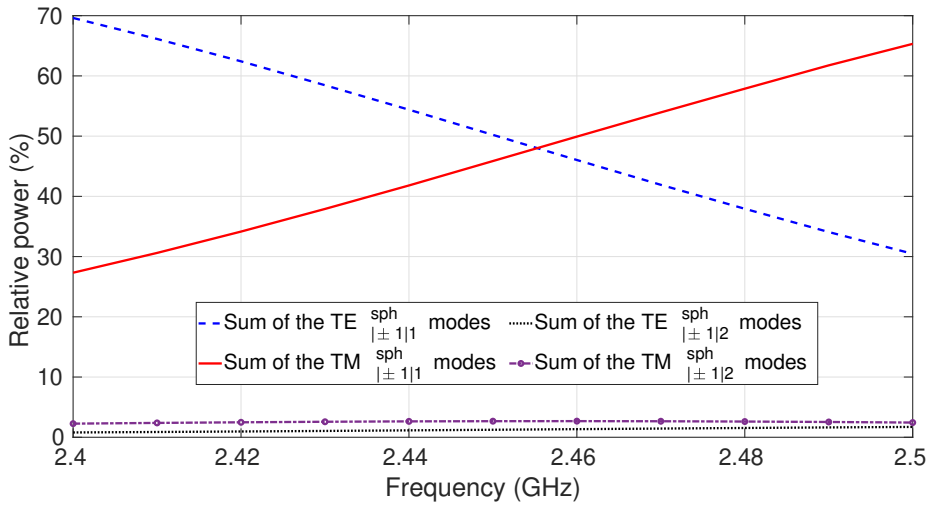

Figure 5.9: Relative power of the spherical mode expansion using two symmetric sources.

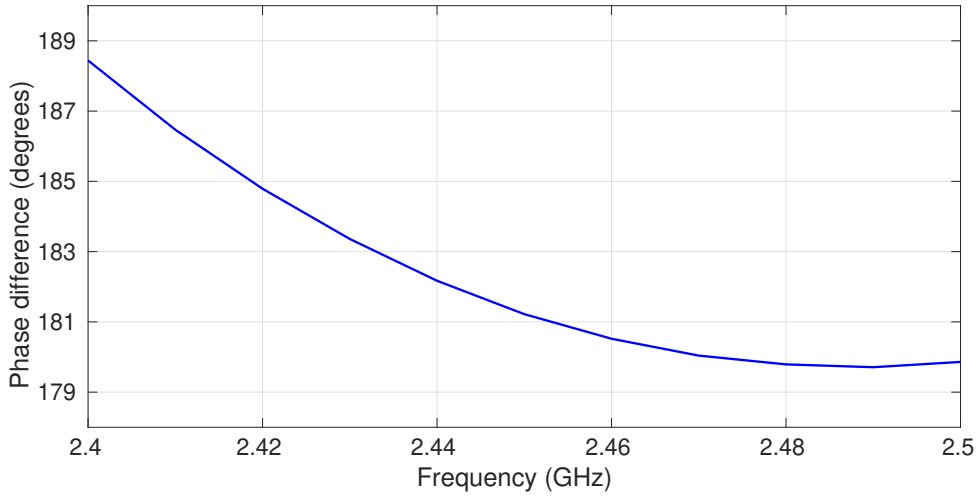

Figure 5.10: Phase difference between fundamental TE_{11}^{sph} and TM_{11}^{sph} modes using two symmetric sources.

As an illustration, Fig. 5.11 depicts the simulated Co-pol. and X-pol. realized gain patterns of the 3-D-printed Huygens source using two symmetrical sources at 2.45 GHz. As observed, the cross-polarization component is lower than -40 dB. This result shows that the use of a single coaxial probe has an important impact on the cross-polarization gain of the proposed antenna.

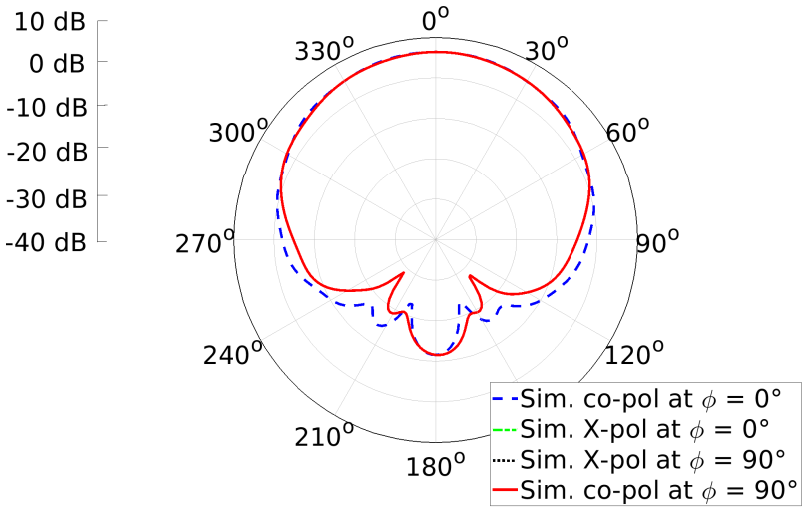

Figure 5.11: Co-pol. and X-pol. gain of the proposed antenna using two symmetrical feeding probes, considering $\phi = 0°$ and 90°.

5.5 3-D-printed Huygens source DRA

5.5.1 Unit cell for uniaxial anisotropy

In order to manufacture a dielectric resonator exhibiting the effective permittivity tensor as in (5.1) with $\varepsilon_{rt} = 13$ and $\varepsilon_{ry} = 21$, the same approach that has been presented in Chapters 3 and 4 is here used. Thus, a periodic structure made up of several identical asymmetric sub-wavelength unit cells is here presented. The proposed unit cell is described in Fig. 5.12a. It is similar to the previous unit cell but the optical axis is here placed at y axis. It leads to the same effective dielectric constant ε_{rt} along the x- and z-directions. Assuming $a_{uc} = 3.50$ mm, both ε_{ry} and ε_{rt} can be controlled by changing the air-filling ratio of the unit cell through the parameters ℓ_{uc}, w_{uc}, and e_{uc}.

Fig. 5.12b shows, for instance, the extracted dielectric constants considering $a_{uc} = 3.50$ mm, $l_{uc} = 2.80$ mm, $e_{uc} = 0.35$ mm, and w_{uc} varying between 0.50 and 1.70 mm. As observed, ε_{ry} can be tuned between 14.53 and 25.0, whereas ε_{rt} varies between 9.3 and 15.8 at the same time. Finally, the optimized dimensions are $a_{uc} = 3.50$ mm, $l_{uc} = 2.80$ mm, $e_{uc} = 0.35$ mm, and $w_{uc} = 0.86$ mm so that $\varepsilon_{ry} = 21$ and $\varepsilon_{rt} = 13$. Note that, the unit cell size a_{uc} remains smaller than one eighth of the wavelength in the dielectric at 2.45 GHz for the largest value of the permittivity tensor, namely $\epsilon_{ry} = 21$.

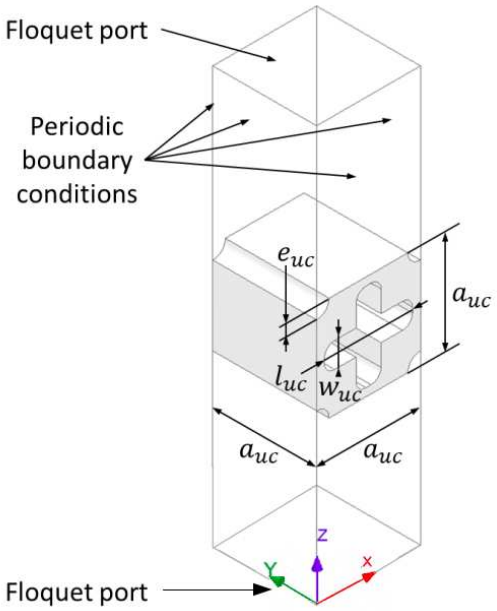

(a) 3-D-printed uniaxial anisotropic unit cell.

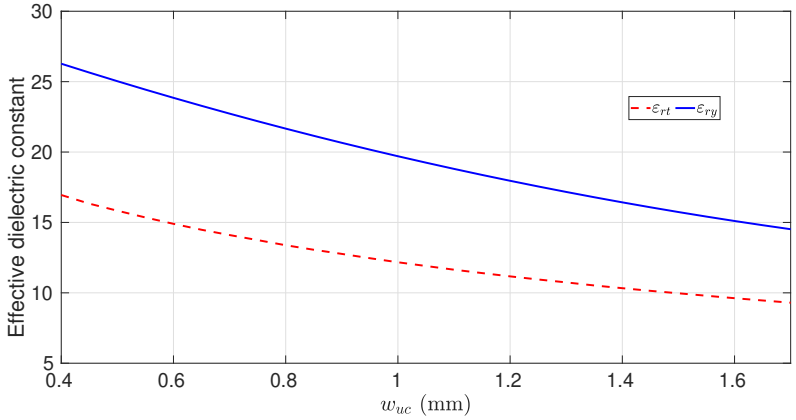

(b) Example of simulated effective permittivity tensor for this unit cell as a function of the dimensions w_{uc} at 2.45 GHz ($a_{uc} = 3.50$ mm, $l_{uc} = 2.80$ mm, and $e_{uc} = 0.35$ mm).

Figure 5.12: Design of the proposed 3-D-printed uniaxial anisotropic unit cell with its simulated effective permittivity tensor as a function of w_{uc}.

5.5.2 Antenna optimization

Fig. 5.13 shows the simulated reflection coefficients of the solid and 3-D-printed model using the aforementioned dimensions. It is possible to notice a frequency shift produced while using the 3-D-printed model. This frequency shift is more specifically produced by the variation of

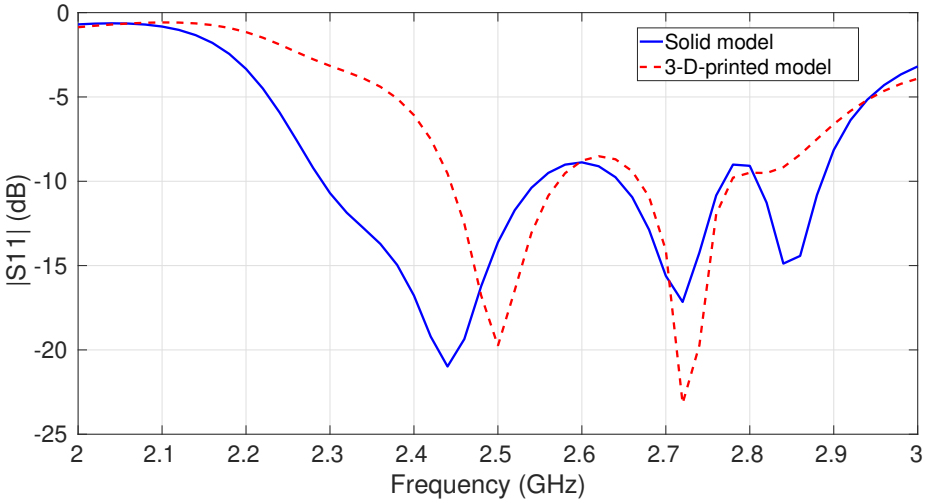

Figure 5.13: Simulated reflection coefficients of the solid and 3-D-printed model Huygens source DRA.

two permittivities, air and zirconia, along the longitudinal z axis. Consequently, the coupling between the dielectric resonator and feeding probe is affected, producing a slight frequency shift of about 50 MHz and an antenna mismatch. This problem will be partially solved later, in section 5.6, by adding a dielectric wall of zirconia around the probe in order to reduce the sensitivity of the feeding probe in the antenna performances.

In order to tune the antenna in the 2.45 GHz ISM band, it is thus optimized directly on the 3-D-printed model. For this purpose, a parametric analysis is performed on the antenna dimensions in order to tune the antenna at $f_0 = 2.45$ GHz by fixing the square dimensions $a = d$. As a result, $b = 19$ mm is found. Fig. 5.14 depicts the 3-D-printed Huygens source antenna. The optimized dimensions of the realized 3-D-printed Huygens source are $a = d = 39.4$ mm and $b = 19$ mm, $l_d = 23.8$ mm, $l_p = 15.3$ mm, $l_m = 7$ mm, and $y_p = 8.4$ mm. The electrical size of the dielectric resonator is finally $0.32\lambda_0 \times 0.32\lambda_0 \times 0.16\lambda_0$.

5.5.3 Simulated results

Fig. 5.15 and Fig. 5.16 show the simulated reflection coefficient and the simulated front-to-back ratio of the 3-D-printed Huygens source antenna, respectively. As a result, it has an impedance bandwidth of 20% from 2.38 GHz to 2.87 GHz, for a reflection coefficient of $|S_{11}| \leq -10$ dB. Furthermore, the 3-D-printed DRA has a maximum F/B ratio of 20.4 dB and 22.0 dB at 2.45 GHz, considering $\phi = 0°$ and $90°$, respectively. The difference in the maximum F/B ratio in the E- and H-planes relies on the fact that the backward radiation is taken from the maximum gain value found in the range of $160° \leq \theta \leq 200°$. The proposed antenna also achieves a F/B ratio bandwidth (F/B ratio ≥ 15 dB) of 4.1%, from 2.40 GHz to 2.50 GHz.

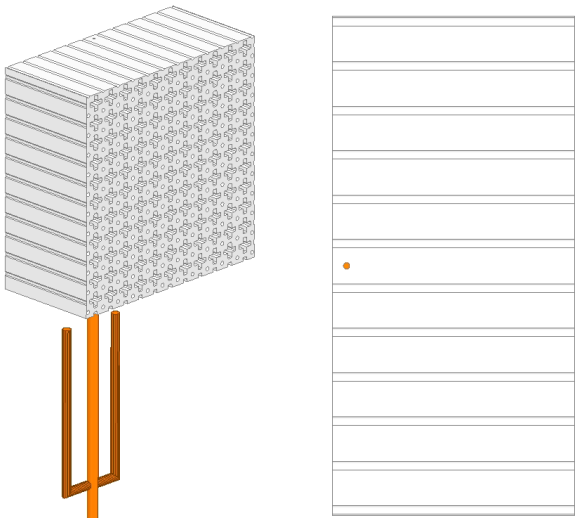

(a) Isometric view. (b) Side view.

Figure 5.14: 3-D-printed uniaxial anisotropic Huygens source DRA.

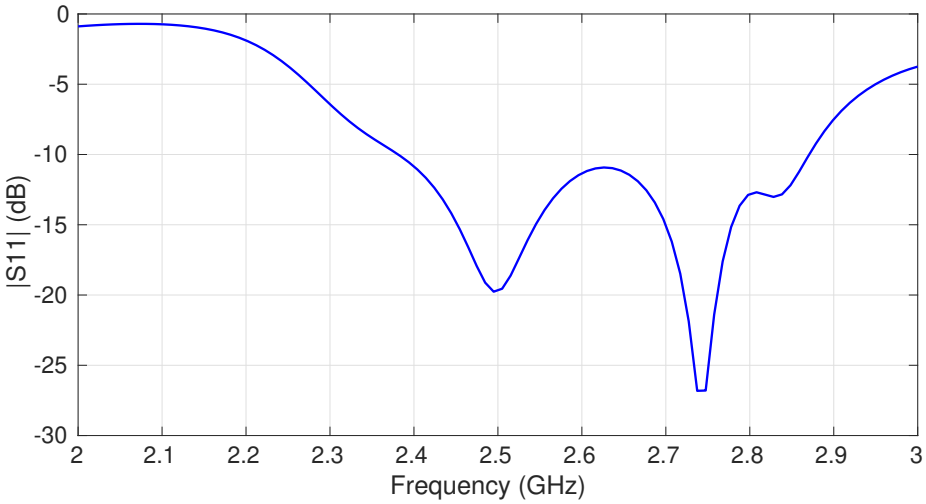

Figure 5.15: Simulated reflection coefficient of the 3-D-printed Huygens source DRA.

Fig. 5.17 shows the simulated total antenna gain, and the simulated Co-pol. and X-pol. realized gain patterns of the 3-D-printed Huygens source at 2.45 GHz, considering $\phi = 0°$ and 90°, respectively. Observe that the 3-D-printed DRA radiates with Huygens source properties. It has a realized gain at boresight of 4.77 dBi at 2.45 GHz. Furthermore, both resulting E- and H-planes of the radiation patterns are here symmetric. This is an important result of this Ph.D. thesis since it is demonstrated that the proper amplitude balance and phase difference between both fundamental TE^{x}_{111} and quasi-TM^{y}_{111} modes in a single dielectric resonator can be achieved using anisotropic dielectric materials within 3-D printing. On the other hand, it has been demonstrated that the existence of the cross-polarization gain at $\phi = 0°$ relies on

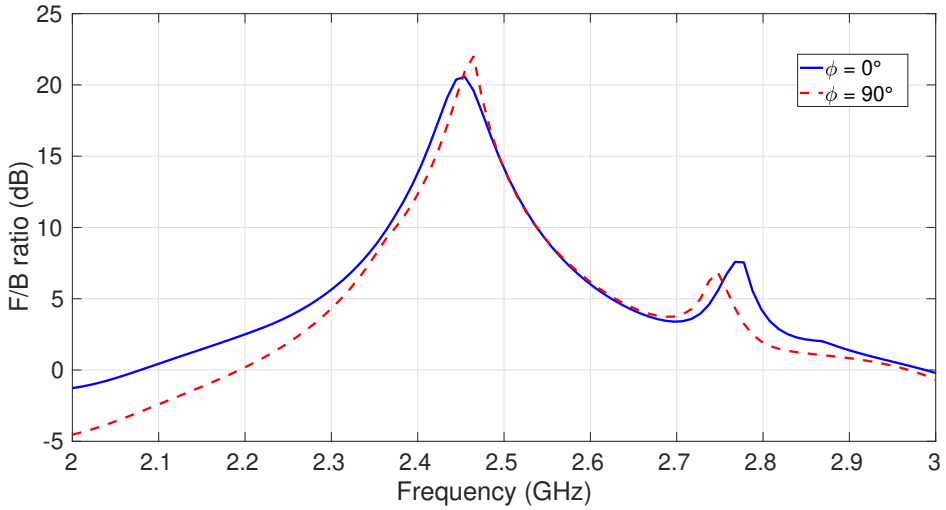

Figure 5.16: F/B ratio of the 3-D-printed Huygens source DRA, considering $\phi = 0°$ and 90°.

the radiation of the spherical TM_{01}^{sph} mode due to the use of a single feeding probe, whereas the X-pol. gain at $\phi = 90°$ is lower than -40 dB.

It has been shown that the proposed Huygens source DRA is very sensitive to the longitudinal variation of the permittivity along the coaxial probe, as shown in Fig. 5.13. For that reason, in the next section, a new Huygens source DRA is designed by adding a cylindrical dielectric wall of zirconia around the probe in order to reduce the impact of the feeding probe on the antenna performances.

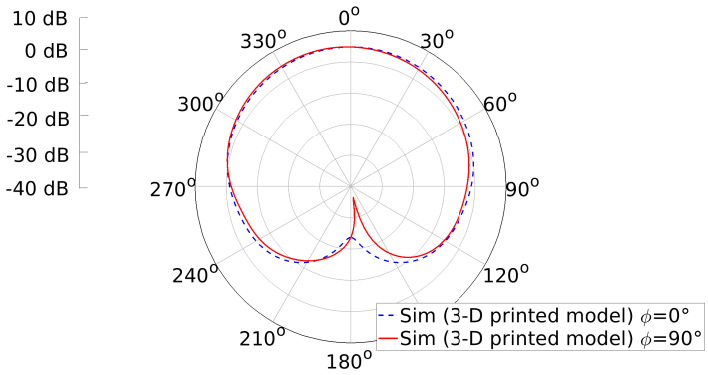

(a) Total gain considering $\phi = 0°$ and 90°.

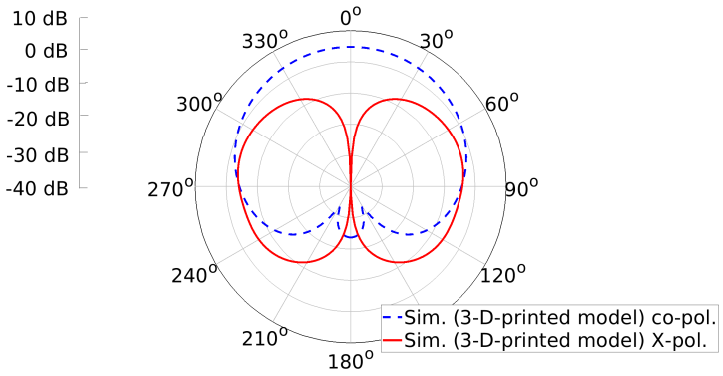

(b) Co-pol. and X-pol. gain considering $\phi = 0°$.

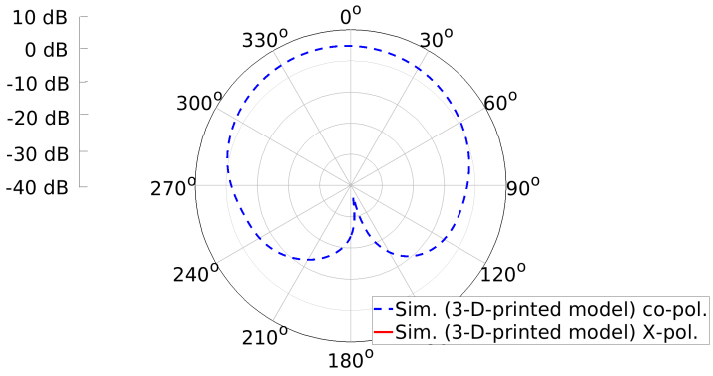

(c) Co-pol. and X-pol. gain considering $\phi = 90°$.

Figure 5.17: Simulated gain of the 3-D-printed Huygens source DRA at 2.45 GHz.

5.6 3-D-printed Huygens source DRA with a wall around the probe

5.6.1 Antenna design

A Huygens source DRA is then designed considering a cylindrical dielectric wall made up of zirconia ($\varepsilon_r = 32.5$), as depicted in Fig. 5.18. The solid dielectric wall around the coaxial probe has 0.5 mm thickness for mechanical reasons. For this purpose, the DRA is first optimized on the solid model using the aforementioned permittivity tensor. As a result, the dimensions of the optimized antenna are $a = d = 40.5$ mm, $b = 19.6$ mm, $l_p = 17.3$ mm, and $l_m = 7$ mm.

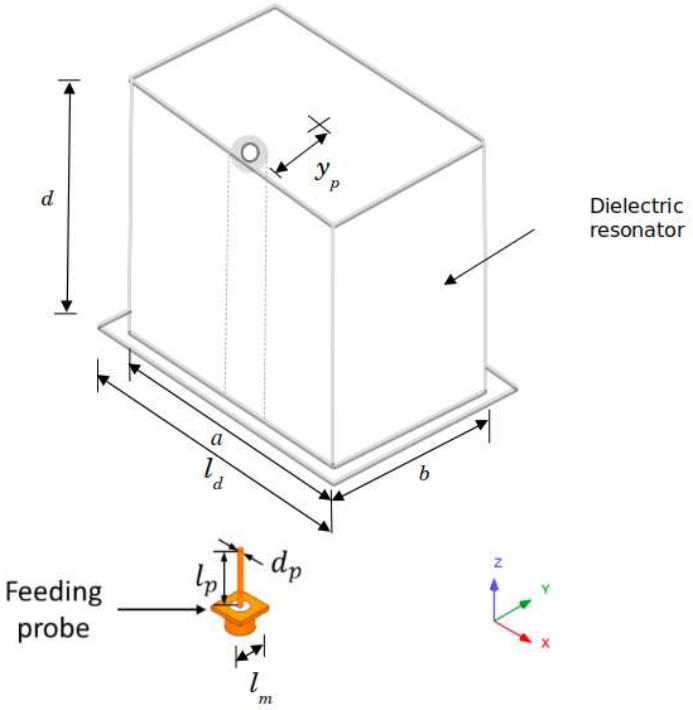

Figure 5.18: Exploded view of the solid uniaxial anisotropic Huygens source DRA with a solid dielectric wall around the probe ($a = d = 40.5$ mm, $b = 19.6$ mm, $l_d = 24.4$ mm, $l_p = 17.3$ mm, $d_p = 0.51$ mm, $l_m = 7$ mm, and $y_p = 8.7$ mm).

Afterwards, the DRA is simulated using the periodized structure of several unit cells, presented in Fig. 5.12, to compare its performances with those obtained using the solid model. As observed in Fig. 5.19, the frequency shift between both solid and 3-D-printed model is reduced while taking into account the dielectric wall around the feeding probe. Besides, both solid and 3-D-printed models remain similar in terms of reflection coefficient and impedance bandwidth.

In order to tune the antenna in the 2.45 GHz ISM band, it is also optimized directly

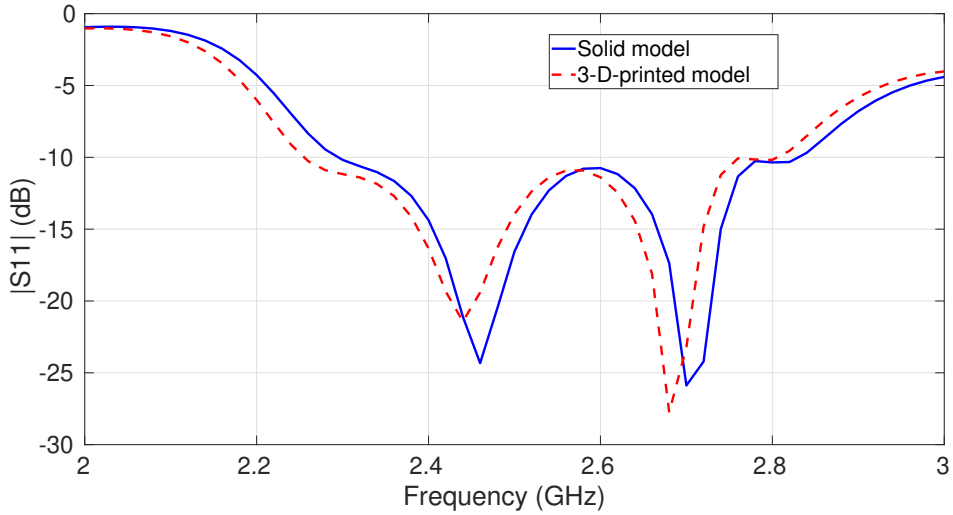

Figure 5.19: Simulated reflection coefficients of the solid and 3-D-printed model Huygens source DRA with a solid dielectric wall around the probe.

on the 3-D-printed model. The optimized dimensions of the realized 3-D-printed Huygens source are $a = d = 39.6$ mm and $b = 19.2$ mm, $l_d = 23$ mm, $l_p = 17.6$ mm, $l_m = 6$ mm, and $y_p = 8.5$ mm. The electrical properties of the dielectric resonator are finally $0.32\lambda_0 \times 0.32\lambda_0 \times 0.16\lambda_0$.

5.6.2 Simulated results

Fig. 5.20 and 5.21 illustrate the simulated reflection coefficient and front-to-back ratio of the 3-D-printed antenna, respectively. As observed, it has an impedance bandwidth of 11.4% from 2.25 GHz to 2.53 GHz, for a reflection coefficient of $|S_{11}| \leq -10$ dB. Furthermore, the 3-D-printed Huygens source DRA achieves a maximum F/B ratio of 17.3 dB and 18.2 dB, considering $\phi = 0°$ and 90°, respectively, at 2.45 GHz. It has a F/B ratio bandwidth (F/B ratio ≥ 15 dB) of 2.9%, from 2.41 GHz to 2.48 GHz.

Fig. 5.22 shows the simulated total antenna gain, and the Co-pol. and X-pol. realized gain patterns of the 3-D-printed Huygens source at 2.45 GHz, considering $\phi = 0°$ and 90°, respectively. The radiation pattern corresponds to a Huygens source with low backward radiation and symmetric E- and H-planes. Besides, it has a maximum gain at boresight of 4.87 dBi at 2.45 GHz. The X-pol. gain at $\phi = 90°$ is lower than -40 dB.

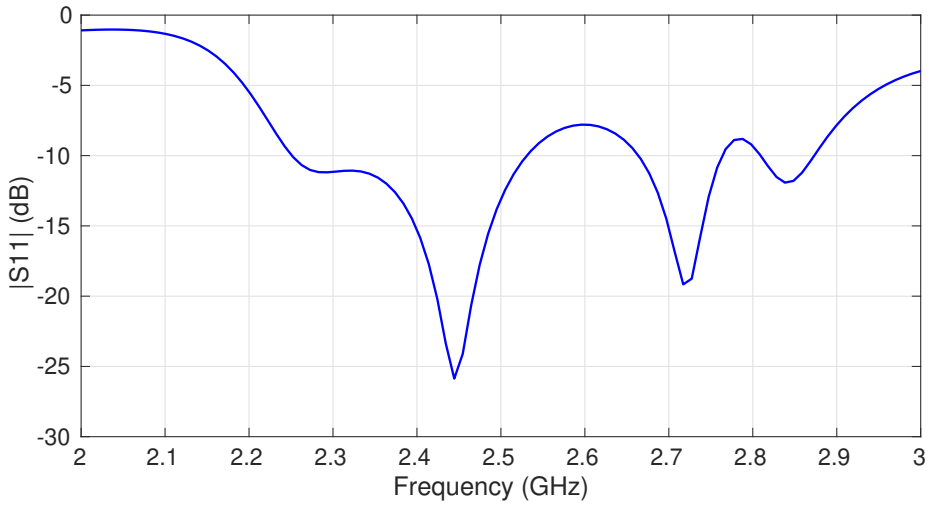

Figure 5.20: Simulated reflection coefficients of the 3-D-printed Huygens source DRA with a solid dielectric wall around the probe.

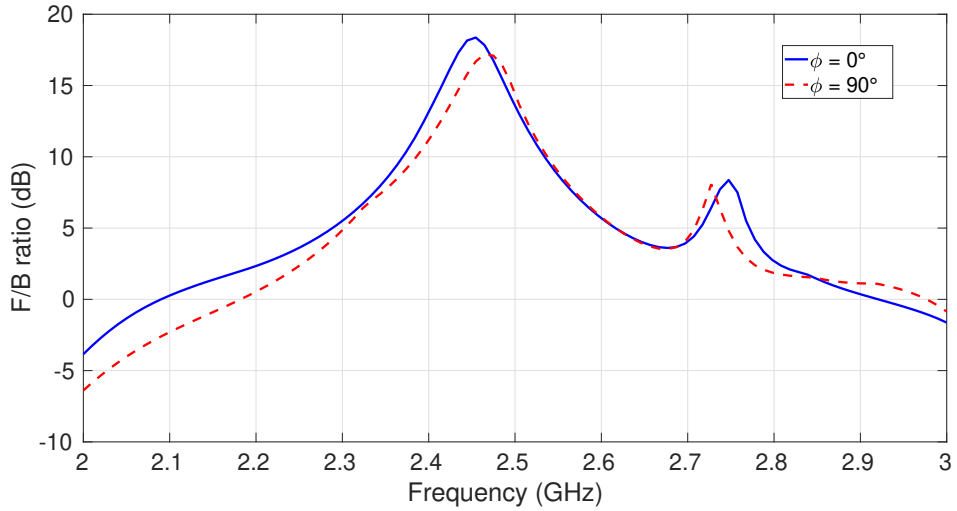

Figure 5.21: Simulated F/B ratio of the 3-D-printed Huygens source DRA with a solid dielectric wall around the probe, considering $\phi = 0°$ and $90°$.

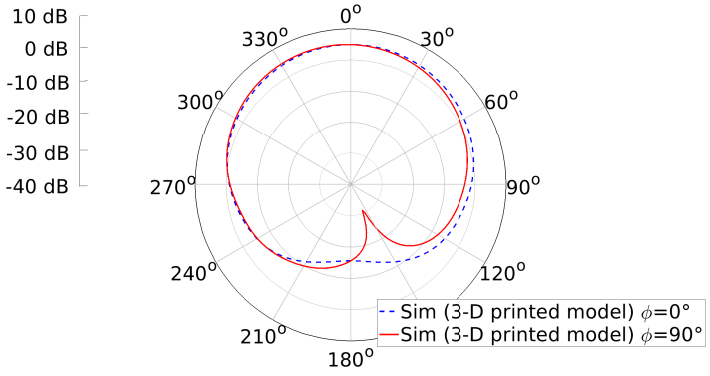

(a) Total gain considering $\phi = 0°$ and 90°.

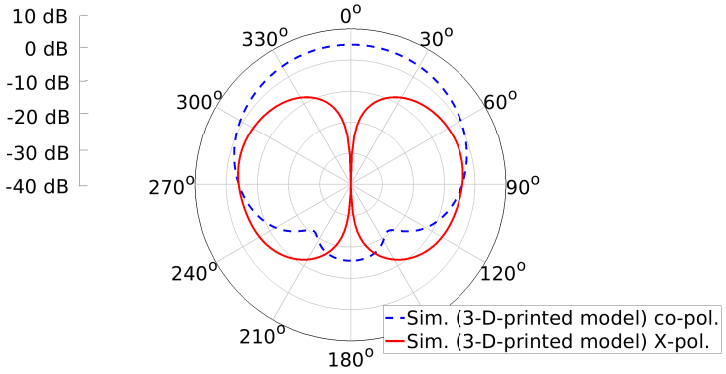

(b) Co-pol. and X-pol. gain considering $\phi = 0°$.

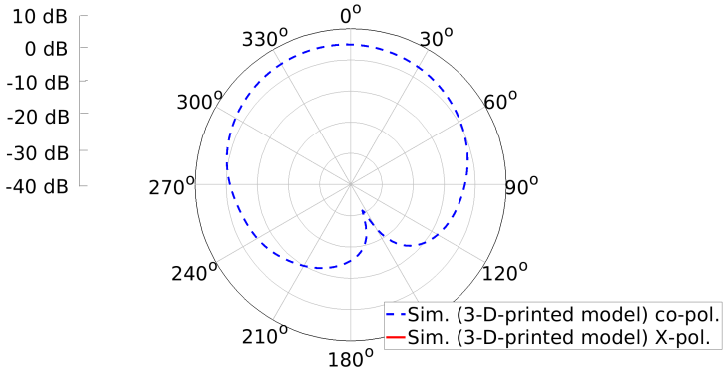

(c) Co-pol. and X-pol. gain considering $\phi = 90°$.

Figure 5.22: Simulated gain of the 3-D-printed Huygens source DRA with a solid dielectric wall around the probe at 2.45 GHz.

Comparing the proposed 3-D-printed Huygens source DRA, it is possible to affirm that the antenna with the solid dielectric wall around the coaxial probe also achieves a Huygens source pattern. However, the F/B ratio bandwidth is slightly lower than that obtained using the 3-D-printed DRA without wall.

5.7 Conclusion

A compact anisotropic dielectric resonator antenna has been designed to achieve a cardioid radiation pattern in linear polarization at the 2.45 GHz ISM band. It relies on the combination of two collocated equivalent electric and magnetic dipoles generated by a dielectric resonator with uniaxial anisotropic properties.

The use of additive manufacturing has been exploited to take advantage of their numerous degrees of freedom in DRA design to control its radiation pattern. More specifically, 3-D printed has been used to reduce the frequency difference between both fundamental TE^{x}_{111} and quasi-TM^{y}_{111} modes in order to generate two collocated and orthogonal electric and magnetic dipoles, radiating with certain conditions in phase and difference to achieve symmetric cardioid radiation patterns in the E- and H-planes, without the use of ground planes or reflectors.

It has been demonstrated that the proposed Huygens source antenna made up of a uniaxial anisotropic dielectric resonator exhibits interesting results in terms of compact size and radiation symmetry while compared with the isotropic DRA formed by two stacked resonators, presented in Chapter 2. The anisotropic DRA with Huygens source properties has an overall height of $0.32\lambda_0$, which represents a reduction in the antenna height of about 16.2% while compared with the stacked DRA. In addition to that, an impedance and F/B ratio enhancement of 1.9% and 2%, respectively, have been achieved in comparison with the stacked DRA.

The possibilities of the 3-D printing has also been studied to determine the impact of a solid wall located around the coaxial probe on the antenna performances. The 3-D-printed Huygens source DRA has achieved maximum front-to-back ratios of 22.0 dB and 17.3 dB, without and with a solid dielectric wall around the coaxial probe, respectively. Similarly, F/B ratio bandwidths (F/B ratio $\geq$ 15 dB) of 4.1% and 2.9% has been accomplished without and with the solid wall, respectively.

The expansion of spherical modes has been analyzed to identify the modes that radiates in the uniaxial anisotropic DRA. It has been demonstrated that the fundamental $\mathrm{TE}^{sph}_{|m|1}$ and $\mathrm{TM}^{sph}_{|m|1}$ modes are the main contributors to the radiation of a cardioid radiation pattern with symmetric planes at $\phi = 0°$ and 90°, *i.e.*, Huygens source patterns.

Conclusion and perspectives

Conclusion

Small and compact Huygens source antennas with a radiation pattern oriented along the $+z$-direction represent an interesting solution to overcome the mechanical and radiation constraints for UAVs and nanosatellite communications. In order to satisfy the requirements to achieve such radiation pattern without the use of a large ground plane, it has been shown that pairs of orthogonal electric and magnetic dipoles must be combined with certain conditions in amplitude and phase. These equivalent dipoles can thus be orthogonally combined by exciting several TE and quasi-TM modes in dielectric resonators.

Dielectric resonator antennas allow great flexibility in their design by modifying their shapes or dielectric properties to control, for instance, their impedance bandwidth or radiation characteristics. It has also been shown that 3-D printing technologies are opening up new perspectives for the fabrication of DRAs with complex and anisotropic/heterogeneous properties. Such properties are particularly interesting for designing new dielectric resonator antennas by controlling their polarization and radiation pattern.

In this Ph.D., several significant milestones towards this objective have been achieved:
I. A Huygens source antenna has been designed using stacked isotropic dielectric resonators in linear and circular polarizations. The flexibility in DRA design has been exploited to generate pairs of electric and magnetic dipoles, required to realize a Huygens source with cardioid radiation properties.
II. A uniaxial anisotropic dielectric material has been engineered and manufactured using additive manufacturing of ceramics.
III. A single-fed circularly polarized antenna using a uniaxial anisotropic dielectric resonator has been designed, manufactured and measured in the 2.45 GHz ISM band. Measured and simulated results have shown a good agreement.
IV. A more compact single-fed uniaxial anisotropic dielectric resonator antenna has been designed at 2.45 GHz to realize a Huygens source pattern in linear polarization. The simulated results validate the good antenna performances for UAV and nanosatellite applications.

The main conclusions are given for each chapter as follows.

Chapter 1 has been dedicated to the state-of-the-art of Huygens source antennas. It has been shown that some antennas with half-space radiation patterns are classically formed by magnetoelectric and complementary sources. However, these antennas generally do not satisfy the mechanical constraints for UAV and nanosatellite applications due to the small volume of their platforms. An original solution to overcome both mechanical and radiation constraints relies on the design of a Huygens source antennas. It has been shown that the orthogonal combination of two equivalent electric and magnetic dipoles, with certain conditions in mag-

nitude and phase, allows the antenna to achieve a half-space radiation pattern. In addition to that, it has been demonstrated that both equivalent sources can be generated in a dielectric resonator antenna by taking advantage of its multiple degrees of freedom. Hence, this chapter has also been focused on the analysis of TE and quasi-TM modes in a rectangular dielectric resonator. Finally, the state-of-the art of Huygens source antennas using dielectric resonators has promoted new challenges to achieve different radiation properties. In fact, instead of obtaining a cardioid-shaped unilateral radiation pattern oriented transversely with respect to the feed position, as classically proposed in the literature, the design of a Huygens source DRA with cardioid radiation properties along the $+z$-direction has represented the main challenge of this Ph.D. thesis.

Chapter 2 has presented the first proposal of this Ph.D. thesis. It has been dedicated to present a Huygens source antenna in the ISM band formed by stacked dielectric resonators with an overall height of $0.38\lambda_0$. The first Huygens source DRA operates in linear polarization with asymmetric cardioid radiation properties in the E- and H-planes. As a result, it achieves a maximum F/B ratio of 31.8 dB, and impedance and F/B ratio bandwidths of 9.5% and 3.3%, respectively. In addition to that, the radiation properties of the proposed Huygens source DRA have been analyzed by means of the spherical mode expansion in order to determine the contribution of the fundamental and higher-order modes on the far-field radiation. It has thus been proved that the fact of not having collocated dipoles due to the relative position of each resonator leads to the radiation of second-order modes. As a consequence, these modes contribute to asymmetric radiation patterns. Similarly, a Huygens source antenna using a cross-shaped dielectric resonator arranged in a stacked configuration has been proposed in the ISM band. The overall height of the antenna is $0.41\lambda_0$, and it operates in circular polarization with a half-space radiation pattern. As a result, it achieves impedance and 3-dB axial ratio bandwidths of 21.2% and 22.9%, respectively. The proposed stacked Huygens source also achieves a maximum F/B ratio of 26.3 dB, and a F/B ratio bandwidth of 4.9%.

Chapter 3 has been dedicated to demonstrate the possibilities offered by additive manufacturing to provide a new degree of freedom for shape and material properties. For this purpose, this chapter has first involved the state-of-the-art of the different 3-D-printing technologies used to manufacture materials with complex structures and homogeneous/heterogeneous properties. Furthermore, it has been shown that additive manufacturing has been widely used to manufacture microwave materials, microwave circuits, and antennas. Afterwards, engineered anisotropy has been studied by structuring a 3-D-printed ceramic dielectric in several sub-wavelength unit cells. It has been shown that the effective permittivity tensor of the anisotropic dielectric material can be controlled by modifying the volume fill rate of its unit cells. In addition to that, the 3-D-printed material has been manufactured, and its dielectric permittivity tensor and losses have been measured. The measured permittivity tensor is consistent but does not match exactly with simulated values. This can be explained by the extraction procedure that is rather designed for moderate permittivities and isotropic materials.

Chapter 4 has been devoted to demonstrate the capabilities of additive manufacturing for DRA applications. This chapter has proposed a theoretical model to calculate the electrical properties and dimensions of a square-based dielectric resonator in circular polarization using a engineered anisotropic dielectric. The single-fed circularly polarized DRA has been designed, manufactured and measured in the 2.45 GHz ISM band. Its principle of operation relies on the excitation of two orthogonal modes with certain conditions in amplitude and phase, which have been tuned by modifying the anisotropy of the dielectric resonator in order to achieve circular polarization. A good agreement has been observed between simulated and measured results. The proposed DRA accomplishes a measured 10-dB impedance bandwidth of 16%, a 3-dB axial ratio bandwidth of 2.4%, and a 6.4 dBi realized gain at 2.47 GHz. In addition to that, the slight difference in magnitude between the simulated and measured axial ratio is due to manufacturing tolerances during the 3-D-printing process. Finally, it has been demonstrated that the use of additive manufacturing opens up interesting perspectives in the design of new dielectric-based antennas to control their polarization and radiation pattern.

Chapter 5 has finally involved the design of a compact Huygens source antenna using a uniaxial anisotropic dielectric resonator. It has been demonstrated that new degrees of freedom for material properties can be exploited using 3-D printing in order to generate a pair of collocated and orthogonal electric and magnetic dipoles in a single and more compact dielectric resonator made up of a uniaxial anisotropic dielectric material. More specifically, the frequency difference between the TE^{x}_{111} and quasi-TM^{y}_{111} modes can be reduced using anisotropic dielectric materials, leading to satisfy the conditions in phase and amplitude to realize symmetric Huygens source patterns in the E- and H-planes with improved radiation properties along the $+z$-direction and low backward radiation. Besides, its maximum height has been reduced by 16.2% while compared with the proposed stacked Huygens source made up of two isotropic dielectric resonators, presented in Chapter 2. The capabilities of additive manufacturing has also been exploited to reduce the antenna sensitive to the effects of coaxial probe by adding a solid wall around the feed. It has been shown that the Huygens source DRA achieves impedance and F/B ratio bandwidths of 11.4% and 2.9% using this solid wall. However, a wider F/B ratio bandwidth has been achieved in absence of the dielectric wall. For this latter, impedance and F/B ratio bandwidths of 20% and 4.1% have been achieved, respectively. Finally, the spherical mode expansion has been used to determine the spherical modes which contribute to the radiation of the Huygens source. This has confirmed that the main contribution to the radiation pattern correspond to the TE^{x}_{111}, and quasi-TM^{y}_{111} resonant modes, which are equivalent to collocated elementary dipoles.

Perspectives for future works

Given the objectives achieved in this Ph.D., further studies could be conducted: a theoretical model to design a Huygens source antenna using a single dielectric resonator, a circularly polarized antenna with Huygens source pattern using a single dielectric resonator, a wideband circularly polarized DRA with large impedance and axial ratio bandwidths, a DRA with

pattern diversity, and 3-D-printed multiband electrically small antennas for small satellites. Furthermore, new techniques to measure anisotropy could be investigated to obtain accurate and reliable results when retrieving its dielectric permittivity tensor and losses. For this latter, the resonances of higher-order modes in the uniaxial anisotropic samples could be deeply analyzed to determine if conventional techniques to measure isotropic dielectric materials with low permittivities could be also applied to anisotropic materials.

For the first proposal, a theoretical analysis based on RLC circuits could be proposed to represent a pair of orthogonal electric and magnetic dipoles so that they resonate with a specific frequency difference in order to satisfy the amplitude and phase requirements to achieve a Huygens source pattern.

Secondly, four resonant modes namely TE^{x}_{111}, TE^{y}_{111}, quasi-TM^{x}_{111}, and quasi-TM^{y}_{111} modes must be excited and adjusted in frequency so that they satisfy the required conditions in phase and magnitude to realize a Huygens source pattern in circular polarization. For this purpose, a uniaxial anisotropic DRA using could be used to reduce the frequency difference between the pairs of equivalent electric and magnetic dipoles. This would require different feed mechanisms.

Finally, the axial ratio bandwidth enhancement could be performed by exciting higher-order modes using trapezoidal [154] and stair-shaped [155, 156] DRAs. Furthermore, different feed mechanisms could be used to excite higher-order modes in a uniaxial anisotropic dielectric resonator. On the other hand, a pattern-diversity DRA could be investigated in order to provide different radiation patterns, *i.e.*, cardioid and omnidirectional patterns. The use of additive manufacturing could be here adopted to excite the unidirectional HEM_{111} and omnidirectional TM_{011} modes by designing a rectangular DRA made up of a uniaxial anisotropic dielectric material and two isolated ports, as previously done in [60].

Publications

International journals

- C.D. Morales, C. Morlaas, A. Chabory, R. Pascaud, M. Grzeskowiak and G. Mazingue. 3-D-printed ceramics with engineered anisotropy for dielectric resonator antenna applications. *IET Electronic Letters*, May 2021.

Communications in international conferences

- C.D. Morales, C. Morlaas, A. Chabory, R. Pascaud, M. Grzeskowiak and G. Mazingue. Circularly polarized Huygens Source Antenna using two Stacked Dielectrics Resonators. *IEEE AP-S International Symposium on Antennas and Propagation and North American Radio Science Meeting*, Marina Bay Sands (Singapore), December 2021.
- C.D. Morales, C. Morlaas, A. Chabory, R. Pascaud, M. Grzeskowiak and G. Mazingue. Huygens Source Antenna using Stacked Dielectric Resonators. *IEEE AP-S International Symposium on Antennas and Propagation and North American Radio Science Meeting*, Montréal (Canada), July 2020.
- C.D. Morales, C. Morlaas, A. Chabory, R. Pascaud, M. Grzeskowiak and G. Mazingue. Single-fed circularly polarized dielectric resonator antenna using a uniaxial anisotropic material. *Antennas and Propagation Conference (APC)*, Birmingham (England), November 2019.

Communications in national (French) conferences

- C.D. Morales, C. Morlaas, A. Chabory, R. Pascaud, M. Grzeskowiak and G. Mazingue. Additive Manufacturing of a Uniaxial Anisotropic Dielectric Material for Antenna Applications. *16èmes Journées de Caractérisation Microondes et Matériaux (JCMM)*, Toulouse (France), November 2020.

Appendix A

Spherical mode expansion

A.1 Theory

The spherical mode expansion (SME) is used to analyze the far-field radiation of the proposed Huygens source antennas. For this, the SME is obtained by expanding the free-space Green's function in a scalar series and using the current distributions obtained with the method of moments (MM) [157]. The result of the combination is a series of the magnetic vector potential with coefficients. The far-field radiation properties are finally calculated by projecting these coefficients onto the unit vectors $\mathbf{a}_\theta$ and $\mathbf{a}_\phi$ [157].

The contribution of each coefficient vectors are defined as $\mathbf{a_{mn}}$ and $\mathbf{b_{mn}}$, where $m = 0, \pm1, \pm2, ..., \infty$, and $n = 0, 1, 2, ..., \infty$.

In order to develop the vector spherical harmonic expansion, the homogeneous Helmholtz wave equation in spherical coordinates is first presented [158]

$$\bigtriangledown^2 \psi + k^2\psi = \frac{1}{r^2}\frac{\partial}{\partial r}\left(r^2\frac{\partial\psi}{\partial r}\right) + \frac{1}{r^2\sin\theta}\frac{\partial}{\partial\theta}\left(\sin\theta\frac{\partial\psi}{\partial\theta}\right) + \frac{1}{r^2\sin^2\theta}\frac{\partial^2\psi}{\partial\phi^2} + k^2\psi = 0 \quad \text{(A.1)}$$

where k is the wavenumber. Hence, (A.1) can be solved by using the method of separation of variables

$$\psi(r,\theta,\phi,t) = R(r)H(\theta)\Phi(\phi)e^{j\omega t}. \quad \text{(A.2)}$$

A ϕ-dependent expression can be written as

$$\Phi_m(\phi) = e^{\pm jm\phi} \quad \text{(A.3)}$$

and the Legendre function of first kind $P_n(\cos\xi)$ can be defined as a θ-dependent solution which is finite over the spherical domain and periodic in θ [158].

On the other hand, since the far-field radiation is here investigated, the free-space Green's function can be defined as [157]

$$e^{-jkR}/R = -jkh_0^{(2)}(kR) = -jk\sum_{n=0}^{infty}(2n+1)j_n(kr')h_n^{(2)}(kr)P_n(\cos\xi) \tag{A.4}$$

where $R = |\mathbf{r} - \mathbf{r}'|$, $\mathbf{r}$ and $\mathbf{r}'$ are the position vectors of field and source points, respectively. Moreover, ξ defines the angle between $\mathbf{r}$ and $\mathbf{r}'$, $j_n(kr')$ the spherical Bessel function of first kind, $h_n^{(2)}$ the spherical Hankel function of second kind, and $P_n(\cos\xi)$ the Legendre function.

The Legendre polynomials P_n can be written as [159]

$$P_n^m(x) = (-1)^m(1-x^2)^{m/2}\frac{\partial^m}{\partial^m x}P_n(x) \tag{A.5}$$

where P_n must satisfy the linear second-order Legendre differential equation [160]

$$(1-x^2)P_n'' - 2xP_n' + n(n+1)P_n = 0 \tag{A.6}$$

with $P_n'' = \frac{\partial^2}{\partial^2 x}P_n$ and $P_n' = \frac{\partial}{\partial x}P_n$. The factor $(-1)^m$ is called the Condon-Shortley phase.

On the other hand, the magnetic vector potential $\mathbf{A}$ can be expressed as [157]

$$\mathbf{A} = \frac{\mu_0}{4\pi}\int_{\triangle S_i} I_i(e^{-jKR}/R)\mathbf{a_{si}}\partial s' \tag{A.7}$$

where $\mathbf{a_{si}}$ is a unit vector in the direction of the ith wire segment of length $\triangle S_i$, and I_i is the current distribution for $i = 1, 2, 3, ..., P$, where P defines the total number of segments used in the MM current distribution.

By combining A.4 and A.7, the following equation is obtained

$$\mathbf{A} = \frac{-j\mu_0 e^{(-jkr)}}{2r}\sum_{i+1}^{P} I_i\mathbf{a_{si}}\sum_{n=0}^{\infty} j^{n+1}\sum_{m=0}^{n} F_{inm}(\theta,\phi) \tag{A.8}$$

with

$$F_{inm}(\theta,\phi) = \frac{(2n+1)}{2\pi}\int_{\triangle S_i} j_n(kr')P_n^m(\cos\xi)\partial s'. \tag{A.9}$$

Using the Legendre function as in A.5, and expanding its terms in a scalar series [157]

$$P_n^m(\cos\xi) = \sum_{m=0}^{n}\epsilon_m\frac{(n-m)!}{(n+m)!}P_n^m(\cos\theta')P_n^m(\cos\theta)\cos\ m(\phi-\phi') \tag{A.10}$$

where ϵ_m is the Neumann's number, with even ($Y^e_{mn}(\theta,\phi)$), and odd ($Y^o_{mn}(\theta,\phi)$) orthogonal spherical harmonics as [161], as follows

$$Y^e_{mn}(\theta,\phi) = \left[\epsilon_m \frac{(2n+1)}{2\pi}\frac{(n-m)!}{(n+m)!}\right]^{1/2} P^m_n(\cos\theta)\cos(m\phi) \tag{A.11}$$

$$Y^o_{mn}(\theta,\phi) = \left[\epsilon_m \frac{(2n+1)}{2\pi}\frac{(n-m)!}{(n+m)!}\right]^{1/2} P^m_n(\cos\theta)\sin(m\phi). \tag{A.12}$$

Thus, (A.8) can be expressed in far-field as [157, 161]

$$\mathbf{A}(r,\theta,\phi) = \frac{-j\mu_0 e^{-jkr}}{2r}\sum_{n=0}^{\infty}\sum_{m=0}^{\infty}[\mathbf{a_{mn}}Y^e_{mn}(\theta,\phi) + \mathbf{b_{mn}}Y^o_{mn}(\theta,\phi)] \tag{A.13}$$

with

$$\mathbf{a_{mn}} = \sum_{i=1}^{P} I_i \mathbf{a_{si}} \int_{\triangle s_i} j^{n+1} j_n(kr') Y^e_{mn}(\theta,\phi)\partial s' \tag{A.14}$$

$$\mathbf{b_{mn}} = \sum_{i=1}^{P} I_i \mathbf{a_{si}} \int_{\triangle s_i} n^{n+1} j_n(kr') Y^o_{mn}(\theta,\phi)\partial s'. \tag{A.15}$$

Finally, the electric field in far-field can be written as

$$\mathbf{E}_\theta = -j\omega \mathbf{a}_\theta \cdot \mathbf{A} \tag{A.16}$$

$$\mathbf{E}_\phi = -j\omega \mathbf{a}_\phi \cdot \mathbf{A}. \tag{A.17}$$

Assuming $r \longrightarrow \infty$, and considering $\mathbf{a}_\phi$ and $\mathbf{a}_\theta$ as unit vectors with Cartesian components, then

$$\mathbf{a}_\theta = \mathbf{a_x}\cos\theta\cos\phi - \mathbf{a_y}\cos\theta\sin\phi - \mathbf{a_z}\sin\theta \tag{A.18}$$

$$\mathbf{a}_\phi = -\mathbf{a_x}\sin\phi + \mathbf{a_y}\cos\phi. \tag{A.19}$$

Thereby, the electric field can be expressed as [157]

$$E_\theta(r,\theta,\phi) = \frac{\omega\mu_0 e^{-jkr}}{2r}\sum_{m=0}^{n}\sum_{n=0}^{\infty}[\mathbf{a_\theta a_{mn}}Y^e_{mn}(\theta,\phi) + \mathbf{a_\theta b_{mn}}Y^o_{mn}(\theta,\phi) \tag{A.20}$$

$$E_\phi(r,\theta,\phi) = \frac{\omega\mu_0 e^{-jkr}}{2r}\sum_{m=0}^{n}\sum_{n=0}^{\infty}[\mathbf{a_\phi a_{mn}}Y^e_{mn}(\theta,\phi) + \mathbf{a_\phi b_{mn}}Y^o_{mn}(\theta,\phi). \tag{A.21}$$

A.2 Expansion of TE and TM fields in vector spherical harmonics

The theory of the spherical mode expansion is used in this Ph.D. thesis to determine which modes contribute to the radiation of a Huygens source antenna. To achieve this goal, the electric field is expanded in terms of vector spherical harmonics in far-field, as previously demonstrated.

It has been demonstrated in [73] that a set of wave functions ($\mathbf{a_{mn}}$ and $\mathbf{b_{mn}}$) describes the TE^{sph} and TM^{sph} components of the electromagnetic field. Thus, the electric field can also be written as an expansion of normalized vector spherical harmonics in terms of the electrical properties of TE and TM modes as follows [73, 74, 158, 162]

$$\mathbf{E}(\mathbf{r}) = \sum_{n=1}^{\infty}\sum_{m=-n}^{n} d^{TE}_{mn}\mathbf{M}_{mn}(\mathbf{r}) + d^{TM}_{mn}\mathbf{N}_{mn}(\mathbf{r}) \tag{A.22}$$

where the coefficients d^{TE}_{mn} and d^{TM}_{mn} describe the strength of the TE and TM components of the radiated field, n and m are the mode indices ($\mid m \mid \leq n$). Moreover, $\boldsymbol{M}_{mn}(\boldsymbol{r})$ and $\boldsymbol{N}_{mn}(\boldsymbol{r})$ define the normalized vector spherical harmonics in far-field as follows

$$\mathbf{M}_{mn}(\mathbf{r}) = j^{n+1}\frac{e^{-jkr}}{kr}\mathbf{k}_{mn}(\theta,\phi) \tag{A.23}$$

$$\mathbf{N}_{mn}(\mathbf{r}) = j^{n}\frac{e^{-jkr}}{kr}\hat{\boldsymbol{r}}\times\mathbf{k}_{mn}(\theta,\phi) \tag{A.24}$$

with

$$\mathbf{k}_{mn}(\theta,\phi) = \left(-\frac{m}{\mid m \mid}\right)\sqrt{\frac{(2n+1)(n-\mid m \mid)!}{(4\pi n(n+1))(n+\mid m \mid)}}e^{jm\phi} \left[\frac{jm}{\sin\theta}P_n^{|m|}(\cos\theta)\hat{\boldsymbol{\theta}}\frac{\partial}{\partial\theta}(P_n^{|m|}(\cos\theta))\hat{\boldsymbol{\phi}}\right] \tag{A.25}$$

and $P_n^{|m|}$ is the associated Legendre function.

The azimuth index m defines the ϕ-variation of the spherical mode for $0 \leq \phi \leq 2\pi$. For $m = 0$, the fundamental TE^{sph} and TM^{sph} modes have no azimuth ϕ-variation, *i.e.*, electric dipole placed at z axis or a loop placed in xy plane. For $m = \pm 1$, the field varies periodically around the z axis. On the contrary, the θ-variation of the spherical modes depends on the indices m and n [74].

The variation of the field can occur in two directions. The rotation from the x axis towards the y axis defines $m = 1$, and the opposite rotation defines $m = -1$. Thus, small magnetic and electric dipoles oriented along x and y axis can be generated from $\mathrm{TE}_{|m|1}^{sph}$ and $\mathrm{TM}_{|m|1}^{sph}$ modes, respectively, when $m = \pm 1$. In addition to that, the combination of $\mathrm{TE}_{11}^{sph}/\mathrm{TE}_{-11}^{sph}$ or $\mathrm{TM}_{11}^{sph}/\mathrm{TM}_{-11}^{sph}$ mode defines a bidirectional radiation of the small dipoles with a peak along the z axis with linear polarization.

Appendix B

Unit cell design using Floquet ports

As detailed in section 3.3, the anisotropy of the 3-D-printed ceramic material is obtained by periodically printing an anisotropic unit cell. To ensure a homogeneous macroscopic behavior of the final material, the unit cell must remain small with respect to the wavelength.

As shown in Fig. 3.27a, the simulation setup is formed by a dielectric material and a vacuum box. Both periodic boundary conditions and Floquet ports are here defined using Ansys HFSS. Hence, master/slave boundary conditions are fixed at the four side walls of the vaccum box along x axis and y axis, as depicted in Fig. B.1. However, the single unit cell is unable to extract the S-parameters in the plane of the unit cell interfaces along the x- and y-direction. For that reason, Floquet ports are embedded in the unit cell interfaces in order to measure the S-parameters [75, 137]. Then, two Floquet ports are here located along z axis, as shown in Fig. B.2, providing normal incident waves with capabilities to control the polarization vector. In addition to that, the Floquet ports must be set using a deembed distance of 1.5 a_{uc}, which correspond to the distance between the two faces of the unit cell and vacuum box along the z-direction.

Given the periodic boundary conditions imposed on the unit cell, the first Floquet mode in x-polarization is excited to extract the S_{11} and S_{21} parameters, allowing to retrieve ε_{rx}. On the other hand, to achieve ε_{ry}, the first Floquet mode in y-polarization is excited to extract the S-parameters. For this, two different options can be done in simulations, either rotating 90° the unit cell around the z axis or exciting two fundamental TE and TM modes in the Floquet ports.

The S-parameters are then used to retrieve the permittivity tensor for the uniaxial anisotropic dielectric [137],[163]. The S-parameters can be calculated given a normally incident wave propagating between the Floquet ports and written as

$$S_{11} = \frac{R_{01}\left(1 - e^{j2nk_0a_{uc}}\right)}{1 - R_{01}^2 e^{j2nk_0a_{uc}}} \tag{B.1}$$

$$S_{21} = \frac{\left(1 - R_{01}^2\right)e^{j2nk_0a_{uc}}}{1 - R_{01}^2 e^{j2nk_0a_{uc}}} \tag{B.2}$$

where $R_{01} = \frac{z-1}{z+1}$, $e^{j2nk_0a_{uc}} = \frac{S_{21}}{1-S_{21}R_{01}}$, k_0 is the free-space wavenumber, and a_{uc} is the

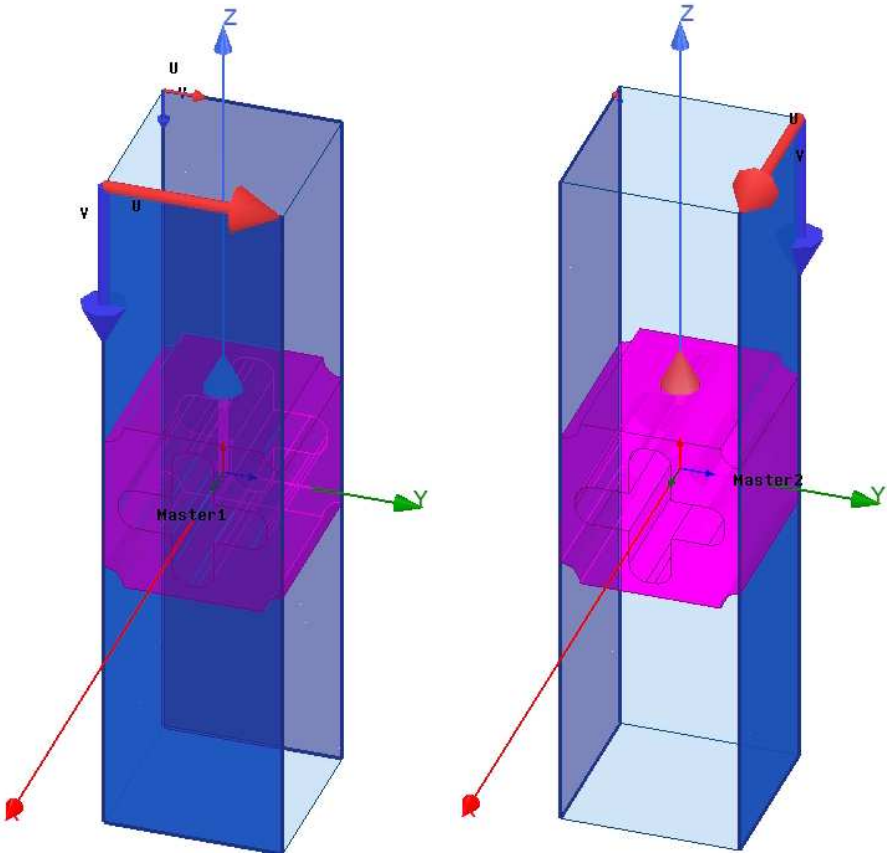

(a) (b)

Figure B.1: Master/slave boundary conditions defined along the (a) x-direction, and (b) y-direction.

maximum length of the unit cell. The impedance of the unit element z and the refractive index n are given by

$$z = \sqrt{\frac{(1+S_{11})^2 - S_{21}^2}{(1-S_{11})^2 - S_{21}^2}} \tag{B.3}$$

$$n = \frac{1}{k_0 a_{uc}} \cos^{-1}\left[\frac{1}{2S_{21}}(1 - S_{11}^2 + S_{21}^2)\right]. \tag{B.4}$$

The permittivity is computed based on the refractive index and impedance of the unit cell as

$$\varepsilon = \frac{n}{z}. \tag{B.5}$$

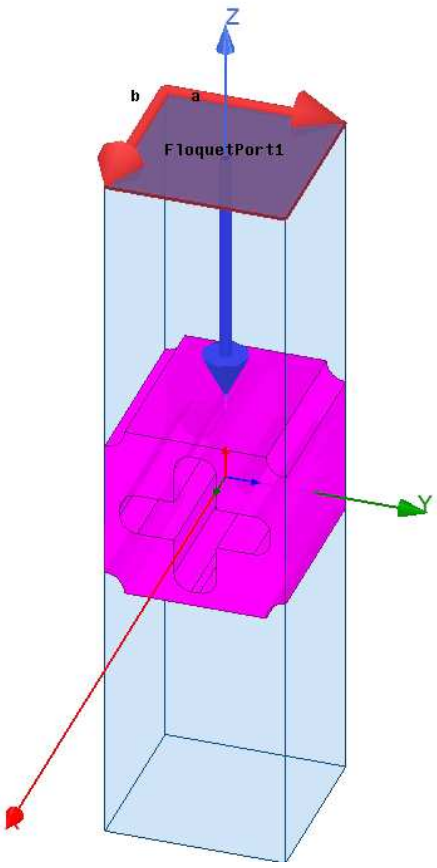

Figure B.2: Floquet port located along the $+z$ direction.

Bibliography

[1] Riccardo Bassoli et al. "CubeSat-Based 5G Cloud Radio Access Networks: A Novel Paradigm for On-Demand Anytime/Anywhere Connectivity." In: *IEEE Vehicular Technology Magazine* 15.2 (2020), pp. 39–47 (cit. on p. 1).

[2] Kirk Woellert et al. "Cubesats: Cost-effective science and technology platforms for emerging and developing nations." In: *Advances in Space Research* 47.4 (2011), pp. 663–684 (cit. on p. 1).

[3] Steven Gao et al. "Advanced Antennas for Small Satellites." In: *Proceedings of the IEEE* 106.3 (2018), pp. 391–403 (cit. on pp. 1, 31).

[4] Nasir Saeed et al. "Cubesat communications: Recent advances and future challenges." In: *IEEE Communications Surveys & Tutorials* 22.3 (2020), pp. 1839–1862 (cit. on p. 1).

[5] Yahya Rahmat-Samii, Vignesh Manohar, and Joshua Michael Kovitz. "For Satellites, Think Small, Dream Big: A review of recent antenna developments for CubeSats." In: *IEEE Antennas and Propagation Magazine* 59.2 (2017), pp. 22–30 (cit. on p. 2).

[6] Nacer Chahat et al. "Advanced CubeSat Antennas for Deep Space and Earth Science Missions: A review." In: *IEEE Antennas and Propagation Magazine* 61.5 (2019), pp. 37–46 (cit. on pp. 2, 31).

[7] Dan Wu et al. "Compact and low-profile omnidirectional circularly polarized antenna with four coupling arcs for UAV applications." In: *IEEE Antennas and Wireless Propagation Letters* 16 (2017), pp. 2919–2922 (cit. on p. 2).

[8] Luz I Balderas et al. "Low-profile conformal UWB antenna for UAV applications." In: *IEEE Access* 7 (2019), pp. 127486–127494 (cit. on p. 2).

[9] A. Chlavin. "A new antenna feed having equal E -and H-plane patterns." In: *Transactions of the IRE Professional Group on Antennas and Propagation* 2.3 (1954), pp. 113–119 (cit. on pp. 2, 8, 12, 118).

[10] Kwai-Man Luk and Hang Wong. "A new wideband unidirectional antenna element." In: *International Journal of Microwave and Optical Technology* 1.1 (2006), pp. 35–44 (cit. on pp. 2, 12).

[11] Mingjian Li and Kwai-Man Luk. "Wideband magnetoelectric dipole antennas with dual polarization and circular polarization." In: *IEEE Antennas and Propagation Magazine* 57.1 (2015), pp. 110–119 (cit. on pp. 2, 12).

[12] P Alitalo et al. "Design and realisation of an electrically small Huygens source for circular polarisation." In: *IET microwaves, antennas & propagation* 5.7 (2011), pp. 783–789 (cit. on pp. 2, 12, 13).

[13] T Niemi et al. "Electrically small Huygens source antenna for linear polarisation." In: *IET microwaves, antennas & propagation* 6.7 (2012), pp. 735–739 (cit. on pp. 2, 13).

[14] Lei Ge and Kwai Man Luk. "A wideband magneto-electric dipole antenna." In: *IEEE Transactions on Antennas and Propagation* 60.11 (2012), pp. 4987–4991 (cit. on p. 2).

[15] Salih Yarga, Kubilay Sertel, and John L Volakis. "Multilayer dielectric resonator antenna operating at degenerate band edge modes." In: *IEEE Antennas and Wireless Propagation Letters* 8 (2009), pp. 287–290 (cit. on pp. 3, 66).

[16] Salih Yarga, Kubilay Sertel, and John L Volakis. "A directive resonator antenna using degenerate band edge crystals." In: *IEEE Transactions on Antennas and Propagation* 57.3 (2009), pp. 799–803 (cit. on pp. 3, 66).

[17] Saeed Fakhte, Homayoon Oraizi, and Ladislau Matekovits. "High gain rectangular dielectric resonator antenna using uniaxial material at fundamental mode." In: *IEEE Transactions on Antennas and Propagation* 65.1 (2017), pp. 342–347 (cit. on pp. 3, 66).

[18] S. Fakhte et al. "Cylindrical Anisotropic Dielectric Resonator Antenna With Improved Gain." In: *EEE Transactions on Antennas and Propagation* 65.3 (2017), pp. 1404–1409 (cit. on p. 3).

[19] S. Fakhte, I. Aryanian, and L. Matekovits. "Analysis and Experiment of Equilateral Triangular Uniaxial-Anisotropic Dielectric Resonator Antennas." In: *IEEE Access* 6 (2018), pp. 63071–63079 (cit. on p. 3).

[20] Edward J Rothwell and Michael J Cloud. *Electromagnetics*. CRC press, 2018 (cit. on p. 8).

[21] Yong-Mei Pan, Kwok Wa Leung, and Kai Lu. "Compact quasi-isotropic dielectric resonator antenna with small ground plane." In: *ieee transactions on antennas and propagation* 62.2 (2014), pp. 577–585 (cit. on pp. 8, 16, 119).

[22] YM Pan, KW Leung, and L Guo. "Compact laterally radiating dielectric resonator antenna with small ground plane." In: *IEEE Transactions on Antennas and Propagation* 65.8 (2017), pp. 4305–4310 (cit. on pp. 8, 27, 28, 33, 118).

[23] HAROLD A Wheeler. "A helical antenna for circular polarization." In: *Proceedings of the IRE* 35.12 (1947), pp. 1484–1488 (cit. on p. 11).

[24] John D Kraus. "The helical antenna." In: *Proceedings of the IRE* 37.3 (1949), pp. 263–272 (cit. on p. 11).

[25] C. Morlaas, B. Souny, and A. Chabory. "Helical-Ring Antenna for Hemispherical Radiation in Circular Polarization." In: *IEEE Transactions on Antennas and Propagation* 63.11 (2015), pp. 4693–4701 (cit. on pp. 11, 13, 14).

[26] Bernard Souny, Christophe Morlaas, and Alexandre Chabory. "Compact self-directional antenna based on a helical ring." In: *2010 IEEE Antennas and Propagation Society International Symposium*. IEEE. 2010, pp. 1–4 (cit. on pp. 11, 13).

[27] Pekka Alitalo et al. "Chiral antennas radiating circularly polarized waves." In: *Proceedings of the Fourth European Conference on Antennas and Propagation*. IEEE. 2010, pp. 1–5 (cit. on p. 12).

[28] Ming-Chun Tang, Ting Shi, and Richard W Ziolkowski. "Electrically small, broadside radiating Huygens source antenna augmented with internal non-Foster elements to increase its bandwidth." In: *IEEE Antennas and Wireless Propagation Letters* 16 (2016), pp. 712–715 (cit. on pp. 14, 15).

[29] Ming-Chun Tang, Hao Wang, and Richard W Ziolkowski. "Design and testing of simple, electrically small, low-profile, Huygens source antennas with broadside radiation performance." In: *IEEE transactions on antennas and propagation* 64.11 (2016), pp. 4607–4617 (cit. on pp. 14, 15).

[30] Ming-Chun Tang, Boya Zhou, and Richard W Ziolkowski. "Low-profile, electrically small, Huygens source antenna with pattern-reconfigurability that covers the entire azimuthal plane." In: *IEEE Transactions on Antennas and Propagation* 65.3 (2017), pp. 1063–1072 (cit. on pp. 14, 15).

[31] Richard W Ziolkowski. "Low profile, broadside radiating, electrically small Huygens source antennas." In: *IEEE Access* 3 (2015), pp. 2644–2651 (cit. on p. 14).

[32] Peng Jin and Richard W Ziolkowski. "Metamaterial-inspired, electrically small Huygens sources." In: *IEEE Antennas and Wireless Propagation Letters* 9 (2010), pp. 501–505 (cit. on p. 15).

[33] Ming-Chun Tang et al. "Dual-linearly polarized, electrically small, low-profile, broadside radiating, huygens dipole antenna." In: *IEEE Transactions on Antennas and Propagation* 66.8 (2018), pp. 3877–3885 (cit. on p. 15).

[34] Su-Hyeon Lee et al. "Low-profile, electrically small planar Huygens source antenna with an endfire radiation characteristic." In: *IEEE Antennas and Wireless Propagation Letters* 18.3 (2019), pp. 412–416 (cit. on p. 15).

[35] S. A. Long, M. W. McAllister, and L. C. Shen. "The resonant cylindrical dielectric cavity antenna." In: *IEEE Transactions on Antennas and Propagation* 31.3 (1983), pp. 406–412 (cit. on p. 15).

[36] A. Petosa and A. Ittipiboon. "Dielectric resonator antennas: A historical review and the current state of the art." In: *IEEE Antennas and Propagation Magazine* 52.5 (2010), pp. 91–116 (cit. on p. 15).

[37] ByungKuon Ahn et al. "High gain spherical DRA operating on higher-order mode excited by microstrip patch." In: *IEICE Electronics Express* 14.23 (2017), pp. 20171049–20171049 (cit. on p. 15).

[38] Byung Kuon Ahn et al. "Pattern reconfigurable high gain spherical dielectric resonator antenna operating on higher order mode." In: *IEEE Antennas and Wireless Propagation Letters* 18.1 (2018), pp. 128–132 (cit. on p. 15).

[39] Utpal Dey and Jan Hesselbarth. "Spherical dielectric resonator antenna operating at 180 GHz." In: *IEEE Antennas and Wireless Propagation Letters* 19.8 (2020), pp. 1380–1384 (cit. on p. 15).

[40] Laila K Hady, Ahmed A Kishk, and Darko Kajfez. "Dual-band compact DRA with circular and monopole-like linear polarizations as a concept for GPS and WLAN applications." In: *IEEE transactions on antennas and propagation* 57.9 (2009), pp. 2591–2598 (cit. on pp. 15, 18, 19).

[41] GD Makwana and Deepak Ghodgaonkar. "Wideband stacked rectangular dielectric resonator antenna at 5.2 GHz." In: *International Journal of Electromagnetics and Applications* 2.3 (2012), p. 2012 (cit. on p. 15).

[42] Longfang Zou, Derek Abbott, and Christophe Fumeaux. "Omnidirectional cylindrical dielectric resonator antenna with dual polarization." In: *IEEE Antennas and Wireless Propagation Letters* 11 (2012), pp. 515–518 (cit. on p. 15).

[43] R Kumar Mongia and Apisak Ittipiboon. "Theoretical and experimental investigations on rectangular dielectric resonator antennas." In: *IEEE Transactions on Antennas and Propagation* 45.9 (1997), pp. 1348–1356 (cit. on pp. 15, 19–23, 26, 27, 102).

[44] Aldo Petosa and Soulideth Thirakoune. "Rectangular dielectric resonator antennas with enhanced gain." In: *IEEE Transactions on Antennas and Propagation* 59.4 (2011), pp. 1385–1389 (cit. on p. 15).

[45] Yong Mei Pan, Kwok Wa Leung, and Kai Lu. "Omnidirectional linearly and circularly polarized rectangular dielectric resonator antennas." In: *IEEE transactions on antennas and propagation* 60.2 (2012), pp. 751–759 (cit. on p. 15).

[46] Pragati Patel, Biswajeet Mukherjee, and Jayanta Mukherjee. "Wideband circularly polarized rectangular dielectric resonator antennas using square-shaped slots." In: *IEEE Antennas and Wireless Propagation Letters* 15 (2015), pp. 1309–1312 (cit. on p. 15).

[47] L. Z. Thamae and Z. Wu. "Broadband Bowtie Dielectric Resonator Antenna." In: *IEEE Transactions on Antennas and Propagation* 58.11 (2010), pp. 3707–3710 (cit. on pp. 15–17).

[48] M. Simeoni et al. "Plastic-Based Supershaped Dielectric Resonator Antennas for Wide-Band Applications." In: *IEEE Transactions on Antennas and Propagation* 59.12 (2011), pp. 4820–4825 (cit. on pp. 15–17).

[49] Amir Altaf et al. "Vertical-strip-fed broadband circularly polarized dielectric resonator antenna." In: *Sensors* 17.8 (2017), p. 1911 (cit. on p. 15).

[50] Xiao-Chuan Wang et al. "Single-feed dual-band circularly polarized dielectric resonator antenna for CNSS applications." In: *IEEE Transactions on Antennas and Propagation* 65.8 (2017), pp. 4283–4287 (cit. on pp. 15, 16).

[51] Raghvendra Kumar Chaudhary, Rajnish Kumar, and Kumar Vaibhav Srivastava. "Wideband ring dielectric resonator antenna with annular-shaped microstrip feed." In: *IEEE Antennas and wireless propagation letters* 12 (2013), pp. 595–598 (cit. on pp. 15, 16).

[52] Tomas Bernabeu-Jimenez et al. "A 60-GHz coplanar-waveguide-fed slot-coupled rectangular DRA design using the theory of characteristic modes." In: *2015 9th European Conference on Antennas and Propagation (EuCAP)*. IEEE. 2015, pp. 1–4 (cit. on p. 15).

[53] Jiahong Lin, Wenhui Shen, and Kang Yang. "A low-sidelobe and wideband series-fed linear dielectric resonator antenna array." In: *IEEE Antennas and Wireless Propagation Letters* 16 (2016), pp. 513–516 (cit. on pp. 15, 16).

[54] AMMA Petosa et al. "Recent advances in dielectric-resonator antenna technology." In: *IEEE Antennas and Propagation Magazine* 40.3 (1998), pp. 35–48 (cit. on p. 15).

[55] Aldo Petosa. *Dielectric resonator antenna handbook*. Artech House Publishers, 2007 (cit. on pp. 15, 20, 21).

[56] Y. Coulibaly, T. A. Denidni, and H. Boutayeb. "Broadband Microstrip-Fed Dielectric Resonator Antenna for X-Band Applications." In: *IEEE Antennas and Wireless Propagation Letters* 7 (2008), pp. 341–345 (cit. on pp. 16, 17).

[57] L. Zou and C. Fumeaux. "A Cross-Shaped Dielectric Resonator Antenna for Multifunction and Polarization Diversity Applications." In: *IEEE Antennas Wireless Propagation Letters* 10 (2011), pp. 742–745 (cit. on pp. 17, 18).

[58] S. Fakhte, H. Oraizi, and R. Karimian. "A Novel Low-Cost Circularly Polarized Rotated Stacked Dielectric Resonator Antenna." In: *IEEE Antennas Wireless Propagation Letters* 13 (2014), pp. 722–725 (cit. on pp. 17, 18).

[59] H. Tang et al. "Differential Dual-Band Dual-Polarized Dielectric Resonator Antenna." In: *IEEE Transactions on Antennas and Propagation* 65.2 (2017), pp. 855–860 (cit. on pp. 18, 19).

[60] N. Yang, K. W. Leung, and N. Wu. "Pattern-Diversity Cylindrical Dielectric Resonator Antenna Using Fundamental Modes of Different Mode Families." In: *IEEE Transactions on Antennas and Propagation* 67.11 (2019), pp. 6778–6788 (cit. on pp. 18, 19, 142).

[61] Jean Van Bladel. "On the resonances of a dielectric resonator of very high permittivity." In: *IEEE Transactions on Microwave Theory and Techniques* 23.2 (1975), pp. 199–208 (cit. on p. 20).

[62] Rajesh K Mongia and Prakash Bhartia. "Dielectric resonator antennas—A review and general design relations for resonant frequency and bandwidth." In: *International Journal of Microwave and Millimeter-Wave Computer-Aided Engineering* 4.3 (1994), pp. 230–247 (cit. on pp. 20, 23).

[63] Yong Mei Pan, Kwok Wa Leung, and Kai Lu. "Study of Resonant Modes in Rectangular Dielectric Resonator Antenna Based on Radar Cross Section." In: *IEEE Transactions on Antennas and Propagation* 67.6 (2019), pp. 4200–4205 (cit. on p. 23).

[64] Yong Pan, Kwok Leung, and Kai Lu. "Omnidirectional linearly and circularly polarized rectangular dielectric resonator antennas." In: *IEEE transactions on antennas and propagation* 60.2 (2011), pp. 751–759 (cit. on p. 23).

[65] Meng Zou and Jin Pan. "Investigation of resonant modes in wideband hybrid omnidirectional rectangular dielectric resonator antenna." In: *IEEE Transactions on Antennas and Propagation* 63.7 (2015), pp. 3272–3275 (cit. on p. 23).

[66] James S McLean. "A re-examination of the fundamental limits on the radiation Q of electrically small antennas." In: *IEEE Transactions on antennas and propagation* 44.5 (1996), p. 672 (cit. on p. 26).

[67] David M Pozar. *Microwave engineering*. John Wiley & Sons, 2009 (cit. on pp. 26, 101).

[68] Lei Guo, Kwok Wa Leung, and Yong Mei Pan. "Compact unidirectional ring dielectric resonator antennas with lateral radiation." In: *IEEE Transactions on Antennas and Propagation* 63.12 (2015), pp. 5334–5342 (cit. on pp. 27, 29, 30, 33).

[69] Lei Guo and Kwok Wa Leung. "Compact unilateral circularly polarized dielectric resonator antenna." In: *IEEE Transactions on Antennas and Propagation* 66.2 (2017), pp. 668–674 (cit. on pp. 27, 29, 30, 33).

[70] Sheng-Jie Guo et al. "Microstrip-Fed Differential Dielectric Resonator Antenna and Array." In: *IEEE Antennas and Wireless Propagation Letters* 17.9 (2018), pp. 1736–1739 (cit. on p. 27).

[71] Ma Boyuan et al. "Unidirectional Dielectric Resonator Antennas Employing Electric and Magnetic Dipole Moments." In: *IEEE Transactions on Antennas and Propagation* (2021) (cit. on pp. 27–29, 33).

[72] Lei Guo, Kwok Wa Leung, and Nan Yang. "Wide-beamwidth unilateral dielectric resonator antenna using higher-order mode." In: *IEEE Antennas and Wireless Propagation Letters* 18.1 (2018), pp. 93–97 (cit. on pp. 28, 29, 33).

[73] Jesper E Hansen. *Spherical near-field antenna measurements*. Vol. 26. Iet, 1988 (cit. on pp. 45, 148).

[74] Mohamed A Elmansouri and Dejan S Filipovic. "Miniaturization of TEM horn using spherical modes engineering." In: *IEEE Transactions on Antennas and Propagation* 64.12 (2016), pp. 5064–5073 (cit. on pp. 45, 148, 149).

[75] C. D Morales et al. "Additive Manufacturing of a Uniaxial Anisotropic Dielectric Material for Antenna Applications." In: *16èmes Journées de Caractérisation Microondes et Matériaux (JCMM)*. 2020, pp. 1–4 (cit. on pp. 65, 85, 151).

[76] Marc Thevenot et al. "A Dielectric Resonator Antenna designed with a structured dielectric material." In: *2018 IEEE Conference on Antenna Measurements & Applications (CAMA)*. IEEE. 2018, pp. 1–2 (cit. on pp. 65, 83, 84).

[77] Gautier Mazingue et al. "3D Printed Ceramic Antennas for Space Applications." In: *14th European Conference on Antennas and Propagation (EuCAP)*. IEEE. 2020, pp. 1–5 (cit. on pp. 65, 83, 84).

[78] Mohammad Vaezi, Hermann Seitz, and Shoufeng Yang. "A review on 3D micro-additive manufacturing technologies." In: *The International Journal of Advanced Manufacturing Technology* 67.5-8 (2013), pp. 1721–1754 (cit. on p. 66).

[79] Choon Wee Joel Lim et al. "An Overview of 3-D Printing in Manufacturing, Aerospace, and Automotive Industries." In: *IEEE Potentials* 35.4 (2016), pp. 18–22 (cit. on p. 66).

[80] Nannan Guo and Ming C Leu. "Additive manufacturing: technology, applications and research needs." In: *Frontiers of Mechanical Engineering* 8.3 (2013), pp. 215–243 (cit. on p. 66).

[81] Mukul Ramola, Vinod Yadav, and Rakesh Jain. "On the adoption of additive manufacturing in healthcare: a literature review." In: *Journal of Manufacturing Technology Management* (2019) (cit. on p. 66).

[82] Oscar A Peverini et al. "Additive manufacturing of Ku/K-band waveguide filters: a comparative analysis among selective-laser melting and stereo-lithography." In: *IET Microwaves, Antennas & Propagation* 11.14 (2017), pp. 1936–1942 (cit. on pp. 66, 68).

[83] Paul Booth and Elena Valles Lluch. "Enhancing the performance of waveguide filters using additive manufacturing." In: *Proceedings of the IEEE* 105.4 (2016), pp. 613–619 (cit. on pp. 66, 75, 76).

[84] Abolfazl Zolfaghari, Tiantong Chen, and Y Yi Allen. "Additive manufacturing of precision optics at micro and nanoscale." In: *International Journal of Extreme Manufacturing* 1.1 (2019), p. 012005 (cit. on p. 66).

[85] Zachary Larimore et al. "Additive manufacturing of Luneburg lens antennas using space-filling curves and fused filament fabrication." In: *IEEE Transactions on Antennas and Propagation* 66.6 (2018), pp. 2818–2827 (cit. on p. 66).

[86] Fan Zhou et al. "Additive manufacturing of a 3D terahertz gradient-refractive index lens." In: *Advanced Optical Materials* 4.7 (2016), pp. 1034–1040 (cit. on p. 66).

[87] Chinwe C Njoku, William G Whittow, and JC Vardaxoglou. "Effective permittivity of heterogeneous substrates with cubes in a 3-D lattice." In: *IEEE Antennas and Wireless Propagation Letters* 10 (2011), pp. 1480–1483 (cit. on p. 66).

[88] Flaviana Calignano et al. "Overview on Additive Manufacturing Technologies." In: *Proceedings of the IEEE* 105.4 (2017), pp. 593–612 (cit. on pp. 66–69).

[89] Kaufui V Wong and Aldo Hernandez. "A review of additive manufacturing." In: *ISRN Mechanical Engineering* 2012 (2012) (cit. on pp. 66, 68, 69).

[90] Mario D'Auria et al. "3-D printed metal-pipe rectangular waveguides." In: *IEEE Transactions on Components, Packaging and Manufacturing Technology* 5.9 (2015), pp. 1339–1349 (cit. on pp. 67, 74).

[91] Paul I Deffenbaugh, Raymond C Rumpf, and Kenneth H Church. "Broadband microwave frequency characterization of 3-D printed materials." In: *IEEE Transactions on Components, Packaging and Manufacturing Technology* 3.12 (2013), pp. 2147–2155 (cit. on p. 70).

[92] Luca Catarinucci et al. "Microwave characterisation of polylactic acid for 3D-printed dielectrically controlled substrates." In: *IET Microwaves, Antennas & Propagation* 11.14 (2017), pp. 1970–1976 (cit. on p. 70).

[93] Shiyu Zhang et al. "Novel 3D printed synthetic dielectric substrates." In: *Microwave and Optical Technology Letters* 57.10 (2015), pp. 2344–2346 (cit. on p. 70).

[94] Stefano Moscato et al. "Infill dependent 3D-printed material based on NinjaFlex filament for antenna applications." In: *IEEE Antennas and Wireless Propagation Letters* 15.1 (2016), pp. 1506–1509 (cit. on pp. 70, 71, 73, 79, 80).

[95] Athanasios Goulas et al. "The impact of 3D printing process parameters on the dielectric properties of high permittivity composites." In: *Designs* 3.4 (2019), p. 50 (cit. on p. 71).

[96] William J Chappell et al. "Ceramic synthetic substrates using solid freeform fabrication." In: *IEEE Transactions on Microwave Theory and Techniques* 51.3 (2003), pp. 752–760 (cit. on p. 71).

[97] Beatriz Martinez et al. "Manufacturing tolerance analysis, fabrication, and characterization of 3-D submillimeter-wave electromagnetic-bandgap crystals." In: *IEEE transactions on microwave theory and techniques* 55.4 (2007), pp. 672–681 (cit. on pp. 71, 72).

[98] DV Isakov et al. "3D printed anisotropic dielectric composite with meta-material features." In: *Materials & Design* 93 (2016), pp. 423–430 (cit. on p. 72).

[99] Shiyu Zhang, William Whittow, and John (Yiannis) C Vardaxoglou. "Additively manufactured artificial materials with metallic meta-atoms." In: *IET Microwaves, Antennas & Propagation* 11.14 (2017), pp. 1955–1961 (cit. on pp. 72, 73).

[100] James Tribe et al. "Additively manufactured heterogeneous substrates for three-dimensional control of local permittivity." In: *Electronics Letters* 50.10 (2014), pp. 745–746 (cit. on pp. 72, 73).

[101] Raymond C Rumpf et al. "Spatially variant periodic structures in electromagnetics." In: *Philosophical Transactions of the Royal Society A: Mathematical, Physical and Engineering Sciences* 373.2049 (2015), p. 20140359 (cit. on p. 73).

[102] Etienne Laplanche et al. "Additive manufacturing of low cost and efficient proof of concepts for microwave passive components." In: *IET Microwaves, Antennas & Propagation* 11.14 (2017), pp. 1997–2004 (cit. on pp. 74, 75).

[103] Junyu Shen and David S Ricketts. "Additive manufacturing of complex millimeter-wave waveguides structures using digital light processing." In: *IEEE Transactions on Microwave Theory and Techniques* 67.3 (2019), pp. 883–895 (cit. on pp. 74, 75).

[104] Michael Kilian et al. "Waveguide components for space applications manufactured by additive manufacturing technology." In: *IET Microwaves, Antennas & Propagation* 11.14 (2017), pp. 1949–1954 (cit. on p. 74).

[105] Giuseppe Addamo et al. "Additive manufacturing of Ka-band dual-polarization waveguide components." In: *IEEE Transactions on Microwave Theory and Techniques* 66.8 (2018), pp. 3589–3596 (cit. on p. 74).

[106] Nicolas Delhote et al. "Ceramic layer-by-layer stereolithography for the manufacturing of 3-D millimeter-wave filters." In: *IEEE Transactions on Microwave Theory and Techniques* 55.3 (2007), pp. 548–554 (cit. on p. 75).

[107] Nicolas Delhote et al. "Innovative Shielded High Q Dielectric Resonator Made of Alumina by Layer-by-Layer Stereolithography." In: *IEEE microwave and wireless components letters* 17.6 (2007), pp. 433–435 (cit. on p. 75).

[108] Carlos Carceller et al. "Development of monoblock TM dielectric resonator filters with additive manufacturing." In: *IET Microwaves, Antennas & Propagation* 11.14 (2017), pp. 1992–1996 (cit. on p. 75).

[109] Andrea Vallecchi et al. "3-D printed bandpass filters with coupled vertically extruded split ring resonators." In: *IEEE Transactions on Microwave Theory and Techniques* 67.11 (2019), pp. 4341–4352 (cit. on pp. 75, 76).

[110] Chiara Mariotti et al. "High-performance RF devices and components on flexible cellulose substrate by vertically integrated additive manufacturing technologies." In: *IEEE Transactions on Microwave Theory and Techniques* 65.1 (2016), pp. 62–71 (cit. on pp. 76, 77).

[111] Mohd Ifwat Mohd Ghazali et al. "Embedded actives using additive manufacturing for high-density RF circuits and systems." In: *IEEE Transactions on Components, Packaging and Manufacturing Technology* 9.8 (2019), pp. 1643–1651 (cit. on pp. 76, 77).

[112] Junqiang Wu et al. "Monopole antenna radiation pattern control via 3-D-Printed dielectrics." In: *IEEE Transactions on Antennas and Propagation* 65.8 (2017), pp. 3869–3876 (cit. on pp. 77, 78).

[113] AM Bobreshov et al. "Biconical antenna with inhomogeneous dielectric lens for UWB applications." In: *Electronics Letters* 56.17 (2020), pp. 857–859 (cit. on p. 77).

[114] Maria García-Vigueras et al. "Cost-effective dual-polarised leaky-wave antennas enabled by three-dimensional printing." In: *IET Microwaves, Antennas & Propagation* 11.14 (2017), pp. 1985–1991 (cit. on pp. 78, 79).

[115] Annaig Martin-Guennou et al. "Direct metal laser sintering process investigation: application to 3D slotted waveguide antennas." In: *IET Microwaves, Antennas & Propagation* 11.14 (2017), pp. 1921–1929 (cit. on p. 78).

[116] Muhannad A Al-Tarifi and Dejan S Filipovic. "On the design and fabrication of W-band stabilised-pattern dual-polarised horn antennas with DMLS and CNC." In: *IET Microwaves, Antennas & Propagation* 11.14 (2017), pp. 1930–1935 (cit. on p. 78).

[117] Kai Lu, Kwok Wa Leung, and Nan Yang. "3-D-printed circularly polarized twisted-ridge horn antenna." In: *IEEE Transactions on Antennas and Propagation* 69.3 (2020), pp. 1746–1750 (cit. on p. 79).

[118] Shiyan Wang, Lei Zhu, and Wen Wu. "3-D printed inhomogeneous substrate and superstrate for application in dual-band and dual-CP stacked patch antenna." In: *IEEE Transactions on Antennas and Propagation* 66.5 (2018), pp. 2236–2244 (cit. on pp. 80, 81).

[119] Karl F Brakora, John Halloran, and Kamal Sarabandi. "Design of 3-D monolithic MMW antennas using ceramic stereolithography." In: *IEEE transactions on antennas and propagation* 55.3 (2007), pp. 790–797 (cit. on pp. 81, 82).

[120] Ngoc Tinh Nguyen et al. "Design and characterization of 60-GHz integrated lens antennas fabricated through ceramic stereolithography." In: *IEEE Transactions on Antennas and Propagation* 58.8 (2010), pp. 2757–2762 (cit. on pp. 81, 82).

[121] Geng-Bo Wu et al. "3-D printed circularly polarized modified Fresnel lens operating at terahertz frequencies." In: *IEEE Transactions on Antennas and Propagation* 67.7 (2019), pp. 4429–4437 (cit. on p. 81).

[122] Kyoung Ho Jeong and Nima Ghalichechian. "3D-printed 4-zone Ka-band Fresnel lens: design, fabrication, and measurement." In: *IET Microwaves, Antennas & Propagation* 14.1 (2020), pp. 28–35 (cit. on pp. 81, 82).

[123] Shiyu Zhang et al. "Ultra-wideband flat metamaterial GRIN lenses assisted with additive manufacturing technique." In: *IEEE Transactions on Antennas and Propagation* 69.7 (2020), pp. 3788–3799 (cit. on p. 81).

[124] JM Poyanco, F Pizarro, and E Rajo-Iglesias. "Wideband hyperbolic flat lens in the Ka-band based on 3D-printing and transformation optics." In: *Applied Physics Letters* 118.12 (2021), p. 123503 (cit. on p. 81).

[125] Payam Nayeri et al. "3D printed dielectric reflectarrays: Low-cost high-gain antennas at sub-millimeter waves." In: *IEEE Transactions on Antennas and Propagation* 62.4 (2014), pp. 2000–2008 (cit. on p. 82).

[126] Shiyu Zhang. "Three-dimensional printed millimetre wave dielectric resonator reflectarray." In: *IET Microwaves, Antennas & Propagation* 11.14 (2017), pp. 2005–2009 (cit. on pp. 82, 83).

[127] B. Li et al. "A 3-D-Printed Wideband Circularly Polarized Dielectric Reflectarray of Cross-Shaped Element." In: *IEEE Antennas Wireless Propagation Letters* 19.10 (2020), pp. 1734–1738 (cit. on p. 83).

[128] Z.-X. Xia, K. W. Leung, and K. Lu. "3-D-Printed Wideband Multi-Ring Dielectric Resonator Antenna." In: *IEEE Antennas Wireless Propagation Letters* 18.10 (2019), pp. 2110–2114 (cit. on pp. 83, 84).

[129] V. Basile et al. "Design and Manufacturing of Super-Shaped Dielectric Resonator Antennas for 5G Applications Using Stereolithography." In: *IEEE Access* 8 (2020), pp. 82929–82937 (cit. on pp. 84, 85).

[130] Quentin Lamotte et al. "Multi-permittivity 3D-printed Ceramic Dual-Band Circularly Polarized Dielectric Resonator Antenna for Space Applications." In: *15th European Conference on Antennas and Propagation (EuCAP)*. IEEE. 2021, pp. 1–5 (cit. on p. 84).

[131] Matias Cuevas et al. "Parametric Study of a Fully 3D-Printed Dielectric Resonator Antenna Loaded With a Metallic Cap." In: *IEEE Access* 9 (2021), pp. 73771–73779 (cit. on pp. 84, 85).

[132] C.D Morales et al. "3D-printed ceramics with engineered anisotropy for dielectric resonator antenna applications." In: *Electronics Letters* (2021) (cit. on pp. 85, 89).

[133] Constantine A Balanis. *Advanced engineering electromagnetics*. John Wiley & Sons, 1999 (cit. on p. 86).

[134] Keqian Zhang et al. *Electromagnetic theory for microwaves and optoelectronics*. Springer, 1998 (cit. on p. 86).

[135] Raymond C Rumpf. "Engineering the dispersion and anisotropy of periodic electromagnetic structures." In: *Solid State Physics* 66 (2015), pp. 213–300 (cit. on p. 88).

[136] F. Doreau, C. Chaput, and T. Chartier. "Stereolithography for Manufacturing Ceramic Parts." In: *Advanced engineering materials* 2.8 (2000), pp. 493–496 (cit. on p. 89).

[137] Ahmad B Numan and Mohammad S Sharawi. "Extraction of material parameters for metamaterials using a full-wave simulator [education column]." In: *IEEE Antennas and Propagation Magazine* 55.5 (2013), pp. 202–211 (cit. on pp. 89, 151).

[138] 3D Ceram Sinto. *Focus on tolerances*. URL: `http://www.3dceram.com.` (cit. on p. 89).

[139] AM Nicolson and GF Ross. "Measurement of the intrinsic properties of materials by time-domain techniques." In: *IEEE Transactions on instrumentation and measurement* 19.4 (1970), pp. 377–382 (cit. on p. 91).

[140] William B Weir. "Automatic measurement of complex dielectric constant and permeability at microwave frequencies." In: *Proceedings of the IEEE* 62.1 (1974), pp. 33–36 (cit. on p. 91).

[141] Paul I Deffenbaugh, Raymond C Rumpf, and Kenneth H Church. "Broadband microwave frequency characterization of 3-D printed materials." In: *IEEE Transactions on Components, Packaging and Manufacturing Technology* 3.12 (2013), pp. 2147–2155 (cit. on p. 92).

[142] C. D Morales et al. "Single-fed circularly polarized dielectric resonator antenna using a uniaxial anisotropic material." In: *Antennas and Propagation Conference (APC)*. IEEE. 2019, pp. 1–5 (cit. on p. 96).

[143] James R James. *Handbook of microstrip antennas*. Vol. 1. IET, 1989 (cit. on p. 96).

[144] William L Langston and David R Jackson. "Impedance, axial-ratio, and receive-power bandwidths of microstrip antennas." In: *IEEE transactions on antennas and propagation* 52.10 (2004), pp. 2769–2774 (cit. on pp. 96, 111).

[145] Joshua M Kovitz and Yahya Rahmat-Samii. "Using thick substrates and capacitive probe compensation to enhance the bandwidth of traditional CP patch antennas." In: *IEEE Transactions on Antennas and Propagation* 62.10 (2014), pp. 4970–4979 (cit. on p. 96).

[146] MB Oliver et al. "Circularly polarised rectangular dielectric resonator antenna." In: *Electronics Letters* 31.6 (1995), pp. 418–419 (cit. on pp. 96, 111).

[147] M Haneishi and H Takazawa. "Broadband circularly polarised planar array composed of a pair of dielectric resonator antennas." In: *Electronics Letters* 21.10 (1985), pp. 437–438 (cit. on pp. 96, 111).

[148] Aldo Petosa and Apisak Ittipiboon. "Dielectric resonator antennas: A historical review and the current state of the art." In: *IEEE antennas and Propagation Magazine* 52.5 (2010), pp. 91–116 (cit. on p. 97).

[149] Saeed Fakhte and Homayoon Oraizi. "Analysis and design of rectangular uniaxial and biaxial anisotropic dielectric resonator antennas." In: *Progress In Electromagnetics Research* 62 (2016), pp. 43–50 (cit. on p. 97).

[150] Rogers Corporation. *RO3000® Series Circuit MaterialsRO3003™, RO3006™, RO3010™ and RO3035™High Frequency Laminates*. 2019. URL: https://rogerscorp.com/-/media/project/rogerscorp/documents/advanced-connectivity-solutions/english/data-sheets/ro3000-laminate-data-sheet-ro3003----ro3006----ro3010----ro3035.pdf (cit. on p. 119).

[151] Pro-power. *Semi Rigid, RG405 datasheet*. 2011. URL: https://datasheet.octopart.com/RG405-Pro-datasheet-11478891.pdf (cit. on p. 119).

[152] J.D Krausand and R.J. Marhefka. *Antennas for All Applications*. 3rd edition. McGraw-Hill, 2003 (cit. on p. 119).

[153] Clemens Icheln, Joonas Krogerus, and Pertti Vainikainen. "Use of balun chokes in small-antenna radiation measurements." In: *IEEE Transactions on Instrumentation and Measurement* 53.2 (2004), pp. 498–506 (cit. on p. 119).

[154] Yongmei Pan and Kwok Wa Leung. "Wideband circularly polarized trapezoidal dielectric resonator antenna." In: *IEEE Antennas and Wireless Propagation Letters* 9 (2010), pp. 588–591 (cit. on p. 142).

[155] Saeed Fakhte et al. "A new wideband circularly polarized stair-shaped dielectric resonator antenna." In: *IEEE Transactions on Antennas and Propagation* 63.4 (2015), pp. 1828–1832 (cit. on p. 142).

[156] Liang Lu et al. "Wideband circularly polarized antenna with stair-shaped dielectric resonator and open-ended slot ground." In: *IEEE Antennas and Wireless Propagation Letters* 15 (2016), pp. 1755–1758 (cit. on p. 142).

[157] Yinchao Chen and T Simpson. "Radiation pattern analysis of arbitrary wire antennas using spherical mode expansions with vector coefficients." In: *IEEE Transactions on Antennas and Propagation* 39.12 (1991), pp. 1716–1721 (cit. on pp. 145–147).

[158] Tomislav Marinovic. "Vector Spherical Harmonic Expansion." In: () (cit. on pp. 145, 148).

[159] Matthew NO Sadiku. *Numerical techniques in electromagnetics*. CRC press, 2000 (cit. on p. 146).

[160] George B Arfken and Hans J Weber. *Mathematical methods for physicists*. 1999 (cit. on p. 146).

[161] Jussi Rahola, Fabio Belloni, and Andreas Richter. "Modelling of radiation patterns using scalar spherical harmonics with vector coefficients." In: *2009 3rd European Conference on Antennas and Propagation*. IEEE. 2009, pp. 3361–3365 (cit. on p. 147).

[162] Billy C Brock. *Using vector spherical harmonics to compute antenna mutual impedance from measured or computed fields*. Tech. rep. Sandia National Labs., Albuquerque, NM, and Livermore, CA (US), 2000 (cit. on p. 148).

[163] Z Hafdi, S Zemouli, and A Chaabi. "Retrieval of effective parameters of left handed materials by using different approaches." In: *8th International Conference on Electrical and Electronics Engineering (ELECO)*. IEEE. 2013, pp. 427–430 (cit. on p. 151).

Abstract —

Unmanned aerial vehicle (UAV) and nanosatellites are being deployed on a massive scale for industrial and research applications. In practice, these small platforms require the integration of several compact antennas to cover the different needs in communication, navigation, or surveillance. The integration of these antennas is even more difficult as these platforms often offer small ground planes. An original solution to provide directive radiation properties without a ground plane relies on the design of Huygens sources. Cardioid radiation pattern can thus be achieved by combining two orthogonal electric and magnetic dipoles radiating the same field in their E- and H- planes, respectively.

In this work, several dielectric resonator antennas (DRAs) exhibiting Huygens source properties are studied. In order to generate both equivalent electric and magnetic dipoles, numerous TE modes can be excited in a rectangular DRA. Thus, by using the numerous degrees of freedom in their design, it is possible to take advantage of their reduced size, ease of excitation, high radiation efficiency, and wide bandwidth. More specifically, additive manufacturing, or 3-D-printing, has here been used to realize the proposed DRAs. 3-D-printing paves the way for new antennas using complex shapes and heterogeneous/anisotropic materials to control, for instance, its impedance bandwidth and radiation characteristics.

During this Ph.D. thesis, two Huygens source antennas in linear and circular polarization using stacked dielectric resonators have first been studied. The stacked configuration is here formed by two resonators with different isotropic dielectric permittivities in order to generate a pair of equivalent electric and magnetic dipoles, required to achieve a cardioid radiation pattern. Then, it is shown that an original solution to reduce the volume of the stacked Huygens consists in using a uniaxial anisotropic dielectric.

Anisotropic dielectric has thus been designed by structuring the 3-D-printed material in several sub-wavelength unit cells to obtain a material which effective dielectric permittivity is controlled by the volume fill rate of its unit cells. In order to demonstrate the possibilities offered by 3-D-printing of anisotropic ceramics, a single-fed circularly polarized DRA in the 2.45 GHz ISM band has first been designed, 3-D-printed, and measured. The anisotropy has here been used to excite two orthogonal modes with certain conditions in magnitude and phase to achieve circular polarization. Finally, the design of a compact Huygens source antenna using engineered dielectric anisotropy within 3-D-printed ceramics in the 2.45 GHz ISM is presented.

Keywords: Dielectric resonator antenna (DRA), Huygens source, three-dimensional (3-D) printing, anisotropic media.

Résumé —

Des véhicules aériens sans pilote (UAV) et des nanosatellites sont déployés à grande échelle dans le but de servir pour des applications industrielles et de recherche. Dans la pratique, ces petites plateformes demandent l'intégration de plusieurs antennes compactes pour différents besoins en communication, navigation, ou encore surveillance. L'intégration de ces antennes sur de telles plateformes est donc plus difficile en raison de ses petits plans de masse. L'une des solutions originales permettant de fournir des propriétés de rayonnement directives sans utiliser des grands plans de masse, repose sur la conception des sources de Huygens. Un diagramme de rayonnement cardioïde peut, de ce fait, être réalisé en combinant deux dipôles orthogonaux électriques et magnétiques rayonnant le même champ, respectivement dans leurs plans E et H.

Dans ce travail, plusieurs antennes à résonateur diélectrique (DRA) avec propriétés d'une source de Huygens sont étudiées. Afin de générer des dipôles électriques et magnétiques équivalents, plusieurs TE modes peuvent être excités dans un résonateur diélectrique rectangulaire. De ce fait, en utilisant les nombreux degrés de liberté de leur conception, il est possible de concevoir des DRAs de tailles réduites avec des propriétés d'efficacité de rayonnement élevées et de larges bandes passantes. En d'autres termes, la fabrication additive, ou l'impression 3D, a ici été utilisée pour fabriquer les DRAs proposés. L'impression 3D ouvre la voie à de nouvelles antennes utilisant des formes complexes et des matériaux hétérogènes/anisotropes afin de contrôler, par exemple, sa bande passante et ses caractéristiques de rayonnement.

Au cours de cette thèse, deux sources de Huygens en polarisation linéaire et circulaire, et utilisant des résonateurs diélectriques empilés, ont d'abord été étudiées. La configuration empilée est ici formée par deux résonateurs avec des permittivités diélectriques isotropes différentes afin de générer une paire de dipôles électriques et magnétiques équivalents, nécessaires à l'obtention d'un rayonnement dans un demi-espace. Il est par la suite démontré qu'utiliser un diélectrique anisotrope uniaxial est une solution originale permettant de réduire le volume de ces sources de Huygens empilées.

Le diélectrique anisotrope a ainsi été conçu en structurant le matériau 3D imprimé en plusieurs cellules unitaires de sous-longueur d'onde pour obtenir un matériau dont la permittivité diélectrique effective est contrôlée par le taux de remplissage de volume de ses cellules unitaires. Afin de démontrer les possibilités offertes par l'impression 3D de céramiques anisotropes, une antenne DRA à alimentation unique et à polarisation circulaire dans la bande ISM 2.45 GHz a d'abord été conçue, imprimée et mesurée. L'anisotropie a ici été utilisée pour exciter deux modes orthogonaux avec certaines conditions de amplitude et phase, afin d'obtenir une polarisation circulaire. Enfin, une source de Huygens compacte est conçu, utilisant un diélectrique céramique anisotrope dans la bande ISM 2.45 GHz.

Mots clés : Antenne à résonateur diélectrique (DRA), source de Huygens, impression tridimensionnelle (3D), matériau anisotrope.